Summer 2009

Microstructural influence on dynamic properties of age hardenable FeMnAl alloys

Ryan A. Howell

MICROSTRUCTURAL INFLUENCE ON DYNAMIC PROPERTIES OF AGE HARDENABLE FeMnAl ALLOYS

by

RYAN ANDREW HOWELL

A DISSERTATION

Presented to the Faculty of the Graduate School of the

MISSOURI UNIVERSITY OF SCIENCE AND TECHNOLOGY

In Partial Fulfillment of the Requirements for the Degree

DOCTOR OF PHILOSOPHY

in

METALLURGICAL ENGINEERING

2009

Approved by

David C. Van Aken, Advisor
Ernest S. C. Chin, Military Advisor
Von L. Richards
Julia E. Medvedeva
Kent D. Peaslee
Greg E. Hilmas

PUBLICATION DISSERTATION OPTION

This dissertation has been prepared in the form of six manuscripts for publication. Pages 6-62 and 119-136 have been published in the Transactions of the Association for Iron and Steel Technology. Pages 163-195 have been published in the Proceedings of the Association for Iron and Steel Technology 2009. Pages 63-89 have been published in the Transactions of the American Foundry Society, 2008. Pages 90-118 have been published in the Transactions of the American Foundry Society, 2009. Pages 137-166 have been prepared in the style utilized by the Metallurgical and Materials Transactions A. The Introduction, Summary, and appendices A, B and C have been added to provide supplemental information to select experimental procedures and calculations.

ABSTRACT

A lightweight castable alloy was sought to reduce the MIL-PRF-32269 class II cast steel perforated armor's weight with the requirement that the material had to be manufactured utilizing existing foundry technology and without incurring large alloy cost increases to meet property requirements. Literature on wrought age hardenable Fe-Mn-Al-C alloys suggested this alloy system could achieve weight reduction through high aluminum concentrations with the highest reported strengths exceeding 2 GPa for a Fe-30Mn-9Al-0.9C composition. Even though ballistic testing had not been conducted on this system, high strain rate data of wrought alloys showed excellent work hardenability; greater than existing ballistic metals. Cast material property information was severely limited, thus, a systematic approach was employed to develop casting and processing techniques and assess related structure property relationships of a nominal silicon modified Fe-30Mn-9Al-0.9C-0.5Mo alloy for ballistic use.

Castability was addressed first as this information was crucial for making test coupons and assisting foundries with production of MIL-PRF-32269 ballistic test plates. Four silicon concentrations were investigated for fluidity, microstructure, liquidus, solidus and dendrite coherency point. Silicon was added because it is known to increase fluidity of other ferrous alloys and has also been shown to eliminate a brittle β-Mn phase in wrought Fe-Mn-Al-C alloys.

Of the four silicon modified fluidity compositions, two were selected for heat treat property evaluation on the basis of microstructure. Hardness, strength, and ductility were measured (hardness is the only MIL-PRF-32269 measured property). The alloy with the highest ductility was selected for high strain rate evaluation. The strain rate testing results were the final means to lock in the alloy composition and heat treatment for solid plate ballistic testing.

While conducting V_{50} ballistic testing, phosphorus content was correlated to ballistic impact energy. Further testing was conducted to examine phosphorus, quench sensitivity, and aging Charpy V-Notch effects.

The culmination of this thesis work resulted with positive ballistic threat testing revealing the alloy investigated here meets the Army's MIL-PRF-32269 ballistic requirements and reduces P900 weight by 13%.

ACKNOWLEDGEMENTS

First and foremost, I am forever indebted to my gracious and wonderful wife Katie for her sacrifices that allowed me to focus and complete this persevering process. I cannot express my love in words nor repay the time allotted by her over the past three years. Without her support and motivation none of this would have been possible. And to my children John, Maggie, and Charlie I am thankful for their never ending source of love and entertainment.

My being able to complete this program would not have been possible without the opportunity and support of the Army Acquisition Corps and the Uniformed Army Scientist and Engineer program. I know mother ARMY will extract its return of service for this degree, but I offer it freely and gratefully as I never envisioned this opportunity during my time as a Field Artillery officer.

Throughout this process I have relearned the importance of team effort as the one assembled here has lifted me up to a higher level of knowledge and understanding, and for their contribution to my success, I single out and offer my thanks to those members.

I thank Dr. David C. Van Aken, Dr. Ernest C. Chin and Dr. Von Richards for their guidance, support and patience as my research advisors throughout the course of my studies and research. I offer a hearty thank you to Dr. Simon Lekakh, Dr. Jonathan Montgomery, Dr. Tusit Weerasooriya and Dr. Julia Medvedeva without whom I could not have tested nor comprehended aspects of my research throughout the process. To Dr. Kent D. Peaslee and Dr. Greg Hilmas I thank them for direction and course correction valuable to the completion of my degree. To Mr. Donnie Little and Mr. Kirk Stoffel I am ever grateful for the testing opportunity without which my personal purpose and goals would have been unfulfilled. I would like to thank the technicians, graduate and undergraduate students who I had the distinct honor of working with and who have assisted me, particularly Mr. Nathan Inskip, Mr. Jack Jones and Mr. Sam Buckholz.

Lastly, I want to the United States Army Acquisition Corps for the educational opportunity and funding of my research. My eyes have been opened unto a world I knew nothing of. I hope to do all that I can in future military and civilian positions to serve admirably to repay this wonderful experience.

TABLE OF CONTENTS

LIST OF ILLUSTRATIONS

Figure Page

PAPER 1

LIST OF TABLES

1. INTRODUCTION

1.1. PROJECT PURPOSE AND OBJECTIVE

The objective of this project was to reduce the weight of class II perforated homogenous armor in accordance with the military performance specification MIL-PRF-32269[1] design criteria with the objective of maintaining or improving the armor class' ballistic performance. The goal was to develop an alloy utilizing existing infrastructure and manufacturing means so as to minimize potential cost increases over current solutions due to alloy selection. Regarding manufacturing, the perforated armor's complex geometric design preferentially favors a cast manufacturing process over a higher cost and greater time consuming wrought alloy machining process.

Class II cast perforated homogenous armor, or P900[2], was historically designed to counter Soviet small arms' threats. This type of armor has found recent application against current threats, and as such, is in demand and under scrutiny for weight reduction as the MIL-PRF-32269 requirements dictated steel chemistries only. Suitable alloy replacements (magnesium, aluminum, titanium, or cast iron alloys) required to achieve equivalent performance and reduce weight have not been found. As such, the added weight of this and other systems to current platforms has taxed and limited their maneuverability, mobility, and lethality.

To achieve the objective, research was focused on developing ferrous alloy alternatives. Alloy exploration led to investigation of non-traditional second generation Fe-Mn-Al-C wrought alloys[3] being examined by the automotive industry that contains 20 to 30% manganese, 5 to 12% aluminum, and 0.3 to 1.2% carbon. The weight reduction and comparable strengths to cast steel alloys[4] held promise, but an extensive literature

review (see Paper 1: A Literature Review of Age Hardening Fe-Mn-Al-C Alloys) showed little or no knowledge of cast Fe-Mn-Al-C alloy properties. Therefore, a set of linearly related tests were designed to evaluate the material; the premise being that manufacturability (and related alloying during melting and pouring) fixed the heat treatment boundaries limiting the usable window of structure property relationships.

1.2 Fe-Mn-Al-C ALLOY COMPOSITION SELECTION

Alloy consideration was restricted to systems that could accommodate open air or limited atmosphere control induction melting and heat treatment, matching common industrial foundry and heat treat capability that would allow rapid technology transition upon successful completion of casting alloy development and ballistic testing. Such resourced facilities were deemed the most likely target audience due to existing P900 production at induction furnace equipped facilities[5]. Further restriction was placed to obtain a light weight steel as steel has shown to be the only alloy capable of meeting quasi-static and ballistic acceptance requirements[6]. The only mechanical property of the military performance specification MIL-PRF-32269 for perforated homogeneous armor was the hardness tolerance range of 302 to 350 BHN for class II cast steel armor[1].

A 2006 investigation into a wrought Fe-26Mn-11Al-1.15C alloy by Frommeyer and Brux showed promising potential to meet both the MIL-PRF-32269 and self imposed manufacturing boundary conditions[1,3]. This nontraditional three phase or TRIPLEX ferrous alloy showed outstanding density reduction for increasing aluminum content, was produced by induction melting under argon cover, and attained yield and tensile strengths greater than 1,000 MPa in an aged condition. Literature investigations revealed that the Fe-Mn-Al-C system is capable of tensile strength exceeding 2,000 MPa[7] for an overall

nominal chemistry of Fe-30Mn-9Al-0.9C. High strain rate testing by Frommeyer and Brux[3] showed that as strength increased with strain rate, ductility exceeded 30% even at 1000 s^{-1}, indicating that ballistic evaluation may be favorable. All of the characteristics sought to meet the project goals appeared to be contained within the Fe-Mn-Al-C system. Replicating the wrought Fe-Mn-Al-C alloy in cast form did present one significant restriction; no means other than mechanical processing was known for producing an equiaxed grain structure. The focus, then, was on achieving wrought properties without replicating the wrought microstructure for ballistic testing.

In addition to its high strength, the Fe-30Mn-9Al-0.9C composition showed that the matrix phase constitution could be reduced to a fully austenitic structure when solution treated[8], maximizing the austenite's aged strength contribution to mechanical properties and confining the microstructure constitution to two phase austenite plus κ-carbide. However, aging produced an extremely brittle and deleterious β-manganese phase in addition to κ-carbide[8]. Silicon additions were shown to prevent β-manganese precipitation[9]. The last alloy consideration was molybdenum since the effect of phosphorus in Fe-Mn-Al-C systems had not been reported and the assumption was that phosphorus could be countered with a molybdenum addition to form a stable phase and minimize fracture toughness phosphorus effects as has been shown in traditional steel alloys[10]. Thus the composition for initial investigation was established as a silicon modified Fe-30Mn-9Al-XSi-0.9C-0.5Mo alloy.

1.3 ALLOY DEVELOPMENT METHODOLOGY

Executing under the premise that the materials' aging kinetics and structure property relationships are related back to foundry practice, the first experiment began with a

fundamental foundry study of the alloy's castability. An embedded study examined cast and solution treated microstructure; the combination of the two studies isolated alloy and solution treatment boundary conditions (see Paper 2: The Effect of Silicon Content on the Fluidity and Microstructure of Fe-Mn-Al-C Alloys). This preceded mold and casting production for aging and mechanical test specimens necessary for structure property relationship investigation (see Paper 3: Tensile, High Strain Rate Compression and Microstructural Evaluation of Lightweight Age Hardenable Cast Fe-30Mn-9Al-XSi-0.9C-0.5Mo Steel). The structure property investigation established down-select criteria for final ballistic testing and failure examination (see Paper 4: Advancements in Steel for Weight Reduction for Weight Reduction of P900 Armor Plate). Ballistic testing showed correlation to phosphorus content and impact energy of aged material forcing a final investigation conducted to relate these items and characterize quench sensitivity (see Paper 5: Phosphorus and Thermal Processing Effects on Charpy V-Notch Impact Toughness of Lightweight Fe-30Mn-9Al-1Si-0.9C-0.5Mo Alloy Steel).

1.3.1. Castability Evaluation. Fluidity spirals were produced for evaluation and comparison of silicon modified nominal Fe-30Mn-9Al-XSi-0.9C-0.5Mo alloys versus low alloy steel, representative of current P900 alloys[1]. Thermocouple equipped molds provided liquidus and solidus information to normalize all data onto a single superheat figure for analysis. From each of the silicon containing alloy spirals, samples were prepared for optical analysis in the as cast condition and solution treated condition. The combined fluidity and solution treated analysis drove silicon content restrictions for mechanical test specimen production and provided modeling parameters to feed casting software for test specimen and P900 mold designs and analysis necessary to transition the

technology to production. Aston Met Services measured chemical content by inductive coupled plasma spectrometry and wavelength dispersive spectrometry. This method was employed throughout due to unavailable arc spectrometer standards for this system.

1.3.2. Aging Kinetics, Quasi-Static and Dynamic Physical Properties. Age hardening curves were established for two silicon containing Fe-Mn-Al-C alloys (1% and 1.4%). An aging temperature was targeted below 550°C to avoid grain boundary precipitation as shown by Acselrad et al.[11] Solution treated and two selected age hardening conditions (capable of attaining the MIL-PRF-32269 302-350 BHN requirement) were selected to measure tensile properties.

Hardness measurements were conducted according to ASTM E18 by Rockwell B and Rockwell C measurements and converted to Brinell 3,000 kg load utilizing ASTM E140 conversion Table 1 and Table 2. This method was employed throughout all experiments requiring Rockwell measurements. Rockwell measurements were selectively utilized due to material size constraints preventing multiple Brinell indentations on a single specimen for statistical analysis. An empirical check comparing measured Brinell versus converted Rockwell data both measured on a large plate found that the converted data was in agreement for this system with an error of ± 4% between measured and converted hardness.

Strength (with a minimum ductility of 10% elongation) and maximum energy absorption tensile characteristics were used as the alloy and heat treat down-select criteria for high strain rate compression testing.

Split Hopkinson Bar compression testing provided the final evaluation restrictions for material and heat treat criteria prior to ballistic testing. Two conditions (solution

treated and solution treated and aged 1% silicon containing alloy) were tested to determine which condition achieved the maximum tensile strength. It was found the age hardened condition attained higher strain rate dependent compressive strength, greater than rolled homogeneous armor (a steel used as a class 1 perforated armor).

1.3.3. Ballistic Property Characterization. Two nominal age hardened 1% silicon containing cast alloys were tested with 0.30 caliber armor piercing and 0.50 caliber fragmentation simulation projectiles. Brinell hardness was measured by 3,000 kg load according to ASTM E10. The 0.30 caliber projectile test was specified to make an equivalent areal density comparison to the acceptance criteria of higher density class II steel MIL-PRF-32269 requirements, and the 0.50 caliber test was executed to correlate phosphorus effects on ballistic plug formation to non-ballistic dynamic Charpy V-notch fracture toughness testing.

1.3.4. Fracture Toughness Analysis. Fracture toughness and 0.50 caliber V_{50} testing showed degraded performance with increased phosphorus content, but consideration for initial testing was not given to cooling rate or aging temperature and time parameters. Those additional concerns, along with phosphorus content, were addressed in the last experiment and analysis. Material was provided by multiple sources and heat treated with varying cooling rates and aging parameters to quantify the effects of the previously mentioned variables and combine the parameters into a single constitutive model. Hardness measurements were conducted according to ASTM E18 utilizing Rockwell C and Rockwell B measurements and converted to Brinell 3,000 kg load utilizing ASTM E140 Table 1 and Table 2.

PAPER

1. A Literature Review of Age Hardening Fe-Mn-Al-C Alloys

R.A. Howell, D. C. Van Aken

Army Research Lab

Missouri University of Science and Technology

Department of Materials Science and Engineering

Rolla, MO 65409

Tel.: 573-341-4717

E-mail: dcva@mst.edu

Key Words: Fe-Mn-Al-C, lightweight steel, age hardenable, TRIPLEX, mechanical properties

Published in the American Iron and Steel Technology April 2009 issue.

This review of Fe-Mn-Al-C alloys reports literature published between 1933 and 2008 on age hardenable Fe-Mn-Al-C alloys with chemistries in the range of 18-28wt.%Mn, 9-12wt.%Al, and 0.7-1.2wt.%C. Fe-Mn-Al-C alloys possess low density (6.5 to 7.2 g/cm^3), tensile strengths from 600 to 2,000 MPa, elongation to failure as great as 70%, and they can exhibit high-energy absorption, e.g. specific energy absorption of 0.43 J/mm^3 at strain rates of 10^2 s^{-1}. Solution treatment of FeMnAl alloys above 900°C produces either a fully austenitic or a duplex ferrite and austenite microstructure. Upon age hardening a coherent $(Fe,Mn)_3AlC$ carbide, known as κ-carbide, with a perovskite crystal structure precipitates in the austenite and classic age hardening behavior is observed. Phase equilibria are reviewed as a function of alloy composition and temperature for solution treated and age hardened alloys. Fatigue, fracture, and environmentally induced embrittlement phenomena are also reviewed. The combination of lower density, extensive formability, the ability to age harden, and to absorb energy in a crash makes the Fe-Mn-Al-C alloys a potential advanced high strength steel candidate for the transportation industry. These steels may also be applied as a light-weight casting alloy for military armor. Lightweight steel alloys are sought to reduce the areal density of steel materials utilized for MIL-PRF-32269 perforated homogenous steel armor.

1. INTRODUCTION

Age hardening Fe-Mn-Al-C alloys typically contain 20 to 30% manganese, 5 to 12% aluminum, and 0.3 to 1.2% carbon. Unless otherwise noted, all compositions are reported in weight percent. The Fe-Mn-Al-C alloys evolved from Robert Hadfield's 1882 investigations of an Fe -13Mn -1.2C steel composition that had high toughness and excellent wear resistance.[1] Aging temperatures and times used in many of the subsequent

Fe-Mn-Al-C alloy studies appear to be based upon Hadfield's tempering work, i.e. 550°C for 16 hours. In 1943, Dean and Anderson patented several Fe-Mn-Al-based alloys[2] showing that the addition of manganese (20 to 50 %) to Fe-Al alloys improved the ductility and in 1945[3] the addition of 10% chromium to the FeMnAl alloy was patented for improved corrosion resistance.

Ham and Cairns published their findings on Fe-Mn-Al-C alloys in 1958[4] in response to the US Navy's request to find alternatives to chromium and nickel containing austenitic stainless steels. The historical driving force for the Fe-Mn-Al-C alloy development (up to the 1980's) was the high cost of chromium and nickel in producing stainless steel.[5,6] High levels of aluminum in these alloys provided corrosion and oxidation resistance.[4-9] Ham and Cairns[4] reported a maximum tensile strength due to strain aging of 730 MPa and elongation to failure of 73% for a Fe-34.4Mn-10.2Al-0.76C composition. The amount of cold working and heat treatments used were not specified.

At sufficiently high aluminum and carbon concentration it was discovered that the Fe-Mn-Al-C alloys age hardened.[7] Age hardening studies were conducted by Kayak[10] and James[7] in 1969. Both researchers observed similar age hardening at 550 to 600 °C with peak hardness values between 345 and 475 Brinell Hardness. Solution treatment above 900°C produced either austenitic or duplex microstructures of austenite and ferrite. Fe-Mn-Al-C alloys contain at least four phases (austenite, ferrite, κ-carbide, and β-Mn) after aging between 400 and 900 °C. The main age hardening constituent is κ –carbide, which is an $E2_1$ perovskite crystal structure with composition $(Fe,Mn)_3AlC$.[11] Over aging results in the formation of β-Mn.[12]

Recent research has examined Fe-Mn-Al-C alloys for use in automotive body frames to reduce weight, but maintain or improve crash worthiness.[11] A combination of lower density, extensive formability, the ability to age harden, and to absorb energy in a crash has identified Fe-Mn-Al-C alloys as potential advanced high strength steel. Furthermore, silicon additions to Fe-Mn-Al-C alloys create a light-weight steel alloy with casting characteristics similar to ductile iron[13] and with improved age hardening characteristics.[12,14]

2. PHASE CONSTITUTION

The Fe-Mn-Al-C compositions that produce γ-austenite as the primary phase and compositional boundaries for equilibrium with α-ferrite, κ-carbide, and β-Mn are reviewed. Most phase investigations combine manganese, aluminum, or carbon variation with isothermal heat treatment between 400°C and 1200°C. Phase identification within the Fe-Mn-Al-C system is derived from the early Fe-Mn-Al ternary investigations. Koster and Torn in 1933 published some of the earliest phase equilibria work on the Fe-Mn-Al ternary system.[15] These initial Fe-Mn-Al phase diagrams provided the basis for Schmatz' 1959 phase stability study and lead to the discovery of β-manganese formation in manganese-rich Fe-Mn-Al-C alloys.[9] Schmatz' work was continued by Krivonogov et al.[16], Ishida et al.[17], Goretskii et al.[18], and Acselrad et al.[19] Varying chemistry and thermal processing of Fe-Mn-Al-C alloys has produced at least five equilibrium phases: γ-austenite, α-ferrite, κ-carbide, M_3C carbide, and β-Mn. Austenite is the primary constituent and forms the continuous matrix.[7,10,11,12,16-18,20-25] Ferrite may be present and increases in volume fraction with increasing aluminum concentration from 7 to 12%.[17,18] Isothermal holding between 450 and 900 °C leads to the formation of κ-carbide and β-

Mn.[7,10,11,12,16-18,20-25] A eutectoid reaction (austenite → ferrite + κ-carbide) was reported by James.[7]

A study by Prodhan and Chakrabarti reported on phase constitution in the as-cast and homogenized condition.[26] Upon solidification, the dendritic matrix was primary austenite with interdendritic ferrite. The austenite contained a complex carbide phase for compositions ranging from 5.5 to 9.8% aluminum, 0.27 to 0.91% carbon, and fixed concentrations of 30% manganese and 1.5% silicon. At a fixed manganese content, the austenite volume fraction of the as-cast microstructure increased by either increasing the carbon concentration from 0.3 to 0.9% or decreasing the aluminum content from 10 to 5% (see Figure 1(a)). Phase determination was also performed after homogenization at 1100°C for two hours followed by water quenching. After homogenization, the percent austenite increased from 50 to 100% at the expense of the ferrite for three carbon levels of 0.3, 0.6, and 0.9% (see Figure 1(b)). The three alloys were nearly 100% austenite at 5% aluminum and maintained a high percentage of austenite up to 8% aluminum. Increasing amounts of ferrite were observed for compositions greater than 8% aluminum.

Goretskii and Gorev investigated forged alloys with a fixed 10% aluminum concentration and four manganese levels of 20, 25, 30, and 35 % and carbon ranging from 0.4 to 1.4 %.[18] Specimens were isothermally held at temperatures of 627, 752, 877, 1002, and 1127 °C for time periods of 15, 30, 65, 100, and 250 hours. Two commonalities were observed among all alloys investigated. First, austenite, ferrite, and κ-carbide were present in all alloys processed at 627°C. Second, either a single-phase austenite for high carbon concentrations or a duplex microstructure of austenite and ferrite for low carbon concentrations existed at 1000°C and above. With the exception of

the 20% manganese alloy, all other compositions produced β-Mn in addition to κ-carbide at 627°C.

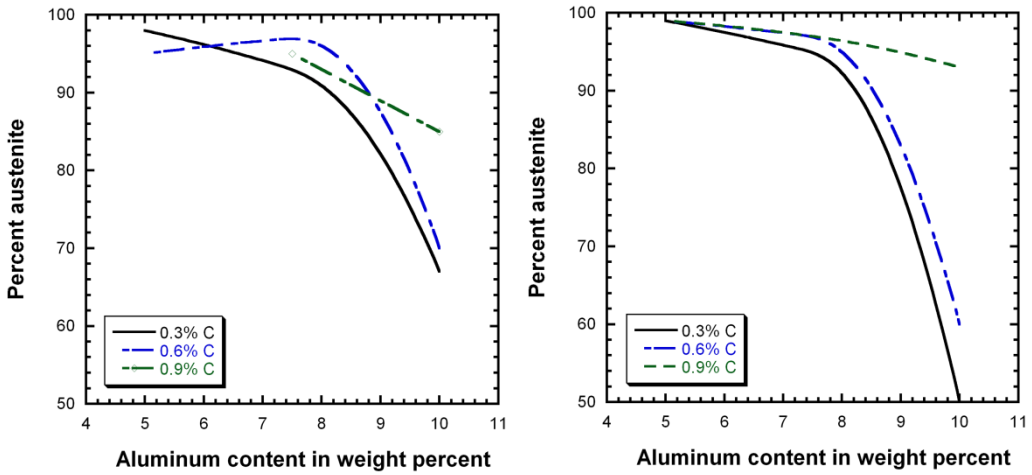

Figure 1. Percent austenite for Fe-30%Mn-1.5%Si as a function of aluminum content for three differing carbon containing alloys of 0.3, 0.6, and 0.9% carbon in the (a) as-cast condition and (b) homogenized at 1100°C for two hours. Austenite volume fraction is the greatest for low aluminum and high carbon amounts. Homogenized specimens are nearly all austenite below 5% aluminum.[26]

Schmatz was the first to report the existence of a β-manganese phase in the manganese-rich corner of the ternary Fe-Mn-Al phase diagram.[9] Steels based on Fe-29Mn-9Al-0.9C contain austenite, ferrite, κ-carbide, and β-Mn when equilibrated at temperatures below 750°C.[20] Increasing the manganese content simultaneously increased austenite and β-Mn stability. Increasing carbon content increased austenite and κ-carbide stability while reducing β-Mn; and, increasing aluminum increased the ferrite content.[17,18]

Phase diagrams for iron- 20 to 35% manganese are plotted as a function of carbon content at various temperatures from 600 to 1200 °C in Figure 2.[18] At 20% manganese, as shown in Figure 2(a), ferrite is not present at 1000°C for carbon concentrations above 1% but is present along with austenite and κ-carbide at lower temperatures. A eutectoid reaction for austenite decomposition to a lamellar ferrite and κ-carbide microstructure occurs at approximately 1.1% carbon. The eutectoid reaction nucleates on ferrite and austenite interfaces or at austenite grain boundaries. β-Mn was not reported. At temperatures below 950°C κ-carbide formation occurs but has decreased stability at lower carbon concentrations.

The 25% manganese phase diagram shown in Figure 2(b) shows an expanded austenite single-phase region; the increased manganese content lowered the κ-carbide solvus line.[18] However at 25% manganese, β-Mn was observed. β-Mn is present up to 752°C at 0.4% carbon, but the further addition of carbon lowers the β-solvus temperature. β-Mn formation was observed in the ferrite and was attributed to the lack of solubility of manganese in the body centered cubic structure. β-Mn was present along with austenite, ferrite, and κ-carbide at 627°C for all carbon concentrations reported.

Increasing manganese content to 30% (see Figure 2(c)) produced a further increase in the stability of the austenite to lower temperatures and lower carbon content. The higher manganese content also increased the stability of the β-Mn to higher temperatures. As manganese increased to 35%, there was an increase in austenite stability to lower carbon concentrations and lower temperatures while β-Mn stability increased at higher temperatures as shown in Figure 2(d). Ferrite was reported when carbon was below 0.7% carbon while κ-carbide stability remained relatively unchanged.

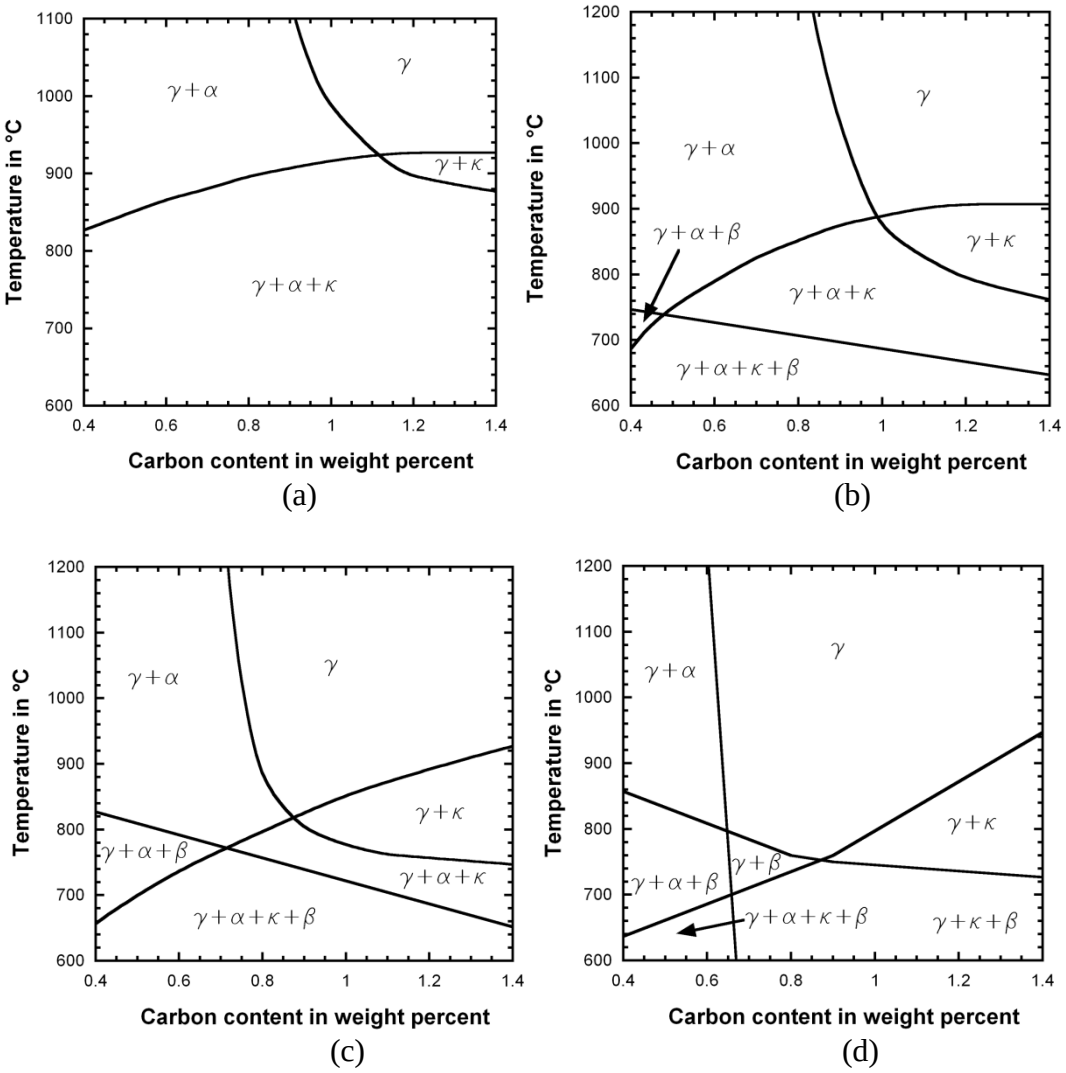

Figure 2. Phase boundaries show γ-austenite, α-ferrite, κ-carbide, and β-Mn equilibria (at a fixed 10% aluminum concentration) as a function of carbon content at manganese concentrations of a) 20%, b) 25%, c) 30%, and d)35% . Data was generated by isothermally holding samples up to 250 hours between the temperatures of 627 °C and 1127 °C. Increasing manganese concentrations increase austenite and β-Mn.[18]

Ishida et al. examined Fe-Mn-Al-C alloys with a fixed 20% manganese content that were equilibrated at 900, 1000, 1100, and 1200 °C with isothermal holds up to 210 hours.[16] The reported isothermal phase diagrams are in agreement with the data reported

by Goretskii et al., but the Ishida et al. studies included carbon contents up to 5%C and aluminum contents between 0 and 18 %Al. Figure 3 shows the 900°C isotherm. For an alloy with 10% aluminum, ferrite is stable for carbon concentrations up to 2%. Cementite, $(Fe,Mn)_3C$, was observed to be stable at aluminum concentrations less than 5% and carbon concentrations of 1 to 5%. Low carbon (0 to 2%) and aluminum (0 to 10%) produce a fully austenitic microstructure. A single-phase κ-carbide was observed at higher carbon (3 to 5 %) and higher aluminum (10 to 18%).

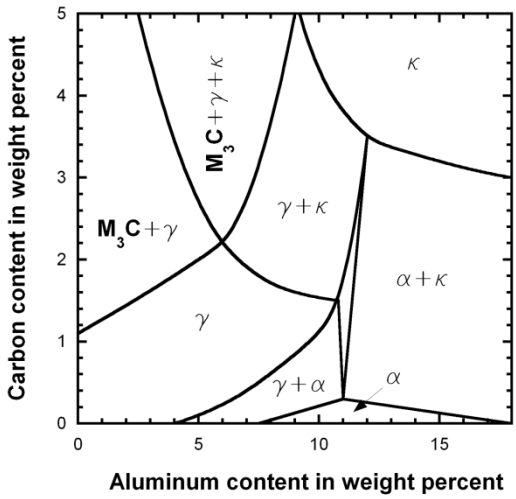

Figure 3. A 900°C Fe-20Mn-xAl-yC isothermal section is plotted as a function of both carbon and aluminum content. Austenite (γ) is stable for low aluminum and low carbon concentrations. κ-carbide is stable for high carbon and high aluminum amounts. Cementite (M_3C) is stable at high carbon, low aluminum levels, and ferrite (α) is stable for high aluminum, low carbon alloys.[16]

Cheng and Lin examined a Fe-23Mn-7.4Al-0.03C alloy homogenized for one hour at 1050°C, hot forged, and subsequently cold rolled.[27] This low carbon alloy was

predominately ferrite (volume fractions were not reported) with equiaxed austenite grains dispersed along ferrite grain boundaries in the homogenized condition. Isothermal aging below 700 °C increased the austenite content with decreasing temperature. Widmanstätten-austenite was observed for aging temperatures between 430 and 600 °C, whereas below 430°C, a DO_3 structure was reported to precipitate homogeneously in the ferrite followed by Widmanstätten-austenite precipitation. The Widmanstätten-austenite had a Kurdjumov-Sachs orientation relationship with the ferrite.

In summary, manganese and carbon have been shown to stabilize an austenitic matrix in Fe-Mn-Al-C alloys while aluminum stabilizes ferrite.[17,18] For Fe-Mn-Al-C alloys with 10% aluminum, a metastable, fully austenitic microstructure can be obtained by solution treatment above 900°C and quenching to room temperature provided the manganese is in the range of 25 to 30% and the carbon concentration is between 0.8 and 1.4%.

3. TRANSFORMATIONS DURING AGE HARDENING

The Fe-Mn-Al-C system increases in strength as a result of κ-carbide precipitation during aging. The κ-carbide forms homogeneously below 650°C, but extended holding time below 650°C (or isothermal holding above 650°C) will produce heterogeneous nucleation of κ-carbide on grain boundaries and interphase boundaries. These heterogeneous κ-carbides are often associated with precipitation of ordered B2 or DO_3 and β-Mn phases.

Prior to aging, specimens are solution treated. Solution treatment typically is performed at temperatures at or above 1000°C.[7,10,11,12,16-18,20-25] The quenched microstructure is either austenite or a duplex microstructure of austenite and ferrite. In

wrought Fe-Mn-Al-C alloys, the austenite appears as an equiaxed grain structure containing annealing twins.[11,12] In wrought duplex alloys ferrite stringers are parallel to the principal rolling direction. Four phases (austenite, ferrite, κ-carbide, and β-Mn) have been identified after age hardening for alloys with compositions in the range of 20 to 35% manganese, 10% aluminum, and 0.4 to 1.4% carbon.[18] Age hardening is associated with homogeneous precipitation of the κ-carbide within the austenite. Increasing aluminum or carbon content increases the κ-carbide volume fraction.[16] Heterogeneous nucleation of κ-carbide is also observed along austenite grain boundaries and in the duplex alloys along ferrite and austenite interfaces, as well. The maximum strength in Fe-Mn-Al-C alloys has been reported after aging 16 hours in a temperature range from 500 to 650 °C.[10,11,20,21,28] Prolonged aging leads to β-Mn precipitation and loss of tensile ductility.

The sequence of phase precipitation in austenite was studied by Han and Choo[23] using x-ray diffraction of specimens aged for varying lengths of time and the following was the reported sequence: (1) chemical modulation, (2) formation of a metastable ordered face centered cubic $L1_2$, (3) κ-carbide formation, and (4) ferrite growth or precipitation followed closely by β-Mn precipitation. Chemical modulation of the austenite with wavelengths between 15 and 30 nm has been shown by x-ray diffraction and transmission electron microscopy to be time and temperature dependent, as well as dependent upon aluminum and carbon concentrations.[24] The modulated structure forms along the austenite <100>. Oshima and Wayman proposed that the modulated structure resulted from spinodal decomposition.[29] The element responsible for the chemical modulation has been reported to be carbon only[12,23,30] or aluminum only[16] or a

combination of aluminum and carbon.[24] Sato et al. calculated an average interdiffusion activation energy of 180 kJ/mol based on the times required at multiple temperatures for the modulation wavelength to reach 20 nm.[24,25] The measured activation energy fell between values for the diffusion of carbon and aluminum in austenitic iron of 120-150 kJ/mol and 235 kJ/mol, respectively. An absence of age hardening was also observed in alloys with low aluminum or low carbon contents (see Figure 4).

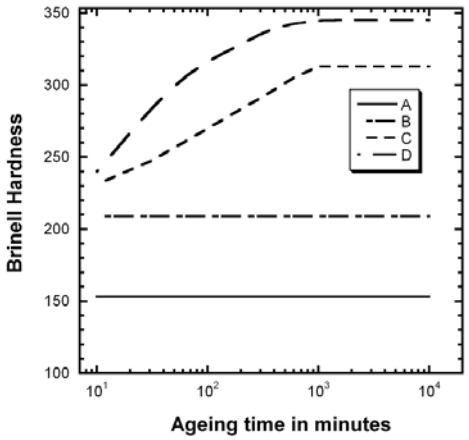

Figure 4. Hardness curves are shown as a function of aging at 550°C for A- Fe-28.5-4.9Al-0.98C, B- Fe-33.7-7.1Al-0.5C, C-Fe-30.8Mn-7.8Al-0.88C, and D- Fe-34.3Mn-11.0Al-0.98C alloy. The lower containing 4.9 wt.% and 7.1wt.% Al containing alloys do not age harden. The 7.8 wt.% Al modified alloy achieves peak hardness at 10^3 minutes. The original hardness scale[24] was converted from Vickers to 3000 kg Brinell Hardness.

Two alloys, Fe-33.2Mn-7.1Al-0.50C and Fe-28.5Mn-4.9Al-0.98C did not increase in hardness for aging times up through 10^4 minutes at 550°C.[24] Neither a chemical modulation nor a κ-carbide precipitation were observed in these alloys. Thus,

Sato et al. proposed that the chemical modulation in Fe-Mn-Al-C alloys required both carbon and aluminum diffusion. Figure 5 shows the modulation wavelength as a function of time for a Fe-29.5Mn-9.2Al-0.94C alloy at 500, 520 and 550°C. Increasing the carbon concentration for a fixed time and temperature produced a longer wavelength.

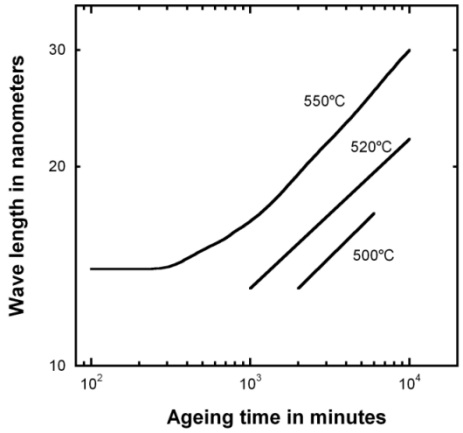

Figure 5. Spinodal wavelength is shown as a function of aging temperature and time for a Fe-29.5Mn-9.2Al-0.94C alloy. The wavelength increases at higher temperatures reflecting greater atomic diffusivity at higher temperatures for carbon and aluminum segregating into alloy-rich and alloy-lean regions of the austenitic matrix.[24]

An increase in yield strength has been associated with coherency strains produced during the spinodal decomposition and can be correlated to the experimentally measured modulation amplitude of carbon concentration and the modulation wavelength.[22] Figure 6 shows the correlation in the change of yield strength to the modulated wavelength and carbon amplitude for aging a Fe-30Mn-10Al-1C alloy at 550°C. During initial aging, up to 10^2 and 10^3 minutes, the wavelength is relatively constant, but strength and hardness increase as a result of an

increasing modulation amplitude. As the wavelength increases the diffusion distance increases and slows the rate of change in the modulation amplitude and strength. Changes in strength with both compositional amplitude and wavelength follow trends predicted by Chan's model for strengthening during spinodal decomposition.[31]

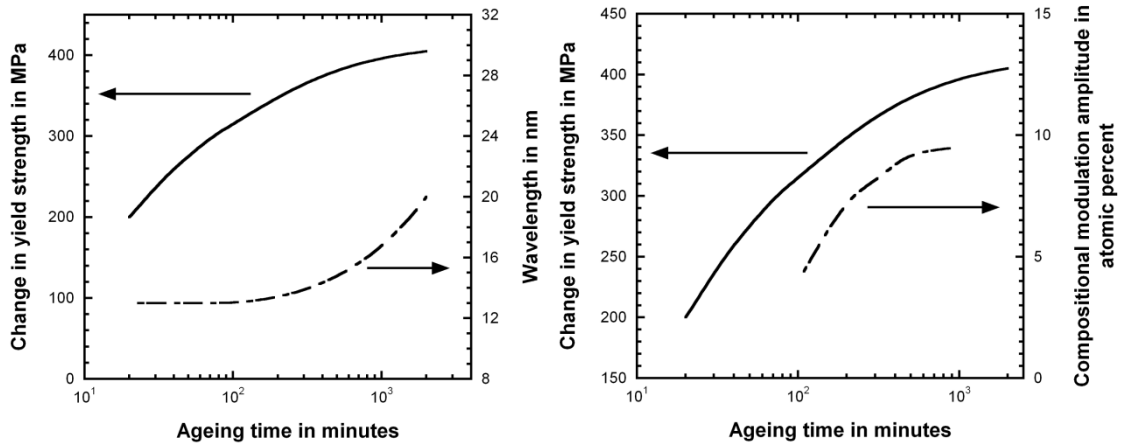

Figure 6. Fe-30Mn-10Al-1C alloy aged at 550°C. (a) The rate of change in yield strength decreases as the wavelength increases. (b) The change in yield strength shows a strong correlation to the calculated carbon composition amplitude of the modulated structure. The slope nears zero at 10^3 minutes or nearly 16 hours.[22]

Precipitation of κ-carbide occurs in the carbon and aluminum rich regions of the modulated microstructure. Some researchers report that these aluminum and carbon rich regions may first order during aging to form a metastable $(Fe,Mn)_3Al$ phase with an $L1_2$ crystal structure, which is similar in fashion to Ni_3Al formation in Ni-Al alloy systems.[22,32] Ordering of carbon to the (½, ½, ½) position produces the κ-carbide with the $E2_1$ perovskite structure and chemical composition $[Fe,Mn]_3AlC$ (see Figure 7).

In Fe-Mn-Al-C alloys, κ-carbide precipitates with a cube on cube orientation relationship, $<100>_{\gamma}//<100>_{\kappa}$ and $\{001\}_{\gamma}//\{001\}_{\kappa}$,and the lattice misfit is less than 3%. Initially the κ-carbide appears cube-shaped in morphology.[14,21,23,24,32,33] The κ-carbide's lattice parameter increases with increased aging times reflecting an increasing carbon and aluminum content.[34] As the κ-carbide lattice parameter increases, the parent phase lattice parameter decreases and this leads to a loss of coherency and a more plate-like morphology. Kalashnikov et al. reported a lattice parameter increase of approximately 2% from 3.72 to 3.76 Å for the κ-carbide after aging at 700°C for 16 hours. In contrast Kimura et al. showed that the misfit is reduced from 2.7% to 2.2% with increasing aluminum concentration.[32]

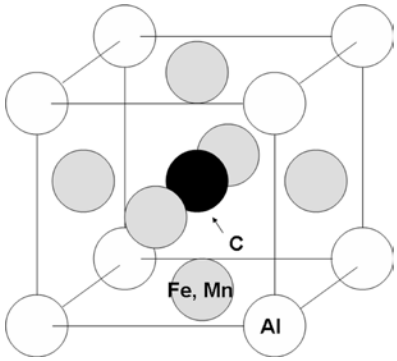

Figure 7. The $E2_1$ structure of the $(Fe, Mn)_3AlC$ κ-carbide orders with aluminum in the cubic positions, iron and/or manganese in the face centered octahedral positions and carbon in the center octahedral position.[14]

It was also observed that increasing the aluminum content from 13 at.% to 17 at.% in the overall alloy chemistry contributed to a simultaneous decrease in the κ-

carbide lattice parameter (3.79 Å to 3.77 Å) while increasing that of the austenite (slightly greater than 3.68 Å to ~3.69Å). This result appears counter intuitive since the lattice parameter of both austenite and κ-carbide would be expected to increase with additional aluminum content since aluminum has a larger atomic radius than either iron or manganese. Kimura et al. also showed that nickel additions up to 2% reduced the matrix and κ-carbide lattice parameters equally thus hardly having any measurable effect on misfit.

Hale and Baker[24] reported precipitate free zones along grain boundaries and related these zones to heterogeneous precipitation of κ-carbide at the grain boundaries. Heterogeneous nucleation of the κ-carbide occurs on grain boundaries prior to homogeneous nucleation within austenite for aging temperatures above 650°C.[16] Below 650°C, the order is reversed and homogeneous nucleation occurs before grain boundary nucleation occurs. The grain boundary precipitates tend to be much larger than the matrix κ-carbide precipitates. A lamellar austenite and κ-carbide microstructure resulting from discontinuous precipitation can also be produced in high aluminum and high carbon alloys, e.g. Fe-30Mn-12Al-1.9C, at or above 1000°C.[17,23,32]

In fully austenitic, solution treated microstructures, ferrite precipitates on grain boundaries during age hardening with a Kurdjimov-Sachs orientation relationship of $(111)_g//(110)_\alpha$ and $[10\bar{1}]_\gamma //[11\bar{1}]_\alpha$.[27] The precipitates are initially coherent with one of the austenite grains, but will lose coherency upon coarsening.[21] In duplex ferrite and austenite microstructures the additional ferrite forms preferentially on the existing ferrite. Intergranular ferrite has been observed after prolonged isothermal holding below the

ferrite solvus temperature. It has been suggested [16] that carbon depletion of the austenite during κ-carbide formation leads to the formation of ferrite and subsequently β-phase precipitation.

β-Mn or complex intermetallic phases form after prolonged aging times and generally after ferrite precipitation or cellular (κ-carbide with ferrite) decomposition.[16,18,23] The ferrite becomes unstable with respect to the high manganese and aluminum contents and β-phase precipitates within the ferrite.[7,10,12,20] In silicon containing Fe-Mn-Al-C alloys a DO_3 intermetallic compound precipitates alongside ferrite with a reported lattice parameter of 5.86Å, and the β-Mn phase does not form.[18,35] The DO_3 phase precipitates on coarse κ-carbide and has a Kurdjimov-Sachs orientation relationship with κ-carbide.[20] In a silicon containing alloy, the grain boundary intermetallic phase was identified as a $Mn_{12}Si_7Al_5$ compound.[36] It was reported that the manganese content in κ-carbide is increased by the presence of silicon thereby reducing the manganese concentration in the austenite and ferrite and thus silicon inhibits β-phase precipitation.[35]

In summary, the precipitation sequence can be described as follows. A spinodal reaction causes modulation of carbon and aluminum within the austenite. The localized chemical potential from the modulation may facilitate the formation of metastable $L1_2$ precipitates that then transform to the $E2_1$ κ-carbide by ordering of the carbon. However, no direct evidence of the $L1_2$ precursor reaction is currently provided in the literature. Precipitation of κ-carbide leads to the destabilization of the remaining austenite and ferrite is precipitated. In alloys without silicon, β-Mn nucleates within the ferrite. In alloys with silicon, a DO_3 intermetallic phase precipitates instead of the β-Mn.

4. PHYSICAL AND MECHANICAL PROPERTIES

Precipitation hardenable Fe-Mn-Al-C alloys produce a wide range of mechanical properties that make this system attractive for many different applications. Ductility at 77% elongation to failure, tensile strength as high as 2.06 GPa, density reductions up to 18% over low carbon, low alloy steels, and comparable oxidation resistance to 304 stainless steel have been reported. However, the Fe-Mn-Al-C system suffers from poor corrosion resistance and stress corrosion cracking. Most of the reviewed research correlates the precipitation of κ-carbide to the observed strengthening.[12,14,21,32,37] Most investigators solution treated their alloys at or above 1000°C, quenched in water, and aged between 500 and 650°C prior to testing.

A more recent investigation examined the reduction in density as a function of aluminum and manganese.[11] A linear reduction in density based upon either lattice dilatation or a combination of dilatation and atomic mass has been mapped out as a function of aluminum concentration for a range of manganese from 14 to 28% (see Figure 8). Manganese concentration had little impact on density as compared to aluminum. The percent density reduction is relative to pure iron at 7.8 g/cm^3. For example a 12% aluminum addition will reduce the density by 17% of which lattice dilatation contributes 10% and mass reduction contributes an additional 7%.

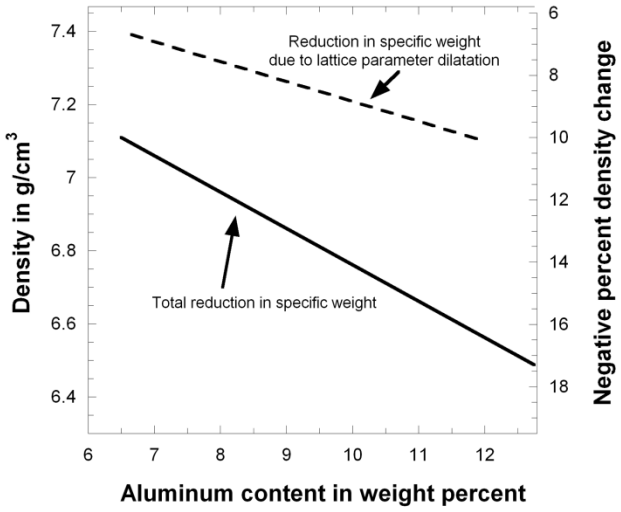

Figure 8. The density reduction as a function of aluminum content for a Fe, 14-28Mn, xAl, 1C is a function of both dilatation and mass reduction. Dilatation of the lattice parameter accounts for as much as a 10% reduction. Increasing the aluminum content drives down the density by as much as 16-17% for an aluminum content of 12 wt.%.[11]

4.1 Solution Treated Condition

In the solution treated condition, Fe-Mn-Al-C alloys have moderate yield strengths that are comparable to other austenitic alloys and have elongations to failure in excess of 40%.[11,12,34] For a wrought Fe-32Mn-8.5Al-0.9C alloy in the solution treated condition, the yield strength, ultimate tensile strength, and elongation to failure is 358 MPa, 823 MPa, and 64%, respectively.[12] Tjong and Zhu investigated the mechanical properties of solution treated Fe-28Mn-9Al-0.4C and Fe-28Mn-9Al-1C alloys tested at temperatures from 25 to 800°C.[34] The microstructure of the low carbon alloy was duplex whereas the high carbon alloy was fully austenitic. Serrated stress-strain behavior with homogeneous slip character was reported between the temperatures of 300 and 600°C; and, Tjong and Zhu concluded that the serrated flow resulted from dynamic strain aging.

However, this dynamic strain aging behavior exhibited anomalous temperature and strain rate behavior, which were related to the precipitation of κ-carbide. Mechanical twinning was reported as a deformation mechanism at temperatures below 300°C and grain boundary sliding was reported at 800°C. Figure 9 shows the temperature dependence of the mechanical properties.

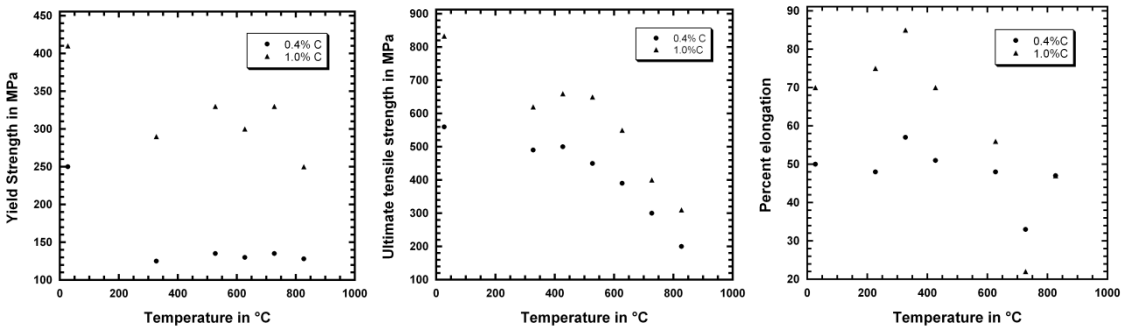

(a) (b) (c)

Figure 9. Yield strength (a), tensile strength (b), and elongation (c) are reported against a testing temperature range from room temperature to ~800°C. Yield and tensile strength decrease to ~300°C with a corresponding increase in elongation to its maximum point. Twin formation is cited as the primary deformation mechanism up to 300°C. From 300 to 600 °C, strength values fluctuate as ductility decreases resulting from κ-carbide formation. Deformation in this temperature regime occurs as homogeneous slip until grain boundary sliding dominates above 600°C.[34]

Yield and ultimate tensile strengths decreased as the testing temperature increases; however, strain aging reduced the rate of decrease in yield strength for testing temperatures above 300°C. Tjong and Zhu also observed that ductility was a maximum at a testing temperature of 300°C.

4.2 Age Hardening Behavior

Fe-Mn-Al-C alloys follow classic age hardening trends where the hardness increases from 182 Brinell Hardness in the solution treated condition to values greater than 342 Brinell Hardness at peak hardness after 2 hours at 600°C.[24] Figure 10 shows the age hardening response of an Fe-30.4Mn-8Al-1C-0.35Si at various aging temperatures.

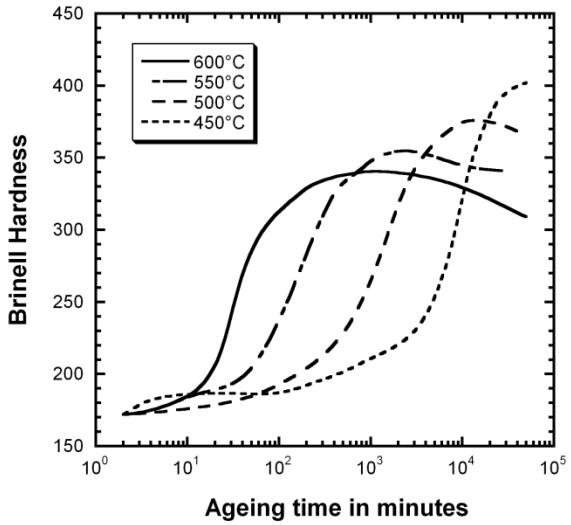

Figure 10. Aging curves are shown for a Fe-30.4Mn-8Al-1C-0.35Si aged at 450, 500, 550, and 600 °C. Classical aging trends are observed. Peak hardness values increase for longer isothermal hold times and lower temperatures. The original hardness scale was converted from Vickers Hardness to 3000 kg load Brinell Hardness.[24]

Peak hardness increases for longer times at lower aging temperature, e.g. 405 Brinell Hardness after 1,000 hrs at 450°C. Similar age hardening behaviors have been reported for Fe-32Mn-11.8Al-1C-0.1Si[12] and Fe-34.3Mn-11Al-1C.[24] Secondary hardening has

also been observed for an Fe-29.5Mn-9.2Al-0.94C alloy (see Figure 11).[24] The additional hardening and loss of ductility was associated with β-manganese formation.

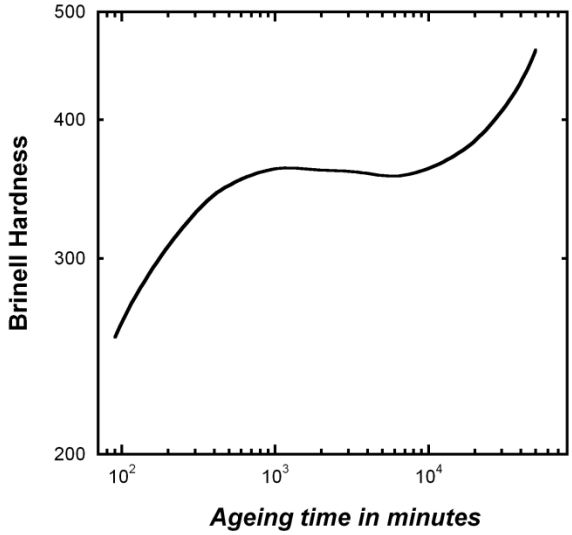

Figure 11. A Fe-29.5Mn-9.2Al-0.94C alloy aged at 550°C shows two hardening stages. First stage hardening occurs from formation of κ-carbides in the austenitic matrix. Further decomposition of the austenite during second stage hardening produces grain boundary precipitates of coarse κ-carbides and β-Mn of which the β-Mn is responsible for the second stage hardening. The original hardness scale was converted from Rockwell A to 3000-kg load Brinell Hardness.[24]

4.3 Alloy Optimization for Age Hardening

The aging temperature of 550°C is the most common aging temperature reported in this system.[10,11,12,16,21,28] Kayak reported strength properties at a fixed aging time at temperatures between 450 and 575 °C on a wrought Fe-27.5Mn-9.1Al-0.9C.[10] For a fixed isothermal hold time of 16 hours, a maximum strength (912 MPa) was achieved at an aging temperature of 550°C, but the corresponding reduction in area was a minimum

(7%). Hale and Baker's investigation of an aged Fe-30.9Mn-8Al-1C alloy affirmed Kayak's trends (see Figure 12); a maximum strength was achieved after aging at 550°C for a fixed time of 16 hours.[21] However, Hale and Baker reported much greater ductility, but lower peak strengths.

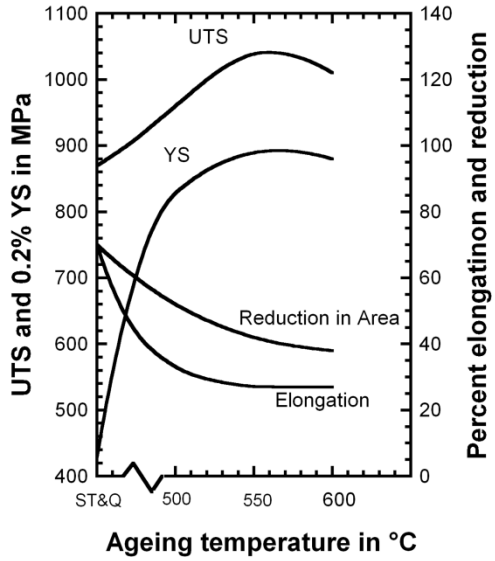

Figure 12. Strength and ductility are shown as functions of aging temperatures for a fixed time of 16 hours for a Fe-30.9Mn-8Al-1C alloy. Maximum strength is attained at 550°C. Below 550°C, strength is reduced but ductility increases. Above 550°C, specimens overage for a hold time of 16 hours and reduce both strength and ductility.[21]

Kalashnikov et al. examined effects of chemistry on aged alloys (550°C for 16 hours) and sought to optimize chemistry composition against this standard aging practice.[28] Figure 13 shows the effect of 3 to 10% aluminum content on strength,

ductility, and impact toughness for two different carbon contents with manganese between 28 and 30%.

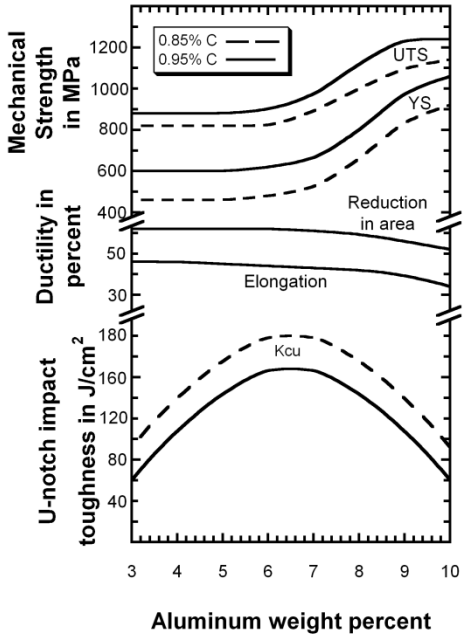

Figure 13. Strength, ductility, and impact toughness are plotted for a Fe-30Mn-xAl-yC alloy. Carbon is fixed at two levels of 0.85 and 0.95%, and aluminum is varied between 3 and 10%. The alloys tested were homogenized at 1050°C, water quenched, and then aged at 550°C for 16 hours. Fe-Mn-Al-C alloy with aluminum content below 7% lacks sufficient driving force to age harden, thus the lack of strength increase. Above 7% aluminum, the alloy age hardens, increases strength, and decreases ductility and impact toughness due to κ-carbide formation. Higher carbon content is good for solid solution strengthening and carbide formation but deleterious to impact toughness.[28]

Strength and ductility remained constant but impact toughness increased as aluminum concentration increased from 3 to 6.5%. Above 6.5% aluminum, strength increased and reached a maximum value at 10% aluminum; however, impact toughness decreased. At

10% aluminum, the solution treated microstructure was duplex and a maximum ultimate tensile strength value of approximately 1200 MPa was reported with an elongation to failure of approximately 35%.

For alloys with 9% aluminum and 30% manganese, properties were measured across a carbon range from 0.4 to 1.3% (see Figure 14).

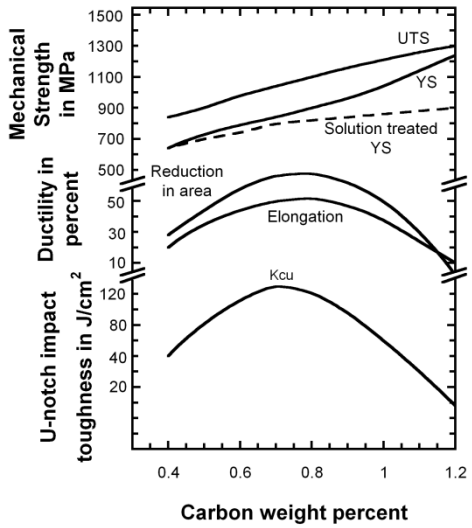

Figure 14. Strength, ductility, and impact toughness are plotted for a Fe-30Mn-9Al-yC alloy. Carbon is varied between 0.4 and 1.2%. The alloys tested were homogenized at 1050°C, water quenched, and then aged at 550°C for 16 hours. Increase in carbon content increases strength, ductility, and impact toughness up to ~0.7% in aged and solution treated conditions. Above 0.7%, strength continues to increase as ductility and impact toughness decrease to their respective minimum values at 1.2% carbon.[28]

The solution treated microstructure was duplex for a carbon content below 0.7%. After aging, both yield and ultimate strengths increased steadily at a rate of approximately 30 to 40 MPa per 0.1% carbon. This increase in strength was related to an

increasing volume fraction of κ-carbide. Impact toughness was a maximum (approximately 125 J/cm^2) at approximately 0.7% carbon and then steadily decreased as carbon increased. Above 1% carbon it was noted that κ-carbide precipitated along the austenite grain boundaries and reduced the impact toughness to approximately 40 J/cm^2. The elongation to failure followed a similar trend as the impact toughness. Ductility was a maximum at 0.8% carbon as shown in Figure 14. Sato et al. showed similar results for two Fe-30Mn-9.5Al alloys with different carbon levels (0.91 and 1.03%) when aged at 550°C.[25] Figure 15 shows Brinell hardness and yield strength for both carbon levels, and greater hardness and strength were obtained with the higher carbon alloy at all aging times.

The effect of manganese content was examined by Kalashnikov et al. using a fixed aluminum and carbon concentration of 9% and 0.9%, respectively. Figure 16 shows the mechanical properties for a range of manganese from 24 to 34%.[28] Yield and ultimate strengths reach a maximum at 26% manganese. Ductility and impact toughness peak at 31% manganese. Kalashnikov et al. concluded that the optimum alloy to achieve the best balance of strength, ductility, and impact toughness requires 25 to 31% manganese, 6.2 to 9.7% aluminum, and 0.7 to 1.0% carbon. This chemistry range has been common to many investigations of the Fe-Mn-Al-C system.[3-30,32-39]

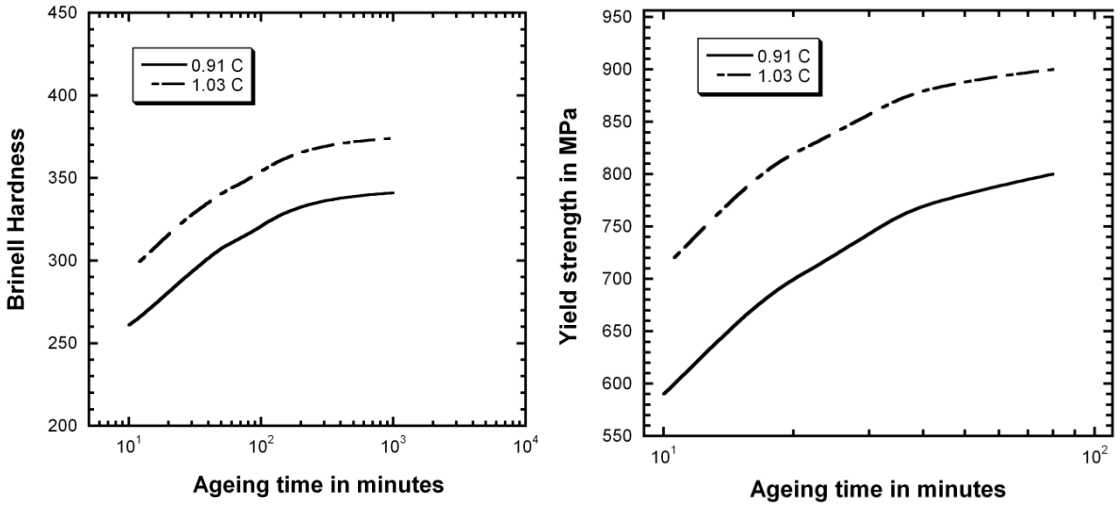

Figure 15. A Fe-Mn-Al-C alloy aged at 550°C with two differing carbon levels of 0.91 and 1.03 wt.% showing (a) hardness and (b) strength. Higher carbon content increases hardness and strength. Hardness was converted to 3000 kg load Brinell Hardness from Vickers Hardness.[25]

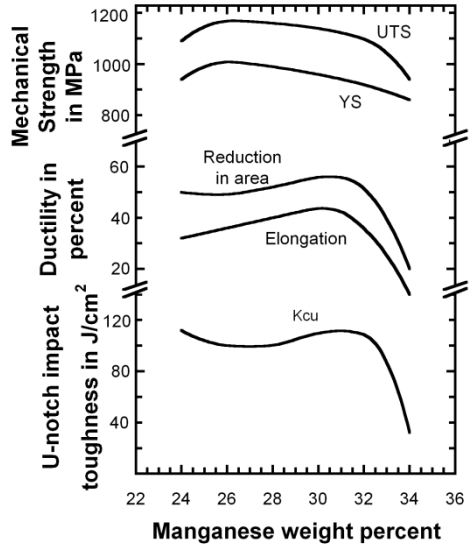

Figure 16. Strength, ductility, and impact toughness are plotted for a Fe-xMn-9Al-0.9C alloy. Manganese is varied between 22 and 34%. The alloys tested were homogenized at 1050°C, water quenched, and then aged at 550°C for 16 hours. Strength increases to a maximum at ~25% manganese. Ductility and impact toughness remain fairly constant until their peak value is attained at 31% manganese. Above 31% manganese, β-Mn precipitates decreasing strength, ductility, and impact toughness.[28]

A recent investigation by Howell et al. reported engineering yield and tensile strength in a cast Fe-30Mn-9Al-1.4Si-0.9C-0.5Mo alloy (aged 10 hours at 530°C) at 1,016 MPa and 1,085 MPa, respectively.[38] Young's modulus for the cast material was 188 GPa. The highest reported ultimate strength of 2.06 GPa was reported in the ASM Metals handbook for a Fe-30Mn- 9Al-1C-1Si alloy; however, the processing of the alloy was not reported.[38]

Alloys of high carbon (>1%) and aluminum content from 7 to 11% have also been produced with lamellar austenite and κ-carbide microstructures by solution treating at 1100°C and furnace cooling.[34] Room temperature properties were poor in comparison to alloys of similar composition that were solution treated and age hardened, and an ultimate strength of approximately 900 MPa with little or no ductility was reported for the lamellar structure.

4.4 Work hardening and deformation mechanisms

Fe-Mn-Al-C alloys work harden at rates comparable to that of austenitic stainless steels.[11,12] Frommeyer and Brux calculated a strain hardening exponent equal to 0.83 (true strain values less than 0.1) for a Fe-28Mn-12Al-1C alloy aged at 550°C for 16 hours.[11] By comparison, 304 stainless has a value of 0.8 whereas a deep drawing steel will have values between 0.18 and 0.23. At higher true strains the strain hardening exponent decreased to 0.58, and by comparison a 304 stainless steel has an exponent in the range of 0.33 to 0.45. Han et al. observed that the work hardening exponent changes little between the solution treated and aged alloys (25 hrs. at 550°C); and thus, concluded that the presence of κ-carbide and the induced coherency strain, does not affect work hardening.[12] The work hardening rate and deformation character of the Fe-Mn-Al-C

alloys appears to be a strong function of the aluminum content in the range 0.5 to 5%.[41] At the lowest aluminum concentrations, there is a strong contribution from transformation induced plasticity via either martensitic transformation or mechanical twinning induced plasticity, which increases the strain hardening at low strains, but decreases the work hardening at high strains.

Lai and Wan observed a high mechanical twin density in a deformed Fe-29.2Mn-0.81C alloy.[42] A lower twin density was observed in a similarly deformed Fe-30.1Mn-7.02Al-0.95C alloy leading to the conclusion that aluminum increased the stacking fault energy and suppressed twin formation. Aluminum concentration has been reported to have the most effect upon the stacking fault energy.[11,42] Yang and Wan calculated stacking fault values for an Fe-30Mn-.9C-xAl alloy[43] using the thermodynamic model proposed by Olson and Cohen.[44] A stacking fault energy of 27.3 mJ/m^2 was calculated for the 0% aluminum alloy and at 8.5% aluminum, the stacking fault energy increased to 99.6 mJ/m^2.[43] Frommeyer and Brux concluded that for stacking fault values greater than 20 mJ/m^2, the martensitic $\gamma_{FCC} \rightarrow \varepsilon_{HCP}$ transformation is suppressed and mechanical twin formation is favored. For an age hardened Fe-28Mn-12Al-1C (550°C for 16 hours) the calculated stacking fault energy value is 110 mJ/m^2 and shear band formation rather than twinning is observed.[11]

4.5 Fracture Behavior

Fracture of FeMnAl alloys is a strong function of age hardening.[45,46] Acselrad et al. studied cleavage fracture of various aging practices on a Fe-29.4Mn-8.8Al-1C alloy with 1.33% silicon. Crack arrest fracture toughness values (K_A) were calculated from instrumented Charpy impact tests.[47] Table 1 shows three sets of mechanical properties

determined for a solution treated specimen, one aged at 550°C for 15 hours, and a sample quenched into a salt bath at 700°C, held for 4 seconds, and subsequently cooled to room temperature at a rate of 0.05 °C/s.[45]

Table 1. Mechanical Properties of a Fe-29.4Mn-8.8Al-1.33Si-1C Alloy for Three Different Processing Techniques

Processing Condition	$\sigma_{0.2}$ (MPa)	UTS (MPa)	Elongation (%)	Brinell Hardness (converted from Rc)	Charpy Energy (J/cm^2)	Fracture Toughness K_A ($MPa\sqrt{m}$)
Sol. Tr.	620	871	77	272	51	330
Aged 16 hr @ 550°C	884	1210	15	434	1.4	84
Controlled Quench	705	1100	32	392	1.2	104

The solution treated specimen (1050°C for 5 minutes and water quenched) yielded the lowest strength but highest elongation, greater Charpy impact energy, and higher fracture toughness. The fully aged specimen (solution treated and aged 15 hours at 550°C) had the highest strength and hardness but lowest ductility and toughness values. A balance in mechanical properties was obtained by controlled cooling from solution treating temperatures. Microvoid coalescence was observed for fracture of the solution treated specimen, and the aged microstructure produced brittle grain boundary or cleavage fracture. Formation and ordering of the κ-carbide was primarily responsible for the simultaneous increase in strength and reduction in impact toughness. Cleavage fracture was not observed in the specimen that had been controlled cooled. The

investigators concluded that the controlled cooling suppressed the degree of ordering to produce both an increase in strength and improved ductility.

4.6 Fatigue Behavior

Chang et al. conducted fatigue testing on three Fe-29Mn-9Al-xC alloys with carbon contents of 1.1, 0.6 and 0.3%.[48] Solution treatment was performed at 1050 °C for 1.5 hours. All three alloys exhibited a similar cyclic life response (see Figure 17) despite differences in microstructure and strength.

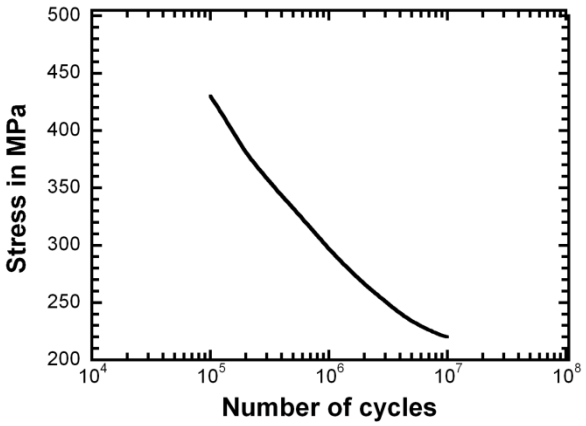

Figure 17. Three Fe-29Mn-9Al-xC alloys with 1.1, 0.6 and 0.3 wt.% C demonstrated nearly identical fatigue cycles to failure and thus is plotted as a single narrow banded region.[48]

The 1.1% carbon alloy was fully austenitic and had the highest strength, which was attributed to solid solution strengthening by carbon. The 0.6% carbon alloy contained 10% ferrite and possessed the lowest yield strength while the 0.3% carbon alloy contained equal volumes of ferrite and austenite. Fatigue crack nucleation occurred

along slip bands in the austenite for the 1.1 and 0.6% carbon alloys. The small amount of ferrite in the 0.6% carbon alloy functioned as crack arresters, thus, despite a lower strength, the 0.6% carbon containing alloy achieved a fatigue life equivalent to the 1.1% carbon containing alloy. In the 0.3% carbon alloy crack initiation occurred in ferrite grains at the specimen surface.

Ho, Wu, and Tjong conducted strain controlled fatigue tests (Figure 18) on a solution treated Fe-30Mn-10Al-0.4 C alloy with duplex microstructure of austenite and ferrite.[49]

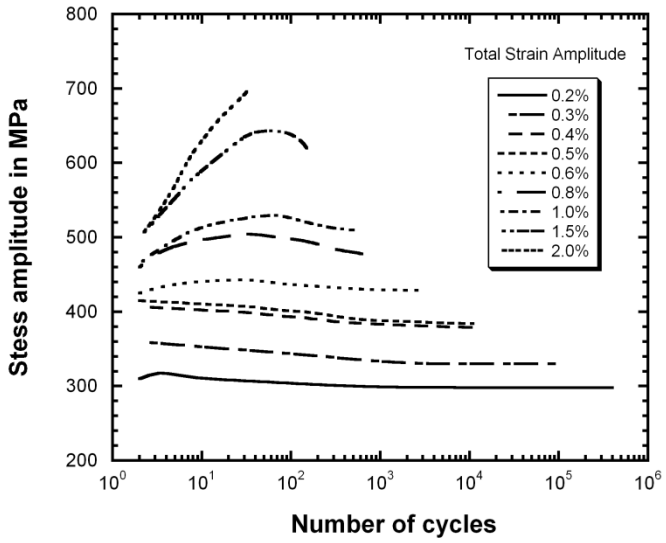

Figure 18. The cyclic response of a Fe-30Mn-10Al-0.4C alloy shows the cyclic hardening above a strain amplitude of 0.6% before a critical stress amplitude was achieved followed by cyclically softening. Only the 2.0% test specimen did not cyclically soften prior to failure. [49]

Strain amplitudes ranged from 0.25% to 2.0%. Below strain amplitudes of 0.6%, the formation of persistent slip bands produced cyclic softening in the austenite and the applied strain was accommodated by these slip bands. At strain amplitudes above 0.6%, fatigue crack initiation occurred in ferrite. Cyclic softening was not observed at strain amplitudes greater than 2.0%.

Fatigue behavior of an aged Fe-Mn-Al-C alloy was also reported by Tjong and Ho.[50] Controlled strain amplitude testing was conducted on a Fe-29.7Mn-8.7Al-1C alloy. Specimens were solution treated at 1100°C and aged at either 550°C for 2 hours, 550°C for 24 hours, or 710°C for 2 hours. Cyclic softening was observed during fatigue for all three aging practices as shown in Figure 19. Cyclic softening was associated with planar slip, shearing of κ-carbide, mechanical dissolution of the precipitates, and formation of persistent slip bands. Tjong and Ho postulated for the 710°C aged alloy that the formation of precipitate free zones was responsible for the cyclic softening, which facilitated slip band formation. The precipitates in the 550°C aged alloy sheared early in the test due to their small size; thus, producing persistent slip bands and cyclic softening behavior similar to solid solution alloys. The 24 hour aged specimen endured higher stress amplitudes (from ~1000 MPa to ~750 MPa) and cyclically softened because of planar slip, dissolution of the precipitates, and formation of persistent slip bands.

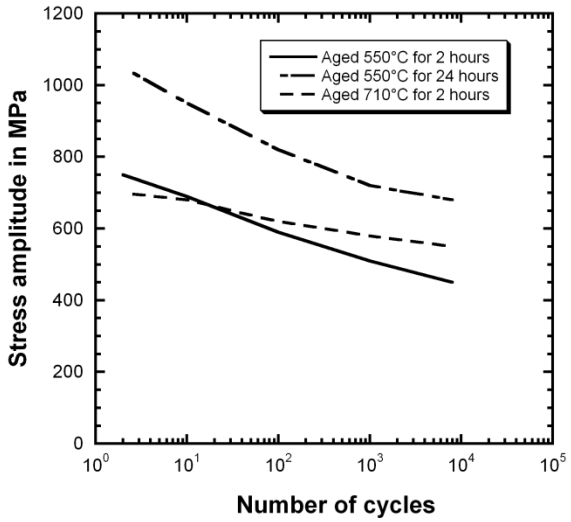

Figure 19. Cyclic responses of a Fe-29.7Mn-9Al-1C alloy after three heat treatments: a) 550°C for two hours, b) 550°C for 24 hours, and c) 710°C for 2 hours. Strain amplitude was constant at 0.8% for each treated specimen. All three exhibit cyclic softening.[50]

Kalashnikov et al. investigated fatigue at a constant strain amplitude on a wrought Fe-28Mn-9Al-0.86C-0.7W-0.43Mo-0.49Nb alloy and on a martensitic stainless steel of composition Fe-12Cr-1.25Ni-0.2V-1.8W-0.5Mo-0.15C.[51] Three tests were conducted at different temperature conditions: one test at 400°C, a second at 20°C , and a third test that included cycling the temperature between 400 and 20 °C. In each case, the stainless steel failed at half the cycles of the Fe-Mn-Al-C alloy. Tempering of the martensite and loss of strength was used to explain the lower cyclic life of the stainless steel at elevated temperatures. Within the Fe-Mn-Al-C alloy, deformation twinning was cited as an obstacle to further plastic deformation. Also, specimen aging occurred at 400°C causing increased fatigue strength and grain boundary precipitation of κ-carbide. Figure 20 shows the cyclical stress response of the Fe-Mn-Al-C alloy for the three thermal tests.

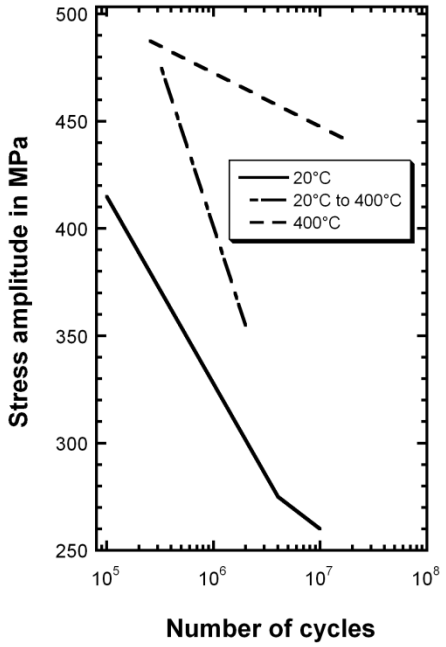

Figure 20. Cyclic responses of a Fe-28Mn-9Al-0.86C-0.7W-0.43Mo-0.49Nb alloy tested in three different temperature regimes: a) 20°C, b) 20 to 400 °C, and c) 400°C. Dynamic strain aging at higher temperatures is responsible for higher stress amplitudes.[51]

4.7 Hydrogen Embrittlement

Pierpoint et al. investigated hydrogen embrittlement of a Fe-30.1Mn-8.3Al-1.07C-0.12Si alloy.[52] Specimens were charged in a sulfuric acid solution with a current density of 4.6 mA/cm^2 for 16 and 24 hours. At either time interval, strength and ductility decreased compared to non-charged specimens. The fracture mode changed from microvoid coalescence to intergranular fracture after hydrogen charging. Sudrshan et al. examined the effect of hydrogen on Charpy impact energy at room temperature.[53] Fe-29.4Mn-7.8Al-0.99C-1.45Si samples were charged in a hydrogen atmosphere at 150°C and 10.53 MPa of air pressure for 56 days. Data was collected using an instrumented Charpy impact test machine at room temperature. A reduction in energy from 16.3 J/cm^2

to 8.1 J/cm^2 was observed with a corresponding decrease in the peak load during impact from 16.9 kN to 12.9 kN for the hydrogen treated material. Sudrshan et al. concluded that the hydrogen embrittlement of the Fe-Mn-Al-Si-C alloy was similar to 304L stainless steel.

4.8 Stress Corrosion Cracking Behavior

Stress corrosion cracking experiments on Fe-30Mn-9Al-1Si-xC alloys were performed in 4% sodium chloride solution at room temperature to examine the effect of ferrite volume fraction.[54] Tensile strength losses from 10% to 20% were reported for each alloy subjected to an aqueous 3.5% sodium chloride solution. Intergranular stress corrosion cracking was observed in solution treated fully austenitic specimens. Transgranular failure of the ferrite in duplex microstructures was observed for specimens aged at 550 and 700 °C. In the aged duplex samples, crack blunting was observed as the crack transitioned from the ferrite to the austenite. The authors concluded that stress corrosion cracking resistance increased for decreasing ferrite content. For example, a fully austenitic solution treated Fe-31.2Mn-8.9Al-0.9Si-0.5C alloy loaded to 60% of its tensile strength did not fail during a 2000 hour test, but after aging at 550°C for 4 hours, the specimen failed at approximately 300 hours due to ferrite precipitation.

Chang et al. investigated stress corrosion cracking of Fe-32Mn-9Al-1C-X alloys solution treated alloys in a 3.5% sodium chloride solution with an imposed electric potential.[55] The base alloy was modified with either 1.23% molybdenum, 2.8% chromium, or 1.27% silicon. The base alloy and alloys with molybdenum or silicon additions stress corrosion cracked in a transgranular fashion at room temperature and at 160°C. An increased susceptibility was observed for the silicon containing alloy. Crack

initiation within the Cr modified alloy occurred at casting defects, thus little could be concluded from this portion of the experiment due to the poor quality of the material.

4.9 Oxidation and General Corrosion Behavior

Oxidation resistance was reported by Garcia et al.[56] and compared six Fe-Mn-Al chemistries (see Table 2) against 304 stainless steel and 1010 carbon steel. Two solution treated wrought samples were produced of each chemistry. One set was exposed to 1 atm flowing oxygen at 700°C and one set was exposed at 500°C for 24 hours and each set monitored for changes in weight. Figure 21 shows the weight gain versus $(\text{time})^{1/2}$ and the linear trends indicate a diffusion controlled oxidation process.

Table 2. Fe-Mn-Al-C Alloy Composition for Oxidation Investigation

Alloy	Al	Mn	Si	C	Cu	P	S	Fe
A	10.84	31.92	3.01	0.74	-------	0.05	0.02	Bal
B	9.05	33.3	1.41	0.88	-----	0.02	0.02	Bal
C	8.63	28.6	2.68	0.69	-----	0.05	0.02	Bal
D	7.25	24.04	2.06	1.01	-----	0.05	0.02	Bal
E	12.4	4.13	2.12	0.03	0.91	0.02	0.01	Bal
F	12.05	4.2	1.93	0.03	8.9	0.02	0.01	Bal

Chemical analysis of the surface revealed an aluminum rich oxide scale. At 700°C, 304 stainless steel resists oxidation better than the Fe-Mn-Al-C alloys. However, at 500°C the Fe-Mn-Al-C specimens had improved oxidation resistance over the 304 stainless steel. This is in agreement with Gau and Wu's[57] study of similar Fe-Mn-Al-C chemistries versus 304 stainless steel exposed to oxygen at 600°C for 300 hours. Their

study also found a parabolic time dependence for the oxidation of the Fe-Mn-Al-C alloys and that the 304 stainless steel rate constant was at least twice as great (see Table 3).

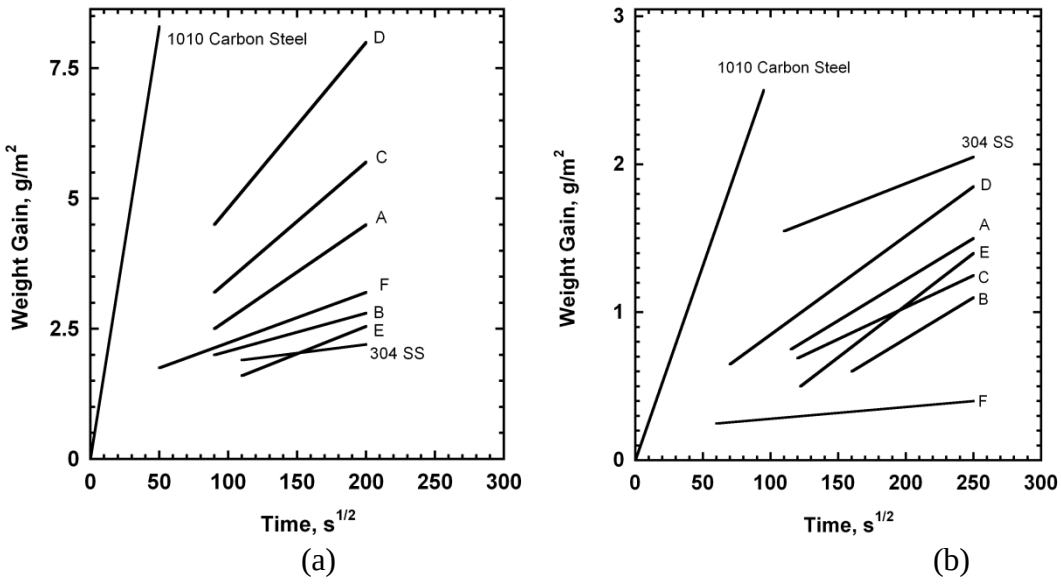

Figure 21. Weight gain is shown for six Fe-Mn-Al-C alloys (compositions A through F in Table 2), 1010 carbon steel and 304 stainless steel as functions of exposure time in 1 atm flowing oxygen at 700°C (a) and 500°C (b).[56]

Gau and Wu[57] investigated Fe-Mn-Al-C alloy corrosion behavior in 3.5% sodium chloride, acetic acid, ammonia, and sodium sulphide solutions of the same alloy compositions listed in Table 3. In every environment, Gau and Wu observed higher corrosion rates (up to two orders of magnitude higher) for the Fe-Mn-Al-C alloys versus 304 stainless (see Table 4). The addition of 5.9% chromium was beneficial in reducing the Fe-Mn-Al-C corrosion rate, but Gau and Wu concluded that further corrosion rate reductions were necessary to consider Fe-Mn-Al-C alloys suitable replacements for 304 stainless steel.

Table 3. Fe-Mn-Al-C Chemical Compositions and Oxidation Parabolic Rate Constants

Alloy	C	Si	Mn	P	S	Al	Ni	Cr	Mo	Fe	Parabolic Rate Constant ($mg/(cm^2\sqrt{hr})$)
A	0.94	0.10	29.80	0.03	0.02	7.6	-	-	-	Bal	0.0109
B	1.7	0.50	36.00	0.03	0.03	7.60	-	-	1.50	Bal	0.0085
C	0.40	0.14	24.4	0.04	0.02	9.20	-	-	-	Bal	0.00522
D	0.43	0.15	26.6	0.03	0.01	9.29	-	3.10	0	Bal	0.00289
E	0.42	0.15	27.7	0.03	0.01	8.9	-	5.9	-	Bal	0.0024
304 SS	0.04	0.67	1.23	0.02	0.14	-	8.20	19.00	0.10	Bal	0.0207
1010 Carbon steel	0.05	0.67	0.23	0.01	0.01	-	0.03	0.06	-	Bal	-

Table 4. Fe-Mn-Al-C Corrosion Potential (CP) vs Saturated Calomel Electrode (SCE) and Corrosion Rate (CR) Versus 304 Stainless Steel and Mild Steel.

Alloy	3.5% NaCl		1N CH3CooH		1N NH4(OH)		1N Na2S	
	CP vs SCE	CR (mpy)	CP vs SCE	CR (mpy)	CP vs SCE	CR (mpy)	CP vs SCE	CR (mpy)
Mild Steel	-0.74	7.30	-0.55	13.70	-0.34	2.44	-0.70	7.00
304 SS	-0.25	0.15	-1.00	0.18	-.20	0.37	-1.50	0.74
A	-0.53	3.80	-0.62	140.00	-0.18	2.10	-1.02	13.00
B	-0.49	3.00	-0.50	71.70	-0.17	1.10	-1.10	5.12
C	-0.61	4.75	-0.61	380.00	-0.18	2.19	-1.02	6.01
D	-0.56	4.00	-0.71	595.00	-0.23	1.10	-1.12	5.12
E	-0.40	2.40	-0.63	439.00	-0.20	1.00	-1.08	4.60

4.10 High strain rate behavior

High strain rate behavior of Fe-Mn-Al-C alloys has been investigated for solution treated[39,58] and age hardened[11,39] conditions. Chiou et al. investigated a solution treated Fe-32Mn-10Al-1.07C-0.36Mo alloy utilizing a split Hopkinson bar compression test for strain rates from 10^3 s^{-1} to 10^4 s^{-1}.[58] Yield strength, as shown in Figure 22, increased

exponentially from 1450 MPa at 10^3 s^{-1} to 1800 MPa at 10^4 s^{-1} whereas the fracture strain decreased in a linear fashion from approximately 0.55 to 0.38.

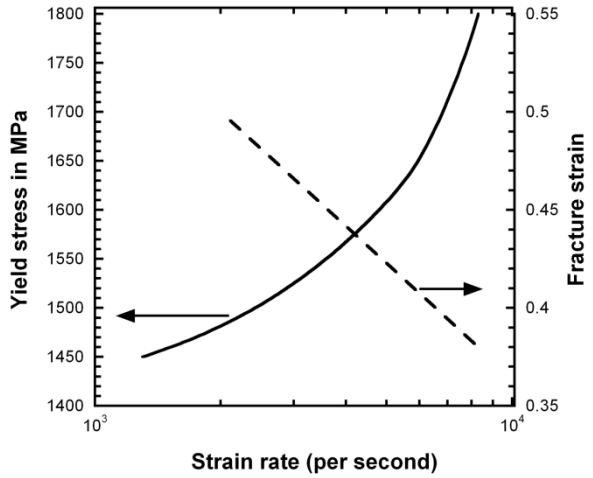

Figure 22. The yield stress and fracture strain is plotted as a function of compressive strain rate for a Fe-32Mn-10Al-1.1C-0.4Mo alloy in the solution treated condition. At the maximum strain rate approaching 10^4 s^{-1}, the alloy yielded at 1800 MPa with ~0.38 strain to failure.[58]

At higher strain rates the work hardening exponent increased from 0.3 to 0.66, the activation volume for dislocation mobility decreased, and the degree of dislocation entanglement increased.

Howell et al. investigated cast materials (Fe-30Mn-9Al-1Si-0.9C-0.5Mo) in the solution treated and aged condition using high strain rate compression specimens by split Hopkinson bar technique and compared those values to rolled homogeneous armor (RHA) of equivalent hardness at a strain rate of 3000 s^{-1}.[39] Fe-Mn-Al-C specimens were solution treated at 1050°C. The aged specimen set was isothermally held for 10 hours at

530°C. The solution treated material yielded at 950 MPa and work hardened to 1,552 MP and the fracture strain was 0.50 (see Figure 23).

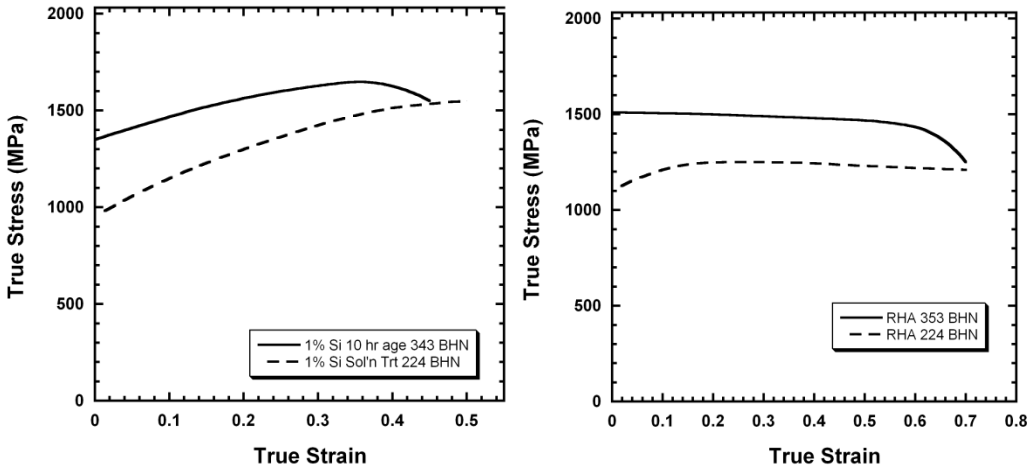

(a) (b)

Figure 23. The Fe-30Mn-9Al-1Si-0.9C-0.5Mo alloy designated in the figure as 1%Si (a) shows work hardening in the solution treated and 10 hour 530°C aged condition at a strain rate of 3000 s^{-1}. Aged hardened material does not work harden as greatly as solution treated material, but age hardened specimens had greater yield and ultimate strength and slightly lower fracture strain. Rolled homogeneous armor (b) does not strain harden to failure. Ultimate strength occurs between 0.1 and 0.2 strain followed by decreasing stress to fracture beyond 0.6 strain.

The 10 hour aged specimen yielded at 1,334 MPa and work hardened to 1,651 MPa and the fracture strain was 0.45. Howell et al. observed that fracture was initiated by shear bands; however, both conditions exhibited work hardening. In contrast, only the RHA (224 BHN) material strain hardened (at less than 0.2 strain) prior to the ultimate stress. More importantly, the ultimate strengths (see Table 5) and specific ultimate strengths (see Table 6) of the Fe-Mn-Al-C are greater than RHA.

Table 5. Comparison of compressive strengths of two heat treated conditions between a 1% silicon containing Fe-Mn-Al-C alloy and RHA tested at 3000 s^{-1} strain rate.

Alloy	Low Hardness Heat Treat Condition 1% Si – 224 BHN RHA – 224 BHN		High Hardness Heat Treat Condition 1% Si – 343 BHN RHA – 352 BHN	
	Yield Strength	Ultimate Strength	Yield Strength	Ultimate Strength
1% Si	950 MPa	1,552 MPa	1,334 MPa	1,651 MPa
RHA	1,100 MPa	1,349 MPa	1,500 MPa	1,500 MPa

Table 6. Comparison of specific compressive ultimate strengths of two heat treated conditions between a 1% silicon containing Fe-Mn-Al-C alloy and RHA tested at 3000 s^{-1} strain rate.

Alloy	Density	Specific Strength 1% Si – BHN 224 RHA – BHN 224	Specific Strength 1% Si – BHN 343 RHA – BHN 352
1% Si	6.7 g/cm^3	231 MPa/ρ	246 MPa/ρ
RHA	7.8 g/cm^3	173 MPa/ρ	192 MPa/ρ

Frommeyer and Brux conducted a split Hopkinson bar investigation of a Fe-26Mn-11Al-1.1C alloy aged at 550°C for 16 hours.[11] As shown in Figure 24, the age hardened alloy also showed an increasing yield strength and decreasing failure strain with increasing deformation rate similar in fashion to that observed for the solution treated material studied by Chiou et al.[58]

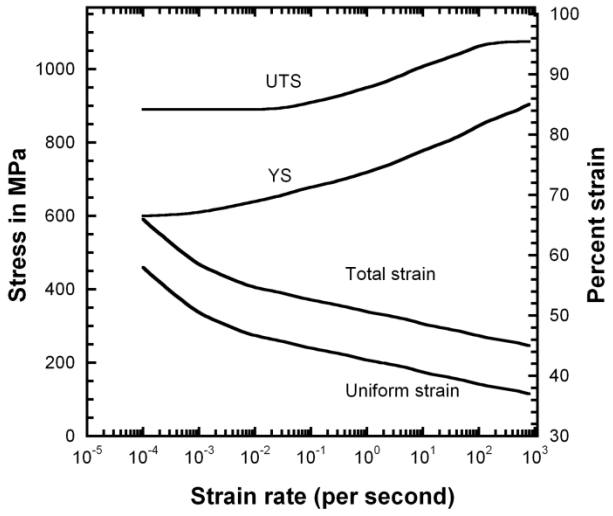

Figure 24. Strain rate dependency of strength and ductility is shown for a Fe-26Mn-11Al-1.1C alloy aged at 550°C for 16 hours. Tensile stress, yield stress, total elongation, and uniform elongation were plotted against strain rates from 10^{-4} s^{-1} to 10^{3} s^{-1}. The alloy strengthens with a corresponding strain loss for increasing strain rates. At the highest measured strain rate ~10^{3} s^{-1}, tensile stress reaches a maximum value ~1100 MPa and uniformly elongates to ~38%.[11]

In the aged condition, Frommeyer and Brux reported a yield strength, tensile strength and a uniform strain of 950 MPa, 1100 MPa and 37% at a strain rate of 10^{3} s^{-1} which was the maximum strain rate tested. The strain rate sensitivity was higher for this Fe-Mn-Al-C alloy than for conventional deep drawing steels within the strain rate range of 10^{-1} to 10^{1} s^{-1}. Additionally, the authors reported a specific energy absorption of 0.43 J/mm^{3}. By comparison, conventional deep drawing steels have an energy absorption range between 0.16 and 0.23 J/mm^{3}.

4.11 Electrical Resistivity and Thermal Conductivity

Manganese and aluminum additions increase the electrical resistivity of Fe-Mn-Al-C alloys.[59] Charles and Issi[59] measured electrical resistivity as a function of manganese content and aluminum content. Eight Fe-Mn-Al-C compositions (Table 7 were tested in the temperature regime -204°C > T > 27° C (see Figure 25).

Table 7. Fe-Mn- Al-C Chemical Compositions for Electrical Resistivity Investigation.

Alloy	Fe	Mn	Al	C
A	Bal	29	-	-
B	Bal	39	-	-
C	Bal	44	-	-
D	Bal	32	2.5	-
E	Bal	29	5	-
F	Bal	34	5	-
G	Bal	40	5	-
H	Bal	30	6	0.3
I	Bal	30	8	1

Manganese increases resistivity by 1.5 x 10^{-6} Ω per wt.% added. Binary Fe-Mn alloys were more conductive than ternary Fe-Mn-Al or quaternary Fe-Mn-Al-C compositions. The resistivity is nearly constant for alloys with 5% aluminum, but resistivity decreases with increasing temperature for alloys containing carbon and with aluminum contents greater than 5%.

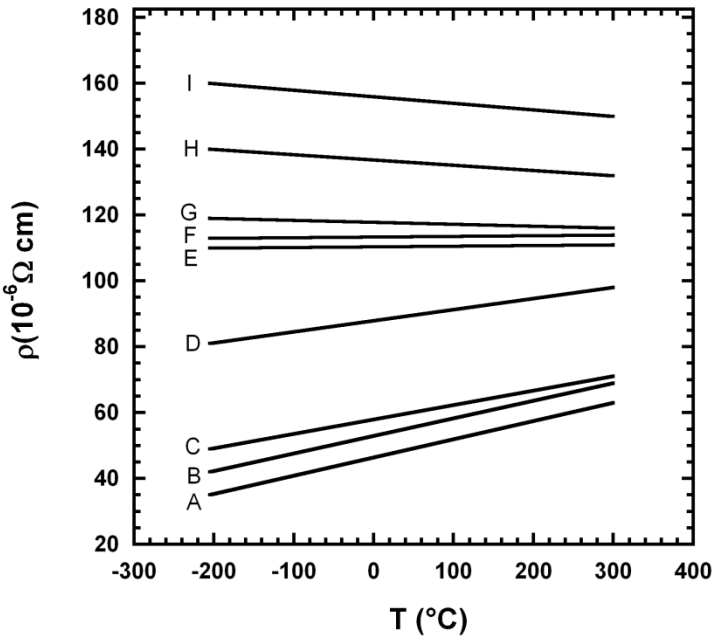

Figure 25. Resistivity is plotted for nine Fe-Mn-Al-C compositions (Table 6) as a function of temperature. Increased amounts of manganese and aluminum increases the electrical resistivity of Fe-Mn-Al-C alloys. Binary Fe-Mn compositions show a linear resistance increase with temperature versus aluminum containing specimens that show a decrease in electrical resistance for increasing temperatures.[59]

Thermal conductivity measurements[59] show binary Fe-Mn alloys possess greater thermal conductivity than ternary Fe-Mn-Al compositions (see Figure 26). Charles and Issi determined that aluminum substitutions into the matrix contribute lattice imperfections responsible for phonon scattering resulting in lower thermal conductivity.

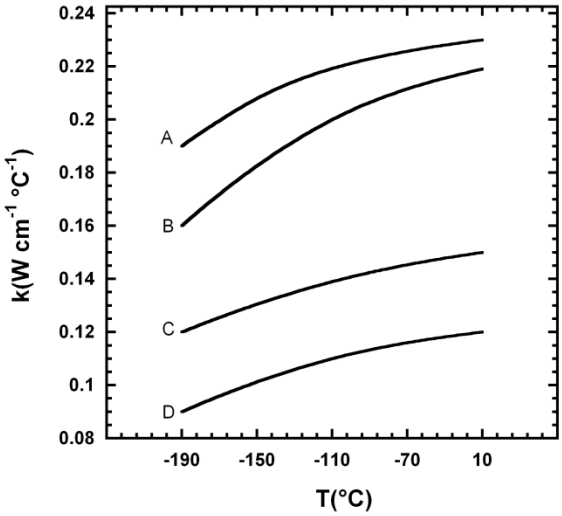

Figure 26. Thermal conductivity is shown for Fe-32Mn (A), Fe-36Mn (B), Fe-32Mn-2.5Al (C), and Fe-29Mn-5Al (D). Thermal conductivity increases with reductions of aluminum and manganese, and all compositions showed a parabolic increase for increasing temperature.[59]

5. Fe-Mn-Al-C-X ALLOYS

Research to improve the mechanical properties and microstructure of Fe-Mn-Al-C by alloy addition has been conducted by numerous investigators. The most common addition studied has been silicon[45,46,55,60-63], but boron[12], vanadium[12,13,64], niobium[13,64], molybdenum[12,54,64], chromium[55], nickel[32], and zirconium[12] have also been investigated. Chromium and nickel additions were covered in previous sections of this paper.

Silicon has shown the greatest influence and benefit to microstructural development and mechanical properties of the Fe-Mn-Al-C alloys studied thus far. In the age hardened condition, silicon reduces the matrix lattice parameter and has been shown to eliminate β-Mn formation even after isothermal times at temperatures up to 900 °C.[35,61] In place of β-Mn, silicon promotes the formation of B2 and/or DO_3 precipitates

in conjunction with κ-carbide that precipitates along austenite grain boundaries.[35] The nucleation sequence of B2 and DO_3 was not stated. A Kurdjimov-Sachs relationship between the κ-carbide and the DO_3 has been reported.[60-63] Figure 27 is the time temperature transformation diagram for a 1.25% silicon containing alloy.[61] The regions on the diagram are divided to include a mapping of the grain structure morphology. Chemical modulation occurs in area 1 followed by homogeneous κ-carbide precipitation in Area 2. Area 3 corresponds to both grain boundary formation of κ-carbide and a DO_3 or B2 precipitate. Area 4 represents a discontinuous reaction product of grain boundary κ-carbide, DO_3 and/or B2 precipitates. All equilibrium phases are present in Area 5; and for alloys without silicon, precipitation of β-Mn is included as Area 6. As expected, higher temperatures result in faster kinetics. Aging at 500°C and below greatly extends the time until grain boundary precipitation occurs. Prodhan and Chakrabarti[36] identified a grain boundary precipitate as a $Mn_{12}Si_7Al_5$ compound.

Acselrad et al. studied the mechanical properties of a Fe-29.4Mn-8.8Al-1.33Si-1C alloy.[65] After solution treating at 1050°C and water quenching the yield strength, tensile strength, and elongation to failure were 620 MPa, 871 MPa, and 77%. Upon aging at 550°C for 15 hours the yield strength, tensile strength and elongation to failure were 884 MPa, 1210 MPa and 15%. In contrast, a similar alloy without silicon (Fe-31.9Mn-8.5Al-0.9C-0.2Mo) was studied in the solution treated state.[12] The non-silicon alloy had a yield strength, tensile strength and elongation of 360 MPa, 820 MPa and 64%; and, after aging for 16 hours at 550°C the tensile strength was 1000 MPa with 40% elongation.

Addition of silicon has also been investigated in the development of Fe-Mn-Al-C alloys for lightweight steel castings. Recent work by Howell et al. found that silicon

additions up to 2.25 wt.% in Fe-30Mn-9Al-1C alloys lower the melting temperature from 1390°C to 1325°C.[67] At equivalent pouring temperatures, silicon additions increase the fluidity greatly, but on a superheat basis silicon has no effect on fluidity (see Figure 28). The Fe-Mn-Al-C alloys are comparable to ductile irons with respect to fluidity and melting temperature. The increased fluidity may be a result of the high manganese content and the addition of silicon reduces the melting temperature.

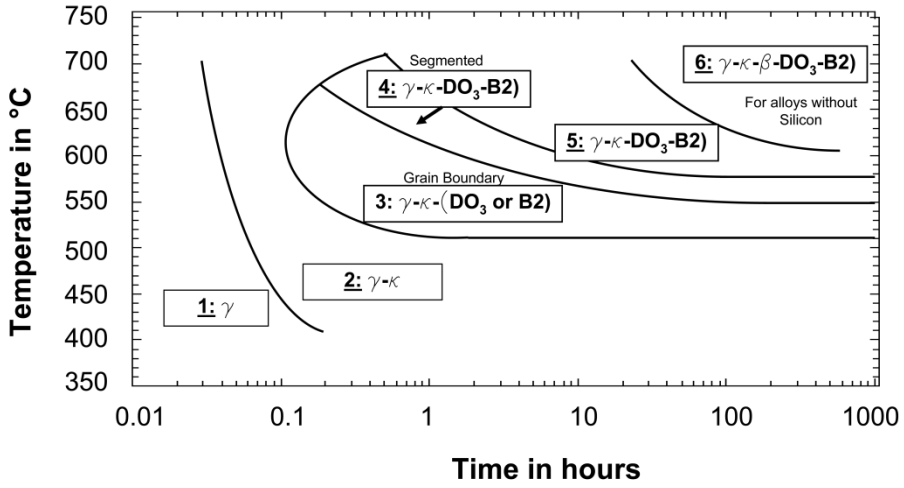

Figure 27. Time temperature transformation for a 1.25 wt.% Si modified Fe-Mn-Al-C alloy is subdivided as follows: 1) chemical segregation and zone formation, 2) matrix κ-carbide nucleation and growth, 3) heterogeneous matrix κ-carbide formation and grain boundary κ-carbide and DO_3 or B2 precipitation, 4) continued growth and decomposition forming discontinuous segmented phases of κ-carbide, DO_3, and B2, 5) final equilibrium phases, and 6) β-manganese for non-silicon containing alloys.[65]

Molybdenum additions to Fe-Mn-Al-C alloys have been investigated for carbide formation and strength contributions. For a Fe-24.6Mn-6.6Al-3.1Mo-1.0C alloy, Peng et al. observed precipitation of complex carbonitrides of the M_6C or $M_{23}C_6$ type within the

austenite grain upon aging at 700°C.[65] M_6C or $M_{23}C_6$ type carbides are aligned crystallographically with close packed planes parallel to {111} of the austenite. Liu et al. reported M_2C type carbide precipitation within the austenite matrix after aging an identical Fe-24.6Mn-6.6Al-3.1Mo-1.0C alloy at 550°C for 36 hours.[68] Neither Peng et al. nor Liu et al. reported precipitation of κ-carbide during aging. Kalashnikov et al. reported tensile strengths greater than 1150 MPa on a 0.6% molybdenum containing Fe-29Mn-9Al-0.9C alloy.[13] The alloy was rolled, solution treated at 1050°C, and aged at 550°C for 16 hours. When alloyed with 0.4% molybdenum and 0.6% tungsten (and after aging for 16 hours 550°C) tensile strength increased slightly to values above 1160 MPa.

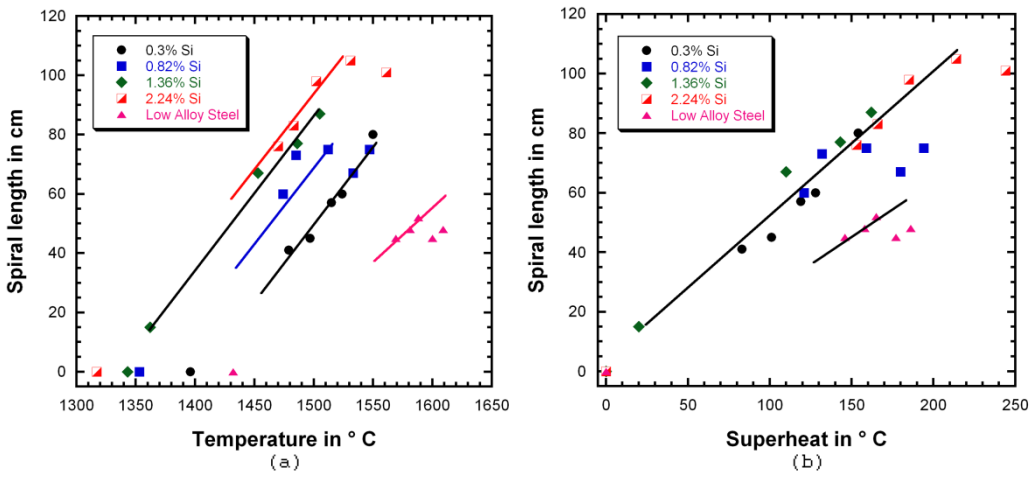

Figure 28. Fluidity spiral lengths for Fe-Mn-Al-C-XSi alloys and low alloy steel versus (a) pouring temperature and (b) superheat. Melting temperatures for each alloy are shown in (a) at zero spiral length.

Vanadium and niobium are effective grain refiners in Fe-Mn-Al-C alloys.[13,64] Vanadium concentrations above 0.75% in a Fe-29Mn-9Al-0.9C alloy proved to be an

effective grain pinning agent up to 1180°C.[13] Niobium carbide was less effective as a grain refining agent since these carbides could not be precipitated to affect recrystallization during hot working. Kim et al. measured mechanical properties of a hot rolled Fe-30Mn-5Al-0.3C alloy modified with either 0.1% vanadium or 0.1% niobium.[64] The niobium modified alloy produced higher strength and ductility than either the vanadium modified alloy or the base material. The niobium containing alloy demonstrated greater impact toughness than the vanadium containing alloy or a 9% nickel steel at testing temperatures from 0 to -200°C. However, the unmodified Fe-Mn-Al-C base alloy had the highest impact energy in the same temperature range. Strength and ductility of the niobium containing Fe-Mn-Al-C alloy increased with decreasing testing temperature (see Figure 29). For example, yield strength was 944 MPa and elongation to failure was 57% at a temperature of -196° versus room temperature tested values of 600 MPa and 29%.

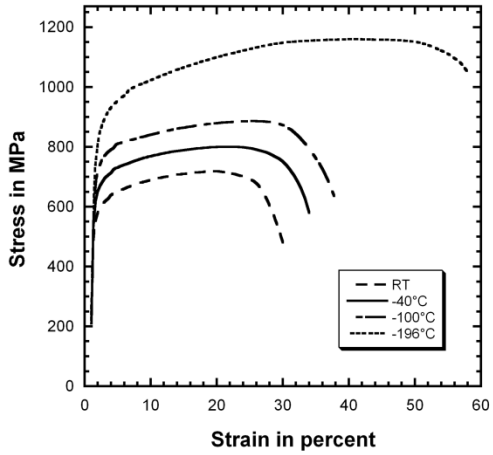

Figure 29. A homogenized and cold rolled Fe-30Mn-5Al-0.3C-0.1Nb alloy's nominal stress strain data is shown for testing at various temperatures. The alloy exhibited higher strength and ductility corresponding to decreasing testing temperatures. Maximum tensile strength of 1100 MPa and failure strain of 57% was achieved at -196°C.[64]

Zirconium and boron additions were investigated by Han et al.[12] In a Fe-33.5Mn-8.24Al-0.9C alloy, the addition of 0.27% zirconium proved to be an effective grain refining agent up to a processing temperature of 980°C. However, in the solution treated state, the zirconium addition reduced ductility. The addition of 0.007% boron promoted β-Mn precipitation at the grain boundary resulting in a decrease in peak aging time and ductility. The investigators concluded that neither of these alloy additions contributed significant benefits to the base alloy composition.

6. CONCLUSION

The Fe-Mn-Al-C system comprises a very property-flexible family of alloys. Typical compositions are in the range of 18 to 30 wt.% Mn, 5 to 12 wt.% Al, and 0.7 to 1.2 wt.% C, with the balance being Fe. Solution treated alloys with sufficient C and Mn have a fully austenitic microstructure. Aging produces equilibrium phase constituents of austenite, ferrite, κ-carbide, and β-Mn. κ-carbide, an $E2_1$ perovskite precipitate, is responsible for strength increases during aging. Aging below 650°C precipitates κ-carbide in a homogeneous fashion throughout austenite and over aging produces heterogeneous grain boundary phases deleterious to mechanical properties. Mechanical properties range from a solution treated 350 MPa yield stress with elongation to failure as high as 77% to alloys with tensile strengths greater than 2 GPa. Fe-Mn-Al-C alloys can also be engineered to have a higher work hardening rate than AISI 304 stainless steel. The Fe-Mn-Al-C alloys are susceptible to stress corrosion cracking and hydrogen embrittlement. Alloy additions of silicon and refractory elements are beneficial to both tensile and fatigue performance. The addition of silicon has been shown to prevent the

formation of β-Mn during age hardening, improving age hardening behavior and strength, and increased castability over non silicon alloyed Fe-Mn-Al-C steels.

This material review is part of an ongoing investigation focused on evaluating Fe-Mn-Al-C alloys to replace traditional quench and tempered AISI 4130 cast steels. Density reduction up to 17% and excellent high strain rate deformation behavior make this alloy family an interesting candidate for select cast steel armor components.

REFERENCES

1. Hadfield, R., Burnham, T. H., "Special Steels", 2nd ed., p.100, The Pitman Press, New York (1933).
2. Dean, R.S., Clarence, T. A., United States Patent Number 2,329,186, (1943).
3. Dean, R.S., Clarence, T. A., United States Patent Number 2,376,869 (1945).
4. Ham, J. L., Cairns, R. E., "Manganese Joins Aluminum to Give Strong Stainless," Product Engineering, Dec, pp. 51-52 (1958).
5. Banerji, S. K., "An Update on Fe-Mn-Al Steels," presented at Vanderbilt University's workshop on "Conservation and Substitution Technology for Critical Material," June 15-17, (1981).
6. National Materials Advisory Board, commission on Sociotechnical Systems, "Contingency Plans for Chromium Utilization," National Academy of Sciences (1978).
7. James, P. J., "Precipitation of the carbide $(Fe,Mn)_3AlC$ in an Fe-Al Alloy," J. Iron and Steel Inst., Jan, pp. 54-57 (1969).
8. Batrakov, V. P., Alekseenko., M. F., Filimonova, L. A., Krivonogov, G. S., Kozyreva, L. G., Sapozhnikova, V. G., Molotova, V.A., "State of the Surface Layer and Corrosion Resistance of Steel 9G28Yu9MVB," Prot. of Metals., Vol. 10, pp. 487-490 (1974).
9. Schmatz, D. J., "Formation of Beta Manganese-Type Structure in Iron-Aluminum-Manganese Alloys," Trans. of Met. Soc. of AIME, Vol. 215, pp. 112-114 (1959).
10. Kayak, G. L., "Fe-Mn-Al Precipitation-Hardening Austenitic Alloys," Met. Sc. And Heat Tr., Vol. 11, pp. 95-97 (1969).
11. Frommeyer, G., Brux, U., "Microstructures and Mechanical Properties of High-Strength Fe-Mn-Al-C Light-Weight TRIPLEX Steels," Steel Research Int., Vol. 77, pp. 627-633 (2006).

12. Han, K. H., Choo, W. K., Choi, D. Y., Hong, S. P., “Age Hardening in Fe-Mn-Al-C Austenitic Alloys,” TMS-AIME, pp. 91-106 (1987).

13. Kalashnikov, I. S., Ermakov, B. S., Acselrad, O., Pereira, L. K., “Alloy of Steels of the Fe-Mn-Al-C System with Refractory Elements,” Met. Sci. and Heat Treat., Vol. 43, pp. 493-496 (2001).

14. Kimura, Y., Handa, K., Hayashi, K., Mishima, Y., “Microstructure Control and Ductility Improvement of the Two-Phase g-Fe/κ-$(Fe,Mn)_3AlC$ Alloys in the Fe-Mn-Al-C Quaternary System,” Intermetallics, Vol. 12, pp. 607-617 (2004).

15. Koster, W., Torn., W., “Die Eisenecke des Systems Eisen-Mangan-Alminium,” Arch Eisenhüttenwes, Vol. 7, pp. 365-366 (1933) in German.

16. Krivonogov, G.S., Alekseyenko, M. F., Solov’yeva, G. G., “Phase Transformation Kinetics in Steel 9G28Yu9MVB,” Fiz. Metal. Metalloved, Vol. 39, No. 4, pp. 775-781 (1975).

17. Ishida, K., Ohtani, H., Naoya, S., Kainuma, R., Nishizawa, T., “Phase Equilibria in Fe-Mn-Al-C Alloys,” ISIJ, Vol. 30, pp. 680-686 (1990).

18. Goretskii, G. P., Gorev, K. V., “Phase Equilibria in Fe-Mn-Al-C Alloys,” Russian Met., Vol. 2, pp. 217-221 (1990).

19. Acselrad, O., Kalashnikov, I. S., Silva, E. M., Simao, R. A., Achete, C. A., Pereira, L. C., “Phase Transformation in Fe-Mn-Al-C Austenite Steels with Si Addition,” Met. Tran A., Vol. 33A, pp.3569-3572 (2002).

20. Storchak, N. A., Drachinskaya, A. G., “Strengthening of Fe-Mn-Al-C Alloys During Aging,” Fiz. Metal. Metalloved., Vol. 44., No. 2, pp. 373-380 (1977).

21. Hale, G. E., Baker, A. J., “Carbide Precipitation in Austenitic Fe-Mn-Al-C Alloys,” Conf. on Alt. Alloying for Env. Res. New Orleans, LA., (1986).

22. Sato, K., Kazuhiro, T., Inoue, Y., “Age Hardening of an Fe-30Mn-9Al-0.9C Alloy by Spinodal Decomposition,” Scripta Met., Vol. 22, pp. 899-902 (1988).

23. Han, K. H., Choo, W. K., “Phase Decomposition of Rapidly Solidified Fe-Mn-Al-C Austenitic Alloy,” Met. Trans. A., Vol. 20A, pp. 205-214 (1989).

24. Sato, K., Tagawa, K., and Inoue, Y., “Modulated Structure and Magnetic Properties of Age-Hardenable Fe-Mn-Al-C Alloys,” Met. Trans A, vol. 21A, pp 5-11 (1990).

25. Sato, K., Igarashi, Y., Inoue, Y., Yamazaki, T., Yamanaka, M., “Microstructure and Age Hardening in Spinodally Decomposed Austenitic Fe-Mn-Al-C Alloys,” Proceedings of the International Conference on Stainless Steels (1991).

26. Prodhan, A., Charkrabarti, A. K., “A Study on Cast Fe-Mn-Al-Si-C Alloys,” AFS Transactions, vol. 37, pp. 35-46 (1990).

27. Cheng, W. C., Lin, H. Y., "The Precipitation of FCC Phase from BCC Matrix in an Fe-Mn-Al Alloy," Mat. Sci. and Eng., Vol. 323, pp. 462-466 (2002).

28. Kalashnikov, I., Acselrad, O., Shalkevich, A., Pereira, L.C., "Chemical Composition Optimization for Austenitic Steels of the Fe-Mn-Al-C System," Journal of Materials Engineering and Performance, Vol. 9, No. 6, pp. 597-602 (2000).

29. Oshima, R., Wayman, C., "Fine Structure in Quenched Fe-Al-C Steels," Met. Trans. B., Vol. 3, pp. 2163-2169 (1972)

30. Choo, W. K., Yoon, J. C., "Phase Decomposition of Fe-30Mn-7.8Al-1.3C Alloy," Proceedings of the Phase Transformations Conference, 6-10 JULY, pp. 47-50 (1987).

31. Cahn, J. W., "Hardening by Spinodal Decomposition," Acta Met., Vol. 11, pp. 1275-1282 (1963).

32. Kimura, Y., Hayashi, K., Handa, K., Mishima, Y., "Microstructural Control for Strengthening the g-Fe/$E2_1$-$(Fe,Mn)_3AlC_x$ Alloys," Mater. Sci. Eng. A329-331, pp. 680-685 (2002).

33. Kalashnikov, I.S., Acselrad, O., Shalkevich, A., Chumakova, L. D., Pereira, L. C., "Heat Treatment and Thermal Stability of Fe-Mn-Al-C Alloys," Journal of Materials Processing Technology, No. 136, pp. 72-79 (2003).

34. Tjong, S. C., Zhu, S. M., "Tensile Deformation Behavior and Work Hardening Mechanism of Fe-28Mn-9Al-0.4C and Fe-28Mn-9Al-1C Alloys," Mat. Trans., Vol. 38, pp. 112-118 (1997).

35. Acselrad, O., Kalashnikov, I. S., Silva, Khadyev, M. S., E. M., Simao, "Diagram of Phase Transformation in the Austenite of Hardened Alloy Fe-28Mn-8.5Al-1C-1.25Si as a result of Aging due to Isothermal Heating," Met. Sci. and Heat Treat., Vol. 48, pp. 543-553 (2006).

36. Prodhan, A., Charkrabarti, A. K., "A Study on Age Hardening in Cast Fe-Mn-Al-Si-C Alloys," J. Mat. Sci., Vol. 25, No. 3, pp. 1856-1862 (1990).

37. Choo, W. K., Kim, J. H., "Microstructural and Mechanical Property Changes on Precipitation of Intermetallic κ' Cubic Carbide Phase in the Fe-Mn(Ni)-Al-C Solid Solution," Conf. on Thermo-mechanical Process. of Steels and Other Mats., pp. 1631-1637 (1997).

38. Brady, G. S., Clauser, H. R., "Manganese-Aluminum Steel," Materials Handbook, 11^{th} Ed., p. 497 (1977).

39. Howell, R. A., Weerasooriya, T., Van Aken, D. C., "Tensile, High Strain Rate Compression and Microstructural Evaluation of Lightweight Age Hardenable Cast Fe-30Mn-9Al-XSi-0.9C-0.5Mo Steel," AFS Transactions – awaiting publication.

40. Chen, S. K., Chour, K. W., Lee, W. B., Wan, C. M., Byrne, J. G., "The Formation of BCC Phase During the Solution Treatment of Duplex Fe-Mn-Al-C Alloys," Mat. Res. Bull., Vol. 25, pp. 1115-1119 (1990).

41. Tian, X., Tian, R., Wei, X., Zhang, Y., "Effect of Al Content on Work Hardening in Austenitic Fe-Mn-Al-C Alloys," Can. Met. Quart., Vol. 43, pp. 183-192 (2004).

42. Lai, H. J., Wan, C. M., "The Study of Deformation Twins in the Austenitic Fe-Mn-C and Fe-Mn-Al-C Alloys," Scripta Met., Vol. 23, pp. 179-182 (1982).

43. Yang, W. S., Wan, C. M., "The Influence of Aluminum Content to the Stacking Fault Energy in Fe-Mn-Al-C Alloy System," J. Mater. Sci., Vol. 25, pp. 1821-1823 (1990).

44. Olson, G. B., Cohen, M., "A General Mechanism of Martensitic Nucleation: Part I: General Concepts and the FCC to HCP Transformation," Met. Trans. A, Vol. 7A, pp. 1897-1904 (1976).

45. Acselrad, O., Pereira, L. C., Amaral, M. R., "Processing Condition, Microstructure and Strength of an Austenitic Fe-Mn-Al-C Alloy," Proceedings of Proc. and Prop. of Mats., pp. 829-834 (1992).

46. Acselrad, O., Dille, J., Pereira, L. C., Delplancke, J. L., "Room-Temperature Cleavage Fracture of Fe-Mn-Al-C Steels," Met. Trans. A, Vol. 35A, pp. 3863-3866 (2004).

47. Server., W. L., "Impact Three-Point Bend Testing for Notched and Precracked Specimens," ASTM J. Test. and Eval., Vol. 6, pp. 29-34 (1978).

48. Chang, S. C., Hsiau, Y. H., "Tensile and Fatigue Properties of Fe-Mn-Al-C Alloys," J. Mater. Sci., Vol. 24, pp. 1117-1120 (1989).

49. Ho, N. J., Wu, L. T., Tjong, S. C., "Cyclic Deformation of Duplex Fe-30Mn-10Al-0.4C Alloy at Room Temperature," Mater. Sci. Eng. A., Vol. 102, pp. 49-55 (1988).

50. Ho, N. J., Tjong, S. C., "Cyclic Stress-Strain Behavior of Austenitic Fe-29.7Mn-8.7Al-1.04C Al7oy at Room Temperature," Mater. Sci. Eng., Vol. 94, pp. 195-202 (1987).

51. Kalashnikov, I. S., Acselrad, O., Kalichak, T., Khadyyev, M. S., Pereira, L. C., "Behavior of Fe-Mn-Al-C Steels During Cyclic Tests," J. of Mat. Eng., Vol. 9, pp. 334-337 (2000).

52. Pierpoint, C. A., Sudarshan, T. S., Loutham, M. R., Place, T. A., "Hydrogen Susceptibility of a Mn-Al Austenitic Stainless Steel," Weld. Fail. Analysis and Met., Vol. 14, pp. 423-435 (1985).

53. Sudarshan, T. S., Harvey, D. P., Place, T. A., "Mechanistic Similarities Between Hydrogen and Temperature Effects on the Ductile-to-Brittle Transition of a Stainless Steel," Met. Trans. A., Vol. 19, pp. 1547-1553 (1988).

54. Chang, S. C., Sheu, T. S., Wan C. M., “Studies of Stress-Corrosion Cracking of Fe-Mn-Al Stainless Steels with Different Carbon Contents,” Str. Of Met. and Alloys (ICSMA 7), Vol. 2, pp. 1081-1086 (1985).

55. Chang, S. C., Liu, J. Y., Juang, H. K., “Environment-Assisted Cracking of Fe-32%Mn-9%Al Alloys in 3.5% Sodium Chloride Solution,” Corrosion, Vol. 51, pp. 399-406 (1995).

56. Garciak, J. C., Rosas, N., Rioja, R. J., “Development of Oxidation Resistant Fe-Mn-Al-Alloys,” Metals Progress, Vol. 122, pp. 47-50 (1982).

57. Gau, Y. J., Wu, J. K., “The Influence of Alloying Elements on the Corrosion Behavior of Fe-Mn-Al Alloys,” Corrosion Prevention and Control, Vol. 44, pp. 55-60 (1997).

58. Chiou, S. T., Cheng, W. C., Lee W. S., “Strain Rate Effects on the Mechanical Properties of a Fe-Mn-Al Alloy Under Dynamic Impact Deformations,” Mat. Sci. and Eng. A., Vol. 392, pp.156-162 (2005).

59. Charles, J., Issi, J. P.,”Electrical and Thermal Conductivities of Fe-Mn-Al Austenitic Alloys,” J. of Appl. Phys., Vol. 17, pp. 2399-2406 (1984).

60. Chou, J. S., Chao, C. G., “Tensile Properties of a DO_3-Containing Fe-Mn-Al-Si-C Alloy at Elevated Temperatures,” Scripta Met., Vol. 26, pp. 1417-1421 (1992).

61. Acselrad, O., Kalashnikov, I. S., Silva, E. M., Simao, R. A., Achete, C. A., Pereira, L. C., “Phase Transformations in Fe-Mn-Al-C Austenitic Steels with Si Addition,” Met. Trans. A., Vol. 33A, pp. 3569-3572 (2002).

62. Chao, C. Y., Liu, T. F., “Phase Transformation in an Fe-7.8Al-29.5Mn-1.5Si-1.05C Alloy,” Met. Trans. A., Vol. 24A, pp. 1957-1963 (1993).

63. Chu, C. M., Huang, H., Kao, P. W., Gan, D., “Effect of Alloying Chemistry on the Lattice Constant of Austenitic Fe-Mn-Al-C Alloys,” Scripta Met., Vol. 30, pp. 505-508 (1994).

64. Kim, Y. G., Park, Y. S., Han, J. K., “Low Temperature Mechanical Behavior of Microalloyed and Controlled-Rolled Fe-Mn-Al-C-X Alloys,” Met. Trans. A, Vol. 16A, pp. 1689-1693 (1985).

65. Liu, T. F., Peng, S. W., Lin, Y. L., Wu, C. C., “Orientation Relationships among $M_{23}C_6$, M_6C and Austenite in an Fe-Mn-Al-Mo-C Alloy,” Met. Trans A, Vol. 21A, pp. 567-573 (1990).

66. Acselrad, O., Pereira, L. C., Amaral, M. R., “Processing Conditions, Microstructure, and Strength of an Austenitic Fe-Mn-Al-C Alloy,” Proceedings from the International Conference on the Processing, Properties, and Applications of Metallic and Ceramic Materials, Vol. II, pp.829-834 (1992).

67. Howell, R. A., Lekakh, S. L., Van Aken, D. C., Richards, V. L., “The Affect of Silicon Content on the Fluidity and Microstructure of Fe-Mn-Al-C Alloys,” AFS Transactions, Vol. 116, pp. 867-878 (2008).

68. Peng, S. W., Chou, C. P., “Orientation Relationships Between M sub 2 C Carbide and the Austenite Matrix in an Fe--Mn--Al--Mo--C Alloy,” Met. Trans. A, Vol. 24A, No. 5, pp.1057-1065 (1993).

PAPER

2. The Effect of Silicon Content on the Fluidity and Microstructure of Fe-Mn-Al-C Alloys

R.A. Howell, S. N. Lekakh, D.C. Van Aken, V.L. Richards

Army Research Lab

Missouri University of Science and Technology

Department of Materials Science and Engineering

Rolla, MO 65409

Tel.: 573-341-4717

E-mail: dcva@mst.edu

Key Words: Fe-Mn-Al-C, lightweight steel, fluidity, liquidus, solidus, dendrite coherency point

Published in the Transactions of the American Foundry Society 2008 issue.

ABSTRACT

Fe-Mn-Al-C steels show promise as lightweight steel for thin-walled casting production. A nominal Fe -30wt.%Mn -9wt.%Al -0.9wt.%C alloy was modified with 0.3, 0.82, 1.36 and 2.24 wt.% Si. Standard fluidity spirals were cast and compared with a low alloy steel. Silicon increased the cast spiral length for equivalent pouring temperatures, and all Fe-Mn-Al-C-Si alloys had longer spiral lengths than the low alloyed steel. Thermal analysis was used to determine that silicon additions lowered liquidus, dendrite coherency point (DCP), and solidus temperatures by approximately 30°C per wt.% Si. Spiral lengths were 70% longer for the Fe-Mn-Al-C-Si alloys than for low alloyed steel at 150°C superheat. Cast Fe-Mn-Al-C-Si alloys had duplex microstructures of austenite and up to 16 vol.% ferrite. At 0.82 wt.% Si, the as-cast microstructure was nearly all austenite and a fully austenitic microstructure was obtained when solution treated above 950°C.

INTRODUCTION

High manganese steels such as Hadfield's steel have a long history of successful application where high wear resistance and impact toughness is required[1,2]. In the last fifty years it was discovered that predominately austenitic steels could be produced with additions of manganese and aluminum; and, that these steels were age hardenable when the aluminum and carbon contents were greater than 5% and 0.3%, respectively[3,4]. All compositions are reported in weight percent (wt.%). These Fe-Mn-Al-C based steels show excellent ductility with greater than 80% strain to fracture when solution treated to produce either a fully austenitic or duplex (austenite and ferrite) microstructure. In the age-hardened condition, these same steels have yield strengths greater than 1,000 MPa

and ductility in excess of 10%. Elastic properties, however, have not been reported[5,6]. In addition, the Fe-Mn-Al-C steels have low density (6.5 to 7.2 g/cm^3) and good corrosion resistance[5]. It is for these reasons during the late 1970s that extensive research was conducted to investigate austenitic Fe-Mn-Al-C alloys for potential replacement of higher cost Cr-Ni stainless steels[3,7]. Most of the early research conducted on the Fe-Mn-Al-C steels focused on wrought products for the transportation industry. Fe-Mn-Al-C alloys are designated as second generation advanced high strength steels. Alloys with a chemistry of 30% Mn, 9% Al, and 1% C are often referred to as TRIPLEX alloys, since they have a three phase microstructure of austenite, ferrite and κ-carbide when age hardened[5].

TRIPLEX steel forms a duplex microstructure of primary austenite with 10-15 vol.% ferrite upon solidification. The final ferrite content is controlled by the homogenization or solution treatment temperature with less ferrite appearing as the solution temperature is increased. The most common temperature for either homogenization or solution treatment is at or above 1050°C for periods in excess of 2 hours. The wrought product will have an austenitic grain structure that contains annealing twins and islands of ferrite that form bands parallel to the principal rolling direction. Upon aging, κ-carbides form homogenously throughout the austenitic phase. The κ-carbide has a perovskite $E2_1$ structure of the form $(Fe,Mn)_3AlC$, which is coherent with the austenite matrix[5,8,9,10]. The homogeneous distribution of κ-carbide is believed to result from a spinodal decomposition related to carbon and aluminum[15] and the most common aging treatment reported is 16 hours at 550° C[1-3,5,6,11-14]. Aging beyond 16 hours at 550°C produces embrittlement resulting from κ-carbides forming continuous

films on grain boundaries and from the formation of β-Mn. Addition of 1.36% Si has been shown to be beneficial in preventing β-Mn formation; however, silicon promotes the formation of B2 and/or DO_3 compounds[16]. The effect of silicon upon the mechanical behavior has not been reported. However, for a wrought TRIPLEX steel that has been aged 16 hrs at 550°C, the tensile strength exceeds 1,100 MPa, the elongation to failure is 40%, and the Charpy impact energy is as high as 100 J/cm^2 in a U-notch specimen[11]. As strain rates increase to 10^3 s^{-1}, these TRIPLEX steels increase in yield strength and ductility decreases. Solution treated materials will exhibit dynamic yield strengths greater than 1,000 MPa and still show significant ductility with elongation to failure up to 40%[17]. The enhanced plasticity has been related to adiabatic shear-band induced plasticity[5]. The light-weight and high energy absorbing characteristics make these materials interesting candidates for military castings.

Significantly less work has been performed on cast Fe-Mn-Al-C alloys. Prodham and Chakrabarti investigated cast Fe-Mn-Al-C-Si alloys[4] and their work looked at mold-metal interactions for sodium silicate and resin bonded sand, phase composition and hardness of cast, homogenized, and aged microstructures. They concluded for cast Fe -30%Mn -x%Al -y%C -1.36%Si that low aluminum (5%) and low carbon (<1%) contents produced moderate aging, but higher aluminum contents of 7.5 to 10% produced rapid age hardening in the temperature range of 500 to 800° C. After long aging times of 30 hrs at 500°C, an $Mn_{12}Si_7Al_5$ intermetallic phase was reported in addition to the austenite, ferrite, and κ-carbide phases. The $Mn_{12}Si_7Al_5$ intermetallic phase was observed to precipitate at ferrite/austenite boundaries and followed precipitation of the κ-carbide. Formation of β-Mn was not reported. Prodham and Chakrabarti reported that the as-cast

and homogenized microstructures of Fe -30.5%Mn -9.8%Al -0.91%C -1.47%Si were predominately austenite with minor volume fractions of ferrite.

Research reported in this paper is part of an ongoing investigation of silicon containing TRIPLEX alloys for steel castings. A Fe -30%Mn -9%Al -0.9%C composition was chosen based upon the TRIPLEX alloy optimization studies of Kalashnikov et al.[11]. The current research was aimed at studying the effect of silicon on castability and phase composition for the cast, homogenized, and solution treated conditions. As a part of the castability studies the liquidus and solidus temperatures for silicon contents of 0.30%, 0.82%, 1.36% and 2.24% were determined by thermal analysis using a single thermocouple and differential thermal analysis (DTA). Thermal analysis was used to determine the liquidus and solidus temperature, solidification kinetics, and the dendrite coherency point (DCP) for the silicon modified Fe-Mn-Al-C alloys. The DCP was calculated from the thermal analysis data using the methodology of Stefanescu et al.[18-22] and Jiang et al.[23] The DCP is a useful parameter in computational solidification modeling and designing patterns for casting. Its importance has been widely recognized because DCP marks the transition from mass flow to interdendritic feeding and when mold filling stops. Standard fluidity spirals were poured for a lower alloy steel and silicon modified TRIPLEX compositions. Fluidity data on the low alloy steel provides a baseline of comparison for steel foundries trying to cast the TRIPLEX alloys. Austenite phase composition of cast, homogenized, and solution treated materials was determined for subsequent alloy optimization and mechanical testing that will be reported in a future paper.

EXPERIMENTAL PROCEDURE

Alloys were prepared in a 100 lb induction furnace under argon gas cover. High purity induction iron, Al, and C were used in conjunction with additions of ferromanganese, ferrosilicon, and ferromolybdenum. A recovery rate of 95% was utilized for the manganese and aluminum based on previous results. The furnace was initially charged with Al, C, ferrosilicon, ferromolybdenum, and 30% of the induction iron. After the initial charge liquefied, the remainder of the induction iron was added to the melt. Ferromanganese was added in the furnace last to ensure maximum solubility in the alloy melt and minimize losses by vaporization and slag formation. A solid electrolyte sensor was used to measure the active oxygen contents, which were all less than 2 ppm due to the high Al content for the TRIPLEX alloys. Thus, no additional deoxidation practice was required at tapping. Melt stirring was limited to that provided by induction heating, natural convection, and by pouring from the furnace to the ladle and casting. Deslagging occurred through application of a low density granular coagulant.

Each heat was poured into a series of five fluidity spiral molds, a rectangular block mold, and a thermal analysis cup. These molds were made using phenolic urethane no-bake (PUNB) silica sand and subsequently coated with a zircon wash. Cope and drag sections were glued together and weighted during pouring to prevent cross filling between spiral rings. A constant head height of 15 cm was maintained for all fluidity spiral tests. The spiral mold was 160 cm in length with a cross sectional area of 1.1 cm^2. S-type (Pt-Pt/Rd) thermocouples were used for temperature measurement in the ladle just before pouring.

The heat chemistries are listed in Table 1 as determined by inductive coupled plasma mass spectrometry backed up with wavelength dispersive spectrometry for the Fe-Mn-Al-C-Si alloys and by arc spectrometry for the low alloy steel. The target chemistry of the low alloy steel was AISI 4130 but higher levels of Mn, Al and Si were obtained because this heat was produced between heats of Fe-Mn-Al-C-Si using the same furnace lining.

Two types of thermal analysis were performed. The first one included thermal analysis of casting solidification. Open type thermal analysis cups (5 cm in diameter 5 cm in depth) made from PUNB silica sand had an exposed Pt-Pt/Rd thermocouple in the cavity bottom. Temperature and time data were recorded using a digital acquisition system. This data was used to compute solidus and liquidus temperatures plus the dendrite coherency point. The second method used a standard DTA system; the purpose of which was to verify data obtained from the open thermal analysis for liquidus and solidus temperatures. DTA samples were prepared from machining chips and melted in alumina crucibles under a flowing argon gas environment. DTA measurements were conducted at a heating and cooling rate of 10°C/minute and a sample size of 200 mg. The reported liquidus and solidus temperatures from DTA represent the average obtained from the heating and cooling curves and are in reasonable agreement with the thermal analysis data. Differences in the reported temperatures may be related to the small sample used in DTA and variations in the casting chemistry where the DTA sample material was taken. Both methods were calibrated by using the solidification point of copper.

The volume fraction of non-austenitic phases was determined using optical microscopy and computer image analysis software. All heat treatments were performed using chemically coated stainless steel bags to prevent decarburization and oxidation. Homogenization was performed on each alloy at 1050°C for two hours with subsequent water quenching. Solution treatment was performed at 900, 950, 1000 and 1050 °C for an additional two hours with subsequent water quenching. Metallographic specimens were etched with 2% Nital, and optical images were recorded using a differential interference contrast technique.

Table 1. Chemical Composition of Cast Steels (weight percent)
Fe-Mn-Al-C-Si Alloys

Si	Mn	Al	C	Mo	Fe
0.30	27.3	8.36	0.65	0.42	Bal
0.82	29.87	8.81	0.97	0.44	Bal
1.36	27.96	8.7	0.85	0.43	Bal
2.24	29.3	9.06	0.87	0.45	Bal

Low Alloy Steel

Mn	Cr	Si	C	Al	Mo	Fe
2.52	1.02	0.86	0.45	0.99	0.22	Bal

RESULTS

THERMAL ANALYSIS

Thermal analysis data for the Fe-Mn-Al-C-Si alloys are shown in Figure 1 after being temperature corrected using the copper standard. Liquidus and solidus

temperatures were determined by examining the cooling curves together with the first derivative of temperature with respect to time. With the exception of the 2.24% Si containing alloy, the cooling curves all reflect a definitive solidus temperature as observed by the final thermal arrest in the cooling curves. The 2.24% Si containing alloy exhibited considerable undercooling to 1240°C, which was followed by recalescence to 1275°C. The base Fe-Mn-Al-C alloy (0.3% Si) exhibited liquidus and solidus temperatures of 1395 and 1333 °C. Increasing concentrations of Si from 0.3% to 2.24% depressed both the liquidus and solidus temperatures at a rate of 30°C /% Si. Liquidus and solidus temperatures determined from thermal analysis and DTA are given in Table 2 and each thermal technique shows that silicon lowers the liquidus and solidus temperatures. The cooling curves obtained from thermal analysis were used to determine solidification kinetics and DCP.

Table 2. Liquidus and Solidus Temperatures as Determined by Thermal Analysis and Differential Thermal Analysis

Si Content (weight %)	Thermocouple Data (°C)			Differential Thermal Analysis (°C)		
	Liquidus	Solidus	ΔT	Liquidus	Solidus	ΔT
0.3	1395	1333	58	1376	1309	67
0.82	1353	1309	50	1365	1312	53
1.36	1343	1247	96	1326	1268	58
2.24	1317	1275	42	1306	1242	64

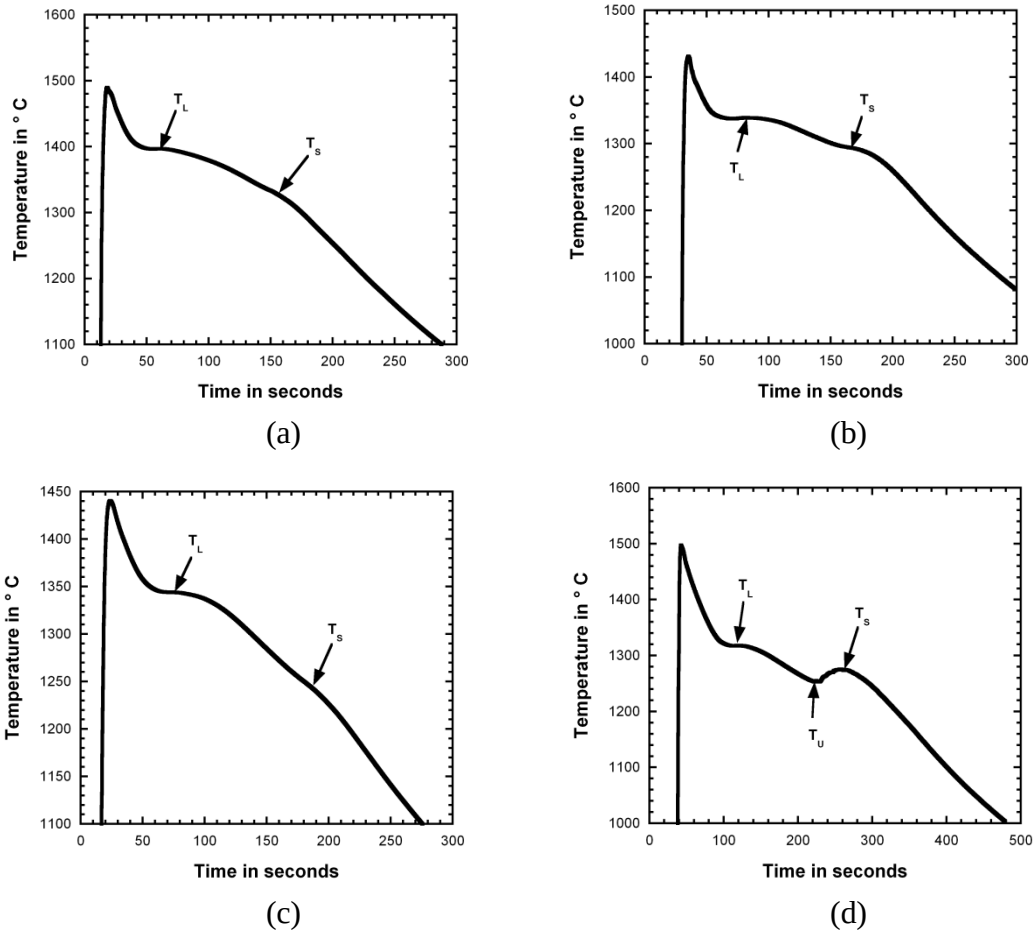

Figure 1. Cooling curves for Si modified Fe-Mn-Al-C alloys highlighting liquidus (T_L), solidus (T_S), and undercooling (T_U) temperatures for (a) 0.3 % Si (b) 0.82 % Si (c) 1.36 % Si and (d) 2.24 % Si alloys.

ALLOY FLUIDITY

Liquidus temperatures and calculated superheats were based upon the thermal analysis data, since pouring temperatures were measured in a similar fashion using the same thermocouple type. Figure 2 shows the spiral lengths cast as a function of pouring temperature and superheat for the Fe-Mn-Al-C-Si alloys and the low alloy steel. Data was collected starting at the highest pour temperature and allowing the melt in the ladle

to cool. The first and second spirals cast were in general shorter in length than subsequent spirals cast at lower pouring temperatures and were not included in establishing the trend lines shown in Figure 2.

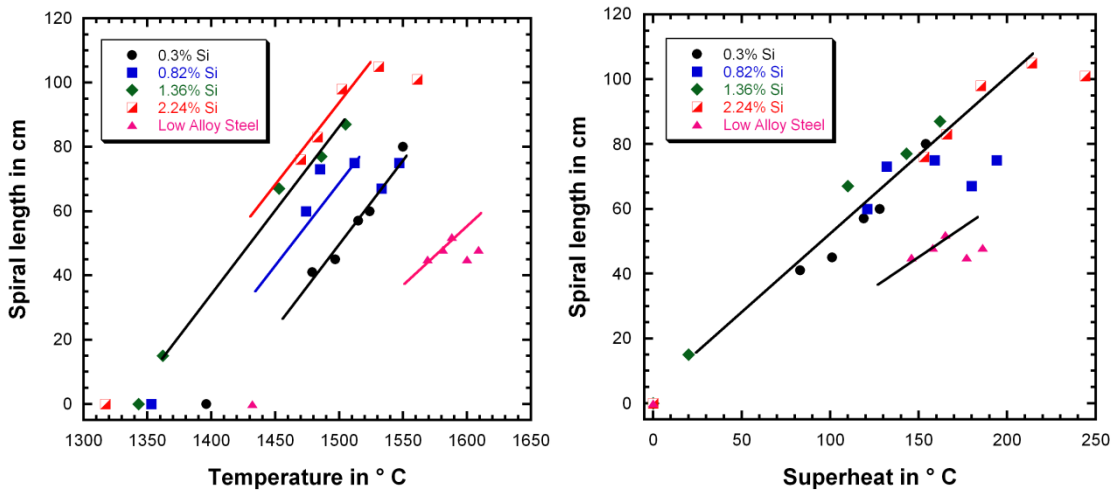

(a) (b)

Figure 2. Fluidity spiral lengths for Fe-Mn-Al-C-Si alloys and low alloy steel versus (a) pouring temperature and (b) superheat. Melting temperatures for each alloy are shown in (a) at zero spiral length.

These short fill lengths at the beginning of each heat were believed to result from excessive heat loss to the ladle pouring lip; and thus, the actual superheat was less than that determined based upon the measured liquid temperature inside the ladle. In general, the Fe-Mn-Al-C-Si alloys exhibited greater fluidity than the low alloy steel. However, the 0.99% aluminum content of the low alloy steel may have adversely affected the fluidity[24,25]. The 2.24% Si alloy exhibited the highest fluidity at an equivalent pouring

temperature, but silicon had little effect on the fluidity spiral length when the Fe-Mn-Al-C-Si alloys were compared on the basis of superheat.

CAST AND SOLUTION TREATED TRIPLEX MICROSTRUCTURES

Cast microstructures were primarily a mixture of austenite and ferrite (see Figure 3). Addition of silicon had three major effects upon the cast microstructure. First, the addition of silicon reduced the secondary dendrite arm spacing (as measured by the mean distance between the ferrite) from approximately 80 μm in the 0.3% Si alloy to 40 μm in the 2.24% Si alloy. Second, the volume fraction of ferrite was reduced in all of the Si containing alloys with a minimum in the ferrite content observed for the 0.82% Si alloy. And third, the 0.82%, 1.36%, and 2.24% Si bearing alloys exhibited a forth phase that appeared within the ferrite or at the ferrite and austenite interface and was most evident in the 1.36% and 2.24% Si containing alloys. The 2.24% Si cast alloy also exhibited a darker etching contrast typical of age hardened Fe-Mn-Al-C alloys[6].

Each Fe-Mn-Al-C-Si alloy was homogenized for 2 hours at 1050°C and subsequently water quenched. Homogenized alloys were solution treated at 900, 950, 1000 and 1050 °C for two additional hours and again quenched in water. The austenite content after solution treatment was determined for each alloy, and these results are reported in Figure 4. Solution treating the Fe-Mn-Al-C-Si alloys at 1000°C and 1050° C produced the highest volume fractions of austenite. There was no evidence of either intermetallic or carbide phases in these high temperature solution treated microstructures. The large decrease of austenite in the 2.24% Si alloy at 900 and 950° C was caused by a combination of increasing ferrite content and the precipitation of an intermetallic phase.

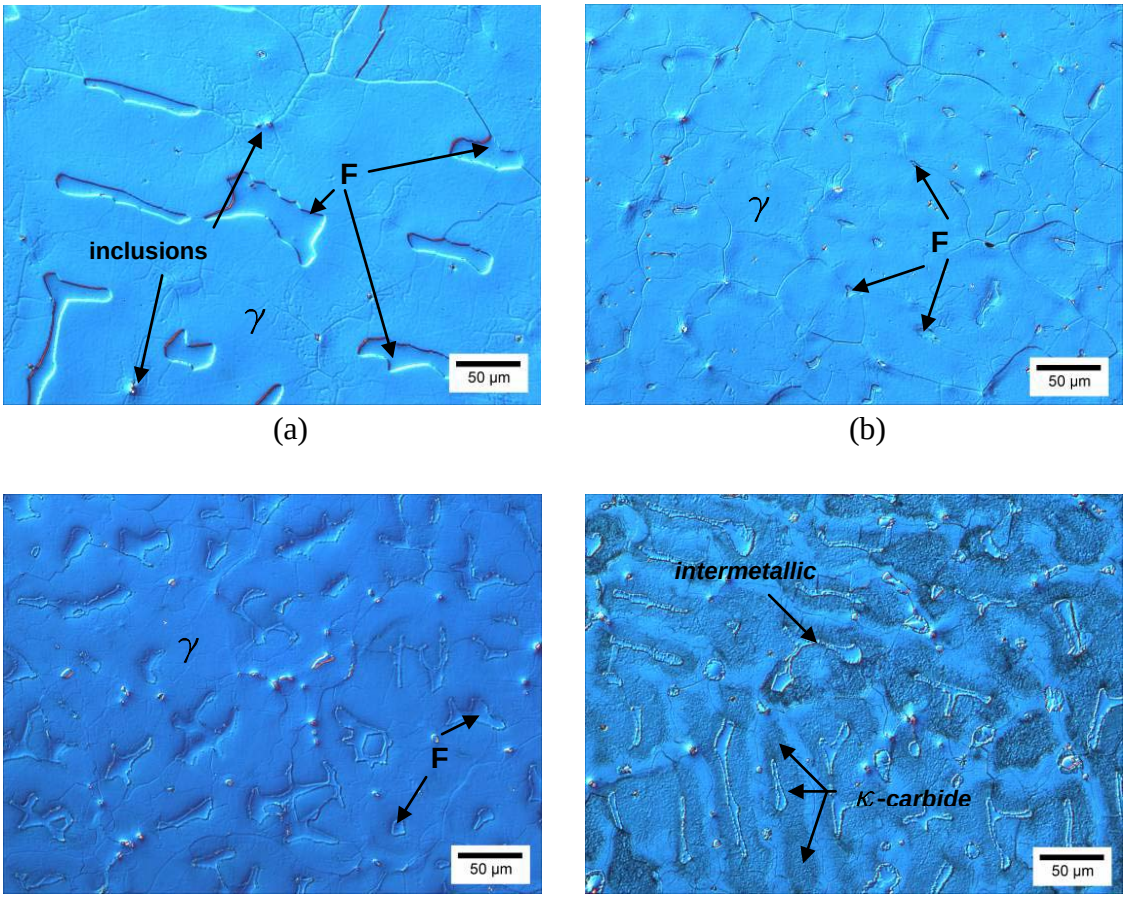

Figure 3. As-cast Fe-Mn-Al-C-Si alloy microstructures of (a) 0.3 % Si (b) 0.82 % Si c) 1.36 % Si d) 2.24 % Si containing alloys. The 0.3% Si alloy contains primary austenite (γ) and interdendritic ferrite (F). Nonmetallic inclusions polish in relief and appear as raised portions. The 0.82% Si reveals a finer interdendritic structure with smaller islands of ferrite. A very fine intermetallic phase is located along the austenite and ferrite interfaces. The 1.36% Si alloy has as fine a dendritic structure as the 0.82% Si alloy, but contains more ferrite and intermetallic phase. The intermetallic phase is best observed in the 2.24% Si which also shows the κ-carbide as the central, darker etching region in the austenite. Secondary dendrite arm spacing (SDAS) decreased as determined from spacing of interdendritic ferrite from 80 μm for 0.3 % Si containing alloy to 40 μm in the 2.24 % Si alloyed steel.

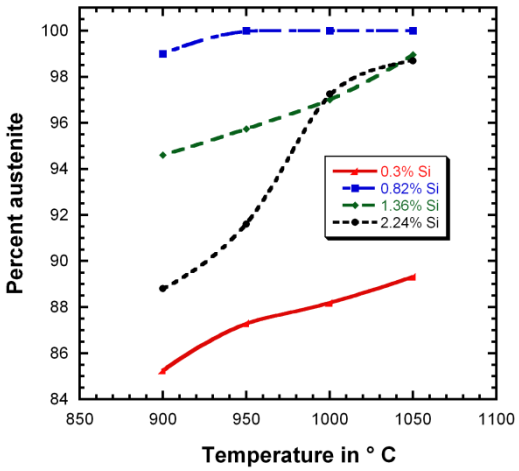

Figure 4. Austenite volume fraction as a function of solution treating temperature for Fe-Mn-Al-C alloys containing 0.3 %, 0.82 %, 1.36 %, and 2.24 % Si.

Microstructural comparisons of the solution treated alloys that are deemed significant are reported in Figures 5, 6 and 7. In Figure 5, the low silicon containing alloy (0.3% Si) is compared with an alloy containing 1.36 % Si to show that the amount of ferrite is drastically reduced after solution treatment at 1050° C. These microstructures would also be typical of those observed after homogenization. A detailed study of the low-silicon containing alloy shows that the ferrite is being dissolved into the austenite at 1050°C as evidenced by the concavity (center of curvature in the austenite) of the ferrite and austenite interface.

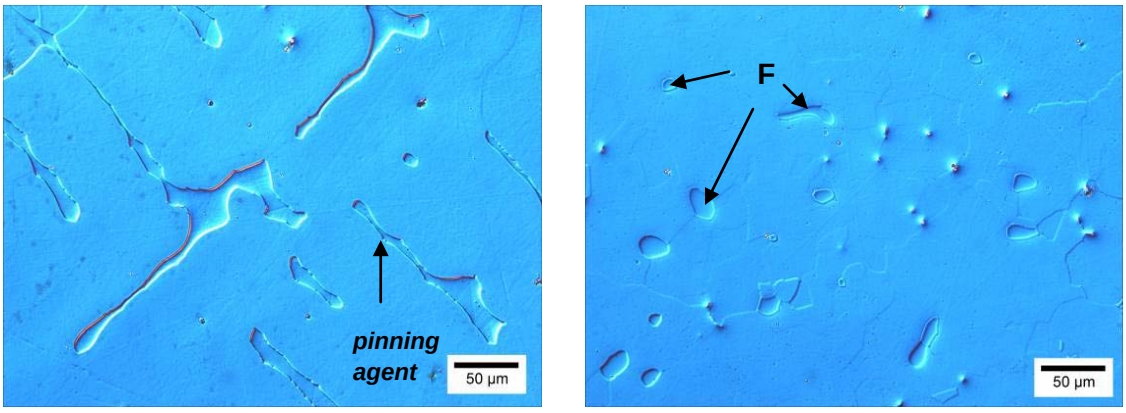

(a) (b)

Figure 5. Microstructure of Fe-Mn-Al-C steels with (a) 0.3 % Si and (b) 1.36% Si, homogenized and solution treated at 1050°C. The concave shape of the austenite and ferrite interface reflects austenitic growth at 1050°C in 0.3 % Si alloy. Ferrite (F) is isolated as small islands throughout the austenitic matrix for the 1.36 % Si alloy.

The 0.82% Si containing alloy had small islands of ferrite at 900°C (see Figure 6(a)) whereas this same alloy was fully austenitic at 1000°C (see Figure 6(b)). Alloys with higher silicon content, 1.36% and 2.24%, had nearly identical volume fractions of austenite and ferrite at the higher solution temperatures of 1000 and 1050 °C, but deviated greatly from each other at the lower temperatures of 900 and 950 °C. Figure 7 compares the 2.24% Si alloy at 950°C and 1000°C. At 950°C the growth of ferrite and the precipitation of an intermetallic phase is apparent whereas the alloy remains predominately austenite with 2 vol.% ferrite at 1000°C. The intermetallic phase appears as prism-rods precipitated along austenite and ferrite boundaries, grain boundaries, and throughout the austenite phase (see Figure 7(a)). No evidence of the intermetallic phase was observed after solution treatment at 1000°C as shown in Figure 7(b), where the microstructure consisted of austenite, small islands of ferrite, and nonmetallic inclusions.

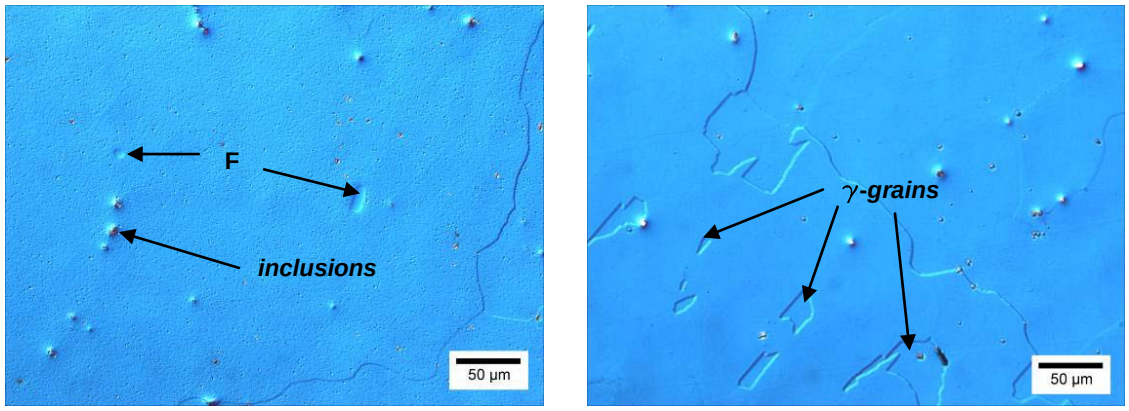

(a) (b)

Figure 6. Microstructure of Fe-Mn-Al-C steels with 0.82 % Si solution treated at (a) 900°C showing the formation of small ferrite (F) islands and (b) at 1000°C that produced a fully austenitic structure upon quenching.

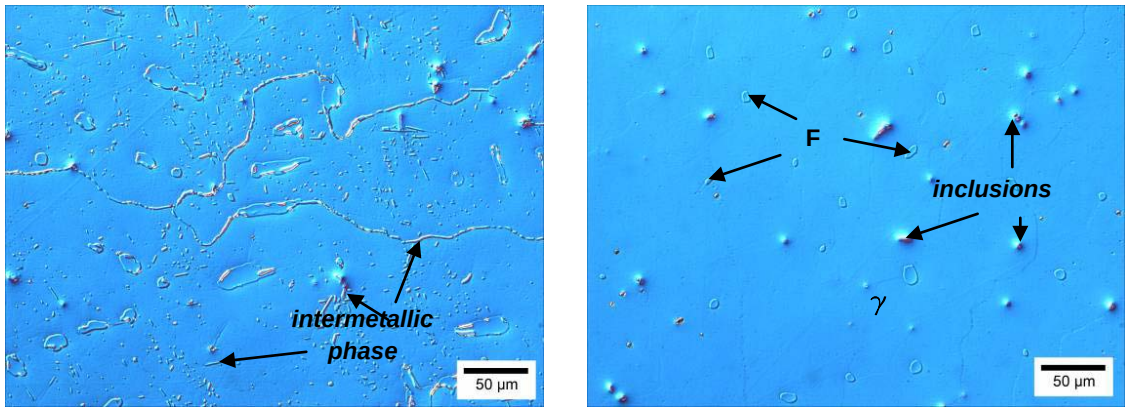

(a) (b)

Figure 7. Microstructure of Fe-Mn-Al-C steels with 2.24% Si solution treated at (a) 950°C and (b) 1000°C. Intermetallic phase(s) are shown in (a) as prism-rod features precipitated along austenite and ferrite boundaries, grain boundaries, and throughout the austenite phase. (b) At 1000°C only small islands of ferrite (F) and nonmetallic inclusions are observed.

DISCUSSION

The most significant effect of adding silicon to the Fe -30%Mn -9%Al -0.9%C composition was the depression of the liquidus and solidus temperatures, which was corroborated by both thermal analysis of castings and DTA methods. Both liquidus and solidus temperatures decreased at a rate of approximately 30°C per wt.% of silicon added. The solidification range (ΔT) for each alloy remained constant at approximately 60 ± 5°C. It should be noted that the large solidification range (96°C) determined by thermal analysis of the 1.36% Si casting was the result of a casting void around the embedded thermocouple. At the highest silicon content of 2.24%, the thermal analysis data exhibited significant undercooling reminiscent of eutectic solidification in graphitic irons. However, no eutectic-like structures were observed in the Fe-Mn-Al-C-Si alloys.

In an effort to better understand the fluidity behavior of the Fe-Mn-Al-C-Si alloys, the fraction of solid formed as a function of temperature was derived from the thermal analysis data using a Newtonian heat-flow analysis proposed by Stefanescu et al.[16-20]. This method first determines a baseline for the specimen and its surroundings prior to the start of solidification and after solidification is complete. This baseline is referred to as the zero line for the Newtonian heat transfer analysis using

$$hA(T - T_0) = V\rho C_p\left(\frac{dT}{d\tau}\right) \qquad \text{Equation 1}$$

where h is the overall heat transfer coefficient, A is surface area of heat transfer, T is the instantaneous temperature of the specimen, T_0 is the ambient temperature, V is the volume of specimen, ρ is density, C_p is specific heat, and $dT/d\tau$ is the cooling rate. For this analysis, the heat transfer coefficient, area, volume, density, and heat transfer

coefficient are assumed constant. The zero line (Z) equation is an exponential function and can be fit to the first derivative ($dT/d\tau$) of the thermal analysis data before and after solidification by a least squares method. The rate of latent heat liberation is proportional to the difference of the first derivative during solidification ($dT/d\tau$) and the calculated value of the zero line (Z) using

$$\frac{dQ}{d\tau} = C_p\left(\frac{dT}{d\tau} - Z\right) \qquad \text{Equation 2}$$

To improve the precision of the solidification analysis, the equation of the zero line was also fitted to the first and second derivatives of the cooling curve after solidification (coefficients A_3, A_4) using the following

$$T = A_1 \exp(A_2\tau) + A_3(\tau - \tau_{start})^3 + A_4(\tau - \tau_{start})^4 \qquad \text{Equation 3}$$

The coefficients A_3 and A_4 account for different specific heat values for the liquid (C_L) and solid (C_S). However the Newtonian heat analysis does not take into account the internal thermal gradient of the specimen and is limited to Biot numbers smaller than 0.1. The best results are achieved when the thermocouple is installed near the thermal center of a small sample and the minimum sample size is limited by the thermal inertia of the thermocouple. From the Newtonian analysis, the fraction solid as a function of temperature was calculated for each alloy (see Figure 8).

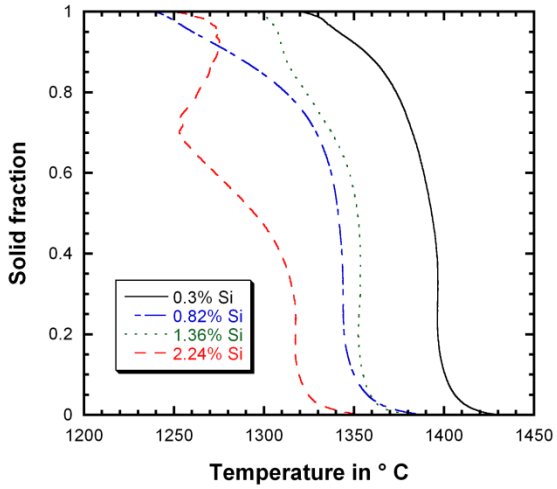

Figure 8. Fraction of solid as a function of solidification temperature in Fe-Mn-Al-C steel with different Si contents.

All four alloys show a sharp increase in initial solid fraction reflecting a rapid increase in solid content for a minimal change in temperature below the liquidus. A delay in the final solidification is observed for the alloys containing the highest two Si contents, but only the 2.24% Si alloy exhibited undercooling and recalescence. The DCP for each alloy was calculated using a modified procedure originally developed by Jiang et. al.[23] for thermal analysis using a single thermocouple. The DCP is defined as the temperature at which an impinging dendrite network is formed. This transition point marks the change from mass feeding to interdendritic feeding and establishes the onset of such phenomena as porosity formation, macrosegregation, and hot tearing. Jiang et al. calculated the DCP as the minimum point of the second derivative of the cooling curve that occurs between the liquidus and solidus temperatures. For the study presented here, the solid fraction

data and the second derivate were plotted as functions of time and temperature. Figure 9 is an example of this procedure for the 0.30% Si alloy.

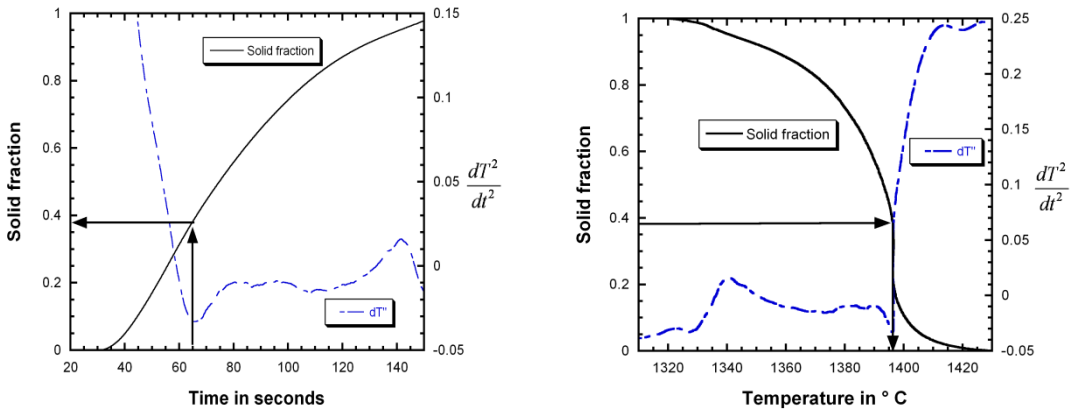

(a) (b)

Figure 9. The fraction of solid as a function of (a) time and (b) temperature for the Fe-Mn-Al-C steel with 0.30 % Si. The second derivative of the thermal analysis curve is shown in each figure. The solid fraction is first determined in (a) as the fraction solid at the minimum in the second derivative. The solid fraction from (a) is then used to determine the corresponding temperature in (b), which becomes the dendrite coherency point temperature.

The solid fraction corresponding to the DCP was first determined from the time function using the minimum point on the second derivative curve (see Figure 9(a)). The solid fraction was then used to determine the dendrite coherency temperature from the temperature plot (see Figure 9(b)). Table 3 and Figure 10 summarize the DCP temperature and solid fraction results for the Si modified Fe-Mn-Al-C alloys. The overall trends show that increasing Si content decreases the DCP temperature with negligible change to the solid fraction at each alloy's respective DCP. Dendrite coherency

temperatures were subtracted from the liquidus temperatures and listed in Table 4 for each alloy.

Table 3. Dendrite Coherency Point Temperature and Solid Fraction in Fe-Mn-Al-C-Si Steels

Si (weight %)	Dendrite Coherency Point Temperature (° C)	Solid Fraction
0.3	1395	0.38
0.82	1351	0.33
1.36	1341	0.34
2.24	1316	0.32

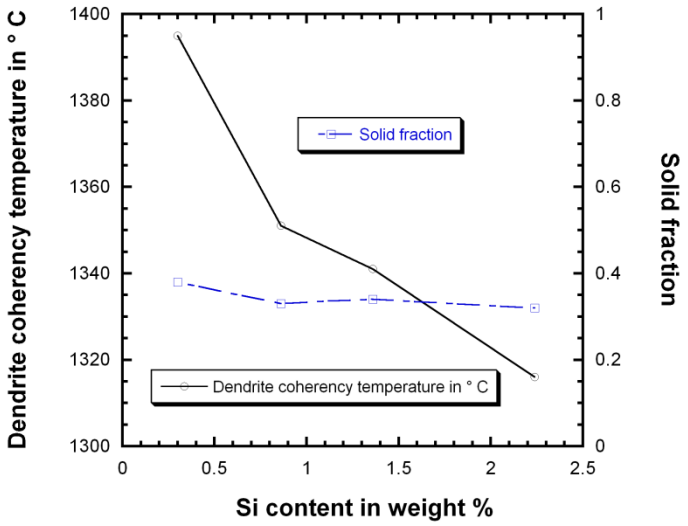

Figure 10. Dendrite coherency point temperature and solid fraction versus Si content.

Table 4. Dendrite Coherency Point and Liquidus Temperatures in Fe-Mn-Al-C Steels with Different Si Content

Si (weight %)	Liquidus Temperature (° C)	Dendrite Coherency Point Temperature (° C)	ΔT (° C)
0.3	1396	1395	1-2
0. 82	1353	1351	2-3
1.36	1343	1341	2-3
2.24	1317	1316	1-2

The results show that the DCP temperature is close to the liquidus temperature, but a significant time offset was observed as the latent heat was transferred from casting to mold before the dendrite network was established (see Figure 9(a)). For Fe-Mn-Al-C-Si alloys, the DCP is less than the liquidus temperature by 1-3° C, which is 2-5% of the temperature range between the liquidus and solidus. However, the time delay to establish the DCP is 30-40% of the total solidification time. This may help explain why the fluidity spiral lengths were the same for all Fe-Mn-Al-C-Si alloys when measured against superheat, since each reached the DCP at roughly the same solid fraction and the same temperature below the liquidus. A similar analysis for the low alloy steel is being pursued to help explain the increased fluidity of the Fe-Mn-Al-C-Si alloys. Failure of the data acquisition system during the low alloy steel pour prevented the analysis for this paper.

The solid fraction at DCP and the temperature difference between liquidus and DCP temperatures are consistent with values reported for Al alloys. It should be noted

here that the solid fraction at DCP for aluminum alloys differ widely and can range from 0.18 to 0.56[26]. Emadi et al. reported liquidus and DCP temperature differences of 1.4 °C to 1.8° C for Al-Si alloys and this difference decreased with increasing silicon content[27].

Fe-Mn-Al-C-Si alloys have two significant advantages relative to casting low alloy steel. First, for an equivalent pouring temperature, a greater superheat is realized for the Fe-Mn-Al-C-Si alloys; and, second the Fe-Mn-Al-C-Si alloys have a nearly 70% increase in spiral length fill for an equivalent superheat and head height as compared to the low alloyed steel. Silicon addition would also be beneficial with respect to lower pouring temperatures, which would reduce mold-metal interactions and refine the cast microstructure. Furthermore, small additions (~1%) of silicon will form a fully austenitic microstructure at lower solution treatment temperatures. It is important to note here that the baseline TRIPLEX alloy was low in carbon content and this increased the proportion of ferrite during solidification. Upon solution treatment, this low carbon composition also had more ferrite in the microstructure than would be observed for an alloy containing 0.9% C. However, the silicon alloys can be compared to the microstructures of TRIPLEX alloys previously reported[4,5,8] and it may be concluded that the addition of silicon up to 1.5% has the beneficial effect of reducing the ferrite content in the solution treated condition. At higher levels, such as the 2.24% Si alloy investigated, a decrease of austenite is observed at the lower solution temperatures of 900 and 950° C, which was related to the formation of additional α-ferrite and the precipitation of an intermetallic phase. The effect of silicon on the stability of the austenitic structure is in agreement with previous cast microstructures and the intermetallic phase observed in this study may be the same phase reported as $Mn_{12}Si_7Al_5$[4]. The studies presented in this paper provide

further guidance to selecting an optimum composition of silicon that should be between 0.8 to 1.2 % Si. Future microstructural and mechanical behavior studies should focus on a Fe-30Mn-9Al-1Si-0.9C composition.

CONCLUSIONS

Silicon additions to Fe-Mn-Al-C steels affects liquidus and solidus temperatures, fluidity, solidification, microstructural evolution of cast and solution treated alloys. Liquidus and solidus temperatures decrease for increasing amounts of Si by 30°C per wt.% Si. All Si containing Fe-Mn-Al-C steels have increased fluidity over low alloyed steel; a 70% greater fill length is obtained at a superheat of 150°C. At a fixed pouring temperature, the cast spiral length increased with increasing addition of silicon, but when compared on the basis of superheat, all of the Fe-Mn-Al-C-Si alloys produced equivalent spiral fill lengths. The fluidity results appear to be related to the dendrite coherency point (DCP) temperature, which is within 3°C of the liquidus temperature for each of the Fe-Mn-Al-C-Si alloys. DCP temperatures dropped from 1395°C for 0.3% Si to 1315°C for 2.24% Si, but the DCP solid fraction is relatively constant between 30-40%. Increasing Si also reduces the secondary dendrite arm spacing with SDAS decreasing from 80 μm to 40 μm in the Si range investigated.

Based upon the results reported here, the 0.82% Si alloy demonstrates the best balance of fluidity, phase composition, and microstructure. Therefore, future studies will narrow the Si content between 0.82% and 1.36% for optimization of castability, strength, ductility, impact toughness, and age hardening.

ACKNOWLEDGMENTS

This research was funded by the Army Research Laboratory and is monitored by Dr. Ernest Chin of Aberdeen Proving Grounds. Financial assistance is being provided by Army Acquisition Corps and the Army Research and Development Command for MAJ Ryan A. Howell's Ph.D. studies at the Missouri University of Science and Technology.

REFERENCES

1. Kleshchevva, I., Shur, E. A., "Effect of Aging and Plastic Strain on the Mechanical Properties of High Manganese Steel," Termicheskaya Obrabotka Metalllov, No. 1, pp. 23-27 (1990).

2. Hadfield, R., Burnham, T. H., "Special Steels", 2nd ed., p.100, The Pitman Press, New York (1933).

3. Banerji, S. K., "An Update on Fe-Mn-Al Steels," presented at Vanderbilt University's workshop on "Conservation and Substitution Technology for Critical Material," June 15-17, (1981).

4. Prodhan, A., Charkrabarti, A. K., "A Study on Cast Fe-Mn-Al-Si-C Alloys," AFS Transactions, vol. 37, pp. 35-46 (1990).

5. Frommeyer, G., Brux, U., "Microstructures and Mechanical Properties of High-Strength Fe-Mn-Al-C Light-Weight TRIPLEX Steels," Steel Research Int., Vol. 77, pp. 627-633 (2006).

6. Kalashnikov, I.S., Acselrad, O., Shalkevich, A., Chumakova, L. D., Pereira, L. C., "Heat Treatment and Thermal Stability of FeMnAlC Alloys," Journal of Materials Processing Technology, No. 136, pp. 72-79 (2003).

7. National Materials Advisory Board, commission on Sociotechnical Systems, "Contingency Plans for Chromium Utilization," National Academy of Sciences (1978).

8. Kimura, Y., Hayashi, K., Handa, K., Mishima, Y., "Microstructural Control for Strengthening the g-Fe/$E2_1$-$(Fe,Mn)_3AlC_x$ Alloys," Vol. 329-331, pp. 680-685 (2002).

9. Gorvetskii, G. P., Gorev, K. V., “Phase Equilibria in Fe-Mn-Al-C Alloys,” Russian Metallurgy, Vol. 2, pp. 217-221 (1990).

10. Krivonogov, G.S., Alekseyenko, M. F., Solov’yeva, G. G., “Phase Transformation Kinetics in Steel 9G28Yu9MVB,” Fit. Metal. Metalloved, Vol. 39, No. 4, pp. 775-781 (1975).

11. Kalashnikov, I., Acselrad, O., Shalkevich, A., Pereira, L.C., “Chemical Composition Optimization for Austenitic Steels of the Fe-Mn-Al-C System,” Journal of Materials Engineering and Performance, Vol. 9, No. 6, pp. 597-602 (2000).

12. Acselrad, O., Pereira, L. C., Amaral, M. R., “Processing Conditions, Microstructure, and Strength of an Austenitic FeMnAlC Alloy,” Proceedings from the International Conference on the Processing, Properties, and Applications of Metallic and Ceramic Materials, vol. II, pp.829-834 (1992).

13. Sato, K., Kazuhiro, T., Inoue, Y., “Age Hardening of an Fe-30Mn-9Al-0.9C Alloy by Spinodal Decomposition,” Scripta Metallurgica, Vol. 22, pp. 899-902 (1988).

14. Sato, K., Igarashi, Y., Inoue, Y., Yamazaki, T., Yamanaka, M., “Microstructure and Age Hardening in Spinodally Decomposed Austenitic Fe-Mn-Al-C Alloys,” Proceedings of the International Conference on Stainless Steels (1991).

15. Sato, K., Tagawa, K., and Inoue, Y., “Modulated Structure and Magnetic Properties of Age-Hardenable Fe-Mn-Al-C Alloys,” Met. Trans A, vol. 21A, pp 5-11 (1990).

16. Acselrad, O., Kalashnikov, I. S., Silva, E. M., Simao, R. A., Achete, C. A., Pereira, L. C., “Phase Transformation in FeMnAlC Austenite Steels with Si Addition,” Met. Tran A., vol. 33A, pp.3569-3572 (2002).

17. Chiou, S. T., Cheng, W. C., Lee W. S., “Strain Rate Effects on the Mechanical Properties of a Fe-Mn-Al Alloy Under Dynamic Impact Deformations,” Mat. Sci. and Eng. A., vol. 392, pp.156-162 (2005).

18. Barlow, J.O., Stefanescu, D. M., “Computer-aided Cooling Curve Analysis Revisited,” AFS Transactions, vol.105, pp 349-354 (1997).

19. Upadhya, K. G., Stefanescu, D. M., Lieu, K., Yaeger, D. P., “Computer-aided Cooling Curve Analysis: Principles and Application in Metal Casing,” AFS Transactions, vol. 97, pp 61-66 (1997).

20. Djurdjevic, M. B., Kierkus, W. T., Byczynski, G. E., Stockwell., T. J., Sokolovski, J. H., "Modeling of Fraction Solid for 319 Aluminum Alloy," AFS Transactions, vol.107, pp 173-179 (1999).

21. Stefanescu, D. M., Upadhya, G., Bandyopadhyay, D., "Heat transfer-Solidification Kinetics Modeling of Solidification of Castings," Metal. Trans. A, vol.21A, pp 997-1005 (1990).

22. Hu, J. F., Pan, E.N., "Determination of Latent Heat and Changes in Solid fraction During Solidification of Al-Si Alloys by the CA-CCA Method," Int. J. Cast Metals Res., vol. 10, pp 307-319 (1998).

23. Jiang, H., Kierkus, W. T., Sokolowski, J. H., "Determining Dendrite Coherency Point Characteristics of Al Alloys Using Single-Thermocouple Technique," AFS Transactions, vol. 68, pp. 169-172 (1999).

24. Moore, W. H., U. S. Patent No. 677,916 (Aug. 13, 1957).

25. Maziasz, P. J., Vought, J. D., U. S. Patent No. 6,436,339 (Aug. 20, 2002).

26. Chai, G., Backerud, L., Rolland, T., Arnberg, L., "Dendrite Coherency during Equiaxed Solidification in Binary Aluminum Alloys," Met. Trans. A., vol. 26A, pp. 965-970 (1995).

27. Emadi, D., Whiting, L. V., "Determination of Solidification Characteristics of Al-Si Alloys by Thermal Analysis," AFS Transactions, vol. 110, pp. 285-296 (2002).

PAPER

3. Tensile, High Strain Rate Compression and Microstructural Evaluation of Lightweight Age Hardenable Cast Fe-30Mn-9Al-XSi-0.9C-0.5Mo Steel

R.A. Howell, T. Weerasooriya, D.C. Van Aken

Army Research Lab

Missouri University of Science and Technology

Department of Materials Science and Engineering

Rolla, MO 65409

Tel.: 573-341-4717

E-mail: dcva@mst.edu

Key Words: Fe-Mn-Al-C, lightweight steel, tensile strength, strain rate, split Hopkinson bar

Published in the Transactions of the American Foundry Society 2008 issue.

ABSTRACT

Age hardenable, castable, and lightweight Fe-Mn-Al-C steels are currently being developed and evaluated for substitution of high strength low alloy steel and to meet MIL-PRF-32269 criteria. Two nominal Fe-30Mn-9Al-0.9C-0.5Mo steels were cast and modified with 1 and 1.4 wt.% silicon. Aging, tensile, and high strain rate compression testing were performed on solution treated and aged samples of both chemistries. Each alloy was solution treated at 1050°C for 2 hours. Microstructures of the solution treated and aged alloys show primary austenite with less than 8 volume % ferrite. The solution treated hardness of the low silicon steel was 230 BHN and the high silicon alloy was 225 BHN. Specimens were aged at 530° C for up to 60 hours. Peak aging occurs after 30 hours with a peak hardness of 371 BHN for the 1% silicon containing alloy and 377 BHN for the high silicon alloy. Tensile strengths of the 30 hour aged specimens were 1065 MPa (154 ksi) and 1080 MPa (156 ksi) for the low and high silicon alloys. High strain rate compression testing was conducted on solution treated and 10 hour aged 1% Si containing alloy. Compressive strength of the 1 wt.% Si alloy exceeded 1,500 MPa (217 ksi) at a strain rate of 3000 s^{-1}.

INTRODUCTION

Fe-Mn-Al-C alloys were developed as a substitute for austenitic nickel-chrome stainless steels by the U.S. Navy[1]. Ham and Cairns designed the alloy with the intent of utilizing high aluminum content to provide corrosion resistance in an austenitic steel stabilized by manganese and carbon[2]. These alloys contain 20-30% Mn, 7-12% Al, and 0.7-1.2% C. All chemistries are in weight percent. The Fe-Mn-Al-C steels have been proven to show excellent ductility with greater than 80% fracture strain in the solution

treated condition[2]. It was later shown that for aluminum content greater than 5% and carbon content greater than 0.3%, the Fe-Mn-Al-C alloys age harden by precipitation of the κ-carbide (see Figure 1). Strengths in excess of 2,000 MPa (290 ksi) and Charpy impact toughness greater than 221 J (300 ft-lbs) have also been reported[3,4]. Fe-Mn-Al-C alloys are 12-18% lighter than high strength low alloy steel[8]. The high strength properties and low density combine for high specific strength. It is for these reasons that recent studies have been conducted on wrought Fe-Mn-Al-C steels for automotive use as a high energy absorbing material in critical structural components due to their exceptional high strain-rate, work hardening behavior[8].

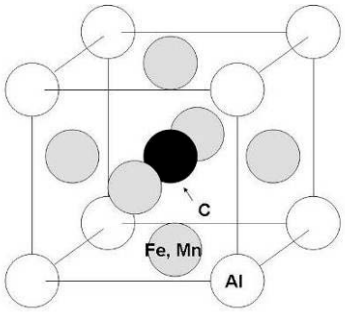

Figure 1. Age hardened strength in Fe-Mn-Al-C alloys results from homogenous precipitation of the κ-carbide. The κ-carbide crystal structure is $E2_1$ and consists of aluminum atoms occupying corners of the unit cell, iron and manganese occupying the face centered positions, and carbon at the body center, i.e. { ½, ½, ½}.

As-cast microstructures consist of primary austenite with 10 to 15 volume % δ-ferrite. Solution treatment can partially or completely dissolve the ferrite. Solution treatment is typically performed at 1050°C for 2 hours[5,6,7]. Wrought microstructures contain equiaxed austenite grains with annealing twins and bands of ferrite parallel to the

rolling direction. When age hardened, κ-carbide precipitates homogeneously in the austenite to produce a three phase, or TRIPLEX microstructure[8]. The κ-carbide is an $E2_1$ perovskite crystal structure with chemical composition $(Fe,Mn)_3AlC$ where aluminum atoms occupy the lattice corner positions, iron and manganese at the face positions, and carbon at the octahedral {½, ½, ½} interstitial position. The homogeneous precipitation of κ-carbide is believed to result from an initial spinodal decomposition involving aluminum and carbon[9]. Most studies have used a 550°C aging temperature with an aging time of 16 hours[10,11]. Aging beyond 16 hours embrittles the material by growth of κ-carbide along grain boundaries and formation of β-manganese[12]. The addition of silicon has been shown to prevent β-manganese by displacing manganese from the austenite to the κ-carbide[13].

In cast form, Howell et al. showed that Fe-Mn-Al-C alloys with up to 2.24% Si are primarily austenitic with less than 20% ferrite in the solution treated condition[14]. Thermal analysis was used to show that silicon additions lower the liquidus, dendrite coherency point, and solidus temperatures by 30°C per weight percent of silicon added, and that silicon additions increased fluidity as shown by the 70% increase in spiral length versus a low alloy steel at 150°C superheat. In previous studies using silicon additions, Prodham and Chakrabarti reported rapid age hardening in a Fe-30Mn-XAl-YC-1.36Si with aluminum content between 7.5 and 10% and carbon less than 1%. Precipitation of an $Mn_{12}Si_7Al_5$ intermetallic was also observed at aging times longer than 30 hours at 500°C.

High strain rate compression testing has not been reported on cast Fe-Mn-Al-C alloys. Wrought alloys in solution treated condition[15] and aged condition[8] have shown

compressive true strengths greater than 1,500 MPa (217 ksi) and true fracture strains exceeding 40% at strain rates between 10^3 s^{-1} and 10^4 s^{-1}. Fracture in this loading regime occurs by highly localized deformation bands or shear bands[8]. The high deformation rate causes momentary localized high temperatures to occur within these bands[16]. Low thermal conducting materials cannot dissipate the heat causing lower stress within the band. This phenomenon has therefore been designated as adiabatic shear band (ASB) formation. Solution treated Fe-Mn-Al-C alloys have demonstrated a resistance to fracture by adiabatic shear bands as work hardening occurs prior to shear localization[15].

The current investigation of silicon additions to Fe-Mn-Al-C alloys is part of an evaluation of these age hardenable, high strength, lightweight steel alloys for cast, perforated armor per MIL-PRF-32269[17]. A nominal Fe-30-Mn-9Al-0.9C was chosen based on historic Fe-Mn-Al-C steel research showing high strength[3] and a wrought mechanical property optimization study conducted by Kalashnikov et al.[18] An aging curve was constructed for both alloys at 530°C, a temperature that constrains heterogeneous grain boundary precipitation of κ-carbide from occurring[19]. From the 530°C aging study, times were selected to produce a hardness within the prescribed MIL-PRF-32269 acceptance range. The dynamic properties of the cast Fe-Mn-Al-C-Si alloys were compared to those of rolled homogeneous armor on a specific strength basis. The resultant tensile and dynamic properties are also a useful contribution to determining Johnson-Cook parameters for finite element analysis models.

EXPERIMENTAL PROCEDURE

Two heats with differing silicon contents were produced. Specimen bars were cast into phenolic no-bake silica sand molds. The molds were coated with a zircon wash

to prevent reaction between the manganese and the silica sand. Cast bars measured 3 cm in diameter and 20 cm in length (see Figure 2). A large center riser with 15 cm of head height over the mid section of the horizontal bar was also utilized as the down sprue. No filter was used. High purity induction iron, aluminum, carbon, ferromanganese, ferrosilicon, and ferromolybdenum were melted in a 45 kg (100 lb) induction furnace under argon cover. A recovery rate of 95% was utilized for the manganese and aluminum. The furnace was charged with aluminum, carbon, ferrosilicon, ferromolybdenum, and 30% by weight of the required induction iron. After the charge liquefied, the remaining induction iron was added followed by the addition of the required ferromanganese. A solid electrolyte sensor measured active oxygen contents. Both heats contained 2 ppm active oxygen. No additional deoxidation practice was conducted. Melt stirring was limited to the induction heating, natural convection, and pouring from the furnace to the ladle and casting. Deslagging was conducted with a low-density granular coagulant.

Castings were solution treated in atmosphere at 1050°C for 2 hours, air-cooled, and then the gating was removed. Round bars were machined in preparation for sectioning hardness specimens, coupons for chemical analysis, machining of tensile bars, and compression specimens. Chemical analysis was conducted by inductive coupled plasma mass spectrometry verified with wavelength dispersive chemistry after sample dissolution in perchloric acid. Aluminum and silicon contents were verified with x-ray fluorescence by single element wavelength dispersive spectrometry. Chemical coupons were taken from end cuts; one from each heat. Nitrogen content was measured by inert gas fusion or thermal evolution method per ASTM E1019. Seven round specimens

measuring 2.5 cm in diameter by 1.25 cm thick were machined and ground parallel per ASTM E18. Measurements were recorded using Rockwell C and Rockwell B hardness scales and converted to Brinell hardness for common reference. Aging curves for 530 °C were constructed from hardness measurements for each alloy. One specimen was retained after initial machining and sectioning to record solution treated hardness. Specimens were aged at 530°C for 1, 3, 6, 10, 30, and 60 hours in atmosphere and subsequently air-cooled to room temperature. The reported hardness is an average of ten measurements and the uncertainty is based upon a sample standard deviation. Tensile specimens were machined per ASTM E8. The gage section measured 2.54 cm in length with a 0.635 cm gage diameter (see Figure 2). One tensile specimen from each heat was retained in the solution treated condition, one was aged at 530°C for 10 hours, and one at 30 hours. The aged conditions were selected to measure and bracket tensile properties corresponding to lower and upper MIL-PRF-32269 hardness requirements. Two sets of cylindrical compression specimens were electrical discharge machined from the low silicon steel for Split Hopkinson Bar (SHB) testing (see Figure 2). The Split Hopkinson Bar principle and testing apparatus are described in detail in Volume 8 of the ASM Handbook[20]. The first set of SHB specimens were machined and tested in the solution treated condition. The second set was machined from material solution treated and aged at 530°C for 10 hours. SHB specimens were lapped to a thickness of 0.3175 cm and measured 0.635 cm in diameter. Testing occurred at a strain rate of 3000 s^{-1}. Specimen load was incrementally increased from 270 Pa (40 psi) to 448 Pa (65 psi) in 34 Pa (5 psi) increments until specimen failure to evaluate shear band evolution.

Post compressive and tensile testing analysis was conducted by optical microscopy and scanning electron microscope (SEM) with energy dispersive x-ray spectrometer (EDS). SEM accelerating voltage was 15 keV with 18 mm of working distance at 0° rotation. Metallographic specimens were etched with 2% Nital and images were recorded using a differential interference contrast technique.

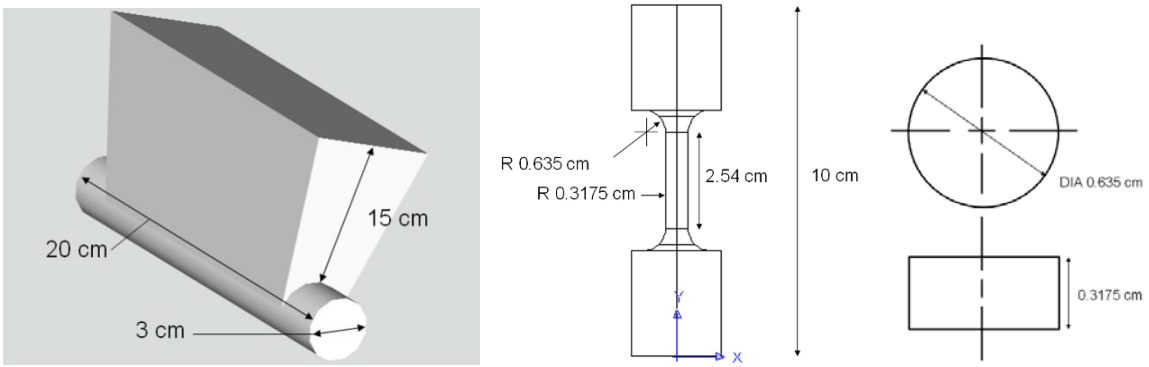

(a) (b) (c)

Figure 2. Fe-Mn-Al-C alloys were cast into a risered bar to produce mechanical test bars and metallographic specimens. The casting (a), tensile (b), and compression specimen (c) drawings are shown with dimensions to illustrate the shape and size of the materials utilized for this investigation.

RESULTS

CHEMICAL ANALYSIS

The chemical analyses of both silicon steels are reported in Table 1. Chemical analysis showed elevated levels of phosphorus whereas sulfur was low; phosphorus and sulfur measured 0.06 and 0.005 % in the low silicon alloy and 0.06 and 0.006 % in the 1.4% silicon modified alloy. Manganese, carbon, and molybdenum contents were equal

in both alloys, but aluminum concentrations varied. Aluminum contents were 8.3 and 7.9 in the low and high silicon alloys, respectively.

Table 1. Chemical Composition of Cast Steels (weight percent)

Si	Mn	Al	C	Mo	P	S	N	Fe
1.0	28.8	8.3	0.9	0.5	0.06	0.005	0.005	Bal
1.4	28.8	7.9	0.9	0.5	0.06	0.006	0.004	Bal

AGE HARDNEING

Figure 3 shows the age hardening curves for the 1 and 1.4 % silicon containing alloys. The 1 and 1.4 % silicon solution treated conditions had hardness ~225 BHN and ~220 BHN.

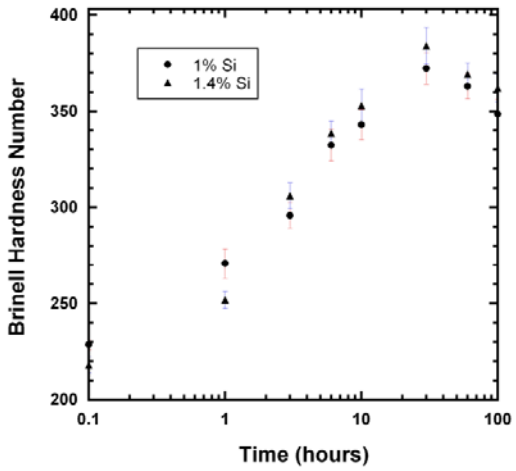

Figure 3. The age hardening curves for 1 and 1.4 % silicon containing Fe-Mn-Al-C alloys show a rapid increase in hardening through the first 6 hours. At times greater than six hours, hardness increases, but the hardening rate decreases. Maximum hardness is achieved after 30 hours for both alloys. The 1% silicon alloy hardens to 372 BHN, and the 1.4% alloy age hardens to 384 BHN.

The Fe-Mn-Al-C alloys increased in hardness to 270 BHN (1% silicon) and 252 BHN (1.4% silicon) after aging 1 hour. Hardness of both alloys increased steadily from 1 hour to 10 hours aging time. After 10 hours, the hardness measurements for each alloy were 343 BHN (1% silicon) and 353 BHN (1.4% silicon). From 10 hours to the peak aged condition at 30 hours, the hardness increased, but hardening rate decreased. Peak aged hardness at 30 hours measured 372 BHN (1% silicon) and 384 BHN (1.4% silicon).

Ferrite volume fraction increased during aging but the observed increase occurred after peak aging. Figure 4 shows solution treated, 10 hour, and 60 hour aged microstructures of both alloys. The 1% silicon solution treated alloy was primarily austenite with less than 1 % ferrite and less than 3% ferrite in the 60 hour aged condition. Dendrite arm spacing measured 53 μm. The 1.4% silicon modified alloy contained 6% ferrite in the solution treated condition and 8% in the 60 hour aged condition. Dendrite arm spacing for the 1.4% silicon alloy measured 48 μm. Figure 4 clearly shows the dendritic microstructure observed for both silicon containing alloys.

Quantitative inclusion measurement and chemical analysis was conducted using an automated scanning electron microscope utilizing energy dispersive chemical analysis. Nitrides, oxides and sulfides are comprised principally of manganese and silicon with a greater number of sulfides and nitrides than oxides as shown by the density of data plotted in Figure 5. Figure 6 shows a histogram of inclusion radii for the combined nitride, sulfide and oxide counts. Ninety-five percent of all inclusions were less than 1.3 μm in radius for each steel.

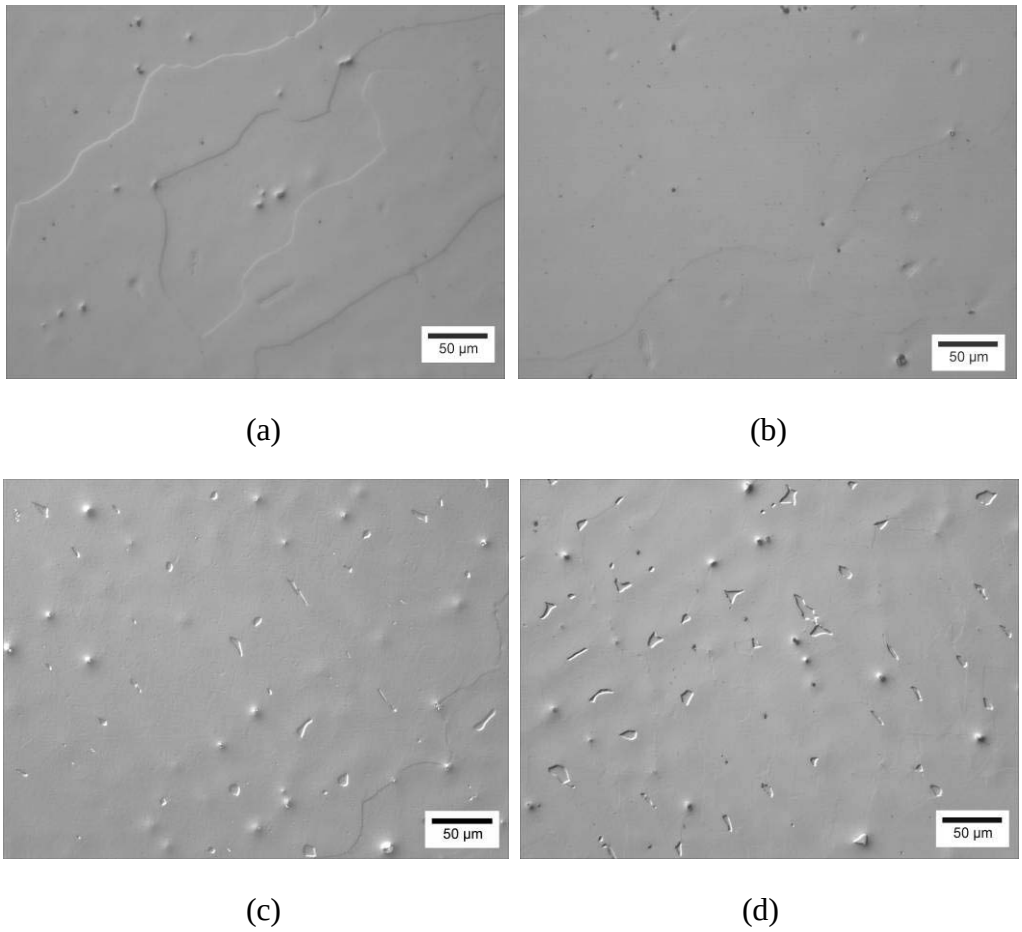

Figure 4. The 1% silicon modified Fe-Mn-Al-C alloy contains less than 1% ferrite (by volume) in the solution treated condition (a) and 3% in the solution treated plus aged at 530°C for 60 hour condition (b). The 1.4% silicon containing alloy contained 6% in the solution treated condition (c) and 8% in the 60 hour aged condition (d).

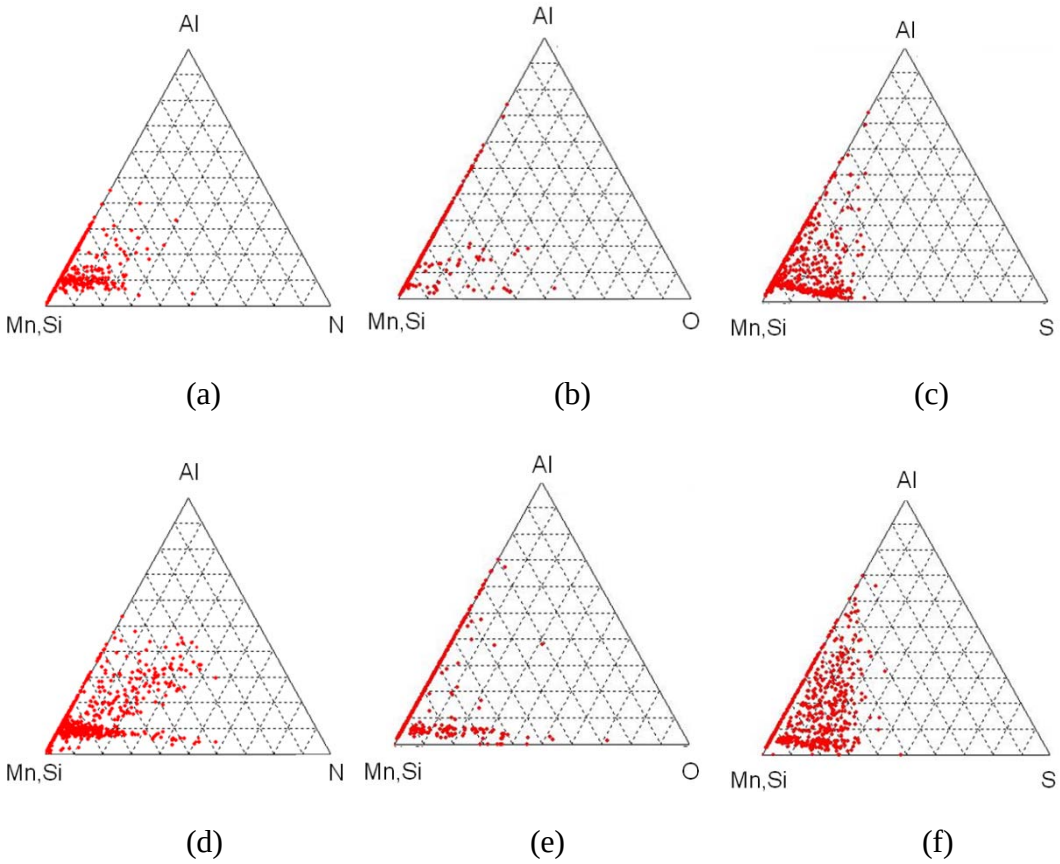

Figure 5. Chemical mapping of non-metallic inclusions for 1 and 1.4% silicon modified Fe-Mn-Al-C alloys. The 1% silicon modified alloy ternaries show nitrides (a) oxides (b) and sulfides (c) are primarily manganese and silicon based. The 1.4% silicon alloy also shows that nitrides (d) oxides (e) and sulfides (f) are also predominantly manganese and silicon rich. Visual inspection and comparison reveals fewer oxides than nitrides or sulfides.

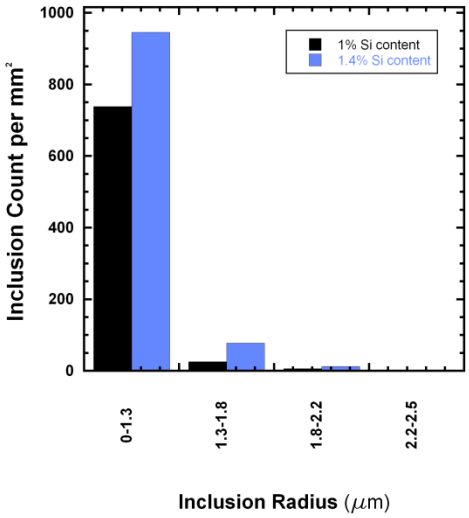

Figure 6. A combined non-metallic inclusion count for the 1 and 1.4% silicon containing alloys as a function of particle radius. The 1.4% silicon alloy inclusion count exceeds the 1% silicon Fe-Mn-Al-C alloy for all radii. Non-metallic inclusion radii greater than 2.5 μm were not detected.

TENSILE STRENGTH

Tensile stress versus strain data is shown in Figure 7 for the two alloys in both the solution treated and aged conditions. In general, the yield and tensile strengths increase and the elongation to fracture decreases with increasing time of age hardening. Greater strengths and lower elongations to failure are observed with the 1.4% silicon alloy. Tensile test results are summarized in Table 2. Young's Modulus was constant for all alloys and measured 188 GPa. A strong work hardening behavior was observed for the solution treated materials with a work hardening exponent of 0.32 and 0.23 for the 1.0% Si and 1.4% Si alloys. The age hardened materials had work hardening exponents that were an order of magnitude lower (see Table 2).

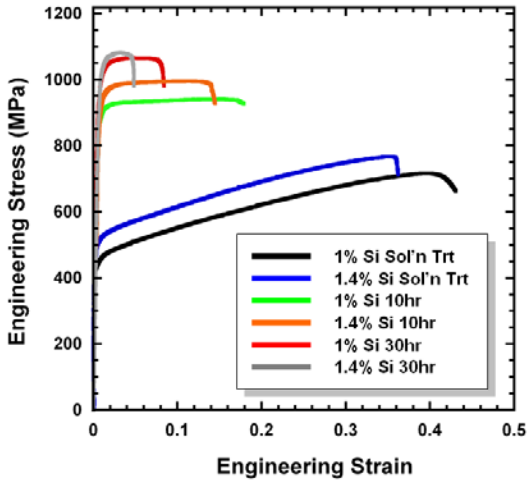

Figure 7. Tensile curves show low strength, high ductility for solution treated 1 and 1.4% silicon containing steels. Aged material showed significant increased strength, but also showed an equally significant reduction in ductility.

Table 2. Tensile properties of 1 and 1.4% silicon containing Fe-Mn-Al-C alloys

Alloy	Heat Treat Condition	BHN	Yield Strength (MPa/ksi)	Tensile Strength (MPa/ksi)	Engineering Strain	Work Hardening Exponent
1% Si	Sol'n Treat	224	458 / 66	687 / 100	0.44	0.32
	10hr 530°C	343	891 / 129	940 / 136	0.18	0.08
	30hr 530°C	372	1,005 / 145	1,065 / 154	0.08	0.06
1.4% Si	Sol'n Treat	219	549 / 79	766 / 111	0.36	0.23
	10hr 530°C	353	922 / 138	995 / 144	0.14	0.07
	30hr 530°C	384	1,016 / 147	1,085 / 157	0.05	0.05

Optical microscopy was performed on the gage sections of each tensile bar to judge the deformation character. Deformation twinning was not apparent and slip bands were

predominately planar in nature. Figure 8 shows slip in the 1 and 1.4% steels aged for 10 hours. The slip is easily seen at the grain boundaries.

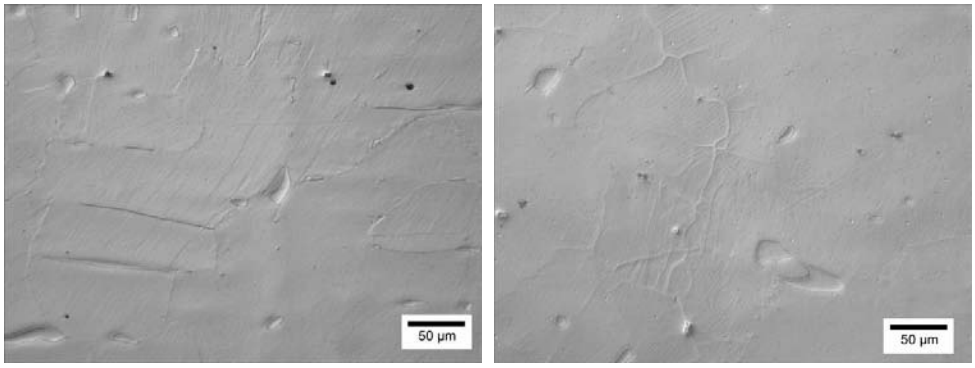

(a) (b)

Figure 8. Deformed gage sections of 1(a) and 1.4(b) % silicon containing Fe-Mn-Al-C alloy showing planar slip. Planar slip is most visible at grain boundaries.

Fracture surfaces were examined using a scanning electron microscope. The solution treated material failed by transgranular microvoid coalescence. Upon aging, the fracture transitioned to transgranular cleavage and followed the dendritic structure. Figures 9(a) and 9(b) shows transgranular dimple rupture of both solution treated materials. Figure 9(c) and 9(d) shows transgranular cleavage.

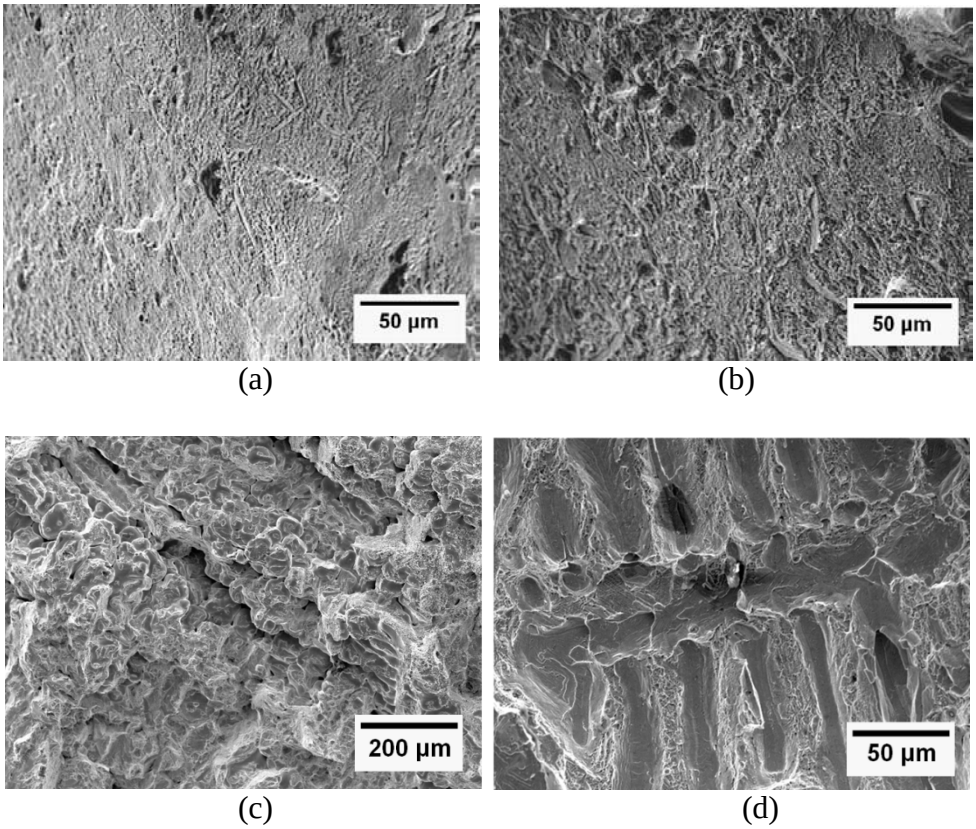

Figure 9. Failure occurs in a ductile fashion in the solution treated low silicon alloy (a) and high silicon alloy(b). Age hardening transitions the failure mode toward transgranular cleavage conforming to the dendrite structures for 1% silicon modified alloy (c) and 1.4% silicon modified alloy (d). The dendrite structure is also revealed by porosity in the 1% silicon alloy (c).

HIGH STRAIN RATE COMPRESSION TESTING

Compression Split Hopkinson Bar specimens of the 1% silicon alloy were tested at a strain rate of 3000 s^{-1}. Figure 10 shows the solution treated and 10 hour 530°C aged specimens' true stress vs. strain responses. MIL-A-12560[21] rolled homogeneous armor compression results[22] are included for comparison. The solution treated specimen yielded at 950 MPa (137 ksi) and work hardened to 1,552 MP (225 ksi) and the fracture

strain was 0.50. The 10 hour aged specimen yielded at 1,334 MPa (193 ksi) and work hardened to 1,651 MPa (239 ksi) and the fracture strain was 0.45.

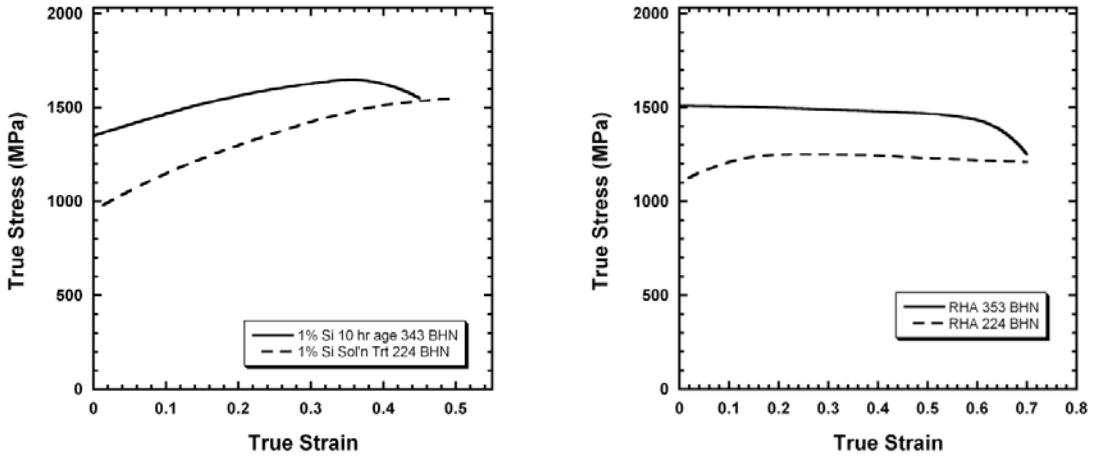

Figure 10. The low silicon Fe-Mn-Al-C alloy (a) shows work hardening in the solution treated and 10 hour 530°C aged condition at a strain rate of 3000 s^{-1}. Aged hardened material does not work harden as greatly as solution treated material, but age hardened specimens had greater yield and ultimate strength and slightly lower fracture strain. Rolled homogeneous armor (b) does not strain harden to failure. Ultimate strength occurs between 0.1 and 0.2 strain followed by decreasing stress to fracture beyond 0.6 strain.

Fracture was observed to occur in locations of prior formed shear bands. Figure 11 shows fracture through a 10 hour aged specimen. Fracture occurred at maximum shear, 45° to the uniaxial loading direction, along the path of prior shear band formation. Specimen failure from through cracking was not observed to preferentially align with inclusions, microporosity, dendrite orientation, or ferrite.

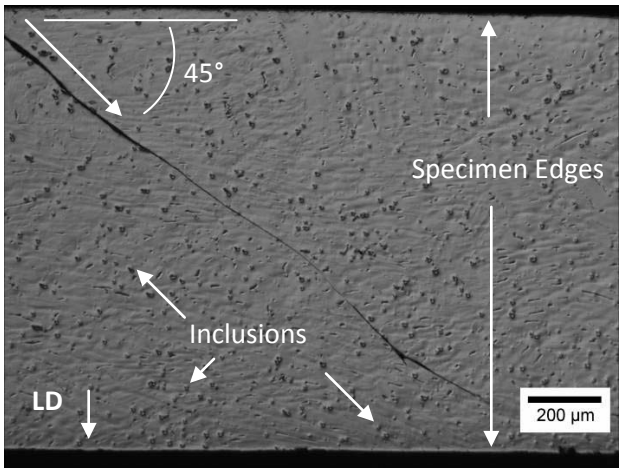

Figure 11. A 10 hour aged 1% silicon specimen was tested to fracture by loading at 448 kPa (65 psi). Crack formation through the thickness is 45° to the loading direction (LD); load direction is indicated in the lower left hand corner. The edges of the specimen and inclusions are indicated.

Crack initiation was observed with different microstructural features. Figure 12 shows a shear band (in an aged alloy) followed by a crack tip that initiated from the outer specimen edge that followed an interdendritic boundary. Edge crack penetration was not observed to be continuous through the specimen. Figure 13 shows shear band formation adjacent to porosity in the solution treated material. The shear bands extend outward in a radial like fashion with nucleated cracks visible in the lower right hand region of the porosity. The crack follows the trace of a shear band.

Nucleation of a shear band occurs in polycrystalline material by the local reorientation of slip planes within individual grains that aligns each with the macroscopic plane of maximum shear. Whenever another slip plane's resolved shear stress exceeds the critical shear stress in that plane, slip will shift to that plane propagating the shear band[16]. Macroscopically, the slip orientation averages out and shear bands form in the plane 45° to the loading direction.

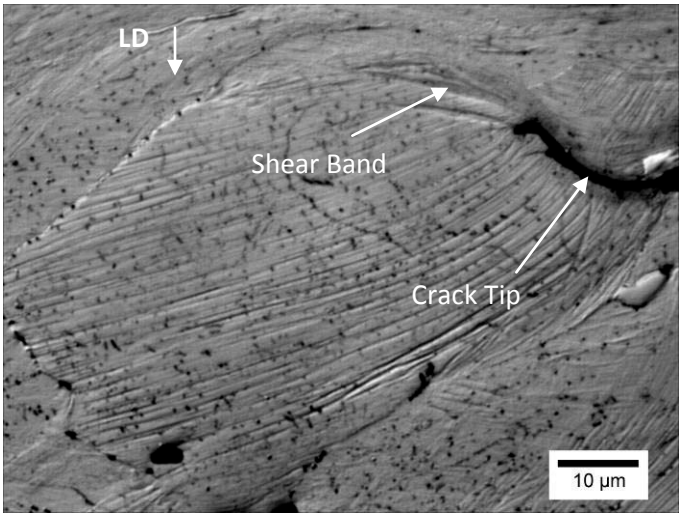

Figure 12. Crack formation is observed following a shear band pathway at a dendrite boundary. Planar slip is observed in the region next to the crack. Failure of this compression specimen originated at internal sites rather than at specimen edges. The loading direction (LD) is indicated in the upper left hand corner.

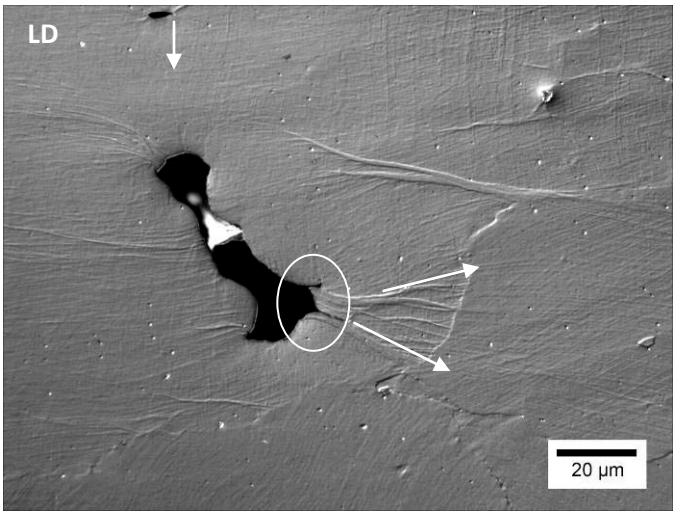

Figure 13. Adiabatic shear bands observed in a solution treated compression specimen extend outward in a radial pattern from the lower right hand region of the porosity. Crack nucleation is seen in the encircled region following the formation of adiabatic shear bands. The loading direction (LD) is marked in the upper left hand corner.

Shear band nucleation at 45° to the loading direction of a 1% silicon, solution treated specimen is visible in Figure 14. The solution treated specimen was loaded at 275 kPa (40 psi); the pressure was insufficient for failure. The 1% silicon alloy shows a resistance to shear localization as evident by the work hardening achieved. A deformed region is highlighted showing the nucleation region of an adiabatic shear band and the rotated crystal structure of adjacent material conforming to the 45° shear band.

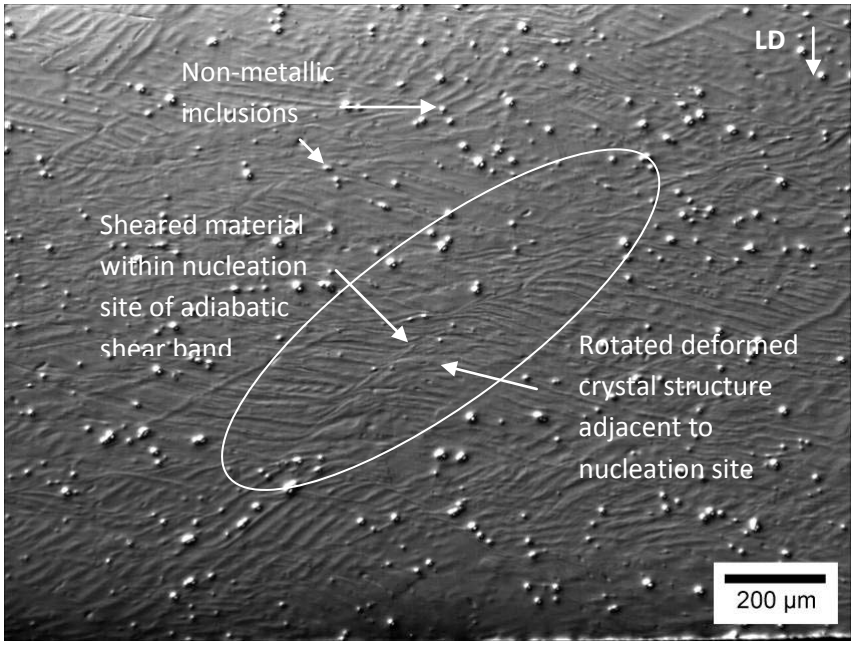

Figure 14. A high strain rate solution treated 1% silicon containing alloy compression sample was not loaded to failure in order to study the adiabatic shear band and crack formation. The encircled and highlighted central region shows the nucleation of an adiabatic shear band rotated 45° to the loading direction (LD). Material adjacent to the nucleation site is deformed and the crystal structure is rotated to conform to the sheared material.

Figure 15 is an image of a shear band in a 1% silicon, 10 hour aged specimen, loaded at 310 kPa (45 psi), which did not fail. The shear band extends nearly the entire specimen. Intense slip and grain rotation is observed adjacent to the shear band. The loading direction (LD) is indicated in the figure's upper right hand corner.

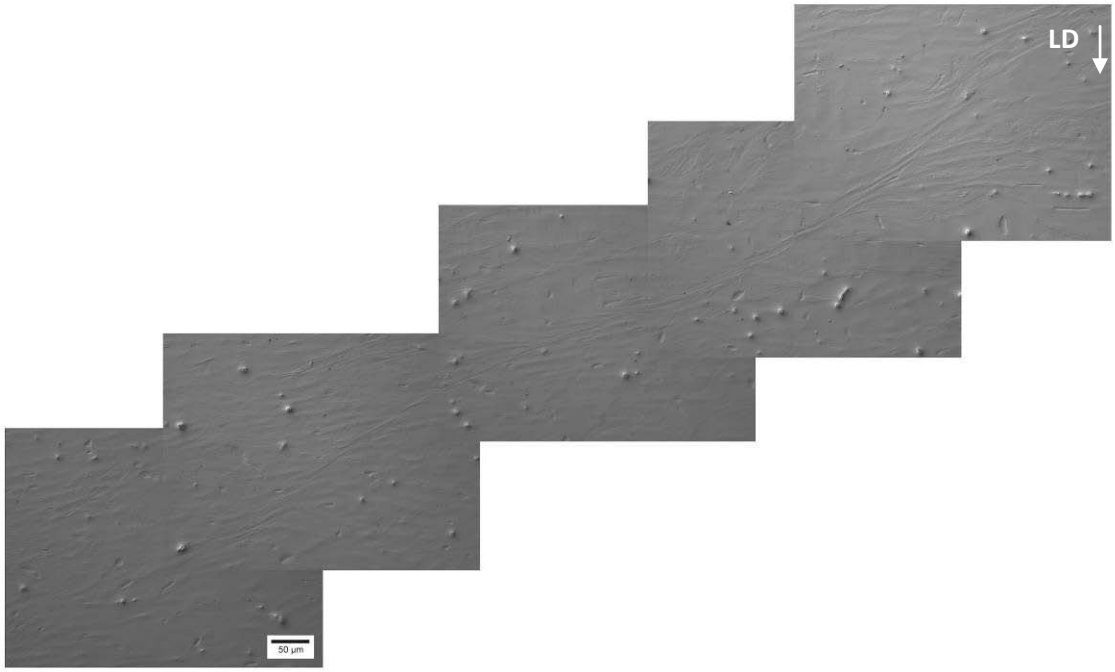

Figure 15. An adiabatic shear band propagated through a 10 hour aged specimen. Shear formation appears independent of inclusion content and ferrite. The loading direction (LD) is indicated in the upper right hand corner.

Figure 16 is an image showing the early stage of shear band formation in the solution treated specimen that was loaded to 345 kPa (50 psi). This specimen did not fracture. Inspection of the deformed microstructure shows multiple shear bands. Planar slip is

visible between the shear bands and the planar slip accommodates deformation not associated with adiabatic shear.

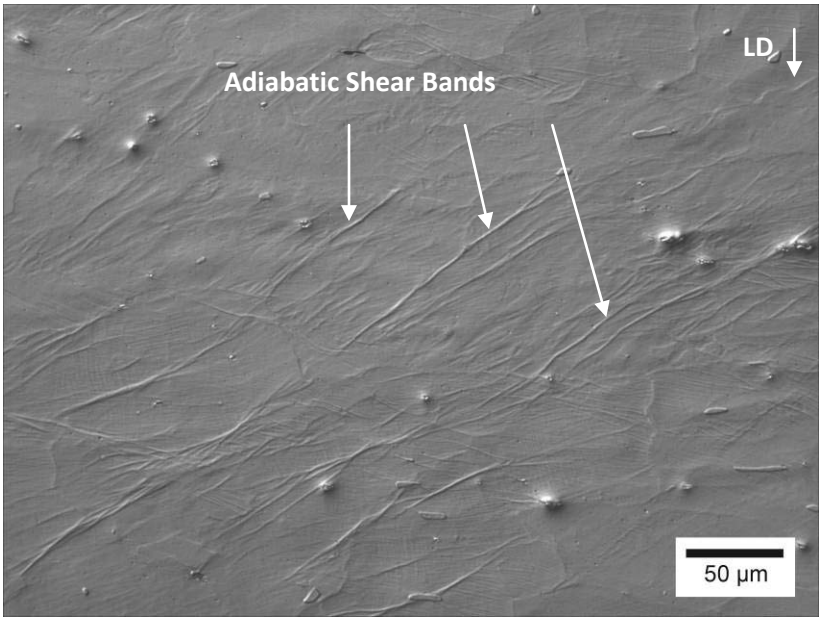

Figure 16. Multiple shear bands are shown in a 1% silicon modified alloy in the solution treated condition after high strain rate testing. Planar slip is visible between shear bands. The loading direction is indicated in the upper right hand corner.

DISCUSSION

The 530°C age hardening behavior follows closely with work by Hale and Baker[23] of a similar composition, i.e. Fe-30.4Mn-7.6Al-0.81C-0.35Si. The Acselrad et al.[19] investigation of time temperature transformation behavior suggested a temperature less than 550°C to reduce heterogeneous precipitation of κ-carbide at grain boundaries and formation of B2 or DO_3 intermetallic compounds. Further reductions in aging temperature (below 530°C) would decrease the nucleation and growth of these

deleterious phases, but the corresponding time necessary to attain MIL-PRF-32269 hardness requirements were deemed unrealistic for production foundries.

For both alloys, the higher number density of sulfides and nitrides is consistent with overall chemistry of the alloy, i.e. oxygen was less than 2 ppm. The 1.4% alloy had a higher number of non-metallic inclusions as can be seen in Figures 4 and 5, but the chemistries of the inclusions in both alloys are similar and are manganese rich. Howell et al. [24] has previously shown that calcium treated alloys have a greatly reduced sulfide content, and has reported an increase in Charpy toughness for a reduction in phosphorus and sulfur content in a similar Fe-Mn-Al-C alloy. The high phosphorus content in the alloys investigated here (0.06 wt.%P) appears to be due to phosphorus in the ferromanganese. However, at 100% recovery, phosphorus contribution from ferromanganese would only account for 0.018%P. Other potential sources include furnace and ladle refractory materials, and residual metal from prior heats. Phosphorus reduction is possible by changing to low phosphorus electrolytic manganese. Improved foundry practice investigations to further reduce phosphorus, sulfur, and inclusion content are ongoing.

Tensile strength, ductility, and work hardening followed classic trends for age hardening materials. Except for the solution treated condition, the 1.4% silicon alloy had a higher strength and hardness, but lower ductility for equivalent aging treatment. The lower ductility may result from an increase in the volume fraction of ferrite and the number density of non-metallic inclusions. Pickering[25] has reported a decrease in ductility for steel for an increase in volume fraction of second phase particles and the same trend is observed for the alloys studied here.

Microstructure of aged and deformed materials were similar between the two silicon levels. Ferrite content followed a trend previously reported[14] where a minimum of ferrite occurs at approximately 1% Si and increases with greater silicon content. It should be noted that the high phosphorus content in the alloys studied here may promote higher volume fractions of ferrite in both the solution treated and aged microstructures. In the previous study, a fully austenitic microstructure was obtained for a 0.82% Si alloy after solution treatment. The tensile deformed microstructure shows evidence of planar slip in both alloys (see Figure 8). Planar slip was also observed in the high strain rate compression samples (see Figure 12). Both solution treated alloys failed by transgranular microvoid coalescence during tensile testing as seen in Figure 9. Aging resulted in a transition to a transgranular cleavage failure that appears to follow the crystallography of the dendrites as shown in Figure 9 (d).

High strain rate compression samples failed by adiabatic shear band formation, which preceded crack nucleation and growth. Three specific examples show this phenomenon. First, the through crack in Figure 11 that occurred at 45° to the loading direction is associated with adiabatic shear band formation. Examples of shear bands that lead to through cracking are shown in Figures 14, 15, and 16, and were observed along a macroscopic plane of maximum shear, i.e. 45° to the loading direction. These shear bands measured between tens of microns to several hundred microns in length. Shear band nucleation and crack formation appears to be promoted by porosity in preference to any other microstructural feature. When nucleated at the specimen edge, shear band and subsequent crack formation followed an interdendritic path for about 50 μm before merging with the macroscopic 45° band (see Figure 12).

Thermodynamic calculations for the stacking fault energy (γ_{SFE}) based on Olsen's[26] model have been used to predict the deformation mechanism in Fe-Mn-Al-C steels. Frommeyer and Brux[8] stated that twinning is suppressed in systems with γ_{SFE} greater than 50 mJ/mm^2. Aluminum additions greater than 3 wt.% suppress twinning. Frommeyer and Brux have shown that a Fe-28Mn-12Al-1C alloy with a γ_{SFE} of 110 mJ/mm^2 deformed by plastic flow in quasistatic testing and by adiabatic shear under high strain rates. The calculated γ_{SFE} for the 1 and 1.4% silicon containing alloys are 100 mJ/mm^2. The silicon difference did not have any significant impact on a change in the calculated γ_{SFE}. The calculated γ_{SFE} energy and observations showing planar slip are in agreement with the observations by Frommeyer and Brux[8].

An interesting comparison can be made between the cast Fe-Mn-Al-C alloys studied here and the wrought alloy typically used to benchmark steel armor, i.e. rolled homogeneous armor. The specific compressive strength of the 1% silicon containing alloy is greater than rolled homogenous armor (RHA); both steels were tested at 3000 s^{-1} strain rate. Figure 10 shows excellent work hardening prior to fracture for the silicon containing Fe-Mn-Al-C steels with higher ultimate strength than RHA. Factoring in the 13% density reduction for the Fe-Mn-Al-C alloy and the specific strengths are greater still. Table 3 compares specific high strain rate compression strengths of the solution treated and aged 1% silicon modified alloy to that of RHA, which has been quenched and tempered to similar hardness values. The 1% alloy exceeded the specific compressive ultimate strength of RHA by 58 MPa/ρ (287 ksi/ρ) in the solution treated condition and 54 MPa/ρ (220 ksi/ρ) for the aged condition.

Table 3. Comparison of specific compressive strengths of two heat treated conditions between the 1% silicon containing Fe-Mn-Al-C alloy and RHA tested at 3000 s^{-1} strain rate.

Alloy	Density	Specific Strength 1% Si – BHN 224 RHA – BHN 224	Specific Strength 1% Si – BHN 343 RHA – BHN 352
1% Si	6.7 g/cm^3 (0.24 lbs/in^3)	231 MPa/ρ (933 ksi/ρ)	246 MPa/ρ (995 ksi/ρ)
RHA	7.8 g/cm^3 (0.28 lbs/in^3)	173 MPa/ρ (646 ksi/ρ)	192 MPa/ρ (775 ksi/ρ)

Observation of work hardening at high strain rates, in both the solution treated and aged Fe-Mn-Al-C-Si alloys, indicates an inherent resistance to the formation of adiabatic shear bands. However, the final failure was still by shear band formation, but at higher stresses than RHA. Casting porosity appears to be the main microstructural feature that nucleates the shear band.

Investigations are ongoing to increase Fe-Mn-Al-C alloy strength and notch toughness through improved foundry practices and a physics based, first principles modeling of alloy additions. Foundry practice studies are focused on grain refinement, porosity minimization, mold design and fluid modeling, reduction of phosphorus, and improving the cleanliness by reducing the number of nonmetallic inclusions.

CONCLUSIONS

Lightweight Fe-Mn-Al-C steels can be solution treated and aged 10 hours at 530°C to meet hardness requirements specified in MIL-PRF-32269. When tested at high strain rates, a combination of lower weight and higher compressive strength for the Fe-30Mn-9Al-1Si-0.5Mo alloy results in a specific strength that is 28% greater than rolled homogeneous armor with equivalent hardness of 352 BHN. More importantly, the Fe-

30Mn-9Al-1Si-0.5Mo alloy exhibits work hardening during high strain rate testing, which indicates an inherent resistance to the formation of adiabatic shear bands. However, casting porosity was observed to promote adiabatic shear bands and crack formation.

Increasing silicon content from 1 to 1.4% in a Fe-30Mn-9Al-XSi-0.9C-0.5Mo alloy increased tensile strength and hardness, but reduced ductility and the work hardening exponent in aged materials. The decrease in tensile ductility appears to be related to an increase in non-metallic inclusions for the 1.4% Si alloy since the additional silicon did not appear to change the tensile fracture or microstructural deformation mechanisms. Improved properties are expected by reducing the phosphorus content. This will require a steelmaking process using charge materials and furnace refractories that are low in phosphorus. The high phosphorus content of the alloys. Lower phosphorus content should also lower the amount of ferrite in the solution treated and aged conditions.

REFERENCES

1. Ham, J. L., Cairns, R. E., “Manganese Joins Aluminum to Give Strong Stainless,” Product Engineering, Dec, pp. 51-52 (1958).
2. Banerji, S. K., “An Update on Fe-Mn-Al Steels,” presented at Vanderbilt University’s workshop on “Conservation and Substitution Technology for Critical Material,” June 15-17, (1981).
3. Brady, G. S., Clauser, H. R., “Manganese-Aluminum Steel,” Materials Handbook, 11th Ed., p. 497 (1977).
4. Acselrad, O., Pereira, L. C., Amaral, M. R., “Processing Condition, Microstructure and Strength of an Austenitic FeMnAlC Alloy,” Proceedings of Proc. and Prop. of Mats., pp. 829-834 (1992).
5. Ishida, K., Ohtani, H., Naoya, S., Kainuma, R., Nishizawa, T., “Phase Equilibria in Fe-Mn-Al-C Alloys,” ISIJ, Vol. 30, pp. 680-686 (1990).

6. Goretskii, G. P., Gorev, K. V., “Phase Equilibria in Fe-Mn-Al-C Alloys,” Russian Met., Vol. 2, pp. 217-221 (1990).

7. Han, K. H., Choo, W. K., “Phase Decomposition of Rapidly Solidified Fe-Mn-Al-C Austenitic Alloy,” Met. Trans. A., Vol. 20A, pp. 205-214 (1989).

8. Frommeyer, G., Brux, U., “Microstructures and Mechanical Properties of High-Strength Fe-Mn-Al-C Light-Weight TRIPLEX Steels,” Steel Research Int., Vol. 77, pp. 627-633 (2006).

9. Sato, K., Tagawa, K., and Inoue, Y., “Modulated Structure and Magnetic Properties of Age-Hardenable Fe-Mn-Al-C Alloys,” Met. Trans A, vol. 21A, pp 5-11 (1990).

10. Kayak, G. L., “Fe-Mn-Al Precipitation-Hardening Austenitic Alloys,” Met. Sc. And Heat Tr., Vol. 11, pp. 95-97 (1969).

11. Acselrad, O., Dille, J., Pereira, L. C., Delplancke, J. L., “Room-Temperature Cleavage Fracture of FeMnAlC Steels,” Met. Trans. A, Vol. 35A, pp. 3863-3866 (2004).

12. Schmatz, D. J., “Formation of Beta Manganese-Type Structure in Iron-Aluminum-Manganese Alloys,” Trans. of Met. Soc. of AIME, Vol. 215, pp. 112-114 (1959).

13. Acselrad, O., Kalashnikov, I. S., Silva, Khadyev, M. S., E. M., Simao, “Diagram of Phase Transformation in the Austenite of Hardened Alloy Fe-28Mn-8.5Al-1C-1.25Si as a result of Aging due to Isothermal Heating,” Met. Sci. and Heat Treat., Vol. 48, pp. 543-553 (2006).

14. Howell, R. A., Lekakh, S. L., Van Aken, D. C., Richards, V. L., “The Effect of Silicon Content on the Fluidity and Microstructure of Fe-Mn-Al-C Alloys,” AFS Transactions, Vol. 116, pp. 867-878 (2008).

15. Chiou, S. T., Cheng, W. C., Lee W. S., “Strain Rate Effects on the Mechanical Properties of a Fe-Mn-Al Alloy Under Dynamic Impact Deformations,” Mat. Sci. and Eng. A., vol. 392, pp.156-162 (2005).

16. Walley, S. M., “Shear Localization: A Historical Overview,” Met. Trans. A, vol. 38A, pp. 2629-2654 (2007).

17. MIL-PRF-32269, Military Performance Specification for Perforated Homogeneous Armor.

18. Kalashnikov, I., Acselrad, O., Shalkevich, A., Pereira, L.C., “Chemical Composition Optimization for Austenitic Steels of the Fe-Mn-Al-C System,” Journal of Materials Engineering and Performance, Vol. 9, No. 6, pp. 597-602 (2000).

19. Acselrad, O., Kalashnikov, I. S., Silva, E. M., Simao, R. A., Achete, C. A., Pereira, L. C., "Phase Transformations in FeMnAlC Austenitic Steels with Si Addition," Met. Trans. A., Vol. 33A, pp. 3569-3572 (2002).

20. Follansbee, P. S., "The Hopkinson Bar," ASM Handbook (9^{th} Edition), vol. 8, pp. 198-203 (1994).

21., "Armor Plate, Steel, Homogeneous," MIL-A-12560H, pp. 1-41 (2007).

22. Weerasooriya, T., Moy, P., "Effect of Strain-Rate on the Deformation Behavior of Rolled-Homogeneous-Armor (RHA) Steel at Different Hardnesses," Presented at the Int'l Congress on Experimental Mechanics, Costa Mesa, CA, June 7-10 (2004).

23. Hale, G. E., Baker, A. J., "Carbide Precipitation in Austenitic Fe-Mn-Al-C Alloys," Conference Proceedings on Alternate Alloying for Environmental Resistance, pp. 67-89 (1986).

24. Howell, R. A., Lekakh, S. L., and Van Aken, D. C., "Quench Sensitivity of Cast Fe-30Mn-9Al-1Si-0.9C-0.50Mo Lightweight Steel," manuscript submitted to AIST Tech.

25. Pickering, F. B., "Physical Metallurgy and Design of Steels," London: Applied Science Publication, pp. 51 (1978).

26. Olson, G. B., Cohen, M., "A General Mechanism of Martensitic Nucleation: Part I: General Concepts and the FCC to HCP Transformation," Met. Trans. A, Vol. 7A, pp. 1897-1904 (1976).

PAPER

4. Advancements in Steel for Weight Reduction for Weight Reduction of P900 Armor Plate

R.A. Howell, J. S. Montgomery, D.C. Van Aken

Army Research Lab

Missouri University of Science and Technology

Department of Materials Science and Engineering

Rolla, MO 65409

Tel.: 573-341-4717

E-mail: dcva@mst.edu

Key Words: Fe-Mn-Al-C, lightweight steel, ballistic, armor, impact toughness

Published in the American Iron and Steel Technology journal.

ABSTRACT

Ballistic tests were conducted on a high manganese and high aluminum austenitic steel that is age hardenable. These lightweight steels (12 to 18% lower in density) were investigated as alternatives to MIL-PRF-32269 steel alloys for application in P900 perforated armor currently used for Army ground combat systems. Two steel plates with nominal composition in weight percent of Fe-30Mn-9Al-1Si-0.9C-0.5Mo were evaluated for V_{50} against 0.30 caliber armor piercing and 0.50 caliber fragmentation simulation projectiles. At equivalent areal densities to current steels, both plates surpassed the required 0.30 caliber acceptance criteria by 188 and 151 ft/s. Against the 0.50 caliber fragmentation projectile, the calcium treated plate exceeded the MIL-A-46100 V_{50} by 225 ft/s, but the non calcium treated plate underperformed by 39 ft/s.

INTRODUCTION

P900 was originally designed in the late 1980's as appliqué armor to counter Soviet small-arms threats (Gooch, 1991). The thin-ribbed section design (see Figure 1) localizes deformation, which allows for multi-hit capability. The original P900 was cast from low alloy steels using the lost foam process without regard to material properties. Computer modeling in conjunction with a re-evaluation of material property requirements and validation by ballistic testing has led to the adaptation of P900 as an armor enhancement in current armor systems. A quenched and tempered martensitic steel (in accordance with alloy tolerances of MIL-A-46100) met the required hardness and ballistic standards. Expanded metal processes and offset punched plates offer alternative designs to P900, but these solutions do not achieve P900's performance and higher ballistic success rate as measured by MIL-PRF-32269.

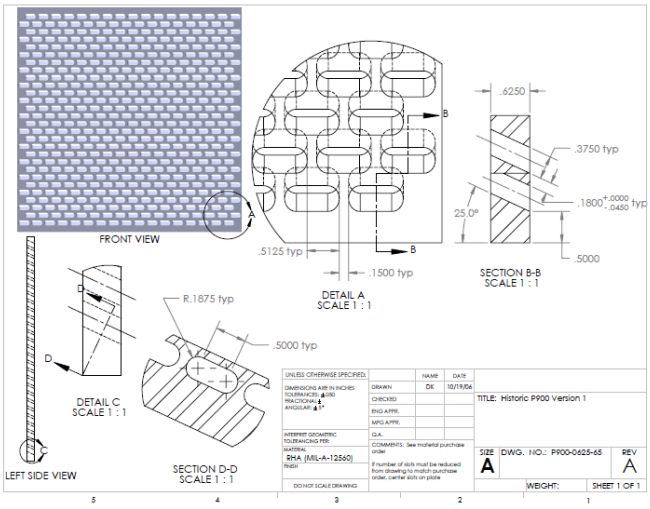

Figure 1. Shown above is the 2-D dimensional specification drawing and image of cast P900 armor plate.

Second generation advanced high strength steels that are being developed (Frommeyer, 2006) as lightweight steels for the automotive industry are potential candidates for the P900 armor application. These steels contain high levels of aluminum, which can lower the density by 12 to 18% relative to mild steel. These steels, which are referred to as FeMnAlC, are austenitic and age hardenable by the precipitation of κ-carbide. Tensile strengths greater than 140 ksi with an elongation to fracture that is greater than 15%, are comparable to quench and tempered low alloy steels currently used. These lightweight steels also have good casting characteristics (high fluidity and low melting temperature) that are comparable to ductile iron (Howell et al., 2008). FeMnAlC alloys do not require high cost alloys, such as nickel, cobalt, or chromium and are less costly than titanium alloys. Tailorable properties via age hardening coupled with reduced density offer a higher specific strength over quench and tempered steel. Challenges still

lie in developing these FeMnAlC alloys to reduce weight without sacrificing P900 armor performance.

EXPERIMENTAL PROCEDURE

Two ballistic test plates were cast in a nominal Fe-30Mn-9Al-1Si-0.9C-0.5Mo chemistry. All chemistries are in weight percent. Foundry grade alloys were melted in an induction furnace under argon cover. Active oxygen content measured 2 ppm in the furnace. Horizontal plate molds were prepared using phenolic no-bake bonded olivine sand in lieu of silica sand to prevent reaction of the manganese with silica sand. One plate measured 12 inches by 18 inches by 0.6 inches, was calcium treated (followed by immediate slag removal), and utilized electrolytic manganese in the steelmaking process. The second plate measured 12 inches by 12 inches by 0.72 inches, was not calcium treated, and employed ferromanganese. The cast plates were vacuum solution treated at 1050°C, nitrogen gas quenched, and aged for 15 hours at 530°C. The non-calcium treated plate was cast at 0.72 inch thickness and subsequently machined to 0.625 inch thickness after solution treatment. The calcium treated plate was shot peened after heat treatment. Brinell hardness of both plates was measured by a 3,000 kg load in accordance with ASTM E10.

Ballistic testing was performed for V_{50} evaluation of 0.30 caliber armor piercing (AP) and 0.50 caliber fragmentation simulation projectiles (FSP) at 0° obliquity. The FeMnAlC ballistic results were compared on an areal density equivalency to the MIL-PRF-32269 acceptance criteria for the 0.30 caliber AP and to MIL-A-46100 steel for the 0.50 caliber FSP requirements. FSP testing is not called for in the MIL-PRF-32269, but there is no historical FSP data on FeMnAlC alloys. FSP test data was compared to MIL-

A-46100 (high hard steel) due to its use in MIL-PRF-32269 as a class 1 material and because of a large historical performance database against the 0.50 caliber FSP.

Chemical analysis was performed on each cast alloy plate using inductive coupled plasma spectrometry and wavelength dispersive spectrometry after dissolving the steel in perchloric acid. Charpy impact specimens were machined from each FeMnAlC alloy plate, and tests were performed at room temperature and -40°F. Post fracture analysis of ballistic and Charpy impact tests were performed using optical microscopy and scanning electron microscopy (SEM). The metallographic specimens were prepared using standard metallographic practices and etched with 2% Nital. An ASPEX-PICA 1020 analytical SEM was used to qualitatively compare material cleanliness and perform a standardless chemical analysis by energy dispersive x-ray spectrometry (EDS) on both fracture surfaces and metallographically prepared specimens. Computer aided analytic software quantified primary phase constitution, inclusion chemical content, and inclusion size distribution. An Hitachi S-4700 Field Emission SEM was used for the inclusion images.

RESULTS

The MIL-PRF-32269 cast armor material is designated class 2 and has an acceptance range of 302-352 Brinell hardness number (HB). The calcium treated plate's hardness measured 351 HB, and the non-calcium treated plate exceeded the hardness range at 364 HB. Chemical analysis of each plate is shown in Table 1. Areal density of each plate was measured to be 35.5 pounds per square foot per inch of thickness (PSF), which is 13% less than rolled homogenous armor (40.8 PSF). The equivalent areal density thickness was 0.525 inch for the calcium treated plate and 0.544 inch for the non calcium treated plate.

TABLE 1. Chemical Content of Tested Alloys

Plate	Fe	Mn	Al	Si	C	Mo	S	P
Calcium Treated	Bal	30.21	8.85	1.01	0.89	0.31	0.0008	0.006
Non-calcium Treated	Bal	29.07	8.28	0.92	0.94	0.33	0.006	0.043

The 0.30 caliber AP V_{50} of the calcium treated plate exceeded the acceptance criteria by 188 ft/s, and the non treated plate exceeded its equivalent thickness value by 151 ft/s. The 0.50 caliber FSP V_{50} for of the calcium treated plate exceeded MIL-A-46100 by 172 ft/s, but the non calcium treated plate was lower by 39 ft/s.

Figure 2 shows the impact and exit sides of both plates for the 0.30 caliber AP testing. The region of deformation on the impact face is more visible on the non calcium treated specimen that was machined. Visible deformation extends 0.5 inch from the center of impact on both plates. Cracking and petal formation are observed on the exit side of each plate.

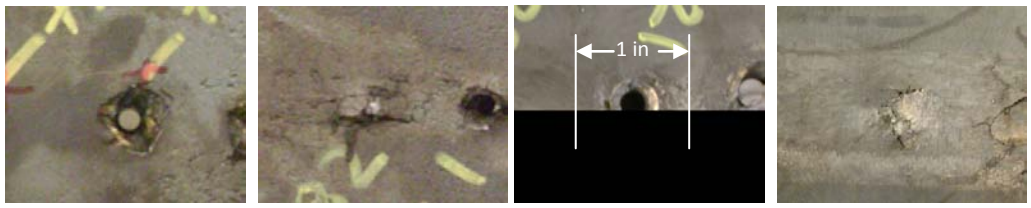

(a) (b) (c) (d)

Figure 2. The calcium treated plate shown with 0.30 caliber AP projectile lodged in the plate (a) and resulting combination of ductile deformation and cracking on the exit face (b). The non calcium treated plate shown with dimensional marker illustrating the deformation region on the strike face (c), and the exit side shows ductile petal deformation and cracking (d).

Figure 3 shows the impact and exit sides for the 0.50 caliber FSP testing. The visible deformation on the impact side of the non calcium treated plate measured approximately 1.25 inch across the surface. Ductile deformation and cracking are observed on the exit side of both plates. Failure occurred by plugging.

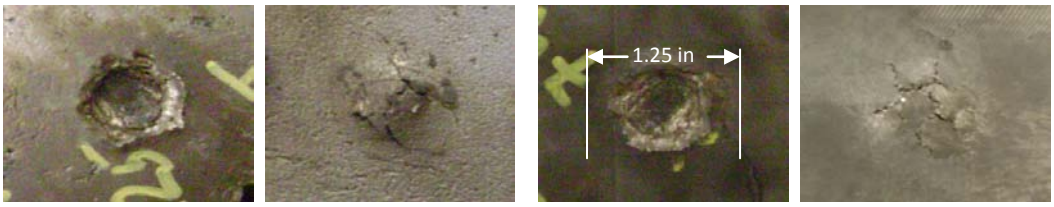

(a) (b) (c) (d)

Figure 3. The calcium treated plate is shown with an impact crater from 0.50 caliber FSP (a) and resulting ductile deformation and cracking on the exit face (b). The untreated plate is shown with dimensional marker illustrating the visible deformation on the strike face (c) and the exit side showing ductile deformation and cracking (d).

Plug formation occurred by adiabatic shear band formation and subsequent cracking. Metallographic examination of the plug formation is shown in Figure 4. Both plates had an austenitic microstructure with 5 volume % ferrite in the interdendritic regions. Figure 4(b) shows clearly the dendritic microstructure and the formation of adiabatic shear bands and crack nucleation between the porosity near the exit side of the calcium treated plate. Cracks were also observed to nucleate at nonmetallic inclusions. A crack tip is seen in Figure 4(c) nucleated from a concentration of nonmetallic inclusions. Figure 5 is a pair of ASPEX-PICA 1020 generated ternary chemical maps of this field showing a high manganese oxide concentratinductive coupled with minor amounts of manganese sulfides and aluminum nitrides.

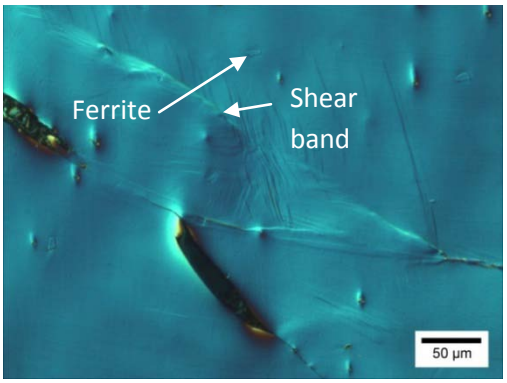

(a)

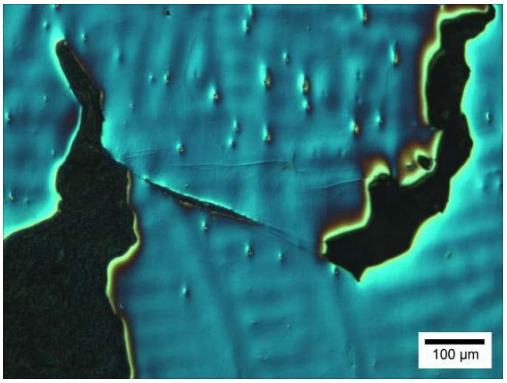

(b)

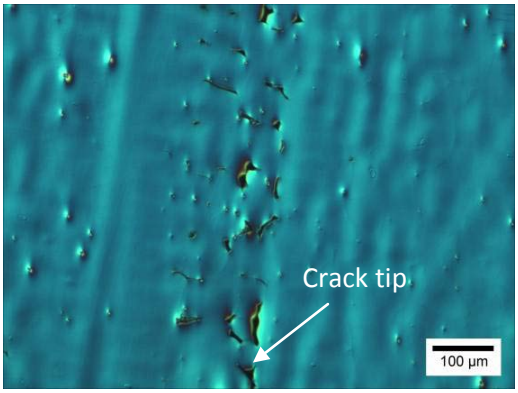

(c)

Figure 4. Adiabatic shear band and crack formation is highlighted in (a). Adiabatic shear bands and crack formation occurred between a larger crack tip and porosity near the exit face shown in (b). A large region of defects is observed next to a crack tip in (c).

Charpy impact energy for the calcium treated plate was 54 ft-lbs at room temperature and 10 ft-lbs at -40°F. The impact energy of the non calcium treated plate was much lower at values of 10 ft-lbs at room temperature and 7 ft-lbs at -40°F.

Varying combinations of ductile and cleavage fracture were observed for both materials (see Figure 6). The proportion of each fracture mode is best illustrated by low magnification images of the fracture surfaces for each casting. Only small areas of dendritic structure are observed in the calcium treated material (Figure 6a) and the majority of the fracture is microvoid coalescence.

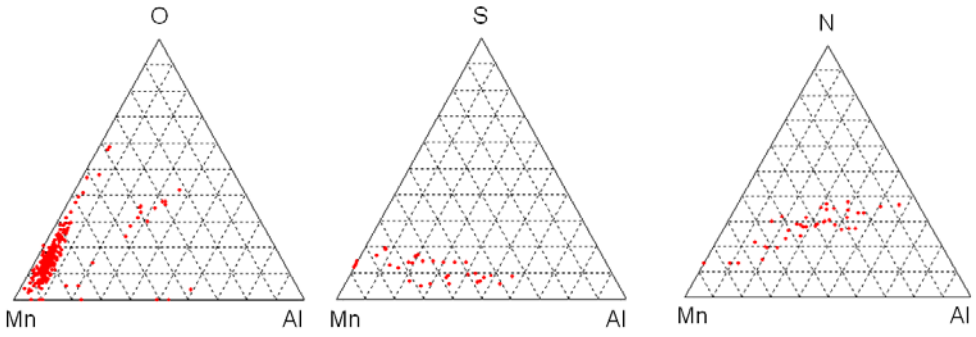

(a) (b) (c)

Figure 5. Chemical mapping of nonmetallic inclusions on Gibb's triangle were made by an EDS mapping of the defect field shown in Figure 4(c). Manganese oxide inclusions dominated the field (a) but also include minor amounts of manganese sulfide (b) and aluminum nitrides (c).

In contrast, the non-calcium treated alloy reveals a dendritic structure dominated by cleavage fracture showing both the main dendrite trunk and secondary arms on both sides of the main trunk (see Figure 6b). This suggests a {001} fracture plane. Selected areas

were imaged to show the combination of fracture modes within the calcium treated alloy (Figure 6c) and the non-treated alloy (Figure 6d).

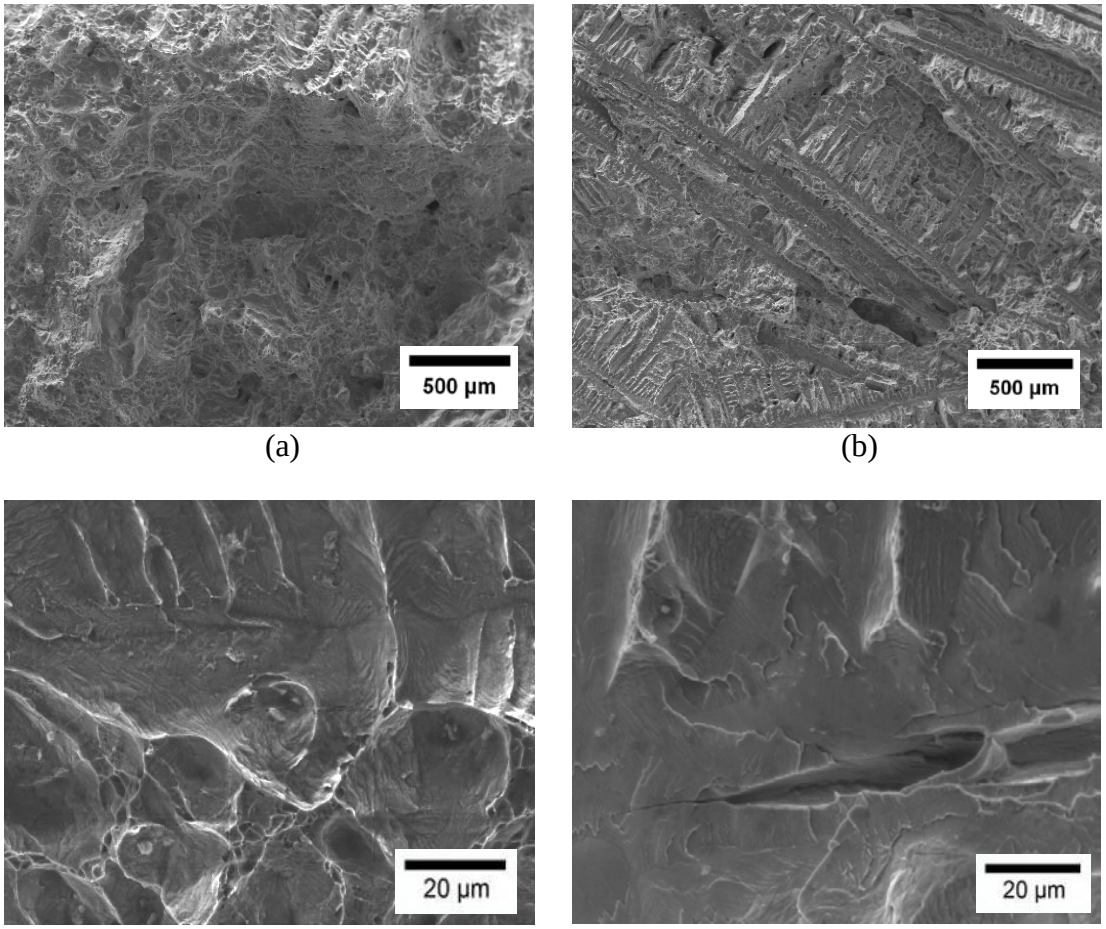

(a) (b)

(c) (d)

Figure 6. Low and high magnification secondary electron images of Charpy V-notch fracture surfaces from the calcium treated low phosphorus alloy (54 ft-lbs; a and c respectively) and non calcium treated high phosphorus alloy (10 ft-lbs; b and d respectively). Both alloys contain transgranular cleavage and microvoid coalescence as shown in the high magnification images, but the proportion of each mode is made evident by the low magnification images. Microvoid coalescence dominates the fracture of the low phosphorus alloy, whereas the high phosphorus alloy is dominated by cleavage fracture revealing a dendritic structure.

An EDS scan of the Charpy impact specimen fracture surfaces (see Figure 7) shows higher amounts of sulfur and phosphorus on the non-calcium treated alloy fracture

surface. The elemental sulfur map shows regions of high concentration on the non calcium treated material. The higher levels of phosphorus and sulfur are corroborated by the wet chemical analysis shown in Table 1. The non calcium treated plate has a sulfur content at 0.06 % and phosphorus content at 0.043 %. The calcium treated plate was lower in both phosphorus and sulfur with levels of 0.006% and 0.0008%, respectively.

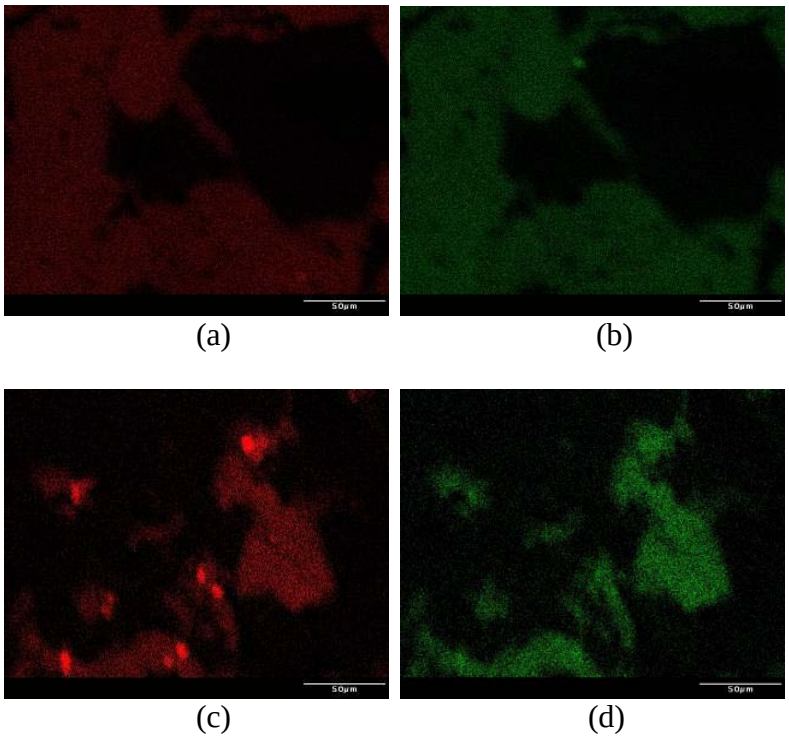

Figure 7. Elemental (EDS) mapping of the fracture surface scans show lower concentrations of sulfur (a) and phosphorus (b) on the calcium treated material as compared to the non calcium treated alloy's sulfur (c) and phosphorus (d) surface content.

A side-by-side comparison of metallographic specimens from the Charpy bars is shown in Figure 8. Both microstructures are primary austenite with less than 5% by

volume ferrite. The dendrite arm spacing in the calcium treated plate measured 81 μm and 42 μm in the non calcium treated plate.

The ASPEX-PICA 1020 inclusion chemical mapping results are shown in Figure 9 and a histogram of inclusion size comparison is shown in Figure 10. Manganese sulfides and aluminum nitrides were observed as a multiphase combined inclusion of the Type-D globular form (ASTM E 45). Manganese sulfides formed an outer rim covering aluminum nitrides (see Figure 11). Overall inclusion chemistry for each steel are comparable; however, the calcium treated steel is much cleaner, i.e. a lower total inclusion count.

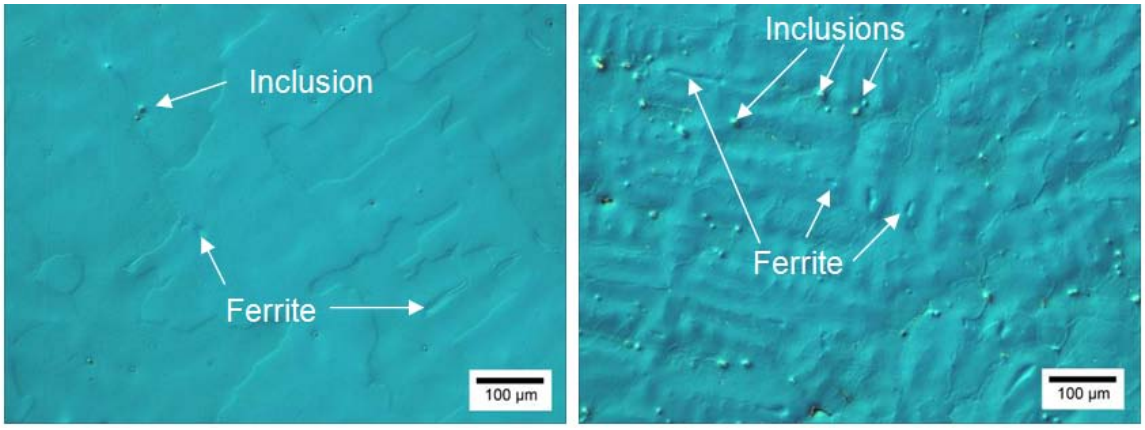

(a) (b)

Figure 8. Optical micrographs of polished Charpy specimens show a dendritic structure with primary austenite and less than 5% by volume ferrite. The calcium treated plate (a) has a secondary dendrite arm spacing of 80 μm and the non calcium treated plate (b) has a secondary dendrite arm spacing of 40 μm. Inclusion content is less visible in the calcium treated plate.

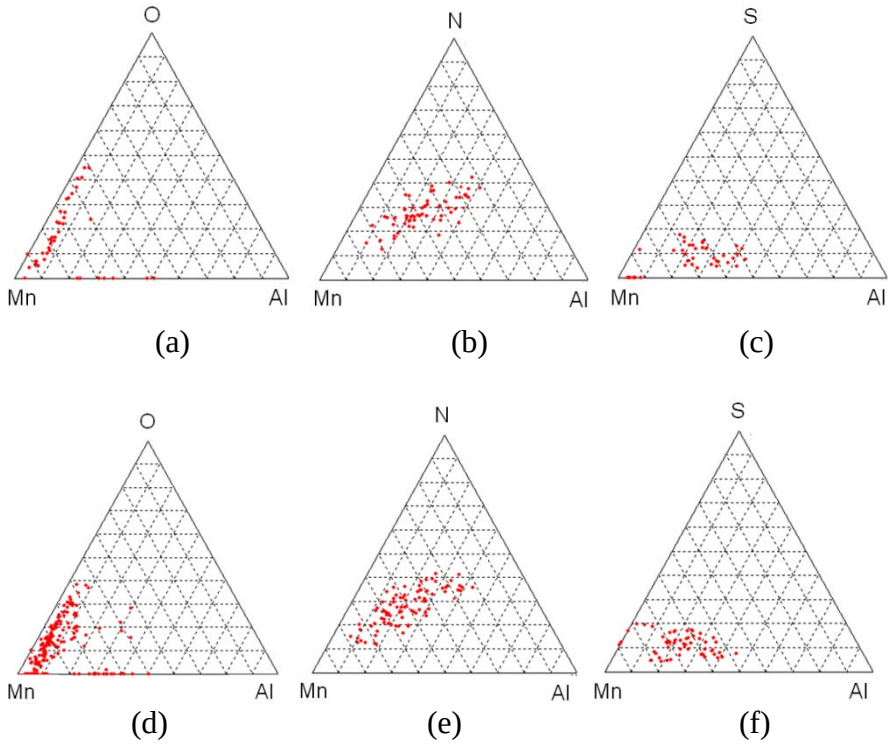

Figure 9. Chemical mapping of non metallic inclusions for both calcium treated, (a, b, and c) and untreated, (d, e, and f) FeMnAlC alloys. Inclusion chemistries are similar for both steels, but the calcium treated steel has fewer inclusions.

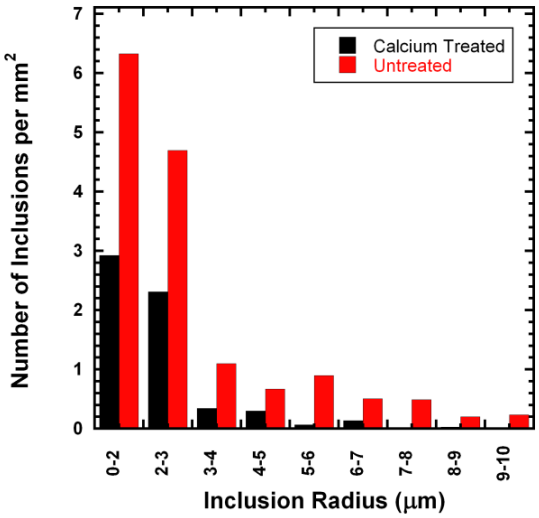

Figure 10. Inclusion areal density is plotted by size range as measured using the ASPEX-PICA 1020 inclusion analysis software. The calcium treated plate has less than half the number of inclusions of the non calcium treated plate in every size category.

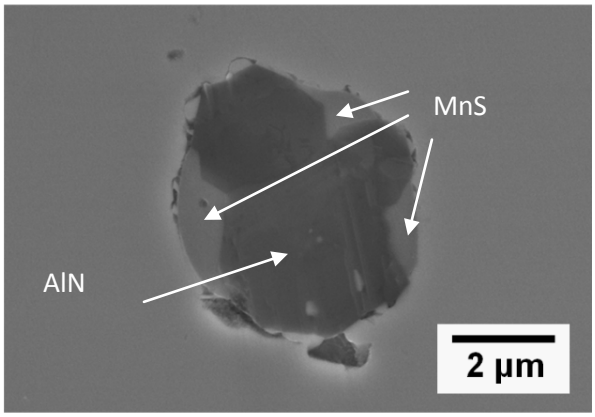

Figure 11. Secondary electron image of a complex multiphase inclusion. A manganese sulfide phase surrounds multiple aluminum nitrides. Sample was etched with 2% Nital.

DISCUSSION

The Fe-30Mn-9Al-1Si-0.9C-0.5Mo alloys meet MIL-PRF-322269 0.30 caliber AP acceptance criteria on an equivalent areal density basis. As measured against high hard steel, only the calcium treated steel met expectations with respect to the 0.50 caliber FSP threat. The 0.50 caliber FSP test shows a greater V_{50} separation between the two cast materials. Even though the calcium treated plate was thinner by 0.020 inches, its FSP V_{50} exceeded that of the untreated plate by 211 ft/s. The FSP V_{50} differences correlated to both differences in inclusion content and differences in notch toughness as measured by Charpy impact energy. Sulfur (Leslie, 1981), phosphorus (Song et al., 2007), and oxide (Wilson, 1981) content has been shown to decrease Charpy impact energy. However, the ductile failure observed in the ballistic plates suggests that the difference in V_{50} is best related to the difference in the size and density of nonmetallic inclusions. It should also be noted that fracture initiation in the ballistic plates was not limited to nonmetallic inclusions. Shear band and crack formation were also observed in

association with porosity. Thus, proper casting design is also a critical consideration in the ballistic performance of these cast steels.

The inclusion content differed principally by size and count between the two test articles. The inclusion concentration shown in Figure 4(c) had chemistries (see Figure 5) that matched those of the Charpy bars (see Figure 9). However, inclusion size and quantity comparison of the Charpy bars (see Figure 10) showed that the non calcium treated alloy has a larger number of inclusions by a ratio exceeding 2:1. The defect content is directly related to the foundry practice in formulating the steel chemistry. Calcium treatment directly impacts the sulfur content. For steels with low active oxygen levels (2 ppm in both alloys) calcium is a late addition that reacts in the melt to form low density sulfides that float out of the melt. However, the resulting surface slag must be immediately removed to prevent reoxidation of the calcium products and subsequent reintroduction of the sulfur.

The high aluminum concentration in these lightweight steels reacts readily with nitrogen and based upon the angular shape and size of the AlN inclusions these nitrides most likely formed in the liquid state. The harmful aspects of these nitrides to fracture may partially be negated by encapsulation with manganese sulfide as shown in Figure 11. The composite structure of MnS and AlN makes the inclusion more spherical and provides a more compliant interface than what might be expected from just the AlN. These complex multiphase inclusions were difficult to separate and classify using the automated software; and as result, the nitrogen chemistry maps show a manganese contribution from the MnS rim and the sulfur chemistry maps show an aluminum

contribution from the AlN core. Thus, the chemical analyses of the inclusions shown in Figures 5 and 9 must be interpreted with this in mind.

Inclusion content alone does not explain the drastic change in fracture morphology observed on the Charpy V-notch specimens. The high phosphorus alloy was more prone to cleavage fracture. Phosphorus has significant toughness effects in manganese steels. Russian researchers (Schul'te, 1964) studied phosphorus' deleterious effects in Hadfield steels, and Howell et al. (Howell, 2009) showed that phosphorus degrades Charpy V-notch toughness in FeMnAlC alloys. Therefore, phosphorus is regarded as the primary culprit responsible for the differences in Charpy V-notch energy and that a higher phosphorus content promotes cleavage in the aged microstructure. Ongoing research Missouri S&T is looking at the effect of phosphorus and aging on the cleavage behavior of κ-carbide.

Regarding the source of phosphorus in these steels, the selection of manganese used during steelmaking may account for some of these differences. The calcium treated alloy was formulated using low phosphorus, electrolytic manganese whereas the non calcium treated alloy was formulated with ferromanganese having a phosphorus content of 0.026%. The use of high phosphorus ferromanganese is not a problem in formulating a typical steel, which will have less than 1.5 weight percent manganese. However, these FeMnAlC based materials will contain as much as 30 weight percent manganese and thus high phosphorus manganese sources should be avoided. Phosphorus bonded refractory materials should also be avoided.

CONCLUSIONS

At equivalent areal densities, FeMnAlC alloys can exceed acceptance criteria of MIL-PRF-32269, and these lightweight steels can achieve greater resistance to the 0.50 caliber FSP than MIL-A-46100 alloys. Oxides, sulfides, phosphorus, and porosity are deleterious to both ballistic and Charpy notch toughness of FeMnAlC alloys. Calcium treating the alloy appears to reduce the total inclusion content and produced a cleaner steel. The reduction in the number of inclusions may account for the observed increases in V_{50} for 0.30 caliber AP and 0.50 caliber FSP. Phosphorus appears to be directly related with the reduced notch toughness and cleavage fracture of these aged materials. Future studies are focused on improving foundry practices to further reduce defect concentrations in cast FeMnAlC alloys and understand the role of phosphorus in producing cleavage fracture.

ACKNOWLEDGEMENTS

This work was supported in part by the Army Research Laboratory, Aberdeen Proving Grounds under the Battelle Memorial Institute agreement W911NF-07-D-0001. The program manager was Dr. E. Chin, Materials Survivability Branch. The authors also gratefully acknowledge the Army Research Office Defense University Research Instrumentation Program (award number W911NF-08-1-0267) for financial support in buying the ASPEX-PICA 1020 SEM.

REFERENCES

Frommeyer, G., Brux, U., 2006: Microstructures and Mechanical Properties of High-Strength Fe-Mn-Al-C Light-Weight TRIPLEX Steels, Steel Research Int., 77, 627-633.

Gooch, William A, 1991: US Patent 5007326

Howell, R. A., Lekakh, S. L., Van Aken, D. C., Richards, V. L., 2008: The Affect of Silicon Content on the Fluidity and Microstructure of Fe-Mn-Al-C Alloys, AFS Transactions.

Leslie, W. C., 1981: The Physical Metallurgy of Steels, 300-303.

Song, S. H., Zhuang, H., Wu, J., Weng, L. Q., Yuan, Z. X., Xi, T. H., 2007: Dependence of ductile-to-brittle transition temperature on phosphorus boundary segregation for a 2.25Cr-1Mo Steel, Mat. Sci. and Eng. A., 486, 433-438.

Wilson, A. D., 1981: Comparing the effect of inclusions on ductility, toughness, and fatigue properties, ASTM Through Thickness Tension Testing of Steel Symposium, St. Louis, MO.

Schul'te, Y., Sherstyuk, A. A., Kubatov, M. I., 1964: The Influence of Phosphorus on the Low-Temperature Embrittlement of High Manganese Steel, Russian Castings Production, 7, 311-313.

Howell, R. A., Lekakh, S. N., Van Aken., D. C., 2009: Quench Sensitivity of a Cast Fe-30Mn-9Al-1Si-0.9C-0.50Mo Lightweight Steel, AIST Proceedings, St. Louis, MO, TBP.

PAPER

5. Phosphorus and Thermal Processing Effects on Charpy V-Notch Impact Toughness of Lightweight Fe-30Mn-9Al-1Si-0.9C-0.5Mo Alloy Steel

R.A. Howell, S. N. Lekakh, J. E. Medvedeva, N. I. Medvedeva, D. C. Van Aken

Army Research Lab

Missouri University of Science and Technology

Department of Materials Science and Engineering

Rolla, MO 65409

Tel.: 573-341-4717

E-mail: dcva@mst.edu

Key Words: Fe-Mn-Al-C, lightweight steel, Charpy, impact toughness, phosphorus, quench sensitivity

Submitted to Metallurgical and Materials Transactions A.

A constitutive model has been established to predict impact toughness of a cast and age hardenable Fe-30Mn-9Al-1Si-0.9C-0.5Mo steel with varying phosphorus content. Five different phosphorus containing Fe-Mn-Al-C alloys were tested in accordance with ASTM E 23 Type-A (Charpy V-notch) to assess quench sensitivity in two heat treated conditions: (1) solution treated and quenched and (2) solution treated, quenched, and aged. Increased cooling rates (determined at 650°C which corresponds to the κ-carbide transformation nose) and the minimization of phosphorus increased notch toughness, decreased ferrite content, and minimized heterogeneous nucleation of κ-carbide on austenite grain boundaries. Room temperature impact energy varied between 115 J/cm^2 for the alloy containing 0.001 wt.% phosphorus (aged 10 hours at 530°C after solution treatment) and 5.4 J/cm^2 for the 0.07 wt.% phosphorus containing alloy in the solution treated condition. Quench rates after solution treatment were 337°C and 0.4°C/s, respectively. A eutectic structure containing a phosphide was observed in the 0.07 wt.% phosphorus containing alloy. *Ab initio* density functional theory was used to calculate the cleavage stress of κ-carbide in an effort to explain the fracture behavior dependence upon quench rate and phosphorus content. Two key discoveries were made: (1) phosphorus will partition to κ-carbide and substitutes for aluminum in the Fe_3AlC structure and (2) phosphorus reduces the {001} cleavage stress.

INTRODUCTION

Lightweight Fe-30Mn-9Al-1Si-0.9C-0.5Mo steel (all chemistries are in weight percent) is under investigation as a replacement to traditional steel chemistries for use in perforated armor[1-3]. These Fe-Mn-Al-C alloys are either fully austenitic or are duplex (austenite and ferrite) after solution treatment, which is usually accomplished at 1000°C[4].

Lowering phosphorus content[5], increasing the solution treatment temperature from 900 to 1050 °C [4], and keeping a nominal 1% silicon content[4] will minimize the ferrite content. Age hardening by spinodal decomposition[6] and precipitation of κ-carbide is observed when aluminum and carbon concentrations exceed 5% and 0.3%, respectively[7]. The *κ*-carbide is an ordered $E2_1$ crystal structure where aluminum atoms occupy 1,0,0 positions, iron and manganese occupy the ½ , ½, 0 face positions, and carbon is located at the central octahedral position (see Figure 1) producing aged microstructures similar to γ-γ' nickel based superalloys[8,9]. The κ-carbide is coherent with the austenite matrix, but little is known of its physical properties[6,7,10]. Addition of aluminum and silicon has the added benefit of lowering the density and the Fe-30Mn-9Al-1Si-0.9C-0.5Mo alloy has a density of 6.7 g/cm^3, which is 12-14% lower than quench and tempered steel. For a more complete review of these age hardening Fe-Mn-Al-C alloys see Howell and Van Aken[11].

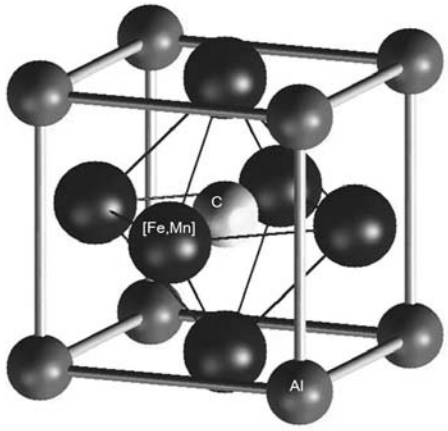

Figure 1. κ-carbide or $(Fe,Mn)_3AlC$ is a cubic perovskite crystal structure ($E2_1$) where aluminum atoms occupying corners of the unit cell, iron and manganese occupy the face centered positions, and carbon sits at the body center, i.e. ½, ½, ½ [9].

High strain rate (3,000 s^{-1}) [12] and ballistic testing (MIL-PRF-32269)[13] of cast Fe-30Mn-9Al-1Si-0.9C-0.5Mo alloys have been reported. The high strain rate testing was performed in compression using a split Hopkinson bar technique and a specific compressive strength that was 28% greater than traditional wrought, quench and tempered, armor steel was reported[12]. Furthermore, ballistic tests against 0.30 caliber armor piercing (AP) projectiles and 0.50 caliber fragmentation simulation projectiles (FSP) revealed differences between two alloys of differing cleanliness and phosphorus content. As expected, the cleaner steel with low phosphorus (0.006% phosphorus) performed the best and exceeded V_{50} ballistic requirements for both MIL-PRF-32269 (AP) and MIL-A-46100 (FSP). In contrast, the 0.043%P alloy failed the MIL-A-46100 (FSP) test and exhibited an 80% reduction in the room temperature notch toughness (Charpy V-notch impact) from 73 J/cm^2 to 13.6 J/cm^2 with a concurrent change in fracture mode from microvoid coalescence to cleavage fracture. Quench sensitivity and phosphorus content has been related to the loss of notch toughness[11]. The study reported here expands upon the quench sensitivity observations and further quantifies the combined effects of phosphorus and cooling rate on Charpy V-notch impact energy. Analyses here correlate the notch toughness with the quench rate after solution treatment, phosphorus content, and the time and temperature used for age hardening. A Jaffe-Hollomon parameter (*JH*) is now incorporated in predicting room temperature notch toughness in order to account for aging temperature T(K) and aging time t (hours). The Jaffe-Hollomon parameter is given as

$$JH=T(\log(t)+C) \qquad \text{(Equation 1)}$$

where C is 20 when time is given in hours[14].

EXPERIMENTAL PROCEDURE

Cast specimens were produced by multiple entities from high purity induction iron, aluminum, ferrosilicon, ferromolybdenum and either electrolytic manganese or ferromanganese in induction furnaces under argon cover. Alloys were cast into olivine or zircon washed silica sand, phenolic no-bake molds and poured without filtering at 100 to 200°C superheat. Solid oxide probes were used to measure dissolved oxygen content after tapping the furnace into the ladle. Heats contained near 2 ppm dissolved oxygen and did not require an additional deoxidation step. A low density coagulant was utilized for deslagging. Chemical analysis after dissolution in perchloric acid was conducted using inductive coupled plasma spectrometry and wavelength dispersive spectrometry and these results are shown in Table 1. All alloying element variations were less than 1 wt.%, but the changes in phosphorus were more than 2 orders of magnitude and ranged from 0.001 to 0.07wt.%. Alloys will be identified by phosphorus content.

Table 1. Chemical Content of Tested Alloys

Fe	Mn	Al	Si	C	Mo	P	Ni	Cr	Cu
Bal	30.42	8.83	1.07	0.90	0.53	0.001	0.05	0.05	<0.05
Bal	30.21	8.85	1.01	0.89	0.31	0.006	<0.05	<0.05	<0.05
Bal	28.22	6.64	1.16	0.94	0.34	0.018	<0.05	<0.05	<0.05
Bal	29.40	7.94	2.02	0.87	0.46	0.030	0.05	0.05	0.08
Bal	29.93	8.24	0.94	0.96	0.36	0.043	0.05	0.06	0.08
Bal	29.11	9.25	1.07	0.90	0.37	0.070	0.09	0.24	0.10

Charpy specimen coupons (nominal size 12.5 mm x 12.5 mm x 55 mm) were cut and solution treated at temperatures from 950°C to 1050°C and cooled to achieve a range

of cooling rates[5]. Cooling rates and aging temperatures were measured directly using embedded or surface welded K-type thermocouples. Cooling rates were calculated at 650°C, which is the nose of the κ-carbide time-temperature-transformation curve. Aged specimens were aged at times greater than 1 hour in furnaces preset to 530°C[5]. After heat treatment, coupons were machined to ASTM E 23 Type-A V-notch Charpy specimens and tested at room temperature in an instrumented Tinius Olsen model 84 Charpy pendulum impact machine with model 892 controller. Hardness was measured by Rockwell C and Vickers Hardness techniques and converted to Brinell hardness for reporting.

Microstructural investigations were carried out by optical microscopy using a differential interference contrast technique and scanning electron microscope (SEM) equipped with an energy dispersive spectrometer (EDS). Fracture surfaces and polished specimens were examined on a Hitachi-S570 SEM at 15 keV and 15 mm working distance. Optical and SEM polished specimens were etched with 2% Nital. Image analysis was conducted using Image-J© computer software. FactSage© thermodynamic software was used for computational phase prediction and predicting segregation during solidification.

RESULTS

In the solution treated condition the room temperature notch toughness ranged from 220 J/cm^2 for the ultra low, 0.001% phosphorus alloy quenched in water at a rate of 337°C/s to a minimum of 5 J/cm^2 for the high 0.07% phosphorus alloy cooled at 0.4°C/s. Charpy V-notch impact energy had a log dependence on cooling rate as shown in Figure 2 for solution treated and quenched 0.006% phosphorus and 0.07% phosphorus alloys.

For a fixed chemistry, the room temperature impact energy is reduced between 30 and 50 J/cm^2 as the cooling rate is decreased by three orders of magnitude. At a fixed cooling rate, the decrease in impact energy is at least 130 J/cm^2 for an order of magnitude increase in phosphorus content, i.e. 0.006% to 0.07% phosphorus. The general trend of decreasing notch toughness with decreasing cooling rate or an increase in phosphorus content was observed for each alloy listed in Table 1.

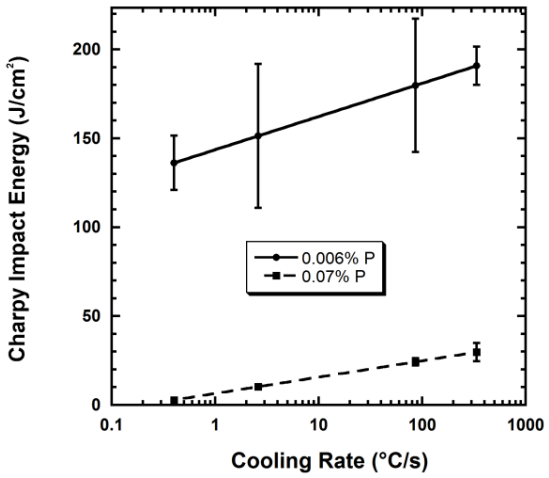

Figure 2. Charpy V-notch impact energy as a function of cooling rate after solution heat treatment. A semi-log plot gives a linear trend where the impact energy increases as the logarithm of cooling rate increases for the 0.006% and 0.07% phosphorus containing alloys.

Age hardening produced an additional loss in notch toughness as shown in Figure 3 for solution treated and oil quenched (58.8°C/s at 650°C) 0.001% and 0.043% phosphorus alloys. Impact energy decreased in a linear fashion with increasing Jaffe-Hollomon parameter (Equation 1); and in general, the notch toughness of 0.043%P alloy was 80 to 90 J/cm^2 lower than the 0.001wt.% phosphorus alloy. Figure 4 shows that

phosphorus decreases Charpy V-notch energy at room temperature and increases hardness for a fixed aging condition of 10 hours at 530°C.

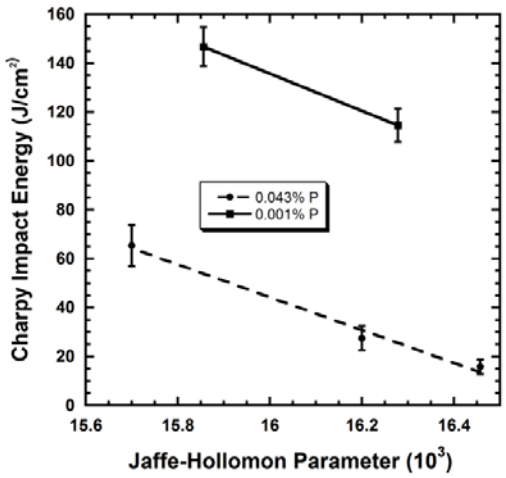

Figure 3. Charpy V-notch impact energy for age hardened 0.001% and 0.043% phosphorus containing alloys that were solution treated and oil quenched (58.8°C/s at 650°C). The Jaffe-Hollomon Parameter was calculated as $T(\log_{10}t+20)/1000$ where the temperature, T, is in K and the aging time, t, is in hours.

The 0.006% phosphorus alloy was used to examine a range of quenching rates and aging conditions. Here the aging temperature was 530±10°C and the aging time ranged from 1 to 25 hours. The measured Charpy V-notch energies at room temperature are plotted in Figure 5 where the impact energy is graphed against both cooling rate and the Jaffe-Hollomon parameter. Increasing quench rate or decreasing the Jaffe-Hollomon parameter produced an increase in the notch toughness. A noticeable change in fracture mode from ductile to brittle cleavage was observed as the phosphorus increased above 0.043%. Cleavage was also observed in the 0.07% phosphorus alloy when in the solution treated condition and water quenched.

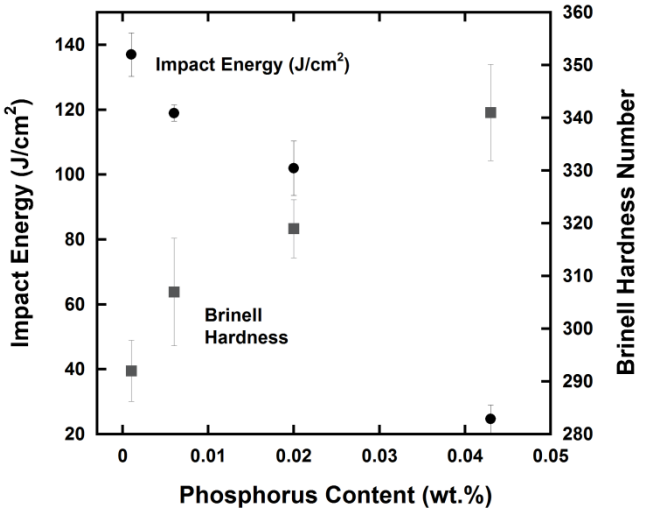

Figure 4. Charpy V-notch impact energy and hardness versus phosphorus content in the solution treated, water quenched, and age hardened (10 hours at 530°C) condition. The figure shows a decrease in impact energy and increased aged hardness with increasing phosphorus content.

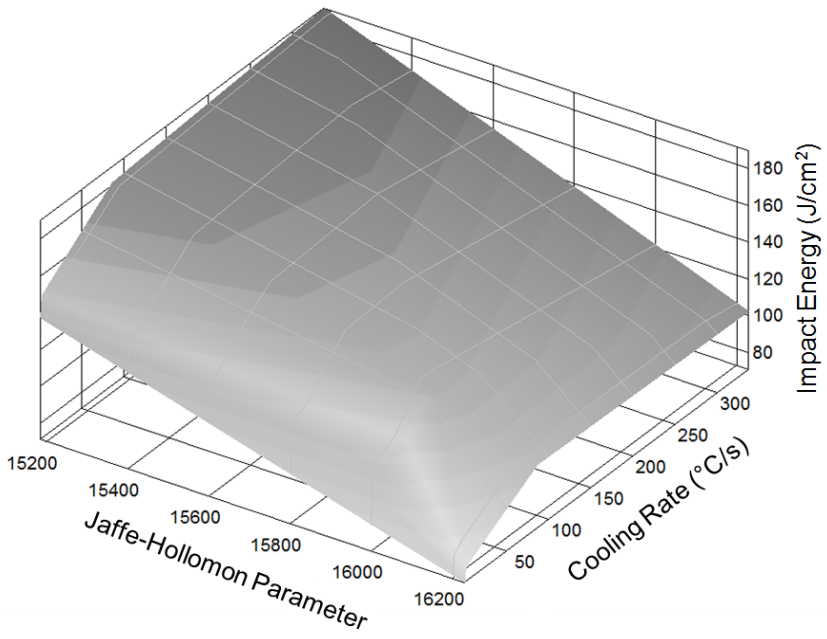

Figure 5. 3-D mapping of impact energy versus Jaffe-Hollomon parameter and cooling rate for 0.006% phosphorus alloy after solution treatment, quenching, and aging.

This behavior was next investigated by examining the temperature dependence of the Charpy V-notch energy for the 0.006% phosphorus alloy (see Figure 6). The test material was solution treated, water quenched, and aged 10 hours at 530°C to produce a Brinell hardness of 307. Impact tests were performed in a temperature range from -40°C to room temperature. The maximum Charpy V-notch impact energy was 115 J/cm^2 at room temperature. As temperature was lowered the material appears to go through a ductile to brittle transition with a lower shelf energy of 39 J/cm^2.

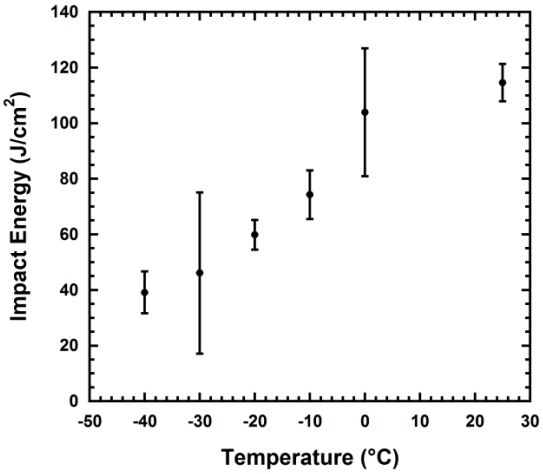

Figure 6. Charpy V-notch impact energy for the 0.006% phosphorus alloy plotted as a function of test temperature showing a ductile to brittle transition. The alloy was solution treated, water quenched (337°C/s cooling rate), and aged 10 hours at 530°C.

In general, the fracture mode at room temperature transitioned from ductile microvoid coalescence to brittle transgranular cleavage with increasing phosphorus content, decreasing quench rate, and increased aging time.

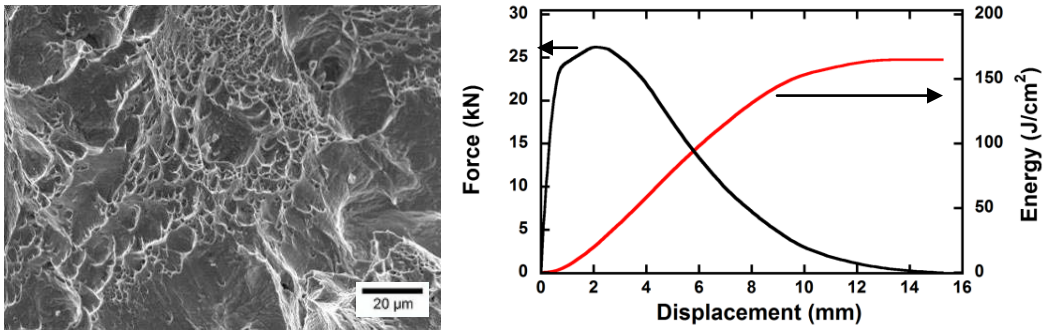

(a) (b)

Figure 7. (a) Ductile fracture of solution treated and cooled at 337°C/s alloy containing 0.006% phosphorus (similar fracture was observed when quenched in oil at 58.8°C/s) and (b) instrumented impact test showing force and energy absorbed with tup displacement.

Ductile fracture was observed for the 0.006% and 0.001% phosphorus containing alloys in the solution treated condition for cooling rates at or above 58.8°C/s. Figure 7(a) shows ductile fracture of a 337°C/s cooled 0.006% phosphorus alloy. A type III ductile failure[15] is shown in Figure 7(b) and is characterized by yield point load behavior, work hardening to a maximum load and followed by a steady and continuous negative slope in the force versus tup displacement curve (or force time curve), which is indicative of void growth during fracture[15].

Transgranular cleavage was the dominant fracture mode in high phosphorus alloys and this was true for solution treated material that was quenched at the highest rate (337°C/s). Figure 8 shows a cleavage fracture mode observed for the 0.07% phosphorus alloy in the solution treated and water quenched condition. One of the striking features of this fracture is a dendritic looking pattern where the cleavage fracture appears to follow the main trunk and secondary arms of the dendrite.

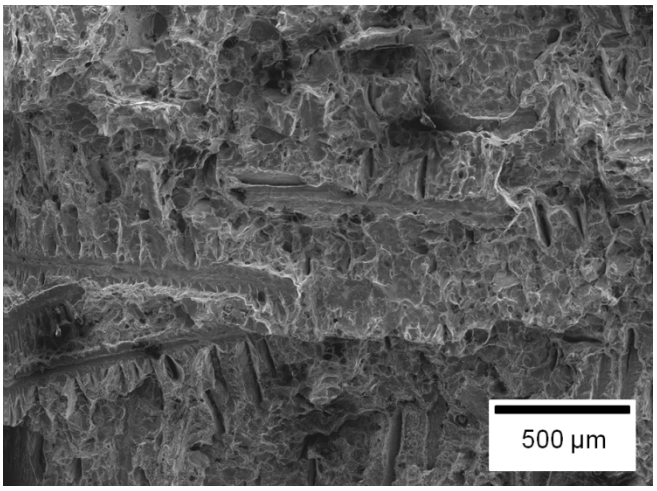

Figure 8. The fracture surface of a 0.07% phosphorus containing alloy solution treated and water quenched (337°C/s) is dominated by cleavage fracture. The cleavage fracture appears to follow the dendrites and in some cases both the main dendrite trunk and secondary arms can be distinguished. The direction of the tup travel is from the bottom to the top of the image.

A combination of ductile and transgranular quasi-cleavage fracture was observed for the 0.006% phosphorus containing alloy in both the solution treated condition (0.9°C/s < $\dot{T}$ < 58.8°C/s) and after age hardening 10 hours at 530°C (see Figure 9). Ductile and transgranular cleavage was also observed for higher phosphorus containing alloys in the solution treated condition for cooling rates greater than 58.8°C/s. Brittle cleavage fracture dominated all other conditions, principally for material cooled at or less than 2°C/s after solution treatment. The 0.07% P alloy, in particular, showed some evidence of intergranular fracture for materials quenched at slower rates after solution treatment, e.g. 0.9°C/s (see Figure 10).

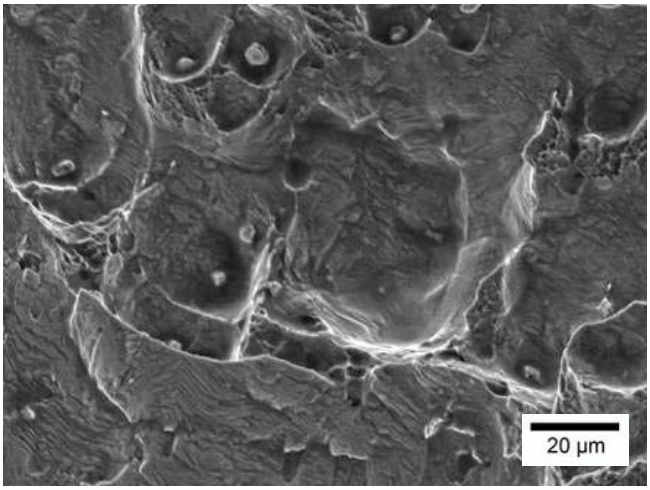

Figure 9. An example of quasi-cleavage fracture where cracks have nucleated at non-metallic inclusions and propagated through the grain structure in a transgranular fashion. This fracture was from the 0.006% phosphorus alloy that was solution treated, water quenched, and aged 10 hours at 530°C. The impact test was performed at 25°C and the direction of the tup travel was from bottom to the top of the image.

Intergranular cracking had not been observed nor reported from previous Charpy V-notch impact data collected from cast materials,[14] since the testing until now had been conducted on water quenched ($\dot{T}$ > 58.8°C/s) and aged material with phosphorus contents less than 0.07% . Confirmation of the intergranular cracking was conducted by polishing into the fracture face and obtaining a grain orientation mapping using an electron backscatter detector (EBSD). Approximately 500µm was removed from the surface during polishing, which left the cracks in question still visible (see Figure 11). A comparison between the EBSD grain map and the cracking shows that indeed the cracks were intergranular. Voids shown in the micrographs are really portions of the original fracture surface that were not removed by polishing and these areas contain Bakelite mounting material.

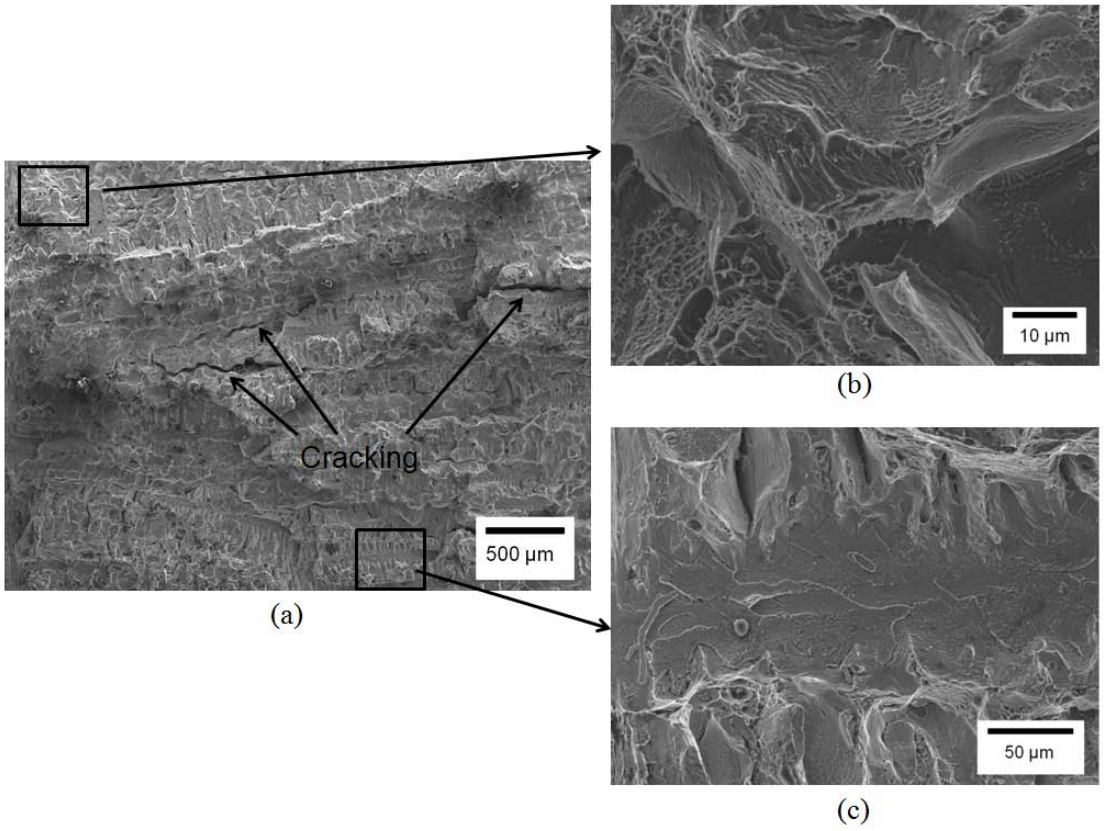

Figure 10. Room temperature fractures from a 0.07% phosphorus alloy that was slow cooled after solution treatment at a rate of 0.9°C/s. Cracks shown in (a) appear intergranular. Transgranular fracture features range from (b) quasi-cleavage to (c) cleavage. Images are again arranged where the tup travel is from bottom to top of the images.

Attempts to determine the cleavage plane normal using EBSD grain orientation mapping were unsuccessful. However, a {100} cleavage plane can be inferred from the dendritic patterns produced by the fracture path.

In many cases the cleavage fracture followed the main branch and secondary dendrite arms to produce an orthogonal pattern, which would be observed by sectioning the main dendrite trunk along <100> and parallel to {010}. Secondary cracks were also observed, which followed the main dendrite trunk parallel to <100>. Figure 12 shows an

example of <100> secondary cracks from a 0.043% phosphorus alloy that was water quenched after solution treatment and aged 10 hours at 530°C.

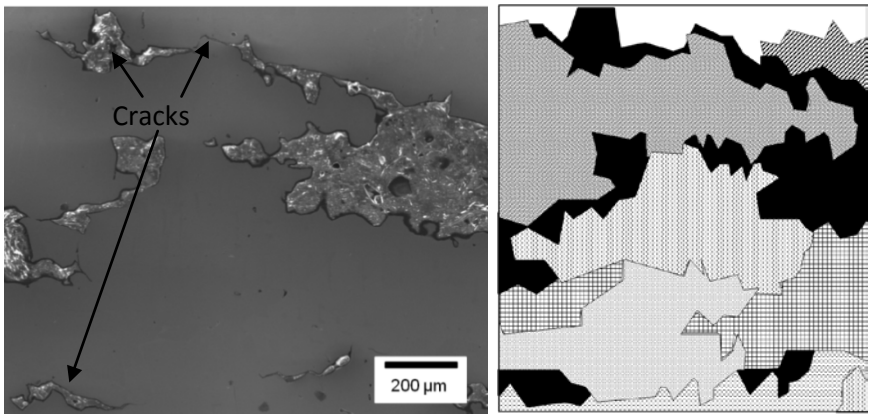

(a) (b)

Figure 11. A secondary electron image of a polished plane (a) from a Charpy V-notch specimen where approximately 500 µm of the fracture surface was removed. Arrows in (a) locate suspected intergranular cracks. Incomplete polishing left areas of the fracture that were filled with bakelite mounting material. Orientation mapping of the grains is shown in (b) and clearly shows that the suspect cracks are intergranular.

A transition from microvoid coalescence to cleavage fracture as being indicative of a ductile to brittle transition was verified in the 0.001% phosphorus alloy, which had been solution treated, water quenched, and aged 10 hours at 530°C. Fracture specimens were obtained from samples that were used to produce the temperature dependent impact energy data shown in Figure 6. Fractography of these specimens show that microvoid coalescence dominates at room temperature (see Figure 13). At -10°C, a mixed mode of ductile and quasi-cleavage fracture is observed, and at -40°C, cleavage is the dominant fracture mode.

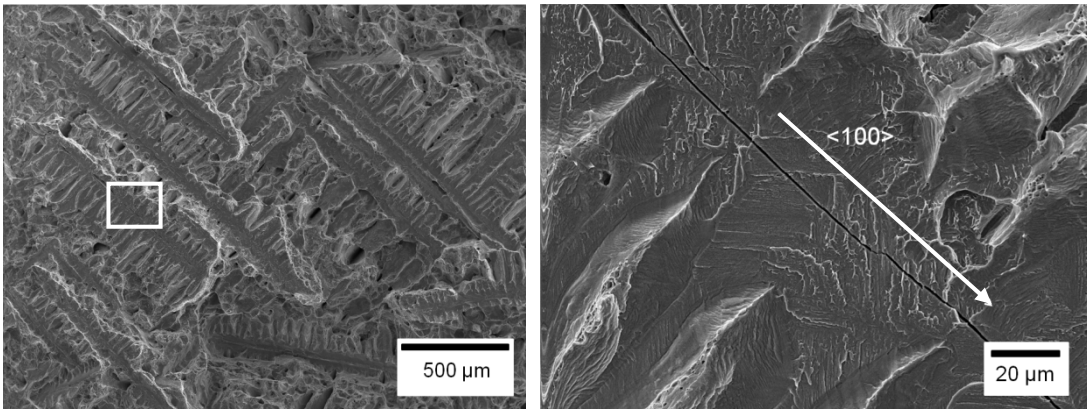

(a) (b)

Figure 12. Low magnification of transgranular cleavage fracture (a) of a solution treated, water quenched and aged high 0.043% phosphorus alloy reveals the alloy's dendritic microstructure. A crack is shown (b) oblique to the fracture surface in the <100> direction of the dendrite. The tup direction was from the left to the right side of the images. White rectangular box depicts location of the higher magnified image.

Metallographic analysis of the various alloys indicated that phosphorus concentration also affected the amount of ferrite and intergranular precipitation during quenching. Minimal ferrite content was observed in the 0.001% and 0.006% phosphorus alloys after water quenching from the solution treatment temperature. Isolated islands of ferrite were observed in the 0.006% phosphorus alloy, but the overall ferrite content was small and on the order of 1%. Decreasing the quench rate below 59°C/s produced a delineation of the austenite grain boundaries as shown in Figure 14(b). At a cooling rate of 2°C/s the austenite grain boundaries polished in relief indicating a greater hardness than the grain interior; however, no evidence of a precipitate was visible using the differential interference contrast technique. Discrete grain boundary precipitation became apparent after age hardening as shown in Figure 14(c).

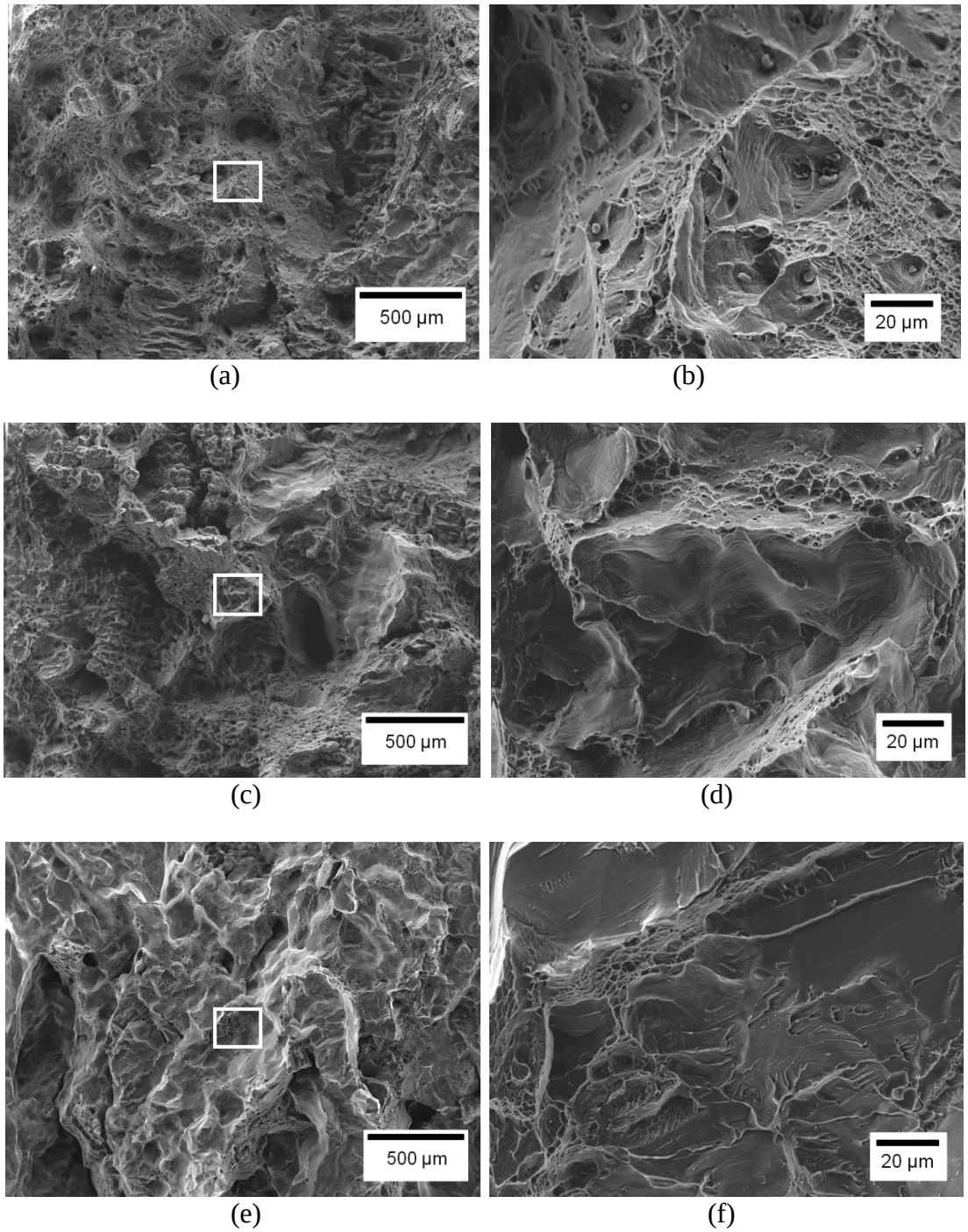

Figure 13. Low and high magnification images illustrate the temperature dependent transition from ductile to brittle fracture (by transgranular cleavage) of the solution treated, water quenched and aged 0.001% phosphorus containing alloy. Ductile failure (a and b) dominate room temperature failure. Mixed mode ductile and cleavage fracture (b and c) are observed at -10°C. Cleavage fracture dominates at -40°C (e and f). The tup direction of travel was from the left to the right side of the images. White rectangular boxes depict location of the higher magnified images.

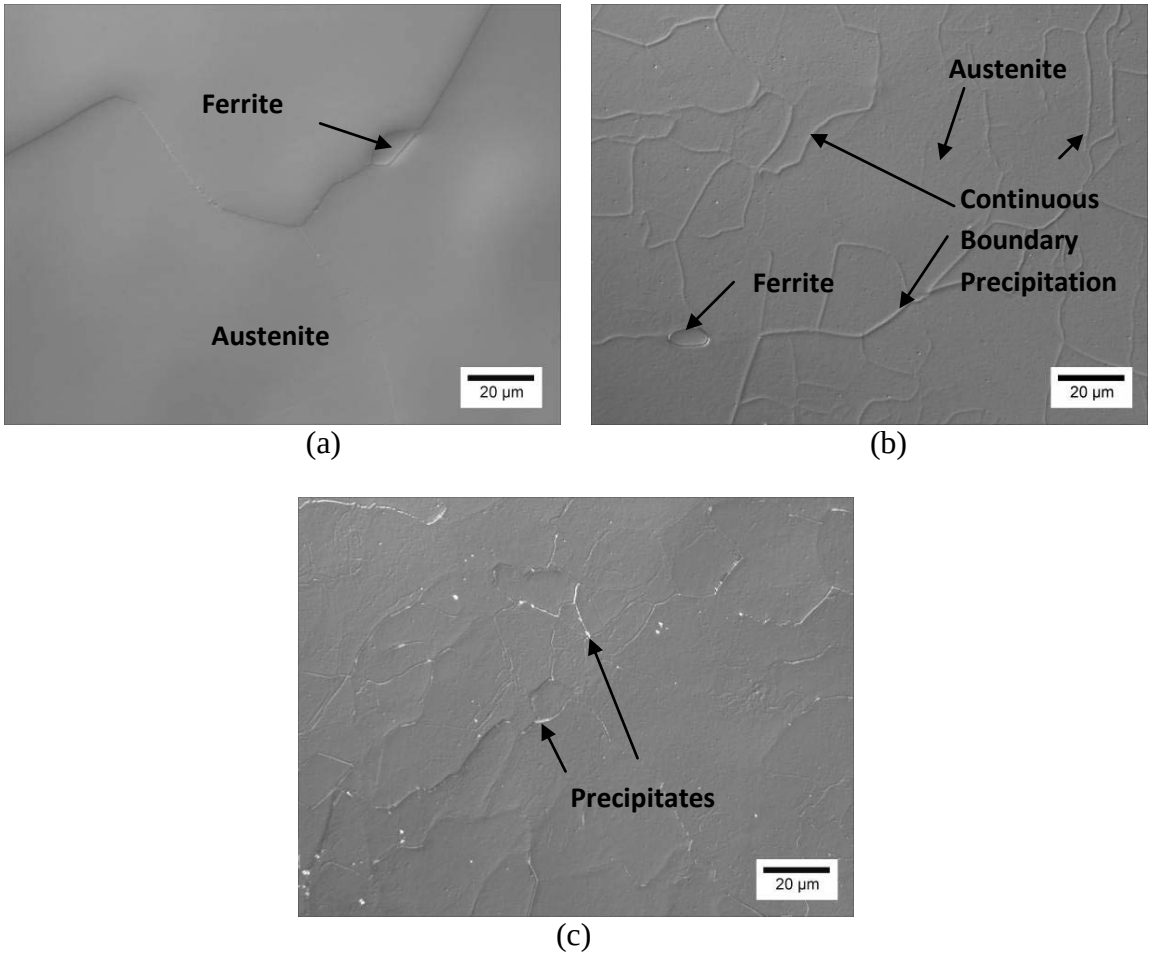

Figure 14. Optical images of a 0.006% phosphorus alloy using differential interference contrast for three different heat treat conditions: (a) solution treated and water quenched at 337°C/s showing an austenitic structure with small islands of ferrite, (b) solution treated and air cooled at 0.9°C/s showing primary austenite, ferrite, and polishing relief of both austenite grain boundaries and possibly subgrain boundaries, and (c) solution treated, water quenched (337°C/s), and aged for 10 hours 530°C with precipitates on dendrite boundaries.

By contrast, the 0.07% phosphorus alloy cooled at 337°C/s contained 7% ferrite (see Figure 15). Decreasing the cooling rate to 0.4°C/s produced visible precipitation in both the matrix and along dendrite boundaries. Precipitate free zones were also observed along the austenite grain boundaries where large precipitates formed as shown in Figure 15(b).

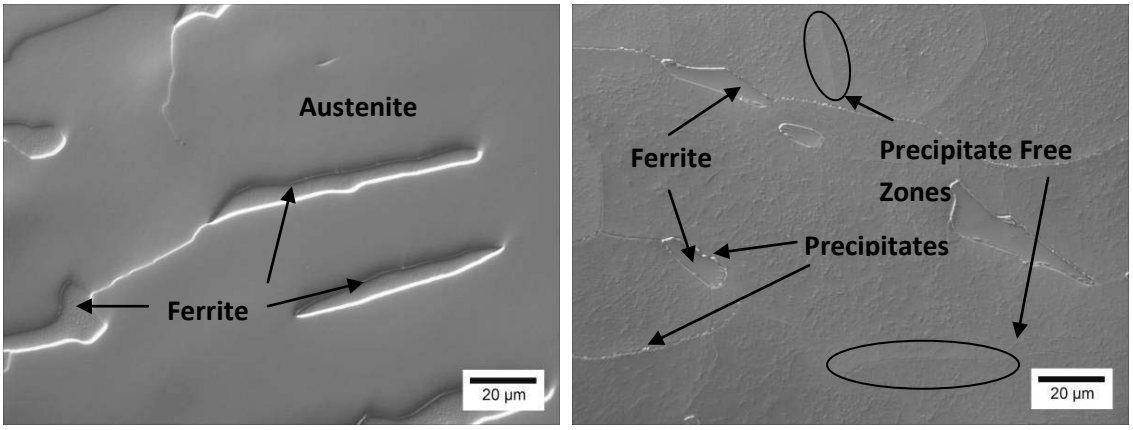

(a) (b)

Figure 15. Differential interference contrast images for the 0.07% phosphorus alloy. Microstructures are shown in two heat treat conditions: (a) water quenched after solution treatment showing a volume increase in ferrite content, and (b) solution treated and slow cooled at a rate of 0.4°C/s to produce precipitation along prior austenite grain boundaries and within the matrix. Precipitate contrast in the matrix also reveals precipitate free zones.

A phosphide containing eutectic structure was also observed in the 0.07% phosphorus alloy and this structure is shown in Figure 16. An EDS scan revealed the structure to be rich in sulfur, silicon, and manganese, but deficient in iron and aluminum. A phosphorus map of the eutectic is shown in Figure 16(b). The phosphide containing eutectic formed interdendritically. Microhardness measurements of the eutectic were 520 BHN while the surrounding matrix was 294 BHN for the water quenched, solution treated material. These eutectic structures are brittle as shown in Figure 17, which was found in close to the fracture surface in a metallographically prepared Charpy V-notch bar. The image plane was polished parallel within 500 µm of the fracture surface.

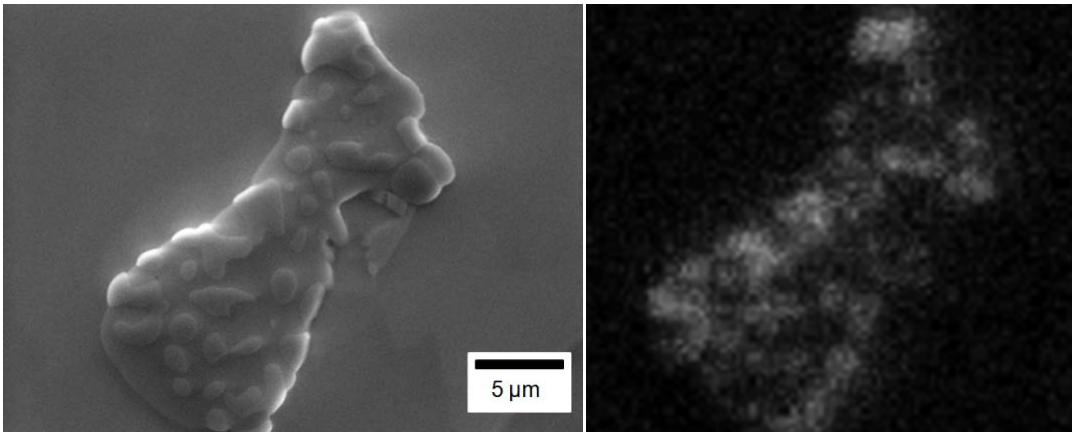

(a) (b)

Figure 16. A phosphide eutectic (a) was observed in an interdendritic region of the 0.07% phosphorus containing alloy's microstructure and (b) EDS mapping reveals the phosphorus rich phases contained within the structure.

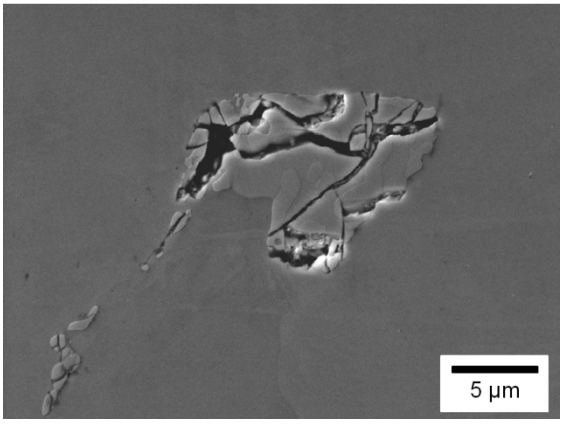

Figure 17. Charpy V-notch impact testing caused crack formation through the hard phosphide phase of a 0.07% phosphorus containing alloy. The polish plane is parallel to and within 500 µm of the fracture surface. The motion of the tup was from the bottom to the top of the image.

Phosphorus segregation was modeled using a thermodynamic free energy minimization software package (FactSage©) for the nominal Fe-30Mn-9Al-1Si-0.9C-0.5Mo composition for three phosphorus levels. The process used involves incremental

decreases in temperature where the solid phase chemistry is removed and the solidification of the remaining liquid is then modeled until the chemistry of the remaining liquid is computed. Figure 18 shows the results of this study, which is similar to that obtained using the Scheil equation[16]. These computations predict a large phosphorus concentration in the interdendritic liquid for phosphorus contents greater than 0.01%. Upon solidification, thermodynamic modeling predicts that the remaining composition will favor the Fe_2P crystal structure.

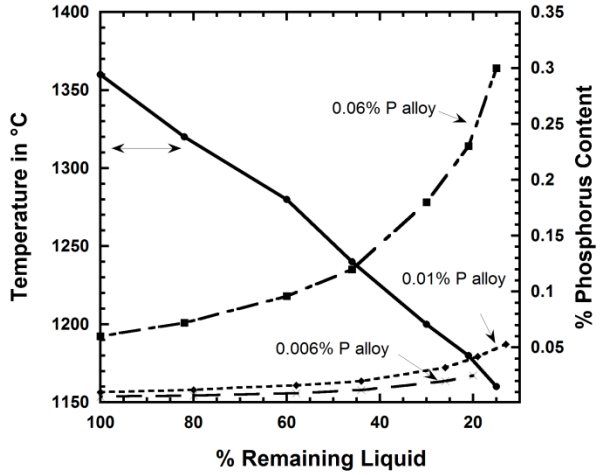

Figure 18. Scheil modeling of the remaining liquid after the start of solidification for three different phosphorus containing alloys (0.006%, 0.01%, and 0.06%) shows phosphorus content rise in the remaining liquid.

DISCUSSION

Phosphorus content had the single greatest degrading effect on notch toughness; however there also appears to be a quench rate sensitivity and an influence of age hardening. A constitutive model was constructed using impact data from end quenched plates produced from the 0.006% and 0.043% phosphorus cast alloys. An empirical fit of the data shows that Charpy impact energy (*ST*, J/cm^2) in solution treated and cooled specimens follows the general equation:

$$ST = F_1 \times Ln(CR) + F_2 \qquad \text{(Equation 2)}$$

where: *CR* (°C/s) is the cooling rate, F_1 (J·s/°C) and F_2 (J) are the functions of phosphorus content given by the equations:

$$F_1 = -64.23 \times (wt.\%\ P) + 8.4954 \qquad \text{(Equation 3)}$$

$$F_2 = -2143 \times (wt.\%\ P) + 156.5 \qquad \text{(Equation 4)}$$

The phosphorus embrittlement effects given by equations for F_1 and F_2 show that at a given cooling rate, impact energy decreases 13% per 0.01 wt.% increase in the phosphorus content. The *ST* value calculated from Equation 2 defines a starting condition, which will then be used to model the effect of precipitation hardening. The final aged toughness, *AT*, will link age hardening kinetics via the Jaffe-Hollomon parameter (Equation 1), the phosphorus content, and the cooling rate after age hardening. The differences observed due to phosphorus content and cooling rates were accounted for by making the Jaffe-Hollomon equation (*JH*) constants functions of phosphorus and cooling rate:

$$AT = F_3 \cdot Log(JH) + F_4 \qquad \text{(Equation 5)}$$

where F_3 and F_4 are functions of the initial condition ST determined by Equation 2, so that $F_3\ (J)$ and $F_4\ (J)$ become:

$$F_3 = 772.96 \times Ln(ST) - 7{,}823.4 \qquad \text{(Equation 6)}$$

$$F_4 = -3{,}126.8 \times Ln(ST) + 32{,}380 \qquad \text{(Equation 7)}$$

Figure 19 shows a plot of all of the measured room temperature Charpy V-notch impact energies versus Equation 5. The predicted energy value from Equation 5 was found to be within the standard deviation of the mean values for each condition plotted. Thus it is possible to show that the notch toughness of the Fe-30Mn-9Al-1Si-0.9C-0.5Mo alloy is quench sensitive, adversely affected by phosphorus, and decreases with age hardening, which suggests that phosphorus may be influencing the fracture behavior of κ-carbide.

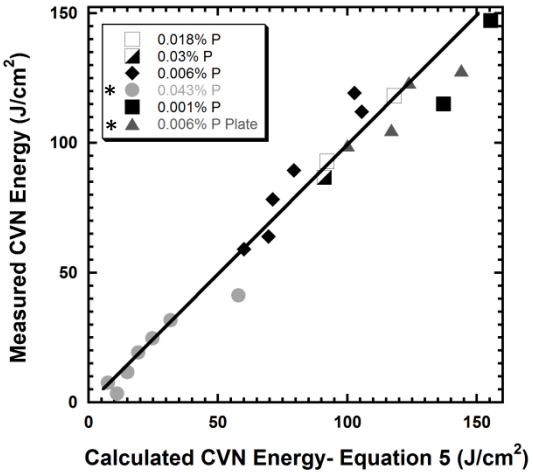

Figure 19. Measured Charpy V-Notch impact energy is plotted against Equation 5. The asterisked (*) phosphorus containing alloys were used to generate the model. All other compositional data was plotted afterword to confirm the model.

Phosphorus embrittlement in low alloy steel[17] and manganese steels[18,19] is well known, but had not been previously reported for age hardenable Fe-Mn-Al-C steels. To help explain the phenomenon, a first principles modeling was performed in two steps. Step one modeled solution enthalpy energies of bulk crystalline and carbide stability of pure and phosphorus doped crystals. This was done in order to determine preferred phosphorus location within the austenite and κ-carbide microstructure. Solution enthalpies were modeled using the projector-augmented waves method as implemented in the Vienna *ab initio* simulation package[20,21] with the generalized gradient approximation (GGA) for the exchange-correlation energy[22]. To find the preferable site for phosphorus in bulk κ-carbide (simulated as stoichiometric Fe_3AlC), solution enthalpies for the substitutional phosphorus at iron, aluminum, or carbon sites were compared using a 40-atom (2x2x2) supercell. The solution enthalpy was estimated as a total energy difference between supercell with phosphorus ($Fe_{23}Al_8C_8P$, $Fe_{24}Al_7C_8P$ and $Fe_{24}Al_8C_7P$ for the iron, aluminum, and carbon substitutions, respectively) and the ideal supercell ($Fe_{24}Al_8C_8$). Calculations were performed for metals in their ground states to determine the total energy.

Energetically preferable sites for phosphorus in α-Fe an d γ-Fe showed substitutional solution enthalpies of 1.65 eV and 2.43 eV, respectively and are in agreement with previous calculations[23]. Interstitial phosphorus solution enthalpy within the α-Fe and γ-Fe were 3 eV greater for both phases. The calculated ground state of Fe_3AlC was ferromagnetic with an equilibrium lattice parameter of 3.753 Å, which is in agreement with experimental data[23] and previous theoretical results[25,26]. Solution enthalpies are positive for all Fe_3AlC substitutions at 2.40, 0.67, and 1.22 eV for

phosphorus in iron, aluminum and carbon sites, respectively. Therefore phosphorus substitution for aluminum is favored in Fe_3AlC over less stable substitution for carbon and iron in the Fe_3AlC structure or even matrix iron atoms, which should result in a (001) Fe_3AlC cleavage plane.

Step two modeled cleavage fracture based on phosphorus location, assuming that crack nucleation occurred in plane with the phosphorus defect. Ideal cleavage characteristics were simulated by the density functional theory[27]. This approach is based on the Griffith model in that intrinsic cleavage fracture occurs when the applied stress exceeds the ideal cleavage energy (G_c), defined as the energy necessary to separate the crystal into two semi-infinite parts. The ideal cleavage energy is dependent on the separation distance between the two crystal slabs and modeled using the universal binding energy relation (UBER) [28, 29]:

$$G_C(x) = G_C[1-(1+x)\,exp(-x)],\ x=u/\lambda \qquad \text{(Equation 8)}$$

where u is the length and λ defines the separation distance. The separation distance pertains to the two newly created fracture surfaces such that surface energy (γ_S) is equal to one half of the cleavage energy ($G_C = 2\ \gamma_S$) due to the applied stress. The ideal cleavage stress (σ) may be calculated as $\sigma(x) = dG_C(x)/dx$ so that the parameter λ corresponds to the maximum stress σ_{max}. To model the cleavage, two slabs each consisting of twelve layers (1x1x6 supercells) and varied in their separation distance obtained by a translation along the z-direction. No relaxation was allowed for the atomic positions in order to obtain ideal brittle cleavage.

The UBER fit results for pure Fe_3AlC gave a cleavage energy of G_C=5.04 J/m^2 and an ideal stress σ_{max}=40 GPa with the maximum stress and separation distance λ at

0.46 Å, which corresponds to an ideal strain of 12.3%. The UBER fit results for a phosphorus doped Fe_3AlC supercell showed that the ideal cleavage energy (2.76 J/m^2) and ideal cleavage stress (22 GPa) were less than half the values of pure Fe_3AlC. Cleavage energies ($G_C(x)$) and stress ($\sigma(x)$) as a function cleavage separation between the (001) layers in Fe_3AlC are shown in Figure 20, where x=0 corresponds to the equilibrium interlayer distance in bulk. The phosphorus substitution of carbon was included with the ideal Fe_3AlC and phosphorus substitution of aluminum modeling data even though it is energetically less favorable. Thus, the modeling shows that the presence of phosphorus in bulk Fe_3AlC favors brittle cleavage along the (001) plane.

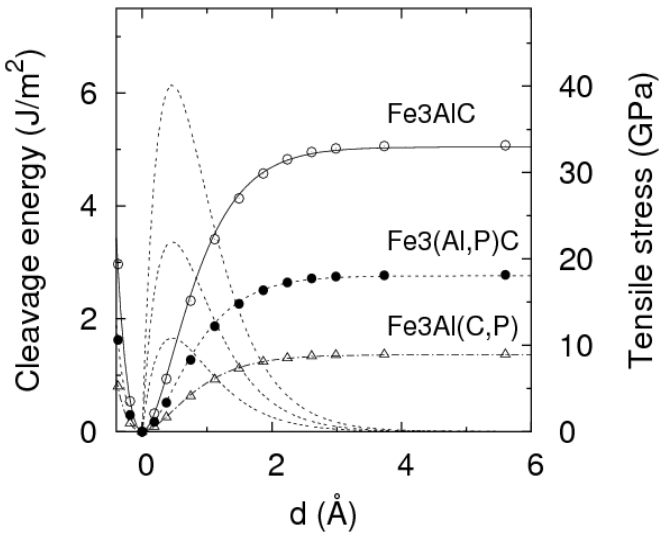

Figure 20. Cleavage energy and tensile strength *ab initio* calculations as a function of separation distance for κ-carbide with and without phosphorus substitution for aluminum.

The role of phosphorus and its relationship to quench sensitivity can now be clearly defined. The lower solution enthalpy of phosphorus when substituted in κ-

carbide would enhance the precipitation kinetics of κ-carbide. At sufficiently low quench rates after solution treatment and when combined with segregation, κ-carbide precipitation along prior austenite grain boundaries would be expected; and, is clearly shown in Figure 14(b). The intergranular fracture in the 0.07% phosphorus alloy may be related to a combination of κ-carbide precipitation, the interdendritic phosphide containing eutectic or simply the segregation of the phosphorus to the grain interface with subsequent lowering of the cohesive strength. The exact cause of the intergranular fracture was not the primary focus of this study.

As the amount and size of κ-carbide increases the propensity of cleavage fracture increased and there is sufficient evidence that the fracture plane is {100} as shown by first principle calculation and experimentally in Figure 12. Literature has also shown that there is a relationship between κ-carbide coarsening and transgranular cleavage[30] or heterogeneous precipitation (B2, DO_3, or κ-carbide) along austenite grain boundaries[31]. What is yet unclear is the role of high manganese and aluminum in the cleavage fracture of austenite and this will be the subject of a future investigation.

CONCLUSIONS

Impact toughness of nominal Fe-30Mn-9Al-1Si-0.9C-0.5Mo alloys has been modeled as a function of phosphorus content, cooling rate, and precipitation hardening. Phosphorus contributes a 13% drop in toughness for a 0.01 wt.% increase in phosphorus. First principle calculations show that phosphorus substitutes directly for aluminum in the κ-carbide structure and lowers the cleavage stress by 50%. However, Charpy V-notch impact energies greater than 100 J/cm^2 can be obtained for age hardened, low phosphorus alloys (<0.02% phosphorus) when quenched at or greater than 58.8°C/s. The highest

aged impact toughness was obtained in the ultra low 0.001% phosphorus containing alloy that was solution treated and water quenched at 337°C/s prior to aging. Large interdendritic phosphides were also discovered in alloys with phosphorus content greater than 0.03% and these eutectic structures show a brittle fracture character and may contribute to lower notch toughness.

ACKNOWLEDGEMENTS

This research was funded by the Army Research Laboratory and is monitored by Dr. Ernest Chin of Aberdeen Proving Grounds. MAJ Ryan A. Howell would also like to acknowledge financial assistance provided by Army Acquisition Corps and the Army Research and Development Command for his Ph.D. studies at the Missouri University of Science and Technology. Nadya Medvedeva also acknowledges the support by RFFI (the Russian Basic Research Foundation, Grant 09-03-00070-a).

REFERENCES

1. MIL-PRF-32269, Military Performance Specification for Perforated Homogeneous Armor.
2. MIL-A-12560, Military Specification for Armor Plate, Steel, Homogeneous.
3. MIL-A-46100, Military Specification for Armor Plate, Steel, High-Hardness.
4. R. A. Howell, S. L. Lekakh, S. L., D. C. Van Aken, D. C. and V. L. Richards, V. L., AFS Trans., 2008, vol. 116, pp. 867-78.
5. R. A. Howell, S. L. Lekakh, D. C. Van Aken, AIST Trans., TBD.
6. K. H. Han and W. K. Choo, 1989, Met. Trans. A., vol. 20A, pp. 205-14.
7. K. Sato, T. Kazuhiro and Y. Inoue, 1988, Scripta Met., vol. 22, pp. 899-902.
8. G. Frommeyer and U. Brux, 2006, Steel Research Int., vol. 77, pp. 627-633.
9. L.J. Huetter, H.H Stadelmaier, 1958, Acta Metallurgica, vol. 6, pp. 367-370.

10. K. H. Han, W. K. Choo, D. Y. Choi, and S. P. Hong, 1987, TMS-AIME, pp. 91-106.

11. R. A. Howell and D. C. Van Aken, J. AIST, 2009, vol. 6, no. 4, pp. 192-213.

12. R. A. Howell, T. Weerasooriya and D. C. Van Aken, AFS Trans., 2009, vol. 117, pp. 751-63.

13. R. A. Howell, J. M. Montgomery and D. C. Van Aken, J. AIST, 2009, TBD.

14. J. H. Hollomon, L. D. Jaffe, Trans. AIME, 1945, pp. 162−223.

15. P. R. Sreenivasan, C. G. Shastry, M. D. Mathew, K. Bhanu Sankara Rao and S. L. Mannan, J. Eng. Mat. Tech., 2003, vol. 125, pp. 225-33.

16. E**.** Scheil**,** Z**.** Metallkunde, 1942, vol. 34, p. 70.

17. W. C. Leslie, *The Physical Metallurgy of Steels*, Hemisphere Publishing, 1981.

18. Y. A. Schulte, A. A. Sherstyuk and M. I. Kurbatov, Russian Castings Prod., 1964, Issue 7, pp. 311-13.

19. L. Zhong, W. Ruqian, A. J. Freeman and G. B. Olson, G. B., Ph. Rev. B, 1997, vol. 55, pp. 133-37.

20. G. Kresse and J. Hafner, Phys. Rev. B, 1993, vol. 47, p. 558.

21. G. Kresse and J. Furthmuller, Phys. Rev. B, 1996, vol. 54, p. 11,169.

22. J. P. Perdew and Y. Wang, Phys. Rev. B, 1992, vol. 45, p. 13,244.

23. C. Domain and C. S. Becquart, Phys. Rev. B, 2005, vol. 71, p. 214,109.

24. P. Willars, A. Prince and H. Okamoto, Handbook of Ternary Alloy Phase Diagrams, 1995, vol. 3.

25. M. Ruda, D. Farkas, and J. Abriata, Scr.Mater., 2002, vol. 46, p. 349.

26. A. Kellou, T. Grosdidier, J.M. Raulot, and H.Aurog, Phys. Stat. Sol. B, vol. 245, p. 750.

27. W. Kohn and L. J. Sham, Phys. Rev. A, 1965, vol. 140, p. 1133.

28. A. Banerjea, J. R. Smith, Phys. Rev. B, 1988, vol. 37, p. 6632.

29. J. H. Rose, J. R. Smith, J. Ferrante, Phys. Rev. B, 1983, vol. 28, p. 1835.

30. G.E. Hale and A. J. Baker, Conf. on Alt. Alloying for Env. Res. New Orleans, LA., 1986.

31. O. Acselrad, I. S. Kalashnikov, E. M. Silva, R. A. Simao, C. A. Achete and L. C. Pereira, Met. Trans. A., 2002, vol. 33A, pp. 3569-3572.

2. CONCLUSIONS

The mission to select and develop a lighter and castable alloy for MIL-PRF-32269 class II homogeneous perforated armor was successful. The greatest impact from this work is that the cast Fe-30Mn-9Al-1Si-0.9C-0.5Mo alloy attained comparable ballistic performance as Rolled Homogenous Armor (RHA) without the need for a grain refined wrought microstructure (mass efficiency (E_M) comparable to RHA against 0.30 caliber armor piercing projectile). This dispels the myths and perception that all castings are inferior to wrought material for armor and that a worked and refined microstructure is a requirement for an armor alloy. The process set forth tying processing to quasi-static and dynamic properties in this thesis to guide alloy design and to achieve the ballistic objective (by investigating castability, thermal processing techniques and assessing related structure properties) was validated. The documentation contained herein provides potential manufacturers the critical information needed to produce this alloy. Related to the research is the advancement towards the Fe-Mn-Al-C composition's recognition as a feasible, if not suitable, casting alloy. Receiving such designation is important in communicating to foundries, fabrication facilities, and end users for a broad range of structural and armor applications. The technical highlights from the work presented are as follows:

1. Silicon does not increase fluidity as a function of superheat, but it lowers liquidus and solidus temperatures. At approximately 1% silicon content, ferrite is minimized, and the addition of silicon prevents β-Mn. This established a range of Si content to control ferrite content for targeted properties.

2. Solution treating at 1050°C and aging at 530°C was sufficient to produce the appropriate range of hardness values to evaluate the system and refine the heat treatment of the ballistic samples.

3. Yield and tensile strengths in excess of 1,000 MPa in the aged condition are possible with a cast dendritic microstructure without the need of replicating the wrought microstructure.

4. Specific high-strain-rate compressive strengths are greater than wrought MIL-A-12560 rolled homogeneous armor (RHA). Post analysis showed internal voids as crack initiation sites implicating higher strengths are possible via subsequent thermomechanical treatment.

5. The alloy system work hardens thus has the propensity to resist adiabatic shear failure, a typical pre-mature failure mode observed during high-strain-rate and ballistic loading.

6. The alloy passes MIL-PRF-32269 ballistic and final threat testing.

7. Presence of phosphorus in the alloy is deleterious to Charpy impact toughness. *Ab initio* calculation showed substitution of aluminum by phosphorus in κ-carbide is the primary candidate for this embrittlement. In addition to phosphorus content, low critical cooling rates and high aging temperature-time parameters also contribute to lower Charpy impact toughness. The reduction in impact toughness was shown to correlate well to decrease ballistic performance against fragmentation simulation projectile (FSP).

Since the work on this system did not include ballistic optimization, areas of recommended future research include (but are not limited to) carbide strengthening, increasing aluminum content for further weight reduction, grain refinement, heat

treatment and phosphorus mitigation. Other areas of recommended research include structure and property effects of aluminum and manganese additions, studies to refine existing thermodynamic databases reflecting known phase constitution, carbide additives (e.g. niobium carbide) for further strengthening, wear characterization, machinability studies, mold-molten metal interactions and compatibilities, shell mold and pouring temperature relations, continuous casting and thermomechanical processing.

Lastly, discussion items and recommendations during the oral defense were as follows:

1. Chemical Analysis Technique

Concerns: All chemical analysis for this thesis was conducted by inductively coupled plasma verified with wavelength dispersive spectrometer analysis and not arc spectrometer.

Discussion: Arc spectrometers are representative of what is typically used at foundries due to lower system cost, processing time per sample and ease of operator usage. Accuracy of arc spectrometers for chemical analysis is acceptable. Arc spectrometer standards are not readily available and prevented their usage for this alloy system during thesis research. To control chemistry in future production, collaborative effort with NIST, SFS and other appropriate agencies will be established to develop commercial production standards .

2. Hardness Measurements

Concern: The Fe-Mn-Al-C system has not been investigated for hardness conversion appropriate for ASTM E140.

Discussion: Rockwell B and Rockwell C techniques were converted to Brinell hardness. The quenched and tempered low carbon steel Tables 1 and 2, ASTM E140, were found to be functional, but this practice is not recommended by ASTM. Minimizing utility and table conversion of different hardness measurement scales whenever possible is the recommended practice. Since hardness measurement scale conversion for comparative purposes was unavoidable during this research (and assumed to be unavoidable in the future), hardness technique and conversion process in experimental procedures should always be clearly specified and its uncertainties noted. As the alloy system gains formal recognition and nomenclature, alloy specific hardness conversion tables should be established and incorporated into ASTM E140.

3. High Strain Rate Reporting

Concern: Reported true stress and true strain for Split Hopkinson Kolsky Bar compressive data was normalized to non-equilibrium conditions during testing but did not reflect the actual true strain measured during testing.

Discussion: During testing, recorded strain was higher than reported strain because the strain data was normalized to account for non-equilibrium stress conditions. This technique failed to report an additional 10% elongation to failure. Additionally, Split Hopkinson Kolsky Bar testing does not have a national or international standard for reporting. Normalized true strain reporting should be avoided. Data can be reported to reflect actual strain to failure and the strain at which steady state was achieved. This is particularly important if the data is to be used by modelers to predict and establish failure criteria.

4. Phosphide Analysis

Concern: The phosphide formation is unexplained in the Fe-Mn-Al-C system.

Discussion: Phosphorus eutectic formations are not new to ferrous based metals. Cast iron also shows similar structures as do Hadfield manganese steels. A more thorough literature review of cast iron and Hadfield systems should assist in understanding the phosphorus formation observed and means to mitigate it for improved mechanical properties. However, under certain ballistic conditions, the phosphorus phase could prove beneficial (i.e. similar to metal matrix composites).

Additional Comments:

Though the present research is focused on a ferrous alloy, the insights gained from understanding property-microstructure-processing-ballistic performance relationships are applicable to other materials systems. The hardening carbide phase can be representative of ceramic particulates in light non-ferrous alloys. The austenite-ferrite relationship can be representative of any dual phase materials. The concept of phase manipulation within casting parameters to achieve wrought material performance creates an enormous opportunity to consider low cost-complex shape materials for ballistic applications. But at the heart of the matter is that the successful results from this effort were due to a threat based material's need providing the driving force for expedient research and determining which attributes within the property-microstructure-processing relationship took priority. In this case, the MIL-PRF-32269 provided a specific problem definition facilitating successful alloy ballistic application development in two years.

APPENDIX A.

PAPER - Quench Sensitivity of Cast Fe-30Mn-9Al-1Si-0.9C-0.50Mo Lightweight Steel

Quench Sensitivity of Cast Fe-30Mn-9Al-1Si-0.9C-0.50Mo Lightweight Steel

R.A. Howell, S. N. Lekakh, D. C. Van Aken

Army Research Lab

Missouri University of Science and Technology

Department of Materials Science and Engineering

Rolla, MO 65409

Tel.: 573-341-4717

E-mail: dcva@mst.edu

Key Words: Fe-Mn-Al-C, lightweight steel, Charpy, impact toughness, phosphorus, cooling rate

Published in the American Iron and Steel Technology journal.

ABSTRACT

Quench sensitivity of Fe-30wt.%Mn-9wt.%Al-1wt.%Si-0.9wt.%C alloys were investigated. Two alloys were examined: a calcium treated low phosphorus alloy (0.006wt.% P) and a non-calcium treated high phosphorus alloy (0.07wt.% P). Samples were solution treated and subjected to differing cooling media to produce various cooling rates. In addition, low phosphorus alloy samples were tested after solution treating and aging. Maximum impact toughness (190 ± 11 J) and lowest hardness (211 ± 11 BHN) was measured in the solution treated low phosphorus specimens for a 337°C/s cooling rate. Minimum impact toughness (5.4 ± 0.3 J) and maximum hardnesses (366 ± 5 BHN) was measured in the untreated high phosphorus alloy specimens for a low 0.4°C/s cooling rate. Reducing the cooling rate increased heterogeneous precipitation in both alloys. The general equations describing the complex effect of phosphorus, cooling rate, and parameters of aging kinetics were developed and could be used for process design and alloy properties prediction.

INTRODUCTION

Lightweight castable steel alloys containing aluminum concentrations greater than 7% (all chemistries are in weight percent) are under current investigation as alternatives to traditional MIL-A-12560[1] and MIL-A-46100[2] armor steel chemistries for application in MIL-PRF-32269[3] perforated homogeneous steel armor. Fe-Mn-Al-C alloys contain 20-30% Mn, 7-12% Al, and 0.7-1.2% C[4]. The Fe-Mn-Al-C family of alloys has shown great potential as their specific strength under quasi-static tensile and high strain rate compression testing exceeded rolled homogeneous armor by 13% and 28% respectively for the two test techniques[5]. The excellent specific properties benefit from weight

reduction of aluminum content. Aluminum concentrations between 7 and 12% reduce density by as much as 18% over conventional steels[4].

Fe-Mn-Al-C alloys age harden by precipitation of the κ-carbide when aluminum concentrations exceed 5% and carbon content is greater than 0.3%[7]. The κ-carbide formation is preceded by spinodal decomposition facilitating homogenous precipitation of the κ-carbide[8]. The κ-carbide is an ordered $E2_1$ crystal structure: aluminum atoms occupy {1,0,0} positions, iron or manganese the {½ , ½, 0} positions, and carbon is located at the center octahedral position[4].

Howell et al. investigated silicon additions to evaluate fluidity, solution treated microstructures[6], and age hardened properties[5]. Thermal analysis from the fluidity study showed that silicon additions lower liquidus, solidus, and dendrite coherency point by 30°C per weight percent increase[6]. The silicon containing alloys' fluidity spirals were 70% greater in length versus a low alloy steel at 150°C superheat[6]. Silicon containing solution treated material is primary austenite and less than 10 volume percent ferrite[6]. Peak hardness during aging at 530°C occurs at 30 hours for 1% silicon containing Fe-30Mn-9Al-0.9C-0.5Mo alloy solution treated at 1050°C (see Figure 1)[5]. Hardness increased from a solution treated 224 ± 2 BHN to peak aged 372 ± 8 BHN[6]. Tensile strength increased from 687 MPa to 1,065 MPa, and ductility decreased as elongation to failure declined from 44 to 8 %[5].

Howell et al. correlated Charpy impact and cast defect content to 0.50 caliber fragmentation simulation ballistic results of two solution treated and aged nominal cast Fe-30Mn-9Al-0.9C-0.5Mo alloy[9]. A calcium treated alloy (with half the defect content

and less then 20% of the phosphorus content of the non-calcium treated alloy) exceeded the non-treated material's V_{50} by 64 m/s and its Charpy impact toughness by 60 J[9].

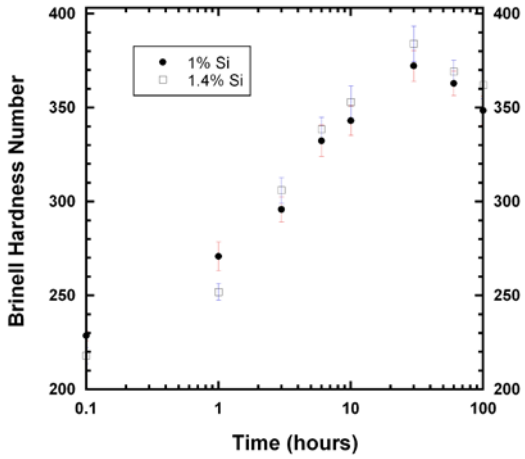

Figure 1. The age hardening curves for 1 and 1.4 % silicon containing Fe-Mn-Al-C alloys show a rapid increase in hardening through the first 6 hours. At times greater than six hours, hardness increases, but the hardening rate decreases. Maximum hardness is achieved at 30 hours for both alloys. The 1% silicon alloy hardens to 372 ± 8 BHN, and the 1.4% alloy age hardens to 384 ± 10 BHN.

The current study is part of an investigation to quantify quench rate and impurity effects of two commercially cast nominal Fe-30Mn-9Al-1Si-0.9C-0.5Mo alloy steels in order to improve fracture toughness and ballistic performance for MIL-PRF-32269. Specimens were solution treated and cooled in various media to achieve multiple cooing rates. Charpy bars were tested in this condition and an additional set of specimens were solution treated, aged and then tested. Impact data was then correlated to phosphorus content, cooling rate, microstructural and fracture surface observances.

EXPERIMENTAL PROCEDURE

Two alloys were commercially produced as cast plates from high purity induction iron, aluminum, ferrosilicon and ferromolybdenum in 225 kg induction furnaces under argon cover. One alloy utilized electrolytic manganese and was calcium treated. The other alloy was manufactured with ferromanganese and not calcium treated. Both alloys were cast into olivine phenolic no-bake sand molds and poured without filtering at 100°C superheat. A solid oxide probe measured oxygen content. Both heats contained 2 ppm oxygen and did not require an additional deoxidation step. Low density coagulant was utilized for deslagging.

Two experimental trials were executed. The first trial consisted of specimen blocks measuring 12.5 mm x 12.5 mm x 60 mm. Blocks were heated to 1000°C and cooled by water quenching, oil agitation, placed on a brick in open air, or insulated by an alumina fiber blanket. Four alloy blocks were produced per each cooling media with additional sets of the treated alloy cooled in the four media and then aged at 530°C for 10 hours (Table 1).

Table 1. Trial 1 Test Matrix for Charpy Impact Data Collection

Alloy / Heat Treat Test Condition	Water Quench	Oil Quench	Air Quench	Alumina Fiber
Calcium Treated / Cooled	4 bars	4 bars	4 bars	4 bars
Non-Calcium Treated / Cooled	4 bars	4 bars	4 bars	4 bars
Calcium Treated / Cooled and Aged	4 bars	4 bars	4 bars	4 bars

A K-type thermocouple was embedded into one of the blocks for cooling rate data collection. Temperature and time data collection occurred at 4 Hz. Blocks were machined to ASTM E 23 Type-A V-notch Charpy specimens and tested at room temperature in a Tinius Olsen Charpy model 84 pendulum impact machine with model 892 controller.

The second trial consisted of specimens machined from a water end quenched plate that measured 127 mm x 177.8 mm x 15.25 mm (Figure 2). The quenched end measured 15.25 mm x 177.8 mm. K-type thermocouples were welded onto the plate at 25, 50, 75, and 100 mm from the quenched end.

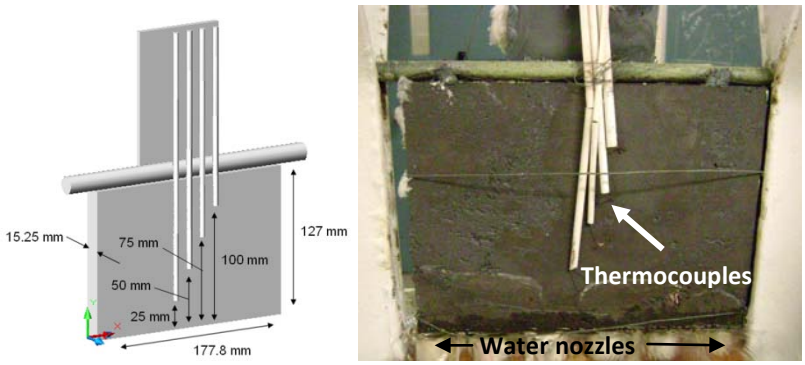

(a) (b)

Figure 2. The quench plate schematic form (a) shows plate dimensions and thermocouple contact spacing distances every 25 mm. The actual plate form (b) is shown at the completion of testing in the quench fixture without its alumina fiber insulation wrap with the water pump engaged.

A stainless steel round bar and a low carbon steel thin plate were welded to the specimen plate to facilitate placement in the quench tank fixture. The plate assembly was wrapped in alumina fiber, less the quenched end. The entire assembly was heated to 950°C and

placed into the quench fixture. Temperature and time data collection occurred at 4 Hz. The plate was then aged at 520°C for 10 hours. ASTM E 23 Type-A V-notch Charpy blocks were cut vertically from the plate to correspond to thermocouple locations (Figure 3). Room temperature instrumented Charpy testing of these specimens also occurred on the Tinius Olsen model 84 machine but with an MPM Impact v5.1 instrumented tup and data acquisition system.

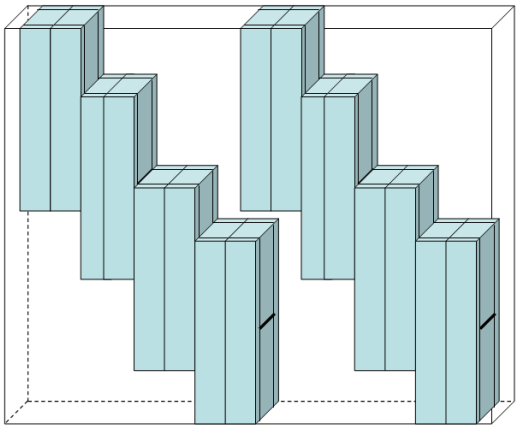

Figure 3. Schematic shows Charpy specimen locations selected to minimize differences in notch toughness and hardness data sensitivity as a function of plate location.

Two Fluent® simulations were conducted to compensate the experimental results because thermocouple data acquisition occurred below 680°C during solid plate end quenching. The first simulation was model verification conducted against available experimental data. The second simulation was end quench modeling for the 950°C solution treatment temperature. Briefly, energy transport within the solid enmeshments is governed by the equation:

$$\frac{\partial}{\partial t}(\rho h) = \frac{\partial}{\partial x_i}(\lambda \frac{\partial T}{\partial x_i}) \quad \text{(Equation 1)}$$

where: t (s) is time, r is the solid plate's density (6.7 g/cm^3), λ (W/m·K) is thermal conductivity, T (K) is temperature, x_i is a coordinate parameter, and h (J) is sensible enthalpy calculated from:

$$h = \int_{T_{REF}}^{T} c_p dT \quad \text{(Equation 2)}$$

Heat capacity (c_p, J/(kg·K)) was assumed that of steel and its relationship is linear with temperature and followed that:

$$c_p = 0.25(T) + 332 \quad \text{(Equation 3)}$$

The convective heat flux (q, w/m^2) for the end quenched plate boundary condition is:

$$q = h_{ext}(T_{plate} - T_{ext}) \quad \text{(Equation 4)}$$

where: the heat transfer coefficient h_{ext} = 5,000 W/K*m^2 was used.

The boundary condition for side walls included an additional layer of low thermal conductivity (0.1 W/m·K) alumina fiber with 5 mm thickness. The fiber/air heat transfer coefficient for was 10 W/m^2·K. Fluent simulations were executed for 0.1 second time step increments over a 30,000 elements enmeshment.

Model inputs required thermal conductivity data. Thermal conductivity of a Fe-28.8Mn-8.3Al-1.0Si-0.9C-0.5Mo alloy was executed to ASTM E 1225-04 standards. This test measures an unknown material's coefficient of thermal conductivity (λ_S, W/m·K) by averaging the heat flow (q, W/m^2) between two known upper (q_1) and lower (q_2) conductive samples, accounting for differences of temperature (ΔT, K) and distance (ΔZ, m) across the two thermocouples of the known thermal conductivity (λ_M, W/m·K):

$$\lambda_S = \frac{(q_1 + q_2)\Delta Z_S}{2\Delta T_S} \quad \text{(Equation 5)}$$

$$q_1 = \lambda_M \frac{\Delta T_1}{\Delta Z_1} \quad \text{(Equation 6)}$$

$$q_2 = \lambda_M \frac{\Delta T_2}{\Delta Z_2} \quad \text{(Equation 7)}$$

A testing apparatus consisted of a water cooled bronze heat sink, three 3 inch diameter machined steel tube sections, two 304 stainless steel standards, one test specimen, two K-type thermocouples welded directly to each specimen, a silicon carbide heating element, and alumina fiber insulation (Figure 4). The 304 stainless steel was selected because of its known thermal conductivity and austenitic crystal structure. The heating element's power was increased incrementally to allow the column temperature gradient to achieve steady state. Calibration also occurred with a 304 stainless steel sample, and calibration error was less than 1%.

Tested Charpy specimens were sectioned for optical and scanning electron microscopy (SEM) with electron dispersive spectrometer (EDS) for chemical mapping. Hardness was measured with Rockwell B and Rockwell C scales and converted to Brinell hardness number (BHN). SEM charging voltage was 15 keV with 18 mm of working distance at 0° rotation, and EDS mapping occurred at 15 keV, 22 mm of working distance, and 15° rotation. Oxide and sulfide inclusion content were measured using an ASPEX-PICA 1020 analytical SEM on metallographically prepared specimens. Inductive coupled plasma spectrometry x-ray fluorescence by single element wavelength dispersive spectrometry were employed for chemical identification.

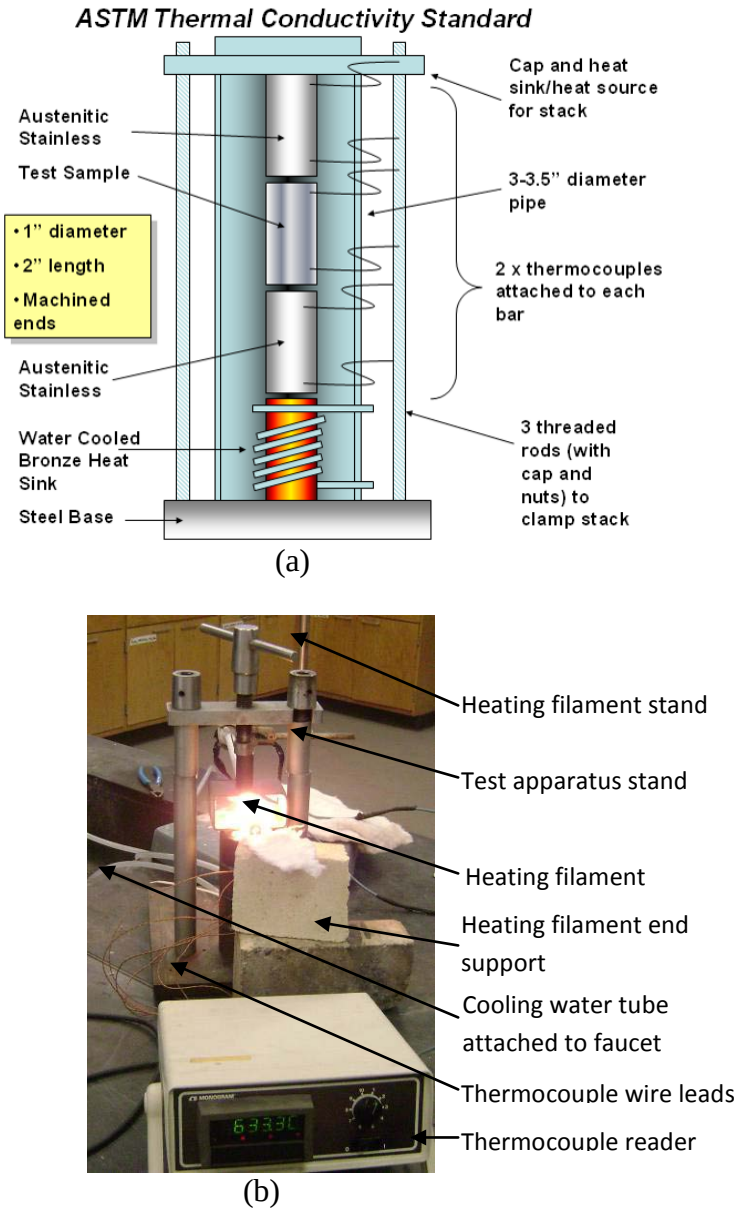

Figure 4. Thermal conductivity apparatus schematic (a) shows the test samples between two austenitic stainless steel standards inside an insulated steel pipe. The thermocouples are labeled Z1 to Z6. The heat sink is shown schematically as a flat plate, but consisted of a solid silicon carbide heating element inside an insulated steel box tube (b).

Metallographic specimens were etched with 2% Nital and images were recorded using a differential interference contrast technique. Image-J ® analytical computer software was used to determine ferrite volume fraction and dendrite arm spacing.

Charpy impact toughness and hardness for all material were plotted as functions of the cooling rate. The cooling rate for this system was calculated at 650°C; the κ-carbide time temperature transformation curve's nose. A Larson-Miller[10] analysis of aging kinetics occurred by comparison of a historic 0.043% phosphorus containing Fe-Mn-Al-C alloy[11]. The Larson-Miller approach is only applicable up to the peak aged condition. Charpy impact energy data, hardness, and dendrite arm spacing experimental measurement errors are reported as the standard deviation with the mean test value[12].

RESULTS

CHEMICAL ANALYSIS

Chemical identification of the two alloys is listed in Table 2. Sulfur and phosphorus levels are dramatically different between the two alloys. Sulfur increased from 0.0008% in the treated alloy to 0.005% in the untreated material. Phosphorus increased from 0.006% in the treated alloy to 0.07% in the untreated materials.

Table 2. Chemical compositions of cast steel (weight percent)

Alloy	Fe	Mn	Al	Si	C	Mo	S	P
Calcium Treated	Bal	30.21	8.85	1.01	0.89	0.31	0.0008	0.006
Non-calcium Treated	Bal	29.11	9.25	1.07	0.90	0.37	0.005	0.07

THERMAL CONDUCTIVITY

Coefficient of thermal conductivity (λ, W/(m·K)) increased linearly with temperature (T, K). At 59°C, the coefficient of thermal conductivity measured 10.4 W/(m·K) and increased to a value of 20.1 W/(m·K) at 516°C (Figure 5).

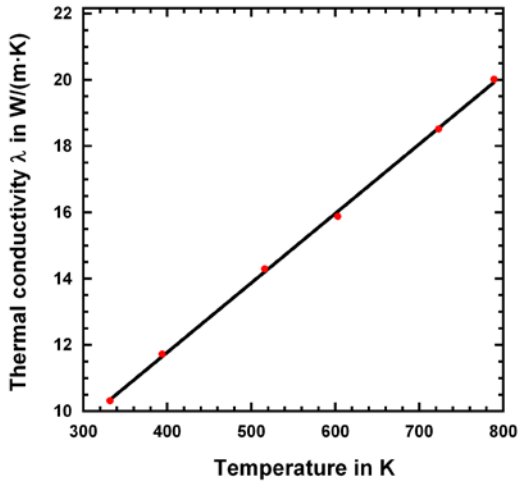

Figure 5. Thermal conductivity of a Fe-28.8Mn-8.3Al-1.0Si-0.9C-0.5Mo alloy.

The linear change increase was expressed as a function of temperature:

$$\lambda = 0.021 \cdot T + 3.41 \qquad \text{(Equation 8)}$$

COOLING RATES

Two cooling procedures were applied. In the first one, different cooling media (water, oil, air, and alumina fiber) were at room temperature (21°C) for the start of each test. Figure 6 shows experimentally measured cooling curves and cooling rates in each cooling media. Cooling rates (at 650°C) were determined from the first derivative (dT/dt) of the cooling curve. In all test conditions, cooling rate in the specimens' center

increases to a maximum value within the first 4 seconds of immersion into each media. Water quenching produced the maximum cooling rate of 341°C/s while a cooling rate was 337°C/s. Oil quenching, air cooling, and alumina fiber cooling showed cooling rates of 86°C/s, 2°C/s, and 0.4°C/s accordingly.

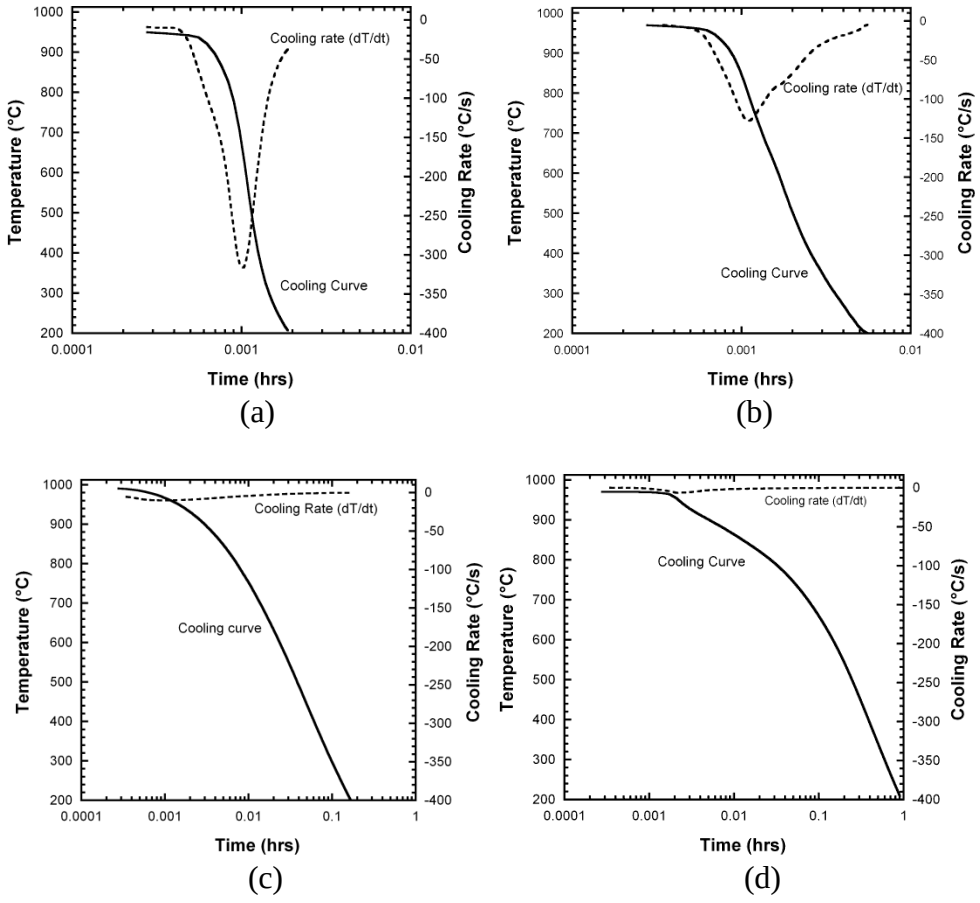

Figure 6. Cooling curves for water (a), oil (b), air (c), and alumina fiber (d) are shown with their first derivative (dT/dt) cooling rate. The cooling rates were 337°C/s (water), 86.1°C/s (oil), 2°C/s (air), and 0.4°C/s (fiber).

The second cooling procedure used a water end quenched plate. The verification step of the Fluent modeled data (used measured coefficient of thermal conductivity from

Equation 8) is shown in Figure 7 alongside the experimental data. The calculated and experimental data for different thermocouple locations were in acceptable agreement and allowed execution of the next iteration for the real quenching temperature (950°C). The predicted cooling profile for 25, 50, 75, and 100 mm from quenched end are shown in Figure 8. Two screen shots illustrating the temperature profile at 50 seconds (0.014 hours) and 300 seconds (0.083 hours) are also shown. Modeled cooling rates for the thermocouple positions are in Table 3. The comparison of these two procedures showed the range of end quenched cooling rate values (58.8°C/s to 0.9°C/s) fell in between the small specimen measured values for oil quenching (86.1°C/s) and alumina fiber cooling (0.4°C/s).

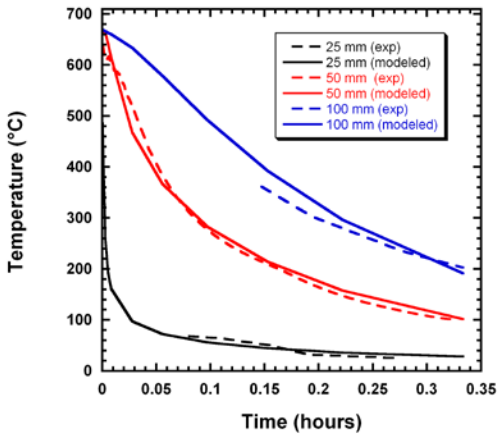

Figure 7. Modeled and experimental end quench cooling curves are shown for three thermocouple positions on a 177.8 mm x 127 mm x 15.25 mm plate. The error in modeled temperature prediction varies up to a maximum difference of 40°C for the thermocouple location 100 mm from the quenched end.

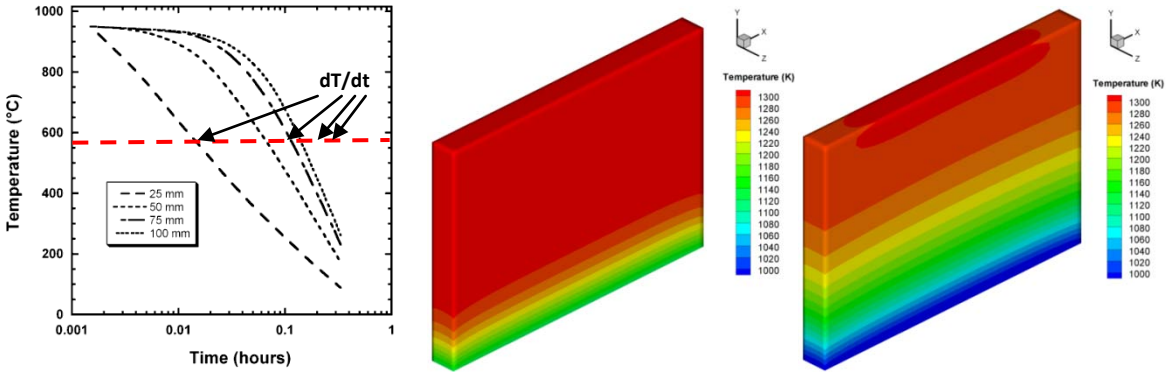

Figure 8. Modeled cooling curves are shown for four thermocouple positions on a 177.8 mm x 127 mm x 15.25 mm solid plate undergoing end quenching from 950°C. The cooling rate (dT/dt) at each location was determined at 650°C, indicated by the horizontal dashed line.

Table 3. Cooling rates from modeled thermocouple locations indicated by their distance from the quenched end

Position	25 mm	50 mm	75 mm	100 mm
Cooling Rate (°C/s)	58.8	26.2	17.3	16.6

CHARPY IMPACT ENERGY AND HARDNESS

Impact energy and hardness values are shown in Figure 9 as a function of cooling rate. Two trends were observed. First, impact energy of both alloys attained maximum toughness in the water quenched condition or maximum cooling rate (337°C/s) and minimum toughness from cooling in alumina fiber (0.4°C/s). Second, minimum hardness corresponded to maximum cooling rate and maximum hardness from the minimum rate. Specific values for both alloys for the four cooling media are reported in Table 4. The 0.006% phosphorus containing alloy attained higher impact energies and lower hardnesses at all cooling rates.

Table 4. Average values of impact energy and hardness of each specimen condition, aligned by cooling rate.

Alloy	Water (337°C/s)		Oil (86.1°C/s)		Air (2°C/s)		Fiber (0.4°C/s)	
	Joules	BHN	Joules	BHN	Joules	BHN	Joules	BHN
Solution Treated 0.006% P	190 ± 11	211 ± 10	182 ± 37	232 ± 7	150 ± 40	256 ± 8	137 ± 15	271 ± 6
Solution Treated 0.07% P	32 ± 5	246 ± 9	23 ± 2	265 ± 12	7 ± 1	348 ± 10	5 ± 0.3	366 ± 5
Solution Treated and Aged 0.006% P	103 ± 7	294 ± 6	105 ± 2	289 ± 5	79 ± 24	289 ± 4	71 ± 6	300 ± 5

Both observed Charpy impact and hardness trends for the aged small individual specimens were also observed in the end quenched and aged plate. Hardness values increased slightly from 261± 4 BHN to 288 ± 5 BHN for a reduction in Charpy impact toughness from 144 ± 12 J to 100 ± 17 J for decreasing cooling rates from 58.8°C/s to 0.9°C/s; corresponding to increasing separation distance from 25 mm to 100 mm away from the quenched end (Figure 10).

The instrumented test procedure collected impact force versus displacement curve information. The integral from this curve presents an overall impact energy. Instrumented yield impact force load results measured between 24 kN and maximum force loads up to 27 kN for all four end quenched specimen sets. Figure 11 shows test outputs for 58.8°C/s and 0.9°C/s cooled end quenched specimens. Impact energy differences correlated to ductility.

In Figure 11a, the 58.8°C/s cooled specimen displaced 3.6 mm at maximum load. By contrast, the 0.9°C/s cooled specimen (Figure 11b) only displaced 1.8 mm at maximum force load. Total ductility also reduced from the 15.5 mm for 58.8°C/s 14 mm for the 0.9°C/s.

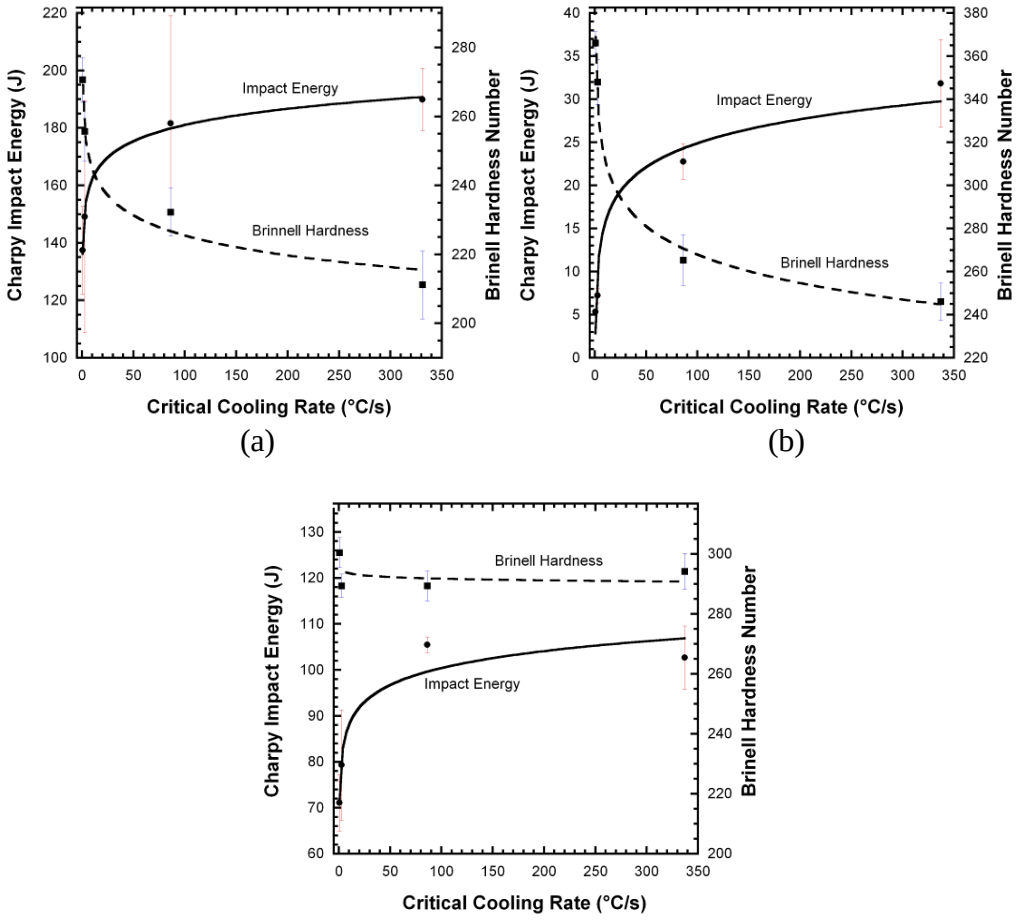

Figure 9. Charpy impact and hardness measurements of the three specimen sets are plotted as a function of cooling rates for the four cooling media. The 0.006% phosphorus alloy (a) had the lowest hardness (211 ± 10 BHN) and highest impact energy (190 ± 11 J). The 0.07% phosphorus alloy (b) had the highest hardness (366 ± 5 BHN) and lowest impact energy (5 ± 0.3 J). The aged (530°C for 10 hours) 0.006% phosphorus alloy showed little change in hardness (294 ± 6 BHN to 300 ± 5 BHN) correlated to broader change in impact energy (103 ± 7 J to 71 ± 6 J).

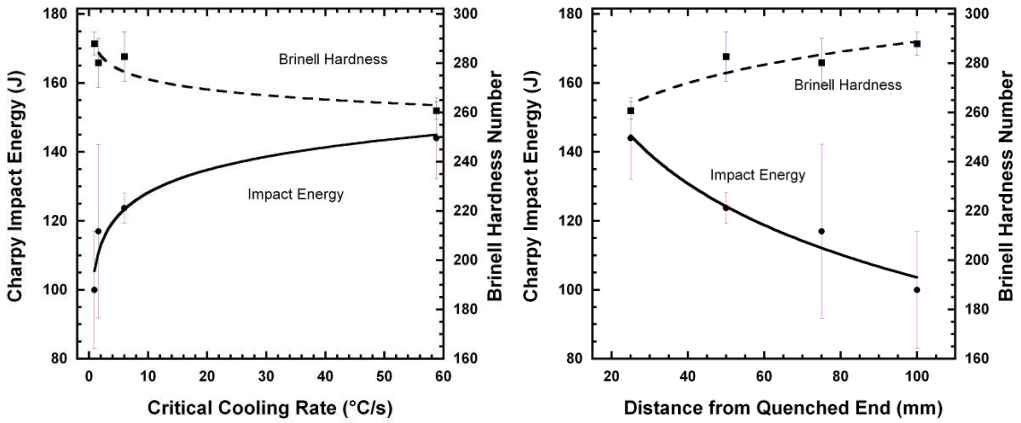

(a) (b)

Figure 10. The end quenched and aged plate's Charpy impact and hardness measurements are shown as a function of quench rate (a) and distance from quenched end (b). The highest Charpy impact energy (144 ± 12 J) and lowest hardness (261 ± 4 BHN) were measured for the highest cooling rate (58.8°C/s) at the 25 mm location. Increasing the separation distanced decreased the cooling rate to a minimum of 0.9°C/s, reduced Charpy impact toughness to 100 ±17 J and increased hardness to 288 ± 5 BHN .

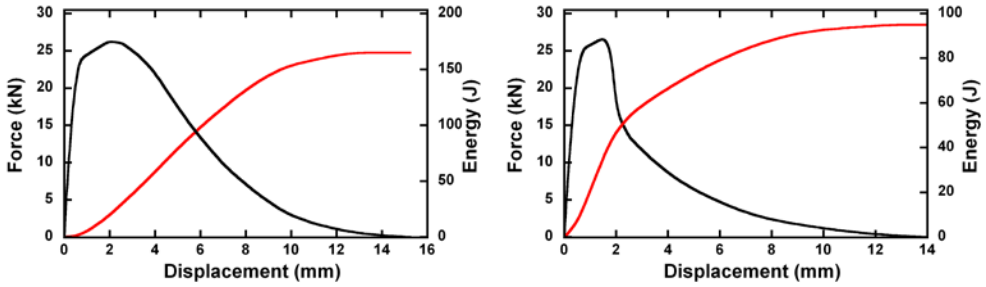

(a) (b)

Figure 11. Impact force/energy curves are shown for specimens cooled at 58.8°C/s (a) and 0.9°C/s (b). Yield force and maximum force load values are similar for both specimens, but ductility is distinctly higher for the 58.8°C/s cooled specimen thus it produced the highest measured impact energy.

FRACTURE SURFACE

Both ductile and cleavage fracture modes were observed. The 0.006% phosphorus containing alloy failed in a ductile fashion for the 337°C/s cooling rate (see Figure 12a). But cleavage along the dendritic structure was observed for the 0.07% phosphorus containing alloy cooled at 337°C/s (Figure 12c). A combination of ductile and transgranular fracture was observed for the cooled (337°C/s) and aged 0.006% phosphorus alloy specimen and for end quenched and aged plate specimens cooled at 58.8°C/s and 6.5°C/s (Figure 12e). A combination of transgranular and intergranular cleavage fracture occurred for all other tested specimens (see Figures 12b, 12d, 12f). Fracture surface chemical mapping by EDS (see Figure 13) of the two alloys revealed higher concentrations of phosphorus and sulfur in the 0.07% phosphorus alloy; confirming wet chemical analysis.

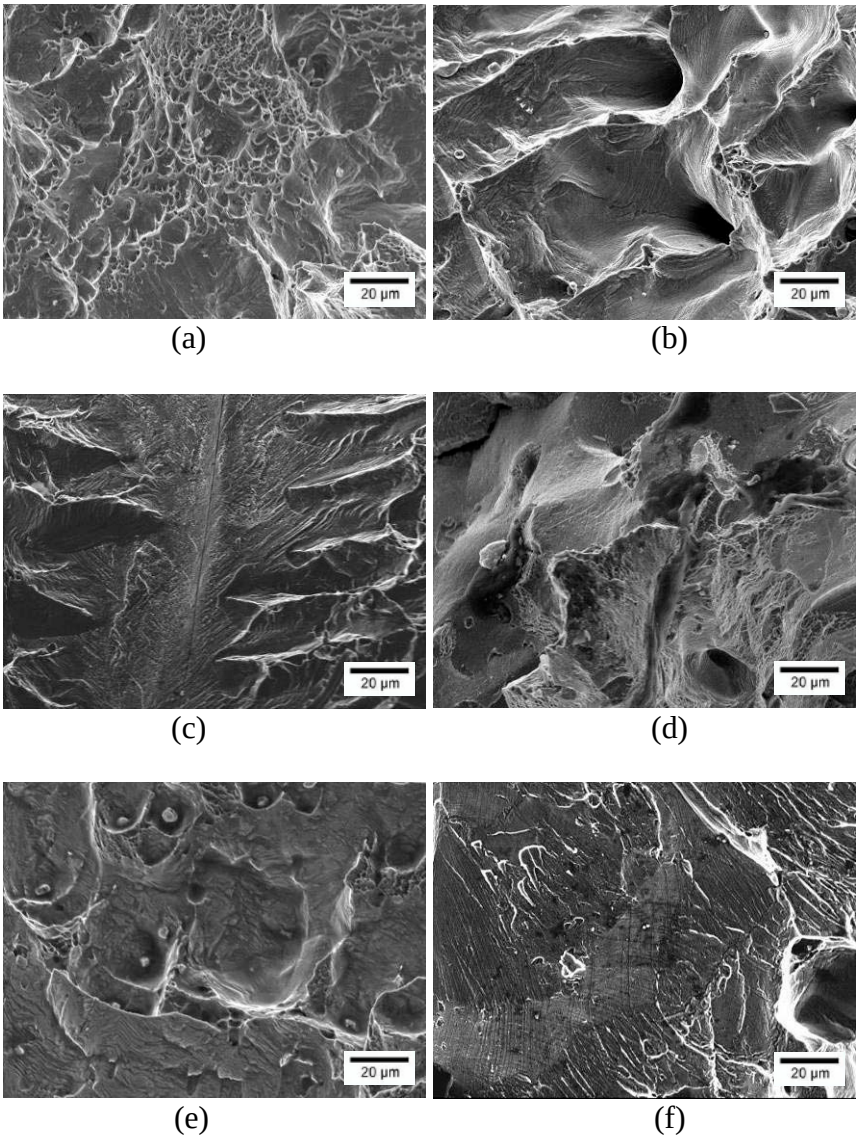

Figure 12. Failure occurs in a ductile fashion for the 337°C/s cooled 0.006% phosphorus alloy (a), but transgranular cleavage for the 337°C/s cooled 0.07% phosphorus alloy (c). A combination of ductile and transgranular fracture was observed for the 337°C/s cooled and aged 0.006% phosphorus alloy and all end quench plate specimens(e). A combination of transgranular and intergranular cleavage was observed on fracture surfaces cooled 0.4°C/s of 0.006% phosphorus (b), 0.07% phosphorus (d), and the 0.006% phosphorus aged material (f).

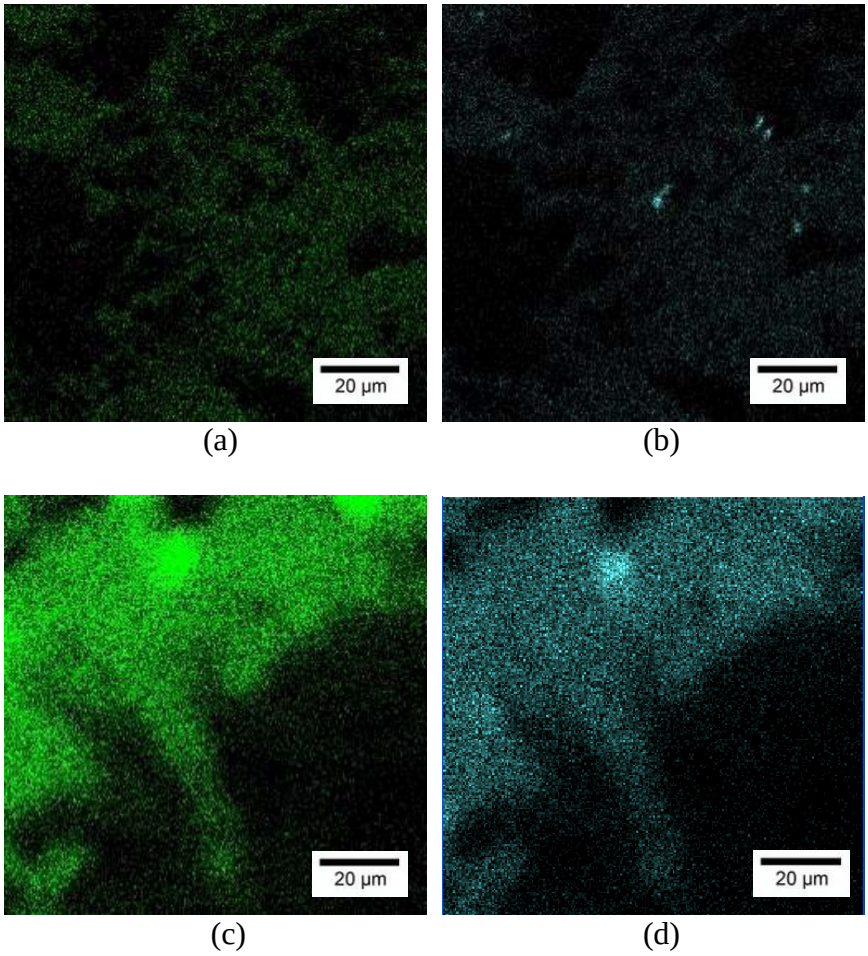

Figure 13. The fracture surface EDS chemical mapping confirms chemical analysis that the treated alloy produced with electrolytic manganese has less phosphorus (a) and sulfur (b) than the phosphorus (c) and sulfur (d) content of the untreated alloy produced with ferromanganese.

MICROSTRUCTURE

Quench rate and phosphorus content affects microstructural features in three ways: ferrite content, dendrite arm spacing, and precipitation of additional phases. Austenite content in the 0.006% phosphorus alloy is 99% by volume with isolated islands of ferrite (Figure 14a) and dendrite arm spacing is 59 ± 2 µm for all evaluated conditions. However, the 0.4°C/s cooled microstructure shows dendrite boundary precipitation

(Figure 14b). The 0.07% phosphorus alloy cooled at 337°C/s contained 7% ferrite (Figure 14c). Dendrite arm spacing measured 31 ± 3 μm. Decreasing the 0.07% phosphorus alloy's cooling rate to 0.4°C/s produced matrix and discrete dendrite boundary precipitation with precipitate free zones adjacent to austenite-austenite boundaries (Figure 14d). Discrete dendrite boundary precipitation is also visible in the solution treated and aged condition of the 0.006% phosphorus alloy (Figure 14e). End quenched plate specimens (Figure 14f) revealed a continuous boundary precipitation amid a primarily austenitic matrix with isolated islands of ferrite. Matrix and discrete precipitates were not observed.

No distinguishable microstructural differences were visible in all end quenched plate specimens. The 58.8°C/s cooling rate specimen (Figure 15a) and the 0.9°C/s cooling rate specimen (Figure 15b) contain austenite, ferrite, and show dendrite boundary and sub grain precipitation. Austenite content was constant and measured the same as the fully immersed specimens at 99%. Grain boundary precipitation is continuous and lacks visible discrete precipitates such as those contained within the fully water quenched and aged microstructure.

Figure 16 shows sulfide and oxide chemical ternary diagrams of both alloys, and a non-metallic inclusion size histogram is shown in Figure 17. The inclusion chemistries of both alloys are equivalent, but the 0.07% phosphorus containing alloy's showed an inclusion count increase by a ratio greater than 5:1.

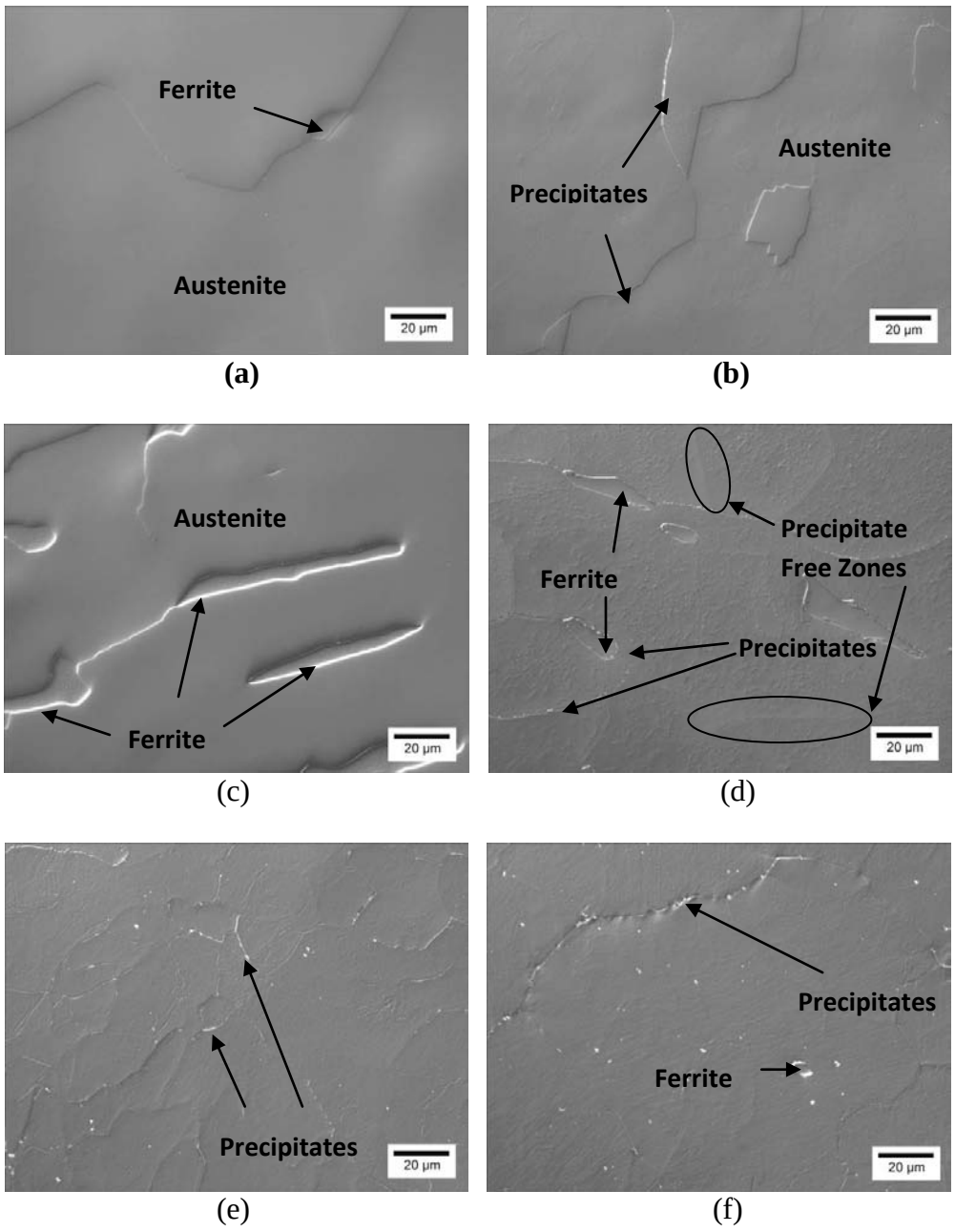

Figure 14. The 337°C/s cooled 0.006% phosphorus containing alloy (a) is composed of primary austenite and small islands of ferrite. Cooling the 0.006% alloy at 0.4°C/s (b) produces austenite to austenite dendrite boundary precipitation. The 0.07% phosphorus alloy shows increased ferrite content (c) and a combination of dendrite boundary and matrix precipitation (d). Precipitate free zones also accompany the precipitation. Small islands of ferrite and dendrite boundary precipitation are visible within the 337°C/s cooled and aged 0.006% phosphorus alloy's microstructure (e). Increased dendrite boundary and matrix precipitation is observed within the 0.4°C/s cooled and aged 0.006% phosphorus microstructure (f).

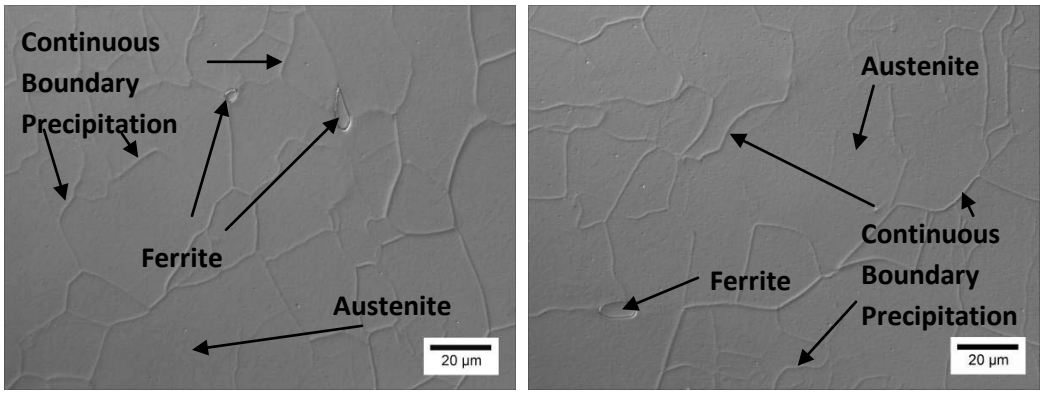

(a) (b)

Figure 15. Microstructures of the 58.8°C/s and 0.9°C/s cooled end quenched specimens shows primary austenite, ferrite and continuous dendrite and sub-grain precipitation. Visual inspection did not reveal distinctive features that differentiate the two cooing conditions.

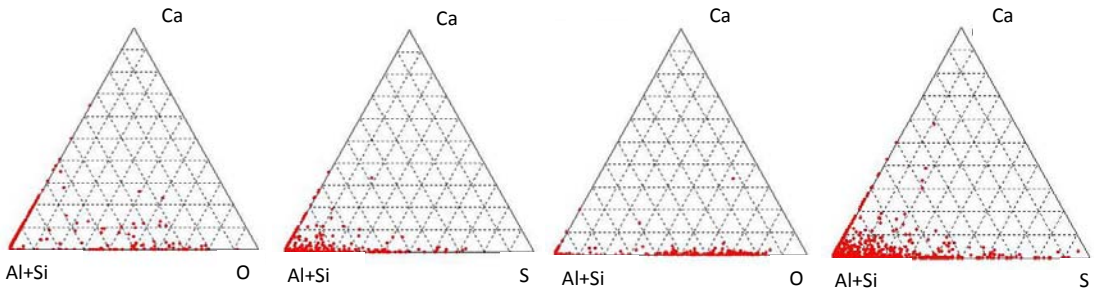

(a) (b) (c) (d)

Figure 16. Sulfide (a) and oxide (b) content of the 0.006% phosphorus containing alloy are shown with the same chemical composition, but in lower quantity, as sulfides (c) and oxides (d) of the 0.07% high phosphorus alloy.

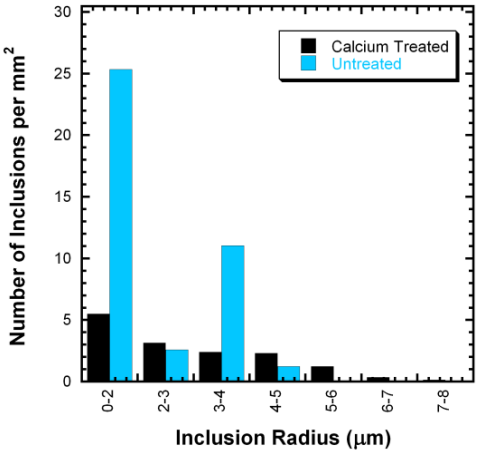

Figure 17. Inclusion content of the untreated high phosphorus alloy is five times greater than that of the calcium treated low phosphorus alloys. Inclusion radius size 0.002 mm and less accounted for the highest inclusion quantity size category for both alloys.

DISCUSSION

IMPACT ENERGY, PHOSPHORUS, AND COOLING RATE

Decreasing quench rate and chemistry defect content had detrimental effects on Charpy impact energy, but phosphorus content had the single greatest degrading effect. Comparison of the two alloys' impact energies as functions of cooling rate in Figure 18, taking into account differences in phosphorus content, reveal the large effect phosphorus plays in toughness of Fe-Mn-Al-C alloys. Similar deleterious impact toughness phosphorus effects have been observed in high manganese steels[13], but exact nature of the Fe-Mn-Al-C phosphorus embrittlement is under investigation.

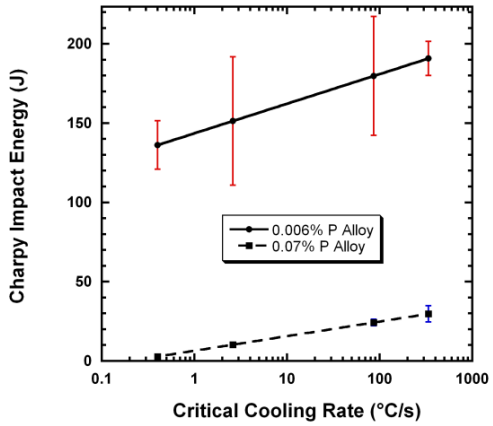

Figure 18. Impact energy is plotted as a function of cooling rate for the 0.006% and 0.07% phosphorus containing alloys. Impact energy reductions of 30 to 50 J occurred within each fixed chemistry for decreasing cooling rates, but the phosphorus content increase from 0.006% to 0.07% decreased toughness by at least 130 J for any equivalent cooling rate.

COOLING RATE EFFECTS ON INSTRUMENTED CHARPY V-NOTCH RESULTS

Type II and Type III failure[14,15,16] characterization of end quenched and aged specimens was observed in all instrumented Charpy tests with Type III failure dominating the majority of the 0.006% phosphorus alloy's tested specimens. A conservative lower bound for dynamic fracture toughness (K_{ID}, MPa$\sqrt{m}$) was estimated assuming Type II failure and multiplying the K_{ID} value by 0.65 as prescribed by Sreenivasan et al. to account for statistical error[15,16]. The equation for determining K_{ID} vaules[15,16] is:

$$K_{ID} = \sqrt{E \cdot J_{ID}} \qquad \text{(Equation 16)}$$

where E is young's modulus taken at 188 GPa[5] multiplied by the elastic plastic fracture toughness (J_{ID}, MPa·m). For Type II fracture loading curves, J_{ID} is estimated by the equation[15,16]:

$$J_{ID}(MPa \cdot m) = \frac{\eta \cdot A}{B \cdot b_0} \qquad \text{(Equation 17)}$$

η is a fixed constant of 1.384 for Charpy V-notch specimens[17], A is the area under the load displacement curve up to crack initiation, B is the specimen thickness (10 mm) and the initial ligament depth below the notch is b_o (8 mm). Sreenivasan et al.[16] defined crack load initiation as the value corresponding to the average of the yield force load or general yield load (P_{gy}) and the maximum force load (P_m) such that $A \rightarrow (P_m + P_{gy})/2$. The lower bound K_{ID} is shown in Figure 19 and decreases with the reductions in the cooling rate.

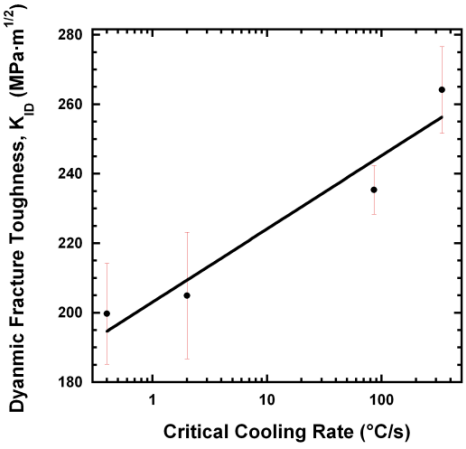

Figure 19. The lower bound K_{ID} is shown to decrease with reductions in cooling rate for end quenched and 10 hour 520°C aged 0.006% phosphorus containing specimens.

MICROSTRUCTURE

Decreasing the cooling rate increased matrix and dendrite boundary precipitation which accounts for the change in hardness within a fixed alloy chemistry. Plotting the small specimen continuous cooling curves over the isothermal time temperature transformation diagram of a 1.25% silicon containing alloy by Acselrad et al.[18] (see Figure 20) approximates that the 0.4°C/s cooling curve that was generated by alumina fiber cooling passes through the transformation curves of homogenous matrix κ-carbide and dendrite boundary κ-carbide , B2 and DO_3 phases.

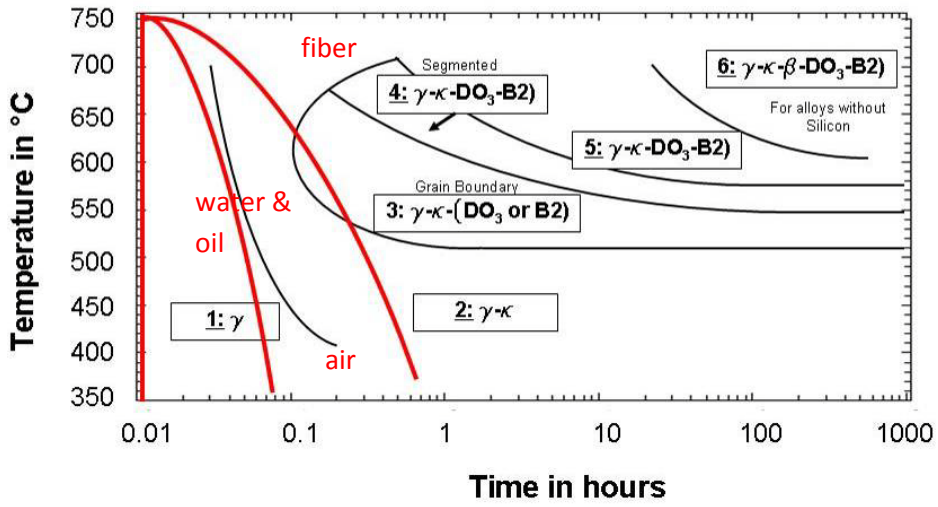

Figure 20. Time temperature transformation for a 1.25% silicon modified FeMnAlC alloy is subdivided as follows: 1) chemical segregation and zone formation, 2) matrix κ-carbide nucleation and growth, 3) heterogeneous matrix κ-carbide formation and grain boundary κ-carbide and DO_3 or B2 precipitation, 4) continued growth and decomposition forming discontinuous segmented phases of κ-carbide, DO_3, and B2, 5) final equilibrium phases, and 6) β-manganese for non-silicon containing alloys. Continuous cooling curves of 1% silicon containing FeMnAlC alloy cooled in water, oil, air, and fiber are plotted as red lines.

Even though the 2°C/s cooling rate curve (air cooling) is not shown to intercept the κ-carbide transformation curve, the observed microstructure and hardness increase is expected to result from precipitation and coherency strain due to spinodal decomposition during the early stages of κ-carbide formation[19]. Hardness differences between dissimilar alloys, subjected to equal cooled rates, is associated with phosphorus content since phosphorus is a known solid solution hardener[20].

Phosphorus[21], sulfides[22], and oxides[23] are known steel containments, responsible for decreasing impact energy. The 0.07% phosphorus alloy and its sulfur content exceeded the 0.006% alloy's by 0.0042%. Figure 16 and Figure 17 show sulfide and oxide chemical ternary diagrams of both alloys, and an inclusion size histogram. The 0.006% phosphorus alloy benefitted from high purity charge materials and late calcium additions to the melt. Calcium additions react with sulfur, forming a buoyant sulfide that floats out of the melt[20,23]. Electrolytic manganese was used in the calcium treated low phosphorus alloy and ferromanganese was utilized for the non-calcium treated high phosphorus alloy. Manganese charge chemistries were not available from the manufacturers; however, Howell et al.[9] suggested possible phosphorus sources included ferromanganese, furnace refractory, and priory heat residual material in the furnace.

Phosphorus content affected ferrite volume fraction and dendrite arm spacing. Phosphorus is a ferrite stabilizer in steel[24] and was shown to stabilize ferrite in FeMnAlC alloys. Ferrite volume fraction increases 1% for a 0.01 wt.% increase in phosphorus. The high phosphorus alloy also reduced dendrite arm spacing by 4 μm for a 0.01% increase in phosphorus.

CONCLUSIONS

Phosphorus was shown to have the single greatest detrimental effect on impact toughness. Charpy V-Notch impact energy reductions as great as 95% were observed for an increase in phosphorus from 0.006% to 0.07%. Cooling rate reductions are also responsible for decreasing toughness and increased hardness but not to the extent that phosphorus impacts these properties as shown by Equations 9 and 13 relating both cooling rate and phosphorus content to impact toughness. The exact nature of why phosphorus is so detrimental in Fe-Mn-Al alloys is under current investigation. Phosphorus increases ferrite content 1% for a 0.01% increase, and phosphorus reduces dendrite arm spacing by an amount of 4 μm per 0.01% increase. Reducing cooling rate increases matrix and dendrite boundary precipitation and correlates to increased embrittlement and hardness. Therefore, under the best of conditions, ultra-low phosphorus with the highest possible quench rate from solution treating temperatures gives the best impact toughness possible in nominal Fe-30Mn-9Al-1Si-0.9C-0.5Mo alloys.

REFERENCES

1. MIL-A-12560, Military Specification for Armor Plate, Steel, Homogenous.

2. MIL-A-46100, Military Specification for Armor Plate, Steel, High Hardness.

3. MIL-PRF-32269, Military Performance Specification for Perforated Homogeneous Steel Armor.

4. Frommeyer, G., Brux, U., “Microstructures and Mechanical Properties of High-Strength Fe-Mn-Al-C Light-Weight TRIPLEX Steels,” Steel Research Int., Vol. 77, pp. 627-633 (2006).

5. Howell, R. A., Weerasooriya, T., Van Aken, D. C., “Tensile, High Strain Rate Compression, and Microstructural Evaluation of Lightweight Age Hardenable Cast Fe-30Mn-9Al-XSi-0.9C-0.5Mo Steel,” AFS Transactions, awaiting publication.

6. Howell, R. A., Lekakh, S. L., Van Aken, D. C., Richards, V. L., “The Affect of Silicon Content on the Fluidity and Microstructure of Fe-Mn-Al-C Alloys,” AFS Transactions (2008).

7. Sato, K., Tagawa, K., and Inoue, Y., “Modulated Structure and Magnetic Properties of Age-Hardenable Fe-Mn-Al-C Alloys,” Met. Trans A, vol. 21A, pp 5-11 (1990).

8. Han, K. H., Choo, W. K., “Phase Decomposition of Rapidly Solidified Fe-Mn-Al-C Austenitic Alloy,” Met. Trans. A., Vol. 20A, pp. 205-214 (1989).

9. Howell, R. A., Montgomery J. S., Van Aken, D. C., “Advancements in Steel for Weight Reduction of P900 Armor Plates,” Transactions of the Army Science Conference, Orlando, FL, awaiting publication.

10. Larson, F.R., Miller, J., “A Time-Temperature Relationship for Rupture and Creep Stresses,” Trans. ASME, Vol. 74, pp. 765−775 (1952).

11. Schulte, A., Unpublished Master’s Thesis in Metallurgical Engineering., Missouri University of Science and Technology.

12. Van Aken, D.C., Hosford, W. F., Reporting Results, Cambridge University Press, New York (2008).

13. Shul’te, Y.A., Sherstyuk, A.A., Kurbatov, M.I., “The Influence of Phosphorus on the Low-Temperature Embrittlement of High Manganese Steel,” Russian Castings, No. 7, pp. 311-313, 1964.

14. Sreenivasan, P.R., “Instrumented Impact Testing-Accuracy, Reliability and Predictability of Data,” Trans. Inidian Institute of Metals, Vol. 49, No. 5, pp. 637-646 (1996).

15. Sreenivasan, P.R. , Moitra, A. Ray, S. K., Mannan, S. L., “Dynamic Fracture Toughness Properties of a 9Cr-1Mo Weld from Instrumented Impact and Drop-weight Tests,” Int. J. Pressure Vessels Piping, Vol, 69, pp. 149-159 (1996).

16. Sreenivasan, P.R., Shastry, C.G., Mathew, M.D., Bhanu Sankara Rao, K., Mannan, S.L., “Dynamic Fracture Toughness and Charpy Transition Properties of a Service-Exposed 2.25Cr-1Mo Reheater Header Pipe,” Vol. 125, pp. 225-233 (2003).

17. Sreenivasan, P.R., Mannan, S.L.,”Dynamic J-R Curves and Tension-Impact Properties of AISI 308 Stainless Steel Weld,” Int. J. Fract., Vol. 101, pp. 229-249 (2000).

18. Acselrad, O., Kalashnikov, I. S., Silva, E. M., Simao, R. A., Achete, C. A., Pereira, L. C., “Phase Transformations in FeMnAlC Austenitic Steels with Si Addition,” Met. Trans. A., Vol. 33A, pp. 3569-3572 (2002).

19. Sato, K., Kazuhiro, T., Inoue, Y., “Age Hardening of an Fe-30Mn-9Al-0.9C Alloy by Spinodal Decomposition,” Scripta Metallurgica, Vol. 22, pp. 899-902 (1988).

20. Leslie, W. C., The Physical Metallurgy of Steels, Hemisphere Publishing (1981).

21. Song, S. H., Zhuang, H., Wu, J., Weng, L. Q., Yuan, Z. X., Xi, T. H.,”Dependence of ductile-to-brittle transition temperature on phosphorus boundary segregation for a 2.25Cr-1Mo Steel”, Mat. Sci. and Eng. A., 486, pp. 433-438 (2007).

22. Wilson, A. D., “Comparing the effect of inclusions on ductility, toughness, and fatigue properties”, ASTM Through Thickness Tension Testing of Steel Symposium, St. Louis, MO (1981).

23. Fruehan, R. J., The Making, Shaping, and Treating of Steel, AISE Steel Foundation, Pittsburg (1998).

24. Li, N., Zhenyu, L., Yiqing, Q., Zhaosen, L., Xianghua, L., Guodong, W., “Solidification Structure of Low Carbon Steel Strips with Different Phosphorus Contents Produced by Strip Casting,” J. Mater. Sci. Tecnol., Vol. 22., No. 6, pp. 755-758 (2006).

APPENDIX B.

SOLID FRACTION DETERMINATION BY NEWTONIAN HEAT-FLOW ANALYSIS

The calculations for solid fraction for determination of the dendrite coherency point in Paper 2: *The Effect of Silicon Content on the Fluidity and Microstructure of Fe-Mn-Al-C Alloys* are derived from Newtonian heat-flow analysis. Current solid fraction modeling is based upon the assumption that Newtonian cooling occurs (i.e. internal temperature gradients are small and neglibilge). From this assumption, the heat balance equation is the phase transformation heat generation minus metal heat loss equal to the heat transferred to the mold:

$$\frac{dQ_L}{dt} - V\rho C_p \frac{dT}{dt} = hA(T - T_o) \quad \text{(Equation 1)}$$

- V – sample volume
- ρ – metal density
- C_p – specific heat of metal
- T – temperature
- t – time
- h – heat transfer coefficient
- A – surface area
- T_o – ambient temperature
- Q_L – latent heat of solidification

Rearranging the terms gives the equation representing the cooling curve captured by the thermocouple:

$$\frac{dT}{dt} = \frac{1}{V\rho C_p}\left[\frac{dQ_L}{dt} - hA(T - T_o)\right] \quad \text{(Equation 2)}$$

Assuming no phase transformation occurs ($\frac{dQ_L}{dt} = 0$), Equation 2 becomes:

$$\frac{dT}{dt} = -\frac{hA(T-T_o)}{V\rho C_p} \quad \text{(Equation 3)}$$

Equation 3 represents the cooling curve without phase transformation otherwise known as the zero curve, Z-curve, or baseline curve. The heat release rate during solidification phase transformation is taken as the difference between the cooling curve (cc) and the zero curve (zc):

$$\frac{dQ_L}{dt} = V\rho C_p[\left(\frac{dT}{dt}\right)_{CC} - \left(\frac{dT}{dt}\right)_{ZC}] \quad \text{(Equation 4)}$$

Integrating over time gives the latent heat of solidification:

$$Q_L = V\rho C_p \int_0^{t_s}[\left(\frac{dT}{dt}\right)_{CC} - \left(\frac{dT}{dt}\right)_{ZC}]\,dt \quad \text{(Equation 5)}$$

Rearranging these terms gives the latent heat formulation:

$$L = \frac{Q_p}{V\rho} = C_p(area\ under\ the\ cc\ first\ derivative\ curve - area\ under\ the\ zc\ first\ derivative\ curve) \quad \text{(Equation 6)}$$

The fraction solid is then determined from ratio of evolved latent heat at time t over the total latent heat during solidification:

$$F_S = \frac{\int_0^t[\left(\frac{dT}{dt}\right)_{CC} - \left(\frac{dT}{dt}\right)_{ZC}]dt}{\int_0^{t_s}[\left(\frac{dT}{dt}\right)_{CC} - \left(\frac{dT}{dt}\right)_{ZC}]dt} \quad \text{(Equation 7)}$$

or

$$F_S = \frac{C_p}{L}\int_0^t[\left(\frac{dT}{dt}\right)_{CC} - \left(\frac{dT}{dt}\right)_{ZC}]dt \quad \text{(Equation 8)}$$

The zero curve was derived from Newton's law of cooling ($\frac{dT}{dt} = kt$) solving for T such that ($T = Cexp(kt)$) and then accounting for heat evolution differences before and after solidification assuming equal heat transfer rate using least squares fit techniques:

$$T_{ZC} = A_1\,exp(A_2 t) + A_3(t - t_o)^3 + A_4(t - t_o)^4 \quad \text{(Equation 9)}$$

- t_o – start time
- A_1 – Newtonian temperature initial condition prior to solidification
- A_2 – Newtonian cooling curve proportionality constant prior to solidification

- A_3 and A_4 – least squares fit constants taking into account temperature initial condition and proportionality constant based on post solidification cooling curve section

A graphical depiction of the mathematical model shows the sequence of the base-line temperature and z-curve plots through to solid fraction calculation. Figure 1 shows the cooling curve collected from a thermocouple experiment (shown as a solid line) and the two z-curves accounting for liquid phase cooling and solid phase cooling. Combining the two z-curves into a singular plot (using Equation 9) is also shown.

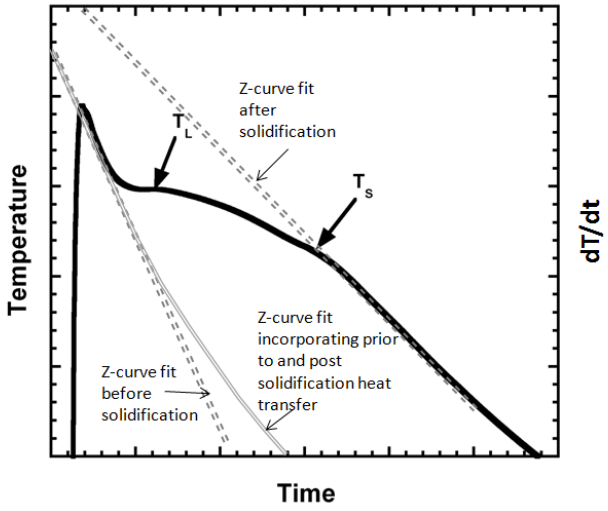

Figure 1. A representative cooling curve is marked with liquidus (T_L) and solidus (T_S) temperatures. The Z-curves are present to show the differences before liquidus and after solidus.

Plotting the first derivative of the temperature and z-curves is shown in Figure 2.

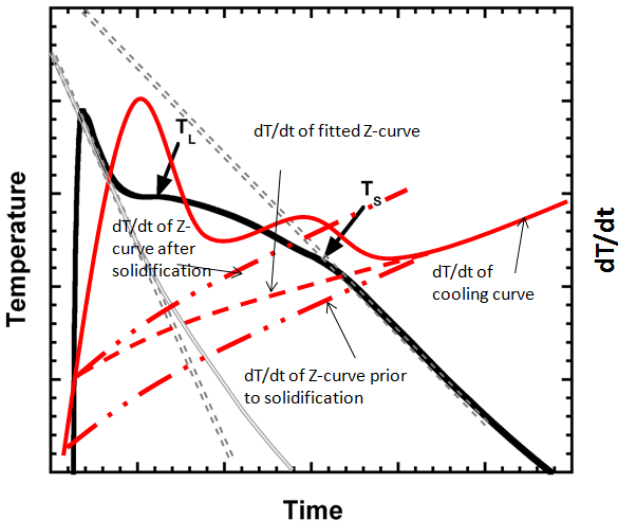

Figure 2. First derivative curves show the differences between the actual cooling curve and the Z-curves. The difference in integral areas between the first derivative fitted Z-curve and cooling curve account for the total latent heat used to calculate the fraction solid.

Lastly, the shaded area shown is the solid fraction computed as difference between the area under the cooling curve first derivative and the area under the zero curve first derivative at time (t) and temperature (T) all over the total difference between the cooling and zero curves.

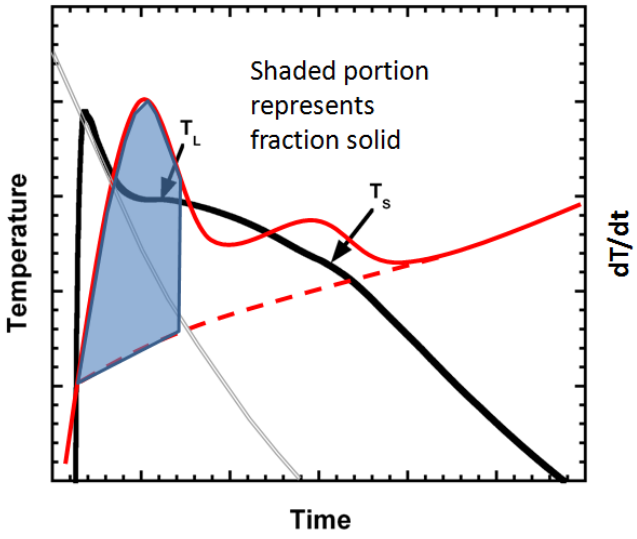

Figure 3. The cooling curve, Z-curve and their first derivatives are shown. The solid fraction is shaded in and taken as a ratio to the total area between the two first derivative curves.

References:

1. Upadhya, K. G., Stefanescu, D. M., Lieu, K., Yaeger, D. P., "Computer-aided Cooling Curve Analysis: Principles and Application in Metal Casing," AFS Transactions, vol. 97, pp 61-66 (1997).

2. Barlow, J.O., Stefanescu, D. M., "Computer-aided Cooling Curve Analysis Revisited," AFS Transactions, vol.105, pp 349-354 (1997).

3. Lekakh, S. L., Missouri University of Science and Technology, Rolla, MO personal communication (March 15, 2009).

APPENDIX C.

SPLIT HOPKINSON-KOLSKY BAR PRINCIPLE

High strain rate ($\dot{\varepsilon} = 3000\ s^{-1}$) material strength and ductility can be measured by compression testing specimens in a split Hopkinson-Kolsky bar. The underlying premise for the split Hopkinson-Kolsky bar (or commonly referred to as the split Hopkinson bar - SHB) is the one dimensional wave theory.

ONE DIMENSIONAL WAVE THEORY (LONGITUDINAL)

The SHB is based on one dimensional wave theory in that all the forces generated to induce a stress strain specimen relation are brought about by a single wave. The wave is produced by a striker bar triggered from a simple valve mechanism and powered by a pneumatic pressure system. The following portion is of wave theory from Weinberger's text explains how a pressure wave can produce stress and strain in a semi-infinite bar.

Infinite bar of constant cross sectional area and dimensioned with respect to position x and annotated by a positive direction (+*x*) and negative direction (-*x*) and the region of interest (Δx). Incident wave of an arbitrary function propagates through the bar from the +*x* to the –*x* direction and exerts a force (*F*) over the cross sectional area (*A*) producing stress (σ_x).

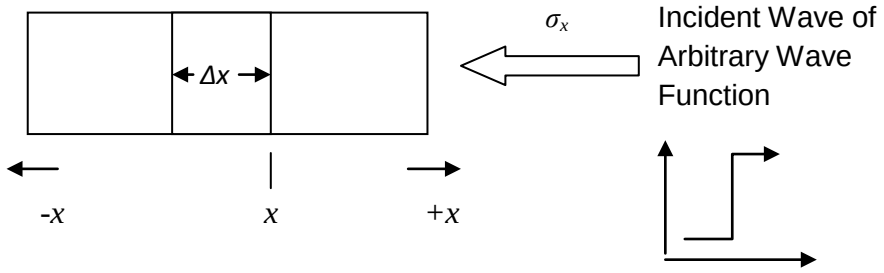

The bar has a density (ρ), modulus (E), and speed of transmitted wave through the bar is (C_o) where:

$$C_o = \sqrt{\frac{E}{\rho}} \qquad \text{(Equation 1)}$$

The force exerted on the bar by the incident wave causes a displacement (*u*) and follows Newton's 2nd Law. Let the displacement in the -*x* direction be a function of the initial condition (*x*) minus the amount it displaced ($C_o t$) due to the incident wave:

$u=f(x-C_o t)$ (Equation 2)

The first derivative of Equation 2 with respect to time (t) gives the velocity due to the incident wave:

$$\frac{du}{dt} = -C_o f'(x - C_o t)$$ (Equation 3)

The second derivative of Equation 2 with respect to time (t) gives the acceleration due to the incident wave:

$$\frac{d^2u}{du^2} = C_o{}^2 f''(x - C_o t)$$ (Equation 4)

The first derivative of Equation 2 with respect to position (*x*) gives the strain from displacement:

$$\frac{du}{dx} = f'(x - C_o t)$$ (Equation 5)

But this is also related to the material modulus:

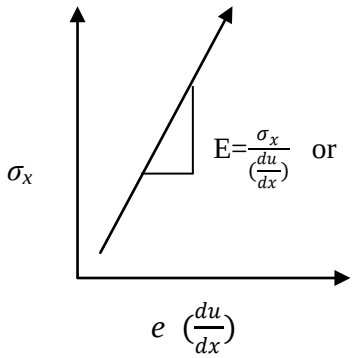

$E=\frac{\sigma_x}{(\frac{du}{dx})}$ or $\frac{du}{dx} = \frac{\sigma_x}{E}$ (Equation 6)

The second derivative of Equation 2 with respect to position (x) is:

$$\frac{d^2u}{dx^2} = f''(x - C_o t) \quad \text{(Equation 7)}$$

By taking the second derivative of Equation 6, Equation 7 is shown to be a function of the modulus and change in stress (σ_x) with respect to position (x):

$$\frac{d^2u}{dx^2} = \frac{1}{E}\left(\frac{d\sigma_x}{dx}\right) \quad \text{(Equation 8)}$$

And Equations 7 and 8 relate by:

$$f''(x - C_o t) = \frac{1}{E}\left(\frac{d\sigma_x}{dx}\right) \quad \text{(Equation 9)}$$

Substituting Equation 9 into Equation 4 yields:

$$\frac{d^2u}{dt^2} = C_o{}^2\left(\frac{1}{E}\right)\left(\frac{d\sigma_x}{dx}\right) \quad \text{(Equation 10)}$$

Substituting Equation 1 into Equation 10 and multiplying both sides by $\rho A \Delta x$:

$$\rho A \Delta x \frac{d^2u}{dt^2} = A \Delta x\left(\frac{d\sigma_x}{dx}\right) \quad \text{(Equation 11)}$$

And rearranging the terms so that:

$$A \Delta x \left(\frac{d\sigma_x}{dx}\right) = \rho A \Delta x \frac{d^2u}{dt^2} \quad \text{(Equation 12)}$$

or

$$Force = A \Delta x \left(\frac{d\sigma_x}{dx}\right) \quad \text{(Equation 13)}$$

Mass = $\rho A \Delta x$ (Equation 14)

Acceleration = $\frac{d^2u}{dt^2}$ (Equation 15)

SPLIT HOPKINSON BAR (COMPRESSION)

History of the split bar as introduced by Kolsky dates back to 1914 in that Hopkinson recognized an elastic pressure bar relates the stresses and length of the wave. The premise is that energy not transmitted or reflected was absorbed by the test specimen. To assist with measurements during experimentation, strain gages were added in the 1960s to measure incident wave, reflected wave, and transmitted wave:

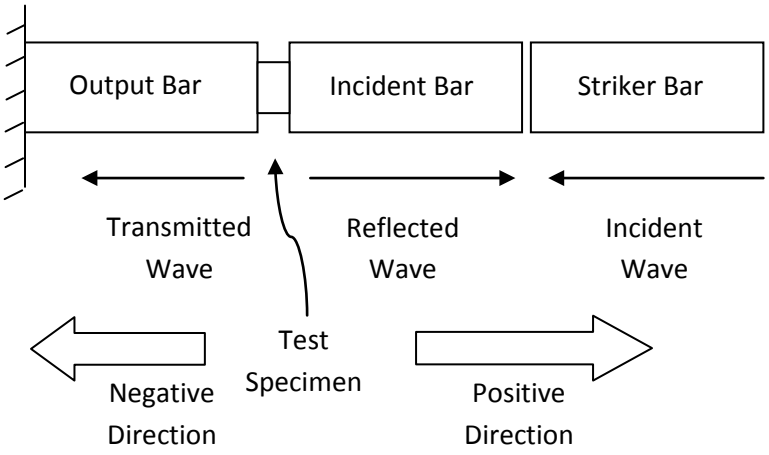

Strain and Velocity in the Incident Bar

Let *f* be an arbitrary wave function in the -*x*-direction and let *g* be an arbitrary wave function in the +*x*-direction so that displacement (*u*) in the incident bar is u_1 and it is a function of the incident wave (u_i) and reflected wave (u_r):

$$u = u_1 = u_i + u_r \quad \text{(Equation 16)}$$

$$u_i = f(x-C_o t) \quad \text{(Equation 17)}$$

$$u_r = g(x+C_o t) \quad \text{(Equation 18)}$$

The total strain is then:

$\varepsilon = \varepsilon_i + \varepsilon_r$ (Equation 19)

or

$\frac{du_i}{dx} = \mathcal{E}_i = f'(x - C_o t)$ (Equation 20)

$\frac{du_r}{dx} = \mathcal{E}_r = g'(x + C_o t)$ (Equation 21)

Velocity at any point in the incident bar is:

$\frac{du}{dt} = u' = u'_i + u'_r$ (Equation 22)

$\frac{du_i}{dt} = -C_o f'(x - C_o t) = -C_o \mathcal{E}_i$ (Equation 23)

$\frac{du_r}{dt} = C_o g'(x - C_o t) = C_o \mathcal{E}_r$ (Equation 24)

Let *u'* for the incident bar be u_1' such that the velocity in the incident bar is then:

$u'_1 = C_o(-\mathcal{E}_i + \mathcal{E}_r)$ (Equation 26)

Strain and Velocity in the Transmitted or Output Bar

Let u_2 be the displacement of the output bar from the transmitted wave and h be the transmitted wave function in the -*x*-direction such that:

$u_t = f(x\text{-}C_o t)$ (Equation 27)

$\frac{du_t}{dx} = \mathcal{E}_t = f'(x - C_o t)$ (Equation 28)

$u'_2 = \frac{du_t}{dt} = -C_o f'(x - C_o t) = -C_o \mathcal{E}_t$ (Equation 29)

$\mathcal{E}_t = \mathcal{E}_i + \mathcal{E}_r$ (Equation 30)

Equation 30 assumes uniform deformation.

NOTE: the wave reflected from the fixed end of the output (transmitted) bar is ignored because it passes after the time of interest.

Strain Rate of Tested Specimen

The strain rate is a function of the difference in bar velocities ($u'_1 - u'_2$) divided by the specimen's instantaneous length (l_s):

$$\dot{\varepsilon}_s = \frac{u'_1 - u'_2}{l_s} \quad \text{(Equation 31)}$$

$$\dot{\varepsilon}_s = \frac{C_o}{l_s}(-\varepsilon_i + \varepsilon_r + \varepsilon_t) = \frac{2C_o\varepsilon_r}{l_s} \quad \text{(Equation 32)}$$

Stress in Specimen

Force in the incident bar (F_1) is a function of the cross sectional area of the incident bar (A_1) the incident bar modulus (E_1) multiplied by the strain ($\varepsilon_i + \varepsilon_r$):

$$F_1 = A_1 E_1(\varepsilon_i + \varepsilon_r) \quad \text{(Equation 33)}$$

Force in the output bar (F_2) is then:

$$F_2 = A_2 E_2 \varepsilon_t \quad \text{(Equation 34)}$$

$F_1 = F_2$ for uniform deformation, therefore:

$$\sigma_s = \frac{F_2}{A_s} = \frac{A_2 E_2 \varepsilon_t}{A_s} \quad \text{(Equation 35)}$$

Where A_s is the instantaneous cross sectional area. Therefore stress and strain given as True Stress and True Strain to account for specimen geometry change

Experimental Calculations

Experimentally derived stress, strain and strain rate data is computed from a strain gauge output voltage which is converted to strain data by accounting for a strain gauge calibration factor and an initial offset value. Strain gauge voltage (*v*) output is a function of the stain gauge's gauge factor (*GF*) times the bridge excitation voltage or bridge factor (*BF*) times the strain ($\mathcal{E}$) divided by a constant (*k*) usually a value of 4:

$$v = \frac{GF \cdot BF \cdot \varepsilon}{4} \approx \frac{GF \cdot BF \cdot \varepsilon}{k} \quad \text{(Equation 36)}$$

The strain (measured in micro strain ($\mu\mathcal{E}$)) requires that the strain gauge output voltage be multiplied by a strain gauge calibration (*SG CAL*) value defined as the strain gauge constant (*k*) divided by the gauge factor (*GF*– provided by the manufacturer at 2.05) and Bridge Factor (*BF*– determined experimentally at 30 volts):

$$SG\ CAL = \frac{\mathcal{E}}{v} = \frac{k}{GF \cdot BF} \quad \text{(Equation 37)}$$

NOTE: *SG1 CAL* (Incident Strain Gauge Calibration) and *SG2 CAL* (Output Strain Gauge Calibration) were equal for the data presented in this thesis.

The strain value of the pressure bar (equal to the value produced by multiplying together equations 36 and 37) in the initial rest condition prior to the start of testing does not equal zero. This prior test strain value is defined as the strain gauge offset (*SG OFFSET*) and is subtracted to account for the initial condition. Thus, the corrected micro strain ($\mu\mathcal{E}$) for each gauge is:

$$SG1 \cdot (SG\ CAL) - (SG1\ OFFSET) = \mu\mathcal{E} \quad \text{(Equation 38)}$$

$$SG2 \cdot (SG\ CAL) - (SG2\ OFFSET) = \mu\mathcal{E} \quad \text{(Equation 39)}$$

For the experiment conducted here, SG CAL = 32,520.3 $\frac{\mu\mathcal{E}}{v}$, and the SG1 OFFSET = 47.425 μƐ and SG2 OFFSET = 8.384 μƐ. Appling equations 36 through 39 to the strain gauge output voltage yields an unshifted set of pulses that look as follows:

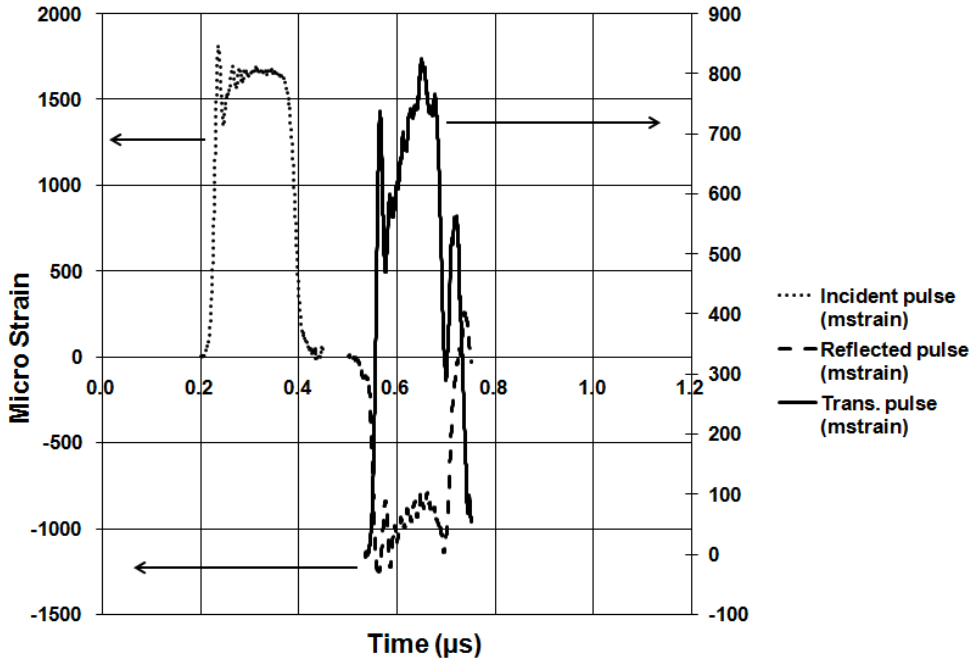

Figure 1. Micro strain data per unit time is collected from two strain gauges (one on the incident bar and one on the output or transmitted bar) showing the incident pulse wave as it is reflected and transmitted through the system. The noise or "ringing" of the pressure bar visible and most apparent at the start of each pulse.

Pulses must be shifted to the same time in order to calculate stress, strain, and strain rate in the test specimen. Since location of the strain gauges is known (x_i – incident bar location or x_{tr} – transmitted or output bar) and the speed of sound through the each bar is known (C_o – both bars composed of the same material), the time shift can be calculated by:

$$t = time\ incident\ wave\ is\ at\ the\ specimen = \frac{x_n}{C_o} \qquad \text{(Equation 40)}$$

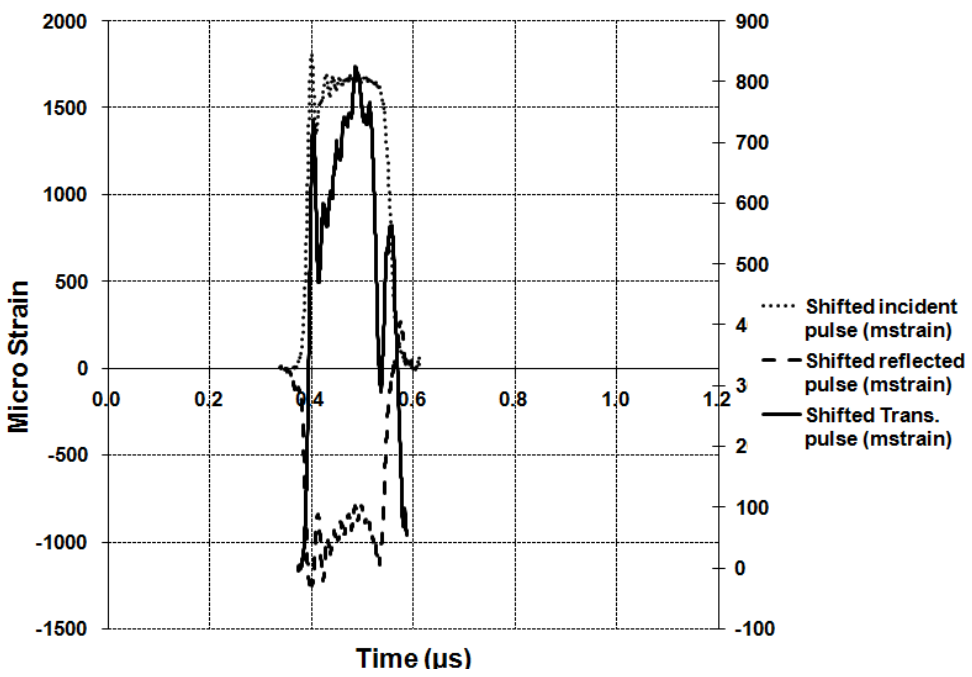

Figure 2. Applying Equation 40 shifts the pulses to the same relative time necessary to compute specimen stress, strain and strain rate.

The incident bar velocity (v_i) is:

$$\frac{\mu\mathcal{E}_i - \mu\mathcal{E}_r}{1E6} C_o = v_i \qquad \text{(Equation 41)}$$

The output (transmitted) bar velocity (v_{tr}) is:

$$\frac{\mu\mathcal{E}_{tr}}{1E6} C_o = v_{tr} \qquad \text{(Equation 42)}$$

The engineering strain rate (e') is:

$$\frac{v_i - v_{tr}}{L} = e' \qquad \text{(Equation 43)}$$

where L is the initial length of the specimen. Engineering strain (e) was engineering strain rate (e') multiplied by time (t).

$$e = e't \quad \text{(Equation 44)}$$

In Microsoft Excel, Equation 44 translates to:

$$e_n = e_{n-1} + \frac{1}{2}(e'_n + e'_{n-1}) \cdot [time\ step\ (for\ \boldsymbol{n}\ to\ \boldsymbol{n-1})]$$

True strain ($\mathcal{E}$) was calculated as:

$$\mathcal{E} = -\ln(1 - e) \quad \text{(Equation 45)}$$

NOTE: the negative value is applied since the test is in compression.

Engineering Stress (S) is then the microstrain ($\mu\mathcal{E}$) divided by 1,000,000 to convert back to strain, times the specimen modulus (E) and times the ratio of the cross sectional areas of the bar (both incident and output bar are the same diameter) and specimen ($\frac{A_{Bar}}{A_{Specimen}}$) to account for the delta:

$$\frac{\mu\mathcal{E}_{tr}}{1E6} E \frac{A_{Bar}}{A_{Specimen}} = S \quad \text{(Equation 46)}$$

True stress (σ) is:

$$\sigma = S(1 - e) \quad \text{(Equation 47)}$$

NOTE: as with the true strain, the true stress is also negative in order to plot the data on a positive binary coordinate axis (see Figure 3).

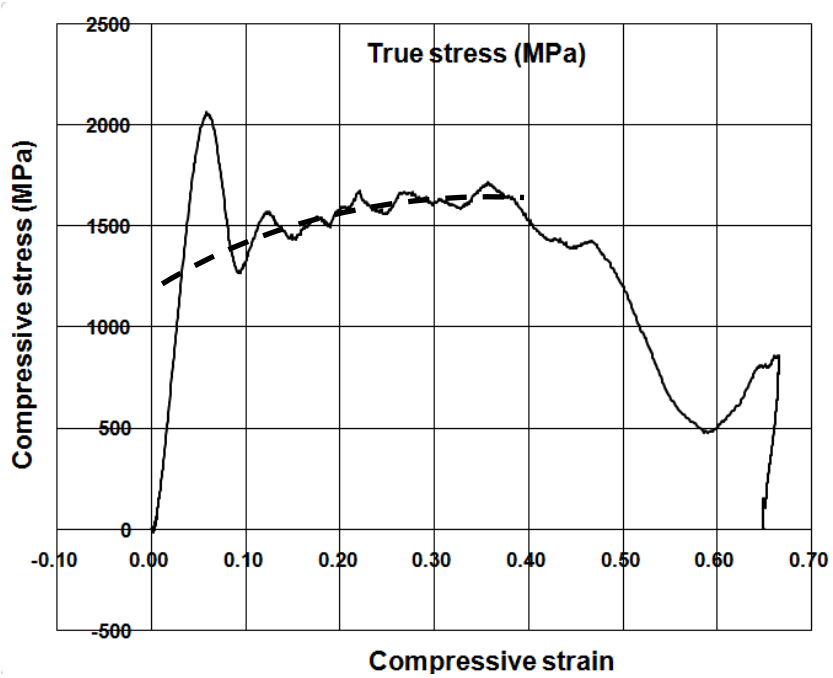

Figure 3. The final plot from equations 45 and 47 shows the noise at the start of the test. Steady state is approximated through the initial period shown by the dotted line.

References:

1. Weinberger, H. F., A First Course in Partial Differential Equiations, Blaisdell Publishing, New York (1965).

2. Kolsky, H., Stress Waves in Solids, Dover Publications (1963).

BIBLIOGRAPHY

[1] MIL-PRF-32269, Military Performance Specification for Perforated Homogeneous Armor.

[2] Hansen, J.S., P.C. Turner. "A Process for Making Lightweight Cast-Steel Armor." Advanced Materials and Processes 144.2 (1993): 22-24.

[3] Frommeyer, G., U. Brux, "Microstructures and Mechanical Properties of High-Strength Fe-Mn-Al-C Light-Weight TRIPLEX Steels." Steel Research International 77 (2006): 627-633.

[4] Technical Steel Data for IC 4130 Alloy (2009) http://www.ruger.com/Casting/T-Steel.html

[5] "$10.5M for MRAP P900 Armor Plating." Defense Industry Daily (2007) http://www.defenseindustrydaily.com/105m-for-mrap-p900-armor-plating-03836/

[6] Kirk Stoffel, Army Research Lab, Private Conversation (2008).

[7] American Society of Metals. "Manganese-Aluminum Steel," Brady, G. S., H.R. Clauser. Materials Handbook, 11th Ed (1977): 497.

[8] Goretskii, G. P., K.V. Gorev. "Phase Equilibria in Fe-Mn-Al-C Alloys." Journal of Russian Metallurgy 2 (1990): 217-221.

[9] Acselrad, O., Kalashnikov, I. S., Silva, E. M., Simao, R. A., Achete, C. A., L.C. Pereira. "Phase Transformation in Fe-Mn-Al-C Austenite Steels with Si Addition." Metallurgical Transactions A 33A (2002): 3569-3572.

[10] "The Physical Metallurgy of Steels." Leslie, W. C. Hemisphere Publishing (1981).

[11] Acselrad, O., Kalashnikov, I. S., Silva, Khadyev, M. S., E. M., Simao. "Diagram of Phase Transformation in the Austenite of Hardened Alloy Fe-28Mn-8.5Al-1C-1.25Si as a result of Aging due to Isothermal Heating." Metal Science and Heat Treatment 48 (2006): 543-553.

VITA

Ryan Andrew Howell was born 20 November 1973 in Joplin, Missouri. He attended the University of Missouri – Rolla from 1992 to 1997 and received a B. S. in Mechanical Engineering (May 1997) and commissioned as a Second Lieutenant into the Field Artillery branch of the United States Army.

Upon graduation, he attended the military's Field Artillery Officer Basic Course at Fort Sill, Oklahoma and was assigned to A Battery, 38th Field Artillery Regiment, Camp Stanley, South Korea where he served as Platoon Leader and Battery Motor Officer from December 1997 to December 1998. He was reassigned to United States Army Garrison Command as the Post Army Emergency Relief Loan Officer and Army Community Service Executive Officer at Fort Carson, Colorado. On 12 June 1999, Ryan married Katherine Marie Dolan of Tipton, IA in Fulton, Missouri where she then joined Ryan in Colorado Springs. Transferring to 3rd Battalion, 29th Field Artillery Regiment, Ryan served as Company Fire Support Officer to C Company, 1st Battalion, 12th Infantry Regiment, was promoted to Captain, and then served as Battalion Fire Direction Officer to 1-12 IN. Ryan moved back to Fort Sill to attend the Field Artillery Captain's Career Course and Command and Staff Services School. In April of 2002, he was assigned as the Battalion Fire Direction Officer for 1st Battalion, 10th Field Artillery Regiment and deployed for Operation Desert Spring to Kuwait through till September 2002. In January 2003, then CPT Howell deployed with 1-10 FA in support of the initial entry force into Iraq for Operation Iraqi Freedom for which he received a Bronze Star. Upon completion of his second tour to the Middle East, he took command of A BTRY, 1-10 FA and completed transition training to deploy as infantry in the city of Ba'quba, Diyala Province

Iraq for his third Middle East tour for which he received his second Bronze Star and Combat Action Badge.

In 2005, CPT Howell was reassigned to serve as Assistant Battalion Operations Officer. During this service he was accepted into the Army Acquisition Corps Uniformed Scientist and Engineer program. Prior to attending graduate school, he attended the Army's Command and General Staff Services School and Intermidiate Qualification courses at Fort Gordon, Georgia and Austin, Texas respectively. He returned to the University of Missouri – Rolla, was promoted to Major, and studied armor material development as a full-time metallurgical engineering graduate student. MAJ Howell was recognized as the outstanding new graduate student and as the outstanding senior graduate student. He received his Ph.D. in Metallurgical Engineering from the Missouri University of Science and Technology in August 2009 under Dr. David C. Van Aken.